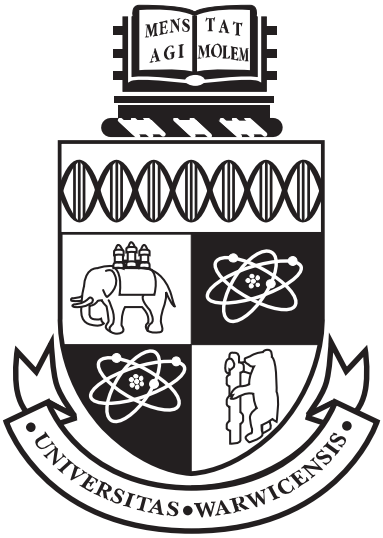

Post-Common-Envelope Binaries from the Sloan Digital Sky Survey

by

Alberto Rebassa Mansergas

Thesis

Submitted to the University of Warwick

for the degree of

Doctor of Philosophy

Department of Physics

November 2008

THE UNIVERSITY OF
WARWICK

Todo pasa y todo queda, pero lo nuestro es pasar,
pasar haciendo caminos, caminos sobre el mar.

Nunca perseguí la gloria, ni dejar en la memoria
de los hombres mi canción; yo amo los mundos sutiles,
ingrávidos y gentiles, como pompas de jabón.

Me gusta verlos pintarse de sol y grana, volar
bajo el cielo azul, temblar súbitamente y quebrarse...

Caminante, son tus huellas el camino y nada más;
caminante, no hay camino, se hace camino al andar.

Al andar se hace camino y al volver la vista atrás
se ve la senda que nunca se ha de volver a pisar.

Caminante no hay camino sino estelas en la mar...

Cuando el jilguero no puede cantar. Cuando el poeta
es un peregrino, cuando de nada nos sirve rezar.
”Caminante no hay camino, se hace camino al andar...”

Golpe a golpe, verso a verso.

Antonio Machado

Contents

List of Tables

List of Figures

Acknowledgments

I deeply thank Dr. Boris Gänsicke for his excellent guidance through my PhD, for his help and suggestions, and most importantly for making it possible for me to develop my qualities as a researcher. I am also deeply thankful for his trust in me in this and other projects. Without him this thesis would have been impossible.

I am greatly indebted to Prof. Tom Marsh for clarifying all kind of data reduction problems, and specially I am deeply thankful for his patience at the beginning of my PhD. I also thank him for providing his software.

I thank Dr. Pablo Rodríguez-Gil for his help in my first individual observations, for his suggestions and comments, and for sharing his vast observing experience. I thank Dr. Matthias Schreiber for his trust in me as his future research assistant, and for clarifying theoretical problems I found during my thesis. I thank Dr. John Southworth for proof-reading this thesis, and for his suggestions and comments. I thank Ada Nebot Gómez-Morán for the interesting discussions on binary evolution. I thank Dr. Linda Schmidtobreik for having me as a visitor student at the European Southern Observatory in Chile. I thank Dr. Jorge Panei for providing me his white dwarf mass-radius relation models. I thank Detlev Koester for for providing his white dwarf model atmospheres. I thank Isabelle Baraffe for discussions on the properties of low mass stars.

I deeply thank Yike for her love, for making me happy, for her support.

Finally thousand thanks to my parents. For being always present, even in the distance. For their education, for their love.

Declarations

I declare that this thesis has not been submitted in any previous application for a higher degree. Chapters 1-6 provide information gathered from the literature, except Chapter 4 (Sect.4.3), where I present observations carried out by myself and/or other collaborators. In Chapters 7-9 I present my own work, and in Chapter 10 I use the results obtained throughout this thesis and other observations that have not been published yet.

Chapter 7 is based on Rebassa-Mansergas et al. [2007]: A.Rebassa-Mansergas, B.T.Gänsicke, P.Rodríguez-Gil, M.R. Schreiber, and D. Koester, ”Post-Common-Envelope Binaries from SDSS. I: 101 white dwarf main-sequence binaries with multiple SDSS spectroscopy” MNRAS.382.1377R (2007).

Chapter 8 is based on Rebassa-Mansergas et al. [2008]: A. Rebassa-Mansergas, B. T. Gänsicke, M.R. Schreiber, J. Southworth, A.D. Schwope, A. Nebot Gómez-Morán, A. Aungwerojwit, P. Rodríguez-Gil, V. Karamanavis, M. Krumpe, E. Tremou, R. Schwarz, A. Staude and J. Vogel: ”Post-Common-Envelope Binaries from SDSS - III. Seven new orbital periods” MNRAS.1.112 (2008)

Chapter 9 is based on: A. Rebassa-Mansergas, B. T. Gänsicke, M.R., D. Koester and P.Rodríguez-Gil ”A catalogue of white dwarf-main sequence binaries from SDSS DR6”. To be submitted to MNRAS.

Abstract

Close binaries containing a compact object make up a wide variety of objects. The evolution of all close binaries depends crucially on the rate at which angular momentum is extracted from the binary orbit. The two most important sources of angular momentum loss are the common envelope phase and magnetic braking. Both processes have been known for long but are still poorly understood, and significant progress will only be achieved if they can be calibrated using innovative observational input. Post-common-envelope binaries are probably among the best-suited class of objects to improve our understanding of close binary evolution, because (1) they are both numerous and well-understood in terms of their stellar components, and (2) they are not contaminated by the presence of an accretion disc. The Sloan Digital Sky Survey provides the possibility of dramatically improving the observational size of known post-common-envelope binaries, with already more than 1500 white dwarf-main sequence binaries having been identified. The major task is now to identify those systems that have undergone a common envelope and to measure their binary parameters. This new, large sample of well-studied post-common-envelope binaries will then provide the much-needed constraints for further development of binary evolution theory.

Through my PhD I dedicated all my efforts towards identifying post-common-envelope binaries, obtaining orbital periods of these new systems, and determining their stellar parameters. For this purpose, I adopted the following strategies:

(1) About 10% of the white dwarf-main sequence binaries in the Sloan Digital Sky Survey have more than one survey spectrum available. By measuring radial velocities from

the Na I $\lambda\lambda$ 8183.27,8194.81 absorption doublet and/or the Hα emission line in the different spectra from each object, I was able to identify radial velocity variable stars, which are prime candidates for being post-common-envelope binaries. This method resulted in the identification of 18 new post-common-envelope binaries among 130 white dwarf-main sequence binaries with multiple Sloan spectra. In addition, using a spectral decomposition/model atmosphere analysis I determined the stellar parameters such as mass, radius, and temperature for the white dwarfs, and spectral types of the main sequence stars in these 130 white dwarf-main sequence binaries, along with the distances to the systems. I discussed also an apparent systematic issue with the spectral type-radius relation of the companion stars in those white dwarf-main sequence binaries.

(2) Follow-up observations by our team have lead to the identification of 89 post-common-envelope binaries from Sloan, which triples the number previously known. Intense radial velocity studies have lead to the determination of orbital periods for 42 of these systems, seven of them discussed in detail in this thesis.

(3) I have developed a procedure based on χ^2 template fitting and signal-to-noise ratio constraints to identify white dwarf-main sequence binary candidates in the Sloan Digital Sky Survey Data Release 6 spectroscopic data base. This catalogue contains 1591 white dwarf-main sequence binaries identified in this way. Using a spectral decomposition/model atmosphere analysis, I have derived white dwarf temperatures, masses, companion star spectral types, and distances, and discussed the distributions of these parameters. In addition, I have analysed the selection effects of white dwarf-main sequence binaries in Sloan. This sample is an excellent data base for future follow-up observational studies of white dwarf-main sequence binaries.

Chapter 1

Overview of Close Binary Evolution

1.1 Introduction

Most stars are formed as parts of binary or multiple systems [1]. Therefore the study of binary star evolution represents an important part of studying stellar evolution. While the majority of wide main sequence (MS) binaries evolve as if they were single stars and never interact, a small fraction are believed to undergo mass transfer interactions (Sect. 1.2.1). Once the more massive MS star becomes a red giant it eventually overfills its Roche-lobe. Dynamically unstable mass transfer exceeding the Eddington limit ensures onto the companion star, which consequently also overfills its own Roche-lobe. The two stars then orbit inside a common envelope (CE, Sect 1.2.2), and friction inside this envelope causes a rapid decrease of the binary separation. Orbital energy and angular momentum are extracted from the binary orbit and lead to the ejection of the envelope, exposing a post-common-envelope binary (PCEB). After the envelope is expelled, PCEBs keep on evolving towards shorter orbital periods through angular momentum loss via gravitational radiation and, for companion stars above the fully convective mass limit ($\simeq 0.3$ $M_{\odot}$), by magnetic wind braking (Sect. 1.3.1). In binaries that do not undergo a CE phase both components evolve almost like single stars and keep their wide binary separations. This is the situation given when

[1] Note though that the binary frequency declines for stars of spectral type later than G, and that only 30% of the M stars are formed as part of binaries [Lada, 2006]. Since the stellar initial mass function broadly peaks at 0.1-0.5 $M_{\odot}$ (M stars, see Chapter 2), then most stellar systems in the Galaxy might consist of single rather than binary or multiple stars.

no mass transfer takes place, or when the mass transfer from the H-core burning donor star (case A; this is the first epoch in which the leaving MS star undergoes a gentle growth of its radius), from the He-core burning donor star (case B; in this case the expansion is more rapid, towards the first giant branch), or from the post-He-core burning donor star (case C; also rapid increase of radius, in this case the expansion is towards the asymptotic giant branch) to the MS companion is stable. A predicted consequence is hence a strongly bi-modal binary separation and orbital period distribution among post-MS binaries, with PCEBs concentrated at short orbital periods, and non-PCEBs at long orbital periods.

The scenario outlined above is thought to be a fundamental formation channel for a wide range of astronomical objects such as double degenerate white dwarfs, cataclysmic variables and super-soft X-ray sources. Some of these objects will eventually end their lives as type Ia supernovae, which are of great importance for cosmological studies.

In the following sections of this Chapter, I give an overview of close binary evolution. In Sect. 1.2, I provide a description of the physical phenomena involved, and give details of the CE phase. In Sect. 1.3, I deal with the evolution of PCEBs. Finally in Sect 1.4, I describe the objectives of my thesis based on the theoretical background detailed in Sect. 1.2 and Sect. 1.3. Throughout this thesis, I will use the term WDMS binary to refer to the total class of white dwarf plus main sequence binaries, and PCEBs to those WDMS binaries that underwent a CE phase. I also define a PCEB as a WDMS binary with an upper limit to its orbital period $\leq 300\,\mathrm{d}$, a PCEB candidate as a WDMS binary with period $300\,\mathrm{d} \leq P_{\mathrm{orb}} \leq 1500\,\mathrm{d}$, following Fig. 10 from Willems & Kolb [2004], which shows the period and mass distribution of the present-day WDMS binary population at the start of the WDMS binary phase.

1.2 Formation of Post-Common-Envelope Binaries

Wide MS binaries are considered to be the progenitors of close compact binaries. Population synthesis models predict that $\sim$25% of the MS binary population suffer mass transfer interactions [Willems & Kolb, 2004]. The stellar components of the remaining $\sim$75% population evolve as if they were single stars. Even though the majority of interacting binaries

are expected to undergo a CE phase and become close compact binaries, the details of their evolution crucially depends on the conditions of mass transfer, and consequently on the initial masses of both stars.

1.2.1 Mass Transfer

Roche geometry

Under the assumptions of Roche geometry (the orbits are circular, and the star that loses mass, or donor star, is tidally locked), two orbiting stars have a total potential given by the sum of the gravitational potential of the stars and the rotational potential of the system (Eq. 1.1, where ω is the angular frequency of the orbit, r_1 and r_2 are the positions of the two stars, M_1 and M_2 are the masses of the stars, being M_1 the more massive component at the initial MS binary configuration, and G is the gravitational constant). The shape and dimension of the equipotential surfaces depend on the masses of the stars (or the mass ratio $q = M_2/M_1$), and the orbital separation, respectively.

$$\phi(\vec{r}) = -\frac{GM_1}{|\vec{r}-\vec{r}_1|} - \frac{GM_2}{|\vec{r}-\vec{r}_2|} - \frac{1}{2}(\vec{\omega}\times\vec{r})^2 \tag{1.1}$$

The equipotential surfaces are mainly spherical for stars of small radius, and the shape is distorted for larger radii. When the radii are sufficiently large the equipotential surfaces of the stars cross each other (Lagrangian points). In Fig 1.1 I provide a schematic representation of Roche geometry for $q = 0.4$. As seen in the figure, there exist five Lagrangian points $L_1 - L_5$[2]. The two surfaces touching at L_1, the inner Lagrangian point, are called Roche-lobes. Mass transfer occurs when one of the stars overfills its Roche-lobe. If both stars remain inside their Roche-lobes the system is *detached*. When one of the stars overfills its Roche-lobe, mass transfer is then initiated towards the companion, and its shape is the same as its Roche-lobe. The system is considered as *semi-detached*, and the Roche-lobe radius of the donor star can be written as [Eggleton, 1983]:

$$R_L = \frac{a\,0.49\,q^{2/3}}{0.6\,q^{2/3} + \ln(1+q^{1/3})} \tag{1.2}$$

where R_L is the radius of a sphere with the same volume as the Roche-lobe. As I will show in Sect 1.2.2, two stars in a binary may both overfill their Roche-lobes. In this case the

[2]Only L_1-L_3 have physical interpretation in this context.

system is in *contact*. When this happens a CE is formed (Sect. 1.2.2), and matter can be expelled through L_2 and L_3.

Mass transfer in MS binaries

When the more massive component in a MS binary departs from the MS, its radius starts to increase. The orbital separations of these binaries are normally wide enough for the Roche equipotential surfaces to be spherical around each star, and to allow their evolution as if they were single, i.e. no mass transfer interactions. Nevertheless, in $\sim$25% of the cases the evolved star is expected to overfill its Roche-lobe and mass transfer is then initiated to the MS companion [de Kool & Ritter, 1993; Willems & Kolb, 2004]. The system's response to the mass loss can be extremely different depending on the initial masses of the stars.

If the donor is less massive than the accretor, and the thermal timescale[3] of the donor star is short enough to adjust the star to its equilibrium radius, the mass transfer will be then dynamically and thermally stable. This can be understood considering the conservation of the total angular momentum of the system: since the donor is less massive, the transferred material ends up closer to centre of mass of the system, consequently losing angular momentum. In order to conserve the angular momentum of the system the binary separation increases, so does the Roche-lobe radius (Eq. 1.2). Henceforth the donor star stops filling its Roche-lobe, and mass transfer is stopped. The radius of the donor star though is continuously expanding, as it is evolving through the giant branch (GB), or asymptotic giant branch (AGB), and consequently overfills its Roche-lobe again, leading to another process of mass transfer, and to an additional increase of the Roche-lobe radius. This situation remains until the donor leaves the GB, or AGB, and becomes a white dwarf. The resulting system is then a wide WDMS binary, with a final orbital separation larger than the initial MS binary separation.

If the donor star is more massive than its companion, the mass transfer will be dynamically unstable. In this case the transferred material moves further from the centre of mass, and the separation decreases in order to conserve the angular momentum. The

[3]Estimate of how long a given star would shine with its current luminosity if the only power source were the conversion of gravitational potential to heat. The thermal timescale is also known as Kelvin-Helmholtz (KH) timescale, and can be written as $\tau_{\rm KH} = \frac{1}{2}\frac{E_{\rm grav}}{L} \approx \frac{GM^2}{RL}$.

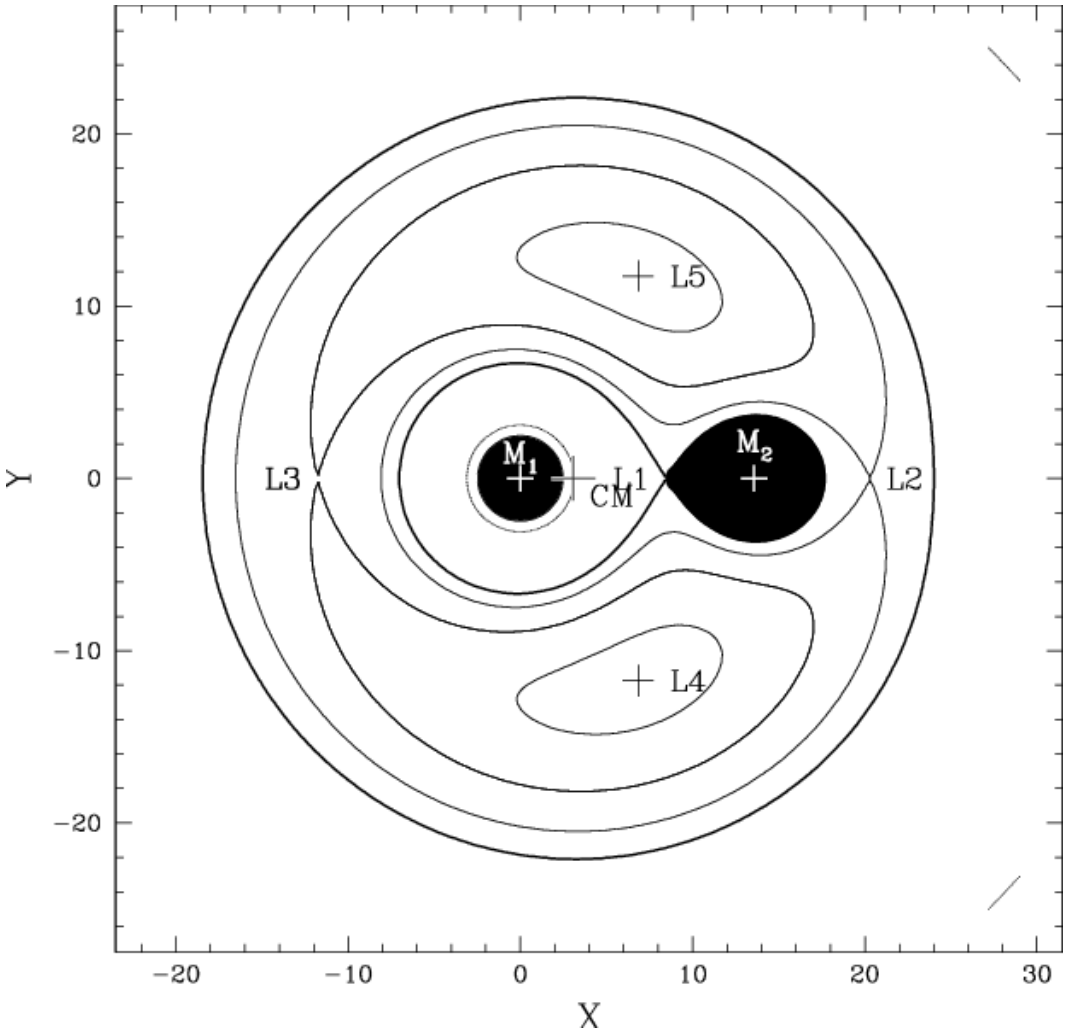

Figure 1.1: Cross section of Roche-lobe equipotential surfaces in the orbital plane of the semi-detached eclipsing binary BP Muscae, a binary with q = 0.4. The Lagrangian points are represented by L_1-L_5. The secondary star with mass M_2 is overfilling its Roche-lobe, and mass transfer results to the primary companion of mass M_1. CM represents the centre of mass of the system. The coordinates are given in $R_\odot$ units. Taken from Carrier et al. [2003].

Roche-lobe radius decreases, and consequently the mass transfer rate increases considerably. Under these circumstances the donor star can never readjust to its thermal equilibrium radius, and consequently the mass transfer is also thermally unstable. The non-stopping inflow of material on to the companion makes itself to be driven out of thermal equilibrium and consequently it will fill its own Roche-lobe. Hence, the system initiates a contact phase, referred to in the literature as the CE phase. The friction inside the envelope drives a rapid ($\sim 10^3$ years) decrease of the binary separation through an in-spiralling process. The energy and angular momentum extracted from the binary orbit ultimately eject the envelope and give birth to a hot sub-dwarf/WDMS binary, surrounded by a planetary nebula. The hot white dwarf cools down and the planetary nebula is dispersed, and the system is finally observed as a PCEB.

The formation of a He- or a C/O- or O/Ne/Mg-core white dwarf depends on when the mass transfer is initiated [Iben & Livio, 1993; Willems & Kolb, 2004]. If mass transfer is initiated before the more massive star in the initial MS binary burns He into C, the white dwarf will contain a He-core ($M_{WD} \lesssim 0.5\ M_{\odot}$). If mass transfer initiates when a substantial amount of He has been burnt into C/O, the resulting white dwarf will have a C/O-core ($0.5M_{\odot} \lesssim M_{WD} \lesssim 1.1M_{\odot}$). In the same way, if mass transfer starts when a substantial amount of C/O has been burnt into Ne/Mg, the resulting white dwarf will contain an O/Ne/Mg-core ($1.1M_{\odot} \lesssim M_{WD} \lesssim 1.38M_{\odot}$).

1.2.2 Common Envelope Phase

Qualitative description

Even though the concept of CE evolution is straightforward, it involves a large number of hydrodynamic and thermodynamic processes on both time and scale lengths spanning very large ranges. Moreover, it is intrinsically a three-dimensional problem.

Paczynski [1976] considered for the first time that the binary components move inside a non-co-rotating envelope, transferring angular momentum and energy, and reducing the orbital separation. The energy extracted from the orbit might be used to expel the envelope before the components merge. The importance of establishing the efficiency of

deposition of orbital energy into the envelope became evident. This efficiency is defined as

$$\alpha_{\rm CE} = \frac{\Delta E_{\rm bind}}{\Delta E_{\rm orb}} \tag{1.3}$$

where $\Delta E_{\rm orb}$ is the change in the orbital energy of the binary between the beginning and the end of the spiral-in process, and $\Delta E_{\rm bind}$ is the binding energy of the ejected material. Eq 1.3 neglects any other source of energy apart from the orbital energy. This comes from the fact that CE evolution is rapid compared to the thermal time scale of the envelope, and so radiative losses are small. Livio [1989] and Iben & Livio [1993] noted that, even though $\alpha_{\rm CE}$ depends strictly on the orbital energy, the efficiency of deposition of energy into the envelope could be modified by other physical processes. Two factors are believed to reduce $\alpha_{\rm CE}$: the efficiency in the energy transport [Taam et al., 1978; Meyer & Meyer-Hofmeister, 1979; Livio & Soker, 1984; Soker et al., 1984], and non-spherical effects [Bodenheimer & Taam, 1984; Taam & Bodenheimer, 1989; Livio & Soker, 1988, see the definition of $\beta_{\rm CE}$ in the next paragraph]. Among the physical processes that can increase the efficiency $\alpha_{\rm CE}$, the recombination energy in the ionisation zones is the most plausible (i.e. the energy released when the material of the envelope recombines is an extra energy that can be used to expel the envelope). In fact, Han et al. [1994, 2002] include a second α-parameter in Eq 1.3, characterising the fraction of the initial thermal energy content on the CE available for its ejection. Nevertheless this has been strongly criticised by Soker & Harpaz [2003], since (1) Eq 1.3 depends strictly on the orbital energy, and (2) an enhancement in mass-loss rate provides final orbital distributions similar to those obtained including an extra α-parameter.

Livio & Soker [1988] not only considered the efficiency $\alpha_{\rm CE}$, but also defined two more parameters: $\beta_{\rm CE}$ and $\gamma_{\rm CE}$. $\beta_{\rm CE}$ parametrises the importance of three dimensional effects, and is defined as $\tau_{\rm decay}/\tau_{\rm kep}$, where $\tau_{\rm decay}$ is the orbital decay timescale, and $\tau_{\rm kep}$ is the Keplerian timescale of the envelope. Thus when $\beta_{\rm CE} \leq 1$ no spherical symmetry can be assumed, as the energy is deposited locally. $\gamma_{\rm CE}$ is defined as $\tau_{\rm spin-up}/\tau_{\rm decay}$, where $\tau_{\rm spin-up}$ is the timescale for the spiralling-in binary to spin up the envelope, and describes the efficiency of spin-up of the envelope as a result of deposition of angular momentum. It is expected that significant spin-up of the envelope will occur for $\gamma_{\rm CE} \leq 1$. This would reduce the relative velocity between the secondary and the envelope prolonging the spiralling-in process, since the drag force decreases.

The α-formalism

The change in gravitational energy $\Delta E_{\rm orb}$ in Eq. 1.3 can be written as

$$\Delta E_{\rm orb} = \frac{GM_2M_{\rm c}}{2a_{\rm f}} - \frac{GM_2(M_{\rm e}+M_{\rm c})}{2a_{\rm i}}, \tag{1.4}$$

where $M_{\rm c}$ is the mass of the giant core, $M_{\rm e}$ is the mass of the envelope, and $M_{\rm g}$ is the mass of the giant (note that $M_{\rm e}$ is approximately the mass lost by the giant and consequently $M_{\rm c}$+$M_{\rm e}$ is approximately the mass of the giant $M_{\rm g}$), M_2 is the mass of the companion, and $a_{\rm i}$ and $a_{\rm f}$ are the initial and final separations, respectively.

Several interpretations of the binding energy $\Delta E_{\rm bind}$ of the envelope and the binary can be found in the literature [Tutukov & Yungelson, 1979; de Kool, 1990; Nelemans et al., 2000; Nelemans & Tout, 2005]. Among them the most commonly used is [Nelemans & Tout, 2005]:

$$\Delta E_{\rm bind} = \frac{G(M_{\rm c}+M_{\rm e})M_{\rm e}}{\lambda R_{\rm g}}, \tag{1.5}$$

where $R_{\rm g}$ is the radius of the giant and λ is a parameter that depends exclusively on the structure of the red giant. Dewi & Tauris [2000] found that λ not only strongly depends on the evolutionary stage, but also that $\lambda \sim 0.2-0.8$[4]. λ can be approximated as [Webbink, 2008]

$$\lambda^{-1} \sim 3.000 - 3.816m_{\rm e} + 1.041m_{\rm e}^2 + 0.067m_{\rm e}^3 + 0.316m_{\rm e}^4, \tag{1.6}$$

where $m_{\rm e}$ is $M_{\rm e}/M_{\rm g}$.

From equations Eq 1.3, Eq 1.4 and Eq 1.5 we obtain

$$\frac{GM_{\rm g}M_{\rm e}}{R_g\lambda} = \alpha_{\rm CE}\left(\frac{GM_{\rm c}M_2}{2a_{\rm f}} - \frac{GM_{\rm g}M_2}{2a_{\rm i}}\right) \tag{1.7}$$

This equation represents the outcome of the envelope as determined from the energy balance between the binding and the orbital energies, referred in the literature as the α-formalism. Values of $\alpha_{\rm CE}$ close to unity imply that the orbital decay is very efficient in expelling the envelope. On the contrary, a low $\alpha_{\rm CE}$ permits the formation of shorter orbital period PCEB systems, as the process is less efficient. Typical values of $\alpha_{\rm CE}$ are in the range $\sim$0.15-1 [Bodenheimer & Taam, 1984; Taam & Bodenheimer, 1989, 1991; Livio & Soker, 1988; de

[4]In some cases, particularly in the AGB, it is possible that $\lambda > 5$.

Kool, 1990; Terman et al., 1994; Maxted et al., 2006; Afşar & Ibanoğlu, 2008]. A plausible value as low as 0.054 was found for V 471 Tau, an eclipsing DA+K PCEB [O'Brien et al., 2001]. These results tell us that α_{CE} is far away from being a universal constant, and that it probably depends on different binary parameters, such as the masses of the stars, the evolutionary stage of the primary, and the nature of the secondary. Politano & Weiler [2007] have initiated a comprehensive population synthesis study of variable CE efficiency parameters. In this work (the first of the series) they assume both a power law dependence, $\alpha_{CE} = M_2^n$, and a dependence in which α_{CE} approaches 1 for large secondary masses and $\alpha_{CE} = 0$ below some assumed cutoff mass, $\alpha_{CE} = 1 - M_{cut}/M_2$, where M_{cut} is the cutoff mass. Politano & Weiler [2007] find that the distribution of PCEB secondary star masses varies significantly depending on the model used, and claim that a well-defined, statistically complete sample of PCEBs would be desirable for a comparison with their population models.

Quantitative remarks of the Common Envelope phase

Although hydrodynamic studies have provided much insight into the phases of the CE stage, calculations at high spatial resolution are still necessary to further quantify the outcome of the envelope. As noted by Taam & Ricker [2006] and Ricker & Taam [2008] "in recent years the development of sophisticated computer methodologies has made it possible to achieve this goal. Specifically, adaptive mesh refinement techniques have advanced to the point where such calculations can now be envisioned".

The γ-formalism

First Nelemans et al. [2000], and then Nelemans & Tout [2005] reconstructed the evolution of observationally confirmed white dwarf binaries (double degenerates or DDs). A double degenerate configuration is in principle achieved after two mass transfer processes, either both being unstable (i.e. two CE phases), or the first being stable and the last unstable (i.e. one CE phase). As expected, the binary separations in DDs are very short, making these systems excellent candidates of Supernova Type Ia progenitors [Langer et al., 2000; Parthasarathy et al., 2007]. Knowledge of the orbital periods and masses of DDs makes it easier to reconstruct their evolution, as one can assume that the observed white dwarfs were

the cores of giant stars from which they ascend. Thus the effect of the CE phase on the orbit can be reconstructed. Nelemans et al. [2000], and Nelemans & Tout [2005] demonstrated that the first phase of mass transfer can not generally be described by the α-formalism, as they measured negative values of $\alpha_{\rm CE}\lambda$. This result was later confirmed by van der Sluys et al. [2006] for the efficiency $\alpha_{\rm CE}$. Thus Nelemans et al. [2000] introduced a new algorithm based explicitely on the equation for angular momentum balance

$$\frac{\Delta J}{J} = \gamma \frac{\Delta M_{\rm tot}}{M_{\rm tot}} = \gamma \frac{M_{\rm e}}{M_{\rm g} + M_2} \tag{1.8}$$

and found that this γ-formalism could explain both phases of the evolution[5]. Unfortunately the γ-formalism still does not give a physical understanding of the process, and the results are still open to debate [Webbink, 2008]. It is worth mentioning though that recently Beer et al. [2007] proposed a physical mechanism that could explain the γ-formalism, based on the accretion energy of some of the transferred matter. This energy could eject the remaining matter and hence the systems could avoid the CE phase. Nevertheless, while comparing their results with the α- and γ-formalisms, neither of them give a full description.

In Fig. 1.2 I provide distributions of reconstructed values of both γ and $\alpha_{\rm CE}\lambda$ from Nelemans & Tout [2005] derived from their analysis of the observed sample of DDs (top), and observed pre-cataclysmic variables (bottom). Values of $\alpha_{\rm CE}\lambda$ cluster below ~ 0.5, implying that the orbital separations after the ejection of the envelope are considerably lower than the initial separations. Consequently the energy equation does not work for DDs because it predicts too short orbital periods. The angular momentum equation though can explain all kinds of mass and $P_{\rm orb}$ combinations with γ values clustering in a small range [Webbink, 2008]. As a consequence, the orbital periods for PCEBs will concentrate to shorter orbital periods in the α-formalism than in the γ-formalism, and a longer tail to longer orbital periods will be expected in the γ-formalism.

[5]Note that γ is not $\gamma_{\rm CE}$. Note also that Nelemans & Tout [2005] never affirmed there is no CE phase at the first stage, but only that the α-formalism does not explain it well. Nevertheless, the fact that $\alpha_{\rm CE}\lambda$ are negative implies that the orbital energy has increased, i.e. quasi-conservative mass transfer. Consequently these DDs have likely not undergone a CE in the first process of mass transfer [Webbink, 2008].

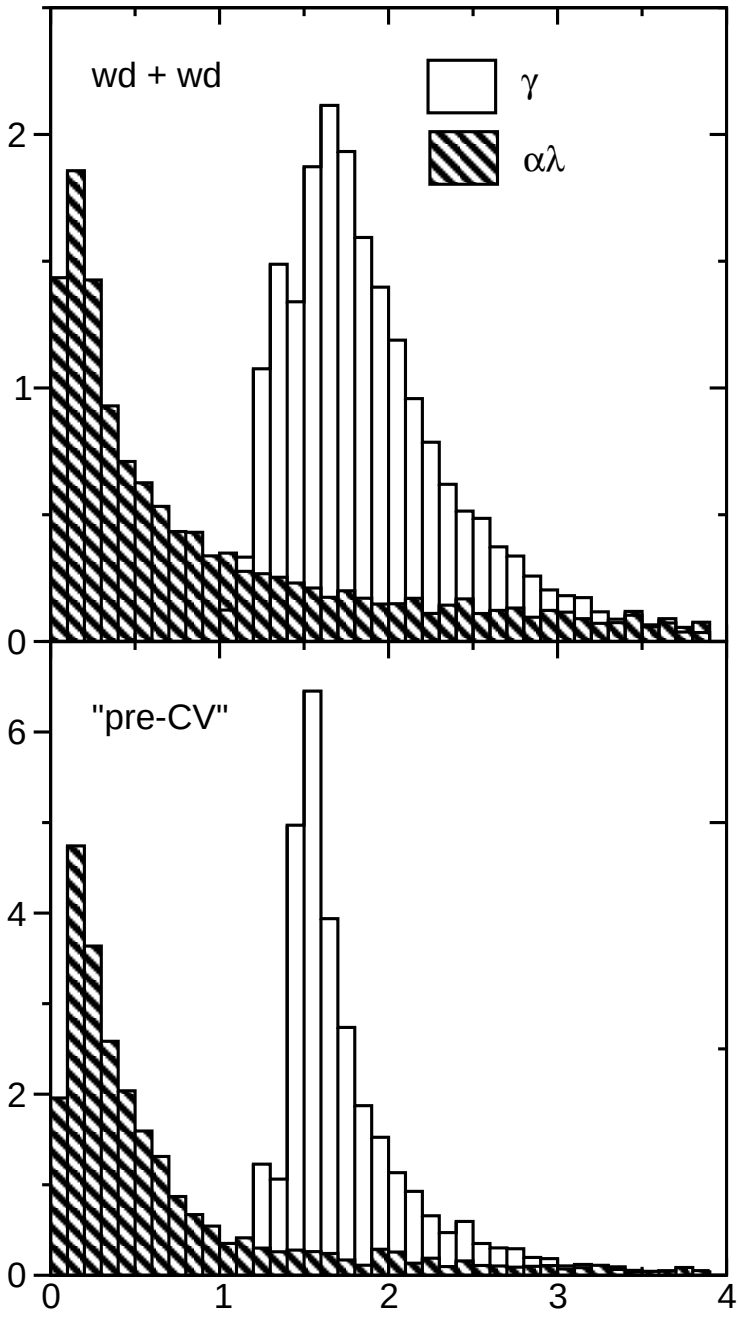

Figure 1.2: Histograms of the reconstructed γ (white) and $\alpha_{CE}\lambda$ (white and black) values for the last phase of mass transfer that leads to the formation of DDs (top) and pre-cataclysmic variables (bottom). Taken from Nelemans & Tout [2005].

1.3 Evolution of Post-Common-Envelope Binaries

After the ejection of the envelope, PCEBs continue decreasing their orbital separations (and orbital periods) through the action of angular momentum loss (AML) via the emission of gravitational waves (referred in the literature as gravitational radiation, GR), and for companion stars above the fully convective mass limit, and orbital periods short enough for the secondary stars to be tidally locked ($P_{orb} \lesssim 10$ days), via the action of magnetic wind braking [MB, magnetically-coupled stellar wind from the tidally locked companion, Verbunt & Zwaan, 1981; Mestel & Spruit, 1987; Hameury et al., 1988]. Depending on the nuclear time scale of the companion star (τ_{nuc}) and the AML timescale (τ_{AML}), the evolution follows two different paths.

In general, PCEBs contain low-mass MS secondaries, and consequently $\tau_{nuc} \gg \tau_{AML}$ in this kind of stars (see Chapter 2). Since $\tau_{AML(MB)} \sim 10^8$ years [Verbunt & Zwaan, 1981], this implies that the orbital separation shrinkage due to AML eventually makes the secondary fill its Roche-lobe and a second phase of mass transfer ensues, in this case from the low-mass companion to the white dwarf. If the mass transfer is thermally and dynamically stable, a cataclysmic variable is formed (see Sec. 1.3.1). If the mass transfer is dynamically stable, but thermally unstable the system appears as a super-soft X-ray source. If the mass transfer is dynamically and thermally unstable the system might enter a second CE phase, which can lead to the coalescence of the two stars. This implies that the secondary star mass has to be significantly larger than the white dwarf mass. In these cases the evolution is more likely to follow the description below.

In some cases PCEB companions are A-F stars, considerably more massive than the above low-mass MS companions. These stars do not experience AML due to MB and consequently they must wait for nuclear evolution to initiate mass transfer, i.e. they evolve into red giants before mass transfer begins. The radius expands, the star overfills its Roche-lobe, and mass transfer is initiated to the white dwarf. Since these stars are generally more massive than the white dwarf primaries, mass transfer is dynamically and thermally unstable, and a second CE phase is likely initiated, which results in the formation of an ultrashort-period DD. It is also possible, but not likely, that the mass transfer is both thermally and adiabatically stable. In this case, the system is a symbiotic star with orbital period of $\gtrsim 1$

day.

1.3.1 Evolution of cataclysmic variables

In the earlier 1970s it was already known that the orbital periods of cataclysmic variables (CVs) are of order of hours, and that the material transferred from the Roche filling secondaries eventually forms an accretion disc [Paczyński, 1971]. Population synthesis studies predict that 0.5-2% of the initial wide MS binary population become CVs [de Kool, 1992]. The time spent to become a CV after the ejection of the envelope is $\sim$2 Gyr [Schreiber & Gänsicke, 2003].

The orbital period distribution of CVs (see Fig. 1.3) reveals three striking features: (1) a long period cutoff at $\sim$ 12 hours, (2) a short period cutoff at $\sim$ 80 minutes, (3) an absence of systems between $\sim 2-3$ hours.

The long period cutoff is a consequence of dynamically stable mass transfer in CVs.

The absence of systems between $\sim 2-3$ hours, known as the period gap, can be easily explained if AML due to MB somehow drops, and AML is driven out by GR. The drop of MB can be associated with the transition of the secondary from a radiative core to a fully convective state ($M_{sec} \simeq 0.3\ M_{\odot}$, $P_{orb} \sim 3$ hours). This produces a reduction in the mass transfer rate (from $\dot{M} \sim 10^{-8} - 10^{-9}\ M_{\odot}\ yr^{-1}$ above the gap to $\dot{M} \sim 10^{-10} - 10^{-11}\ M_{\odot}\ yr^{-1}$ below the gap, where $\dot{M}$ symbolises the mass transfer), and allows the secondary to shrink towards its thermal equilibrium radius, causing a period of detachment [Rappaport et al., 1983; Spruit & Ritter, 1983]. The CV remains detached until the star fills its Roche-lobe again at $P_{orb} \sim 2$ hours.

The minimum period cutoff occurs when the mass of the secondary star is so low that it becomes degenerate. Mass loss in this kind of star produces an increase in radius, and consequently the orbital orbital separation and orbital period of the CV increase also [Paczynski & Sienkiewicz, 1981; Rappaport et al., 1982]. Another way of understanding this is by considering the thermal timescale of the secondary. When the secondary approaches the minimum period the thermal timescale is extremely long, and the star can not readjust to its mass loss, consequently increasing its radius.

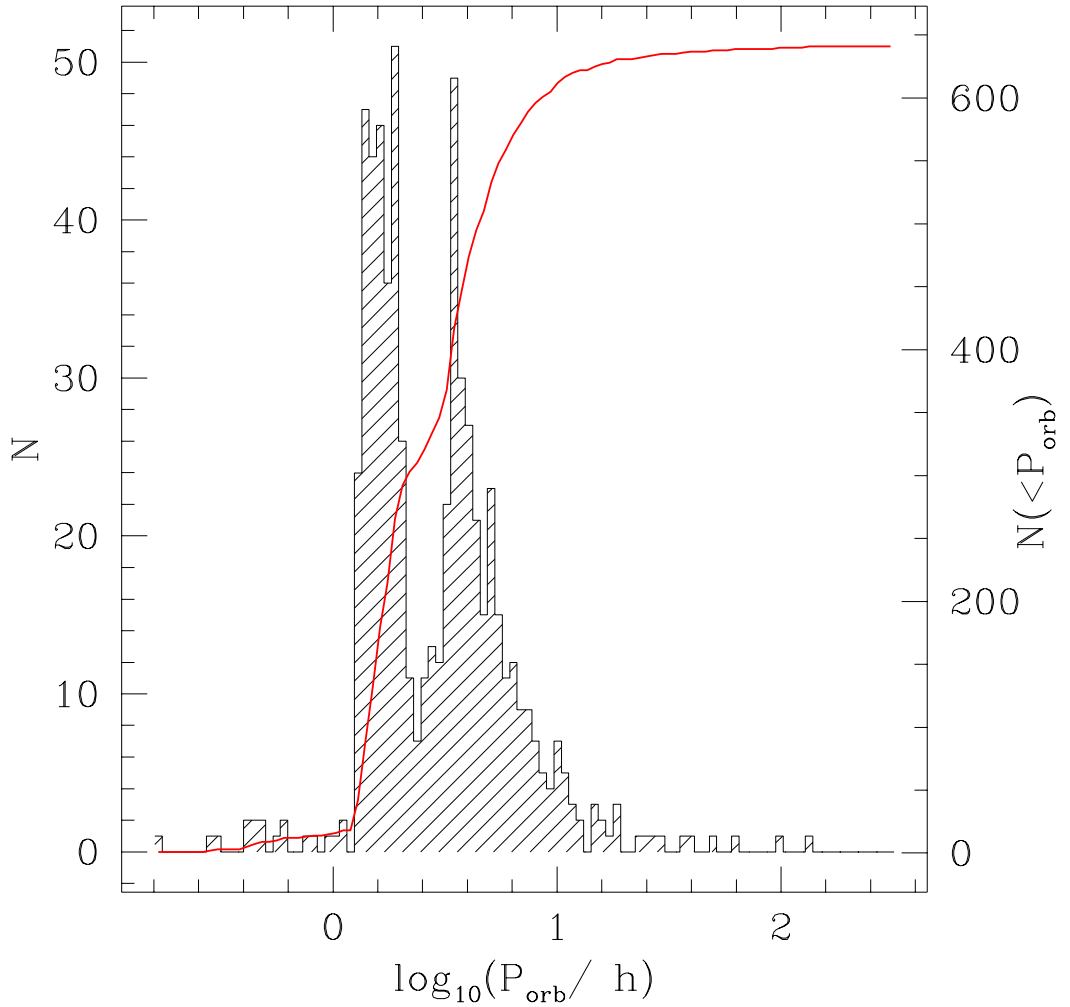

Figure 1.3: Current observed orbital period distribution of CVs. The most striking features are the minimum period cutoff at ∼80 minutes, the absence of systems between $\sim 2-3$ hours, the period gap, and the long period cutoff at $\sim$ 12 hours. The red solid line represents the cumulative distribution with numbers, $N < P_{\rm orb}$, as labelled on the right axis. Taken from Davis et al. [2008].

Disagreement with the observations

The standard evolutionary scenario of CVs provided above, together with the CE theory presented in Sect 1.2.2 were used to develop population synthesis models for CVs. When comparing these results with those obtained from observational studies, discrepancies arise. Space densities obtained from population synthesis studies [$\rho \sim 10^{-4} - 10^{-5}$ pc^{-3} de Kool, 1992; Kolb, 1993; Politano, 1996; Howell et al., 1997], are one order of magnitude larger than those obtained from observational studies [$\rho \sim 10^{-5} - 10^{-6}$ pc^{-3}, Downes et al., 1986; Ringwald, 1996; Schreiber & Gänsicke, 2003; Pretorius et al., 2007; Ak et al., 2008]). Population synthesis models predict that $\sim$99% of the intrinsic current CV population are below the gap, $\sim$70% of them are minimum period bouncers [Kolb, 1993], and that 18% of the zero-age CV population contain brown-dwarf secondaries, $\sim$80% of them formed as CVs below the minimum period [Politano, 2004]. In contrast to this, an accumulation of systems near the minimum period is not observed [Patterson, 1998, see though Gänsicke et al. 2008, in preparation], and similar numbers of systems can be found above and below the period gap of the observed orbital period distribution (see Fig 1.3). The fact that the minimum period calculated [$\sim$70 minutes, Kolb & Baraffe, 1999; Barker & Kolb, 2003; Howell et al., 2001] is shorter than the observed minimum period ($\sim$80 minutes, Fig 1.3) exacerbates the mismatch between the observed and calculated distributions. In fact different theories have been proposed as an alternative to the standard scenario [Schenker et al., 2002; Andronov et al., 2003; Taam & Spruit, 2001]. However, none of them have been successful in matching all features found in the observed orbital period distribution, and the issue is still open to debate.

1.4 Motivation and structure of the thesis

Close binary evolution has been mainly developed from the efforts carried out by theoretical studies. As shown in the previous sections both population synthesis and empirical studies demonstrate that theoretical results are far from describing the CE phase and MB completely. A fundamental problem in advancing our understanding of CE evolution and MB in close binaries is then the shortage of stringent observational constraints that can be used

to test and calibrate the theory. Attempts to understand close binary evolution were initially focused on the study of double cores inside a planetary nebula [de Kool, 1990; Livio, 1996]. These cores are the most direct evidence of a CE phase, and the study of their properties are ideal to test the theoretical predictions, as a planetary nebula ensures that the observed parameters are the same as those at the end of the CE phase. Unfortunately this kind of system is very rare, as most PCEBs are very old and have undergone significant orbital evolution after the CE [Hjellming & Taam, 1991]. Observational tests of the CE phase, based on measurements of $^{12}C/^{13}C$ and $^{16}O/^{17}O$ ratios on the surface of the secondary star, were carried out by Sarna et al. [1995] and Marks & Sarna [1998]. However, results provided by these studies were not conclusive [Dhillon et al., 2002].

Real progress in our understanding of close binary evolution is most likely to arise from the analysis of PCEBs that are both numerous and well-understood in terms of their stellar components – such as PCEBs containing a white dwarf and a MS star. Furthermore, PCEBs are nearby and accessible with 2-8 meter telescopes, and they are not contaminated by the presence of an accretion disc. Schreiber & Gänsicke [2003] showed that the sample of well-studied PCEBs is not only small, but being drawn mainly from "blue" quasar surveys, it is also heavily biased towards young systems with low-mass secondary stars – clearly not representative of the intrinsic PCEB population, and can hence not be used for comparison with population models [e.g. Willems & Kolb, 2004]. The Sloan Digital Sky Survey (SDSS, Chapter 6) is currently dramatically increasing the number of known white dwarf plus main sequence binaries, paving the way for large-scale observational PCEB population studies (Chapter 9).

We have initiated an observational programme to identify the PCEBs among the SDSS WDMS binaries, and to determine their binary parameters. Identifying all PCEBs among the SDSS WDMS binaries, and determining their binary parameters is a significant observational challenge. A large sample of PCEBs will answer three important questions in close binary evolution: (1) The disrupted MB scenario predicts an increase of the relative numbers of PCEBs by a factor $\sim$1.8 in the range of secondary spectral types M3-M5 [Politano & Weiler, 2006, see Fig. 1.4 left panel]. Assuming that MB is indeed disrupted, it is expected in the case of 100 new PCEBs an increase from $\sim$35 for M3-M4 to $\sim$65 for

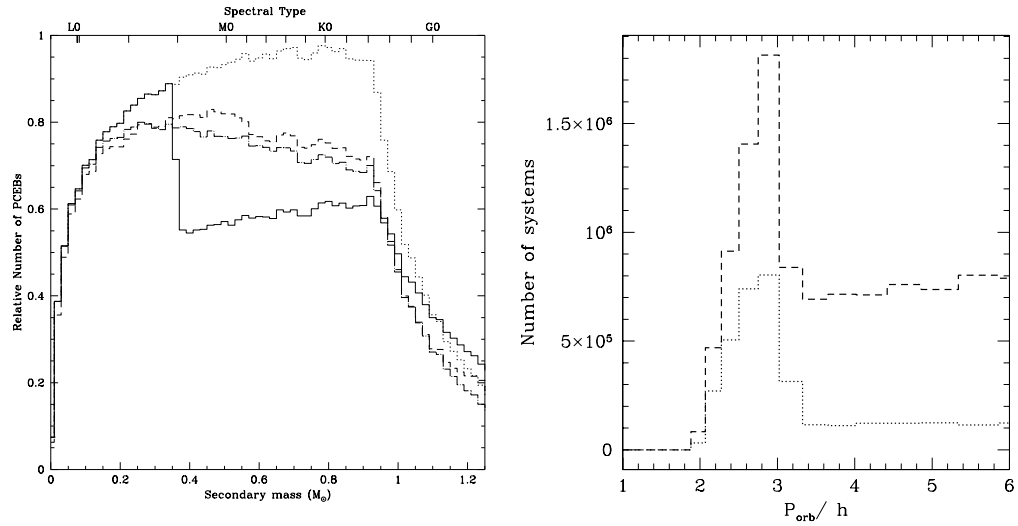

Figure 1.4: Left: Theoretical distributions of the secondary mass in present-day PCEBs for four different assumed AML models: GR only (dotted line), GR+RMB (reduced MB, dashed line [Andronov et al., 2003]), GR+IMB (intermediate MB, dash-dotted line, [Ivanova & Taam, 2003]), and GR+DMB (solid line, disrupted MB or standard scenario). The y-axis has been arbitrarily normalised to facilitate comparison. Taken from Politano & Weiler [2006]. Right: orbital period distribution of the combined population of detached CVs and PCEBs for an initial mass ratio $n(q) = 1$, $\alpha_{\rm CE} = 0.6$ (dashed line) and $\alpha_{\rm CE} = 0.1$ (dotted line). The peak apparent in all the distributions is due to the population of detached CVs, the PCEB orbital period distribution increases monotonically with $P_{\rm orb}$. Taken from Davis et al. [2008].

M4-M5. An additional test for the validity of MB is also discussed in Davis et al. [2008]: assuming that MB is disrupted, the orbital period gap distribution of detached WDMS binaries (considering as detached the combination of those WDMS binaries with orbital periods between 2-3 hours, and detached CVs crossing the period gap), shows a peculiar distribution that can be observationally tested (see Fig. 1.4 right panel); (2) The strength of AML can be estimated by comparing the orbital period distributions of PCEBs at different times of the PCEB binary evolution; (3) The α-formalism and γ-formalism differ in particular in the predicted orbital period distribution of long orbital period PCEBs (Sect. 1.2.2). Consequently, identifying the long orbital period end of the PCEB population will clearly constrain current theories of CE phase.

It is expected that a fraction of WDMS binaries will be eclipsing. Eclipsing binaries are the key to determine accurate stellar masses and radii. Because short-period WDMS binaries underwent CE evolution, they are expected to contain a large range of white dwarf masses, which will be important to populate the empirical white dwarf mass-radius relation (see Chapter 2). Eclipsing WDMS binaries will also be of key importance in filling in the mass-radius relation of low-mass stars at masses $\lesssim 0.4$ M$_{\odot}$ (see Chapter 2).

In this thesis I present preliminary results of our ongoing project dedicated to identify and measure orbital periods of PCEBs and the stellar parameters of both WDMS binaries and PCEBs. The structure is as follows. In Chapter 2 I give details of the physical properties of white dwarfs and low-mass MS stars. In Chapter 3 I give some insight into the spectral properties of WDMS binaries. In Chapter 4 I provide a full description of the observations carried out for the analysis presented in this thesis. In Chapter 5 I explain the methods I used to measure the orbital periods of PCEBs. In Chapter 6 I provide a description of the Sloan Digital Sky Survey. In Chapters 7, 8 and 9 I present my results: in Chapter 7 I make use of SDSS spectroscopic repeat observations to identify 18 PCEBs and PCEB candidates from radial velocity variations. In Chapter 8 I present follow-up spectroscopy and photometry of 11 PCEB candidates identified in Chapter 7. In Chapter 9 I present a catalogue of 1591 SDSS WDMS binaries. Finally, in Chapter 10 I discuss my results and give the conclusions of my thesis.

Chapter 2

Physical Properties of White Dwarfs and M-type Stars

In this Chapter I give some insight into the physical properties of both white dwarfs and M-type MS stars, and I point out how the study of WDMS binaries can help improving our understanding of these kinds of stars.

2.1 White Dwarfs

2.1.1 Luminosity of a white dwarf

White dwarfs [see reviews by D'Antona & Mazzitelli, 1990; Koester, 2002; Hansen, 2004] are the end product of stellar evolution for the vast majority of MS stars, with the exception of the most massive stars. Contrary to normal MS stars, where the gravitational collapse is prevented by the thermal pressure generated by nuclear energy, in white dwarfs this contraction is balanced by the pressure of the degenerate electrons. White dwarfs evolve in time as they decrease their luminosity, a process referred to in the literature as the white dwarf cooling [Mestel, 1952][1] (standard notation, where time is given in Gyrs, and mass in solar units):

[1] There exist updated versions of the model [Wood, 1995; Hansen, 1999; Chabrier et al., 2000]. The Mestel [1952] model though remains a reasonable order of magnitude description for the white dwarf cooling [Hansen, 2004].

$$L(t)/L_{\odot} = (2.3 \times 10^{-3}) \times M \times t^{-7/5} \tag{2.1}$$

At the stage of transition from progenitor to white dwarf the luminosity is given by the energy generated by nuclear fusion in the core of the star. Nuclear fusion stops once the star enters the white dwarf cooling track, and the luminosity of the white dwarf is given by the thermal energy that the white dwarf possesses.

Energy transport

In the core of the white dwarf, the transport is dominated by the electron conduction, whilst in the thin, non-degenerate envelope the transport is carried out by radiative and/or convective diffusion on a much slower time-scale.

2.1.2 Atmospheres

Sion et al. [1983] classified white dwarfs according to their stellar atmospheres. Thus DA white dwarfs have H dominated atmospheres, and DB white dwarfs He dominated atmospheres, the DA-type being the most dominant among white dwarfs. The reason why white dwarfs are composed of pure H atmospheres is that the gravity is so strong that all heavier elements sediment/sink down below the visible layers, i.e. the atmosphere. For moderately warm (young) white dwarfs, the diffusion time scales of metals are only of the order of days, so this happens very quickly [Koester & Wilken, 2006]. In the case of DB white dwarfs (pure He atmospheres), the outer H layer has been completely lost, and He as the next lightest element floats up to the top. There is no yet completely consistent explanation for the DB white dwarfs [Wolff et al., 2002]. A small number of white dwarfs though are composed of different elements in their atmospheres, such as C (DQ) and other heavy elements (DZ). Hot white dwarf atmospheres composed of ionised He are called DO, and cool stars which show no identifiable features, i.e. a continuous spectrum (see Chapter 3 for a definition of spectrum), are labelled as DC. Pre-white dwarf atmospheres are mainly composed of He and/or a mixture of C, N and O, or H depending on the previous evolution from the MS. The H-rich stars remain their whole lives as DA. He- and CNO-rich stars initiate their life as hot DO, or PG1159 stars, and the diffusion of heavy elements is supposed

to leave behind a surface of H as they cool. Thus at $T_{\rm eff} \sim 30000$ K there appear to be no He dominated atmospheres (DB gap). Nevertheless, the convection zone develops as these systems cool, and consequently at $T_{\rm eff} \sim 30000 - 12000$ K, 25% of these objects revert back to DB-type. Below $T_{\rm eff} \sim 10000$ K, the chemical evolution becomes more complicated, and is not fully understood [Bergeron et al., 2001].

2.1.3 White dwarf mass distribution and mass-radius relation

It has been shown that the mass distribution of (DA) white dwarfs peaks sharply around $\sim$0.6 $M_{\odot}$ [Koester et al., 1979; Bergeron et al., 1995a; Finley et al., 1997; Liebert et al., 2005, see also Chapter 7 and Chapter 9]. White dwarf masses can in principle be measured indirectly under the assumption of a mass-radius ($M-R$) relation [Chandrasekhar, 1935; Hamada & Salpeter, 1961; Wood, 1995; Panei et al., 2000, 2007]. This implies knowledge of the effective temperature and surface gravity of the white dwarf, that can be obtained fitting the Balmer absorption lines (see Chapter 3 for a definition of Balmer lines, and Chapter 7 and Chapter 9 for the application of the method), and/or knowledge of the gravitational redshift, that can be measured if the systemic velocity of the white dwarf is known (e.g. in a wide binary).

$M-R$ relations make use of several assumptions regarding the composition of the interior and the surface layers. However, it has to be stressed that the $M-R$ relation has not yet been observationally tested. In fact, the distribution of empirical masses and radii shows a large scatter around the theoretical $M-R$ relations [Schmidt, 1996; Reid, 1996; Provencal et al., 1998, see Fig. 2.1]. Procedures in which no $M-R$ relation for white dwarfs is assumed to estimate the mass and the radius separately can then help constraining these relations. Eclipsing binaries in which at least one of the components is a white dwarf, such as WDMS binaries, are excellent systems to measure the mass and the radius separately [Pyrzas et al., 2008, and references therein].

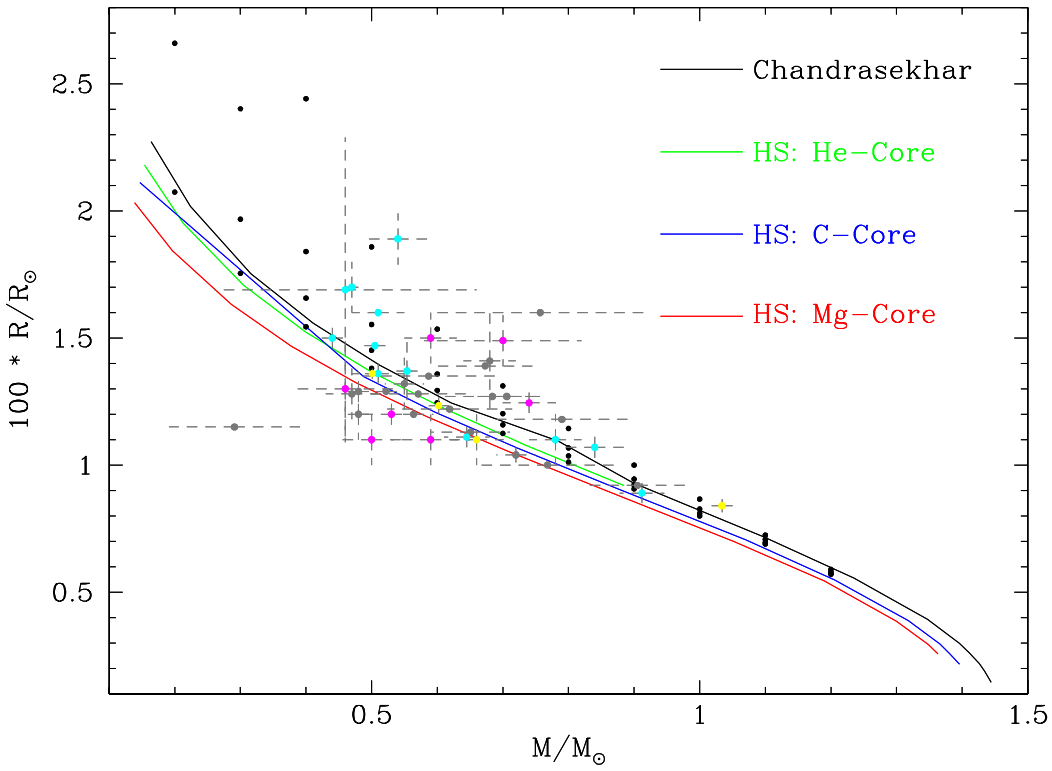

Figure 2.1: White dwarf $M-R$ relation. The black line represents the theoretical Chandrasekhar [1935] relation, the green, blue and red lines the He-core, C-core and Mg-core zero temperature $M-R$ relations obtained by Hamada & Salpeter [1961]. Black solid dots represent the $M-R$ relation provided in Bergeron et al. [1995b] for $T_{\rm eff}$ = (5-10-20-40)$\times 10^3$ K at a given mass (except for M = 0.2 $M_{\odot}$ and M = 0.3 $M_{\odot}$, which show $T_{\rm eff}$ = (5-10)$\times 10^3$ K and $T_{\rm eff}$ = (5-10-20)$\times 10^3$ K, respectively). Dark gray solid dots are empirical measurements for field DA white dwarfs obtained from Provencal et al. [1998] and Reid [1996], and magenta solid dots represent empirical values measured for the visual binaries provided in Provencal et al. [1998] (except for 40 Eri B, Procyon B, Stein 2051 B, and Sirius B, where I use the more recent values of Provencal et al. [2002], yellow dots). Finally, in cyan are shown the masses and radii measured from eclipsing WDMS binaries [Pyrzas et al., 2008, and references therein].

2.2 M-type stars

2.2.1 Interior

M-type stars [see Chabrier & Baraffe, 2000; Chabrier et al., 2005] are the coolest among the MS stars, with effective temperatures of less than ~ 3800 K (and higher than ~ 2200 K, see Chapter 7), and also the most abundant in our Galaxy [Chabrier, 2003]. The mass in this kind of star ranges from ~ 0.5 to ~ 0.1 $M_\odot$, and consequently the temperature in the interior is low enough for the electrons to be partially degenerate ($T_c \sim 10^6 - 10^7$ K). Because of the low effective temperature M-type stars have convective cores and envelopes, which grow in depth with decreasing temperature. When the convective envelope reaches the convective core the star becomes fully convective.

MS stars find themselves in hydrostatic equilibrium, in which the thermal pressure balances the gravitational force. In this stage of the evolution, the thermal pressure comes from the burning of H into He in the core of the star, with the proton-proton (p-p) chain being the burning mechanism at work in M-type stars. The rate at which stars burn H determines the time spent in the MS. A direct consequence of this is that for p-p H burning low-mass main sequence stars, the time spent on the MS is considerably larger than for those stars which burn H through the CNO chain. This time can be estimated from the following equation [Tuffs et al., 2004, see the appendix]:

$$t_{\rm MS} = 4800 \left(\frac{M}{M_\odot}\right)^{-1/3} \times 10^7, M < 0.4 M_\odot \tag{2.2}$$

$$t_{\rm MS} = 1100 \left(\frac{M}{M_\odot}\right)^{-3} \times 10^7, 0.4 M_\odot \leq M \leq 8.1 M_\odot \tag{2.3}$$

where the resulting $t_{\rm MS}$ is in years. Thus M-type stars are not yet able to leave the MS, as the time needed to do so is larger than the Hubble time.

Energy transport

The presence of both the convective envelope and the convective core makes it easier for the M-type stars to transport the energy via convective flux. This is true in all areas of the star except in the radiative zone between the envelope and the core, where the radiative flux is dominant. However, when the temperature is cool enough the star becomes fully

convective, and consequently the total energy transport is given mainly by convective flux in the entire star.

2.2.2 Atmospheres

Given the low temperature, most of the H and C in the atmospheres of low-mass MS stars are locked into H_2 and CO molecules, respectively. Excess O is bound to form molecules such as TiO, VO, and H_2O, with some amounts also of OH. Metal oxides and hydrides such as FeH, CaH and MgH are also present (see Chapter 3 for further details).

2.2.3 Rotation-age-activity relations

Stellar magnetic fields are believed to be caused within the convective zone of stars. A localised magnetic field exerts a force on the plasma, which rises to the photosphere and creates starspots on the surface of the star. This phenomenon is referred to as stellar activity, and the reaction of stars to stellar activity on their surface is known as *spottedness*. Due to the differential rotation that the star undergoes, starspots inhibit convection and produce zones of lower temperature.

Even though significant progress concerning the rotation-age-activity relations for M stars has been made, more studies are needed to fully understand such relations. Given the complexity of the issue, and the fact that this topic is not the central part of this thesis, I summarise here the most important findings up to date: (1) old stars rotate slower than young stars, i.e. the rotational period $P_{\rm rot}$ increases in time [Kiraga & Stepien, 2007]; (2) magnetic activity decreases with time [West et al., 2008]; (3) there is a strong increase in the active lifetimes of stars in the spectral-type range from M3 to M5 [West et al., 2008]; (4) fast rotation excites magnetic activity up to a saturation threshold of $v_{\rm rot} \sin i \sim 10\,{\rm km\,s^{-1}}$, where $v_{\rm rot}$ is the rotational velocity, and i is the rotation axis inclination of the star[2]. Nevertheless rotation and activity are not always linked [West & Basri, 2008, see also Chapter 10], (5) activity-$P_{\rm rot}$ relations found for young stars are not modified below Sp = M3.5-4, where stars are supposed to become fully convective [Delfosse et al., 1998], (6) $P_{\rm rot}$ decreases linearly with increasing mass at a given age [Cardini & Cassatella, 2007], (7) M stars in

[2]Note that magnetic activity depends on the rotational velocity, but that we only see $v_{\rm rot} \sin i$.

close binaries rotate faster than single M stars, or M stars in wider binaries [Cardini & Cassatella, 2007].

2.2.4 Theory versus observations

Studies have been developed to create evolutionary stellar models, and to derive theoretical relations between the physical parameters of low-mass MS stars [Baraffe & Chabrier, 1996; Baraffe et al., 1998, 2002, 2003]. However, when comparing empirical results with the theoretical expectations numerous discrepancies arise [Ribas, 2006; Ribas et al., 2008]. Thus for example, current models predict radii that are $\sim$ 15% smaller than the observed values, and effective temperatures that are $\sim$ 5% higher for star masses above $\sim 0.3\,\mathrm{M}_{\odot}$ (see Fig. 2.2). Problems are thought to arise due to the high magnetic activity level that a large number of this kind of star display, which is likely to affect the $M-R$ relation [López-Morales, 2007; Chabrier et al., 2007; Morales et al., 2008]. Moreover, the properties of low-mass stars are expected to change depending on their metallicities [Berger et al., 2006]. The spectral type-radius relation for M stars is also extremely affected by these features (see Chapter 7). Below $\sim 0.3\,\mathrm{M}_{\odot}$ there is a good agreement between the observational measurements and the models (Fig. 2.2). Nevertheless, this result can be misleading, since "all objects in this range have rotational velocities $\mathrm{v}_{\mathrm{rot}} \sin i < 10$ km s^{-1}" [López-Morales, 2007]. Consequently more radius measurements of active stars in this range are still necessary to confirm the apparent good agreement between the theoretical values and the empirical measurements.

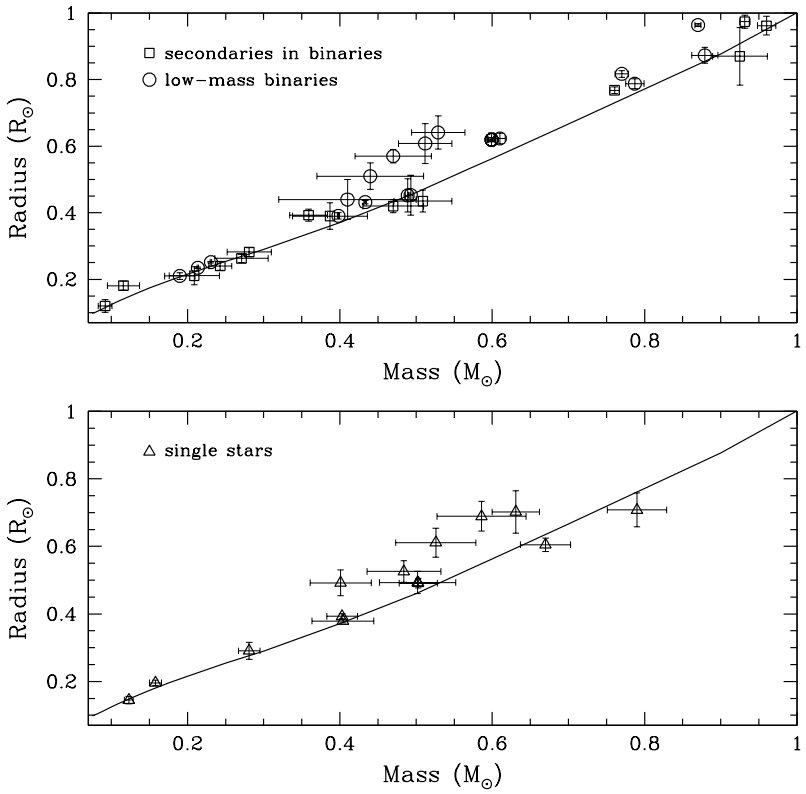

Figure 2.2: Observational $M-R$ relation for stars below 1 $M_{\odot}$. Top: empirical values from low-mass secondaries to eclipsing binaries with primaries more massive than 1 $M_{\odot}$ (squares) and the components of eclipsing binaries below 1 $M_{\odot}$ (circles). Bottom: all the measurements from single stars. The solid lines represent the theoretical isochrone model from Baraffe et al. [1998]. Taken from López-Morales [2007].

Chapter 3

Spectral Properties of White Dwarf-Main Sequence Binaries

In the previous Chapter I have discussed in some detail the physical properties of both white dwarfs and M-type MS stars. In this Chapter I will focus on the spectral features observed in these kinds of stars, and also on the spectral properties of WDMS binaries. For this it becomes necessary first to introduce spectroscopy as a technique in astrophysics, and to understand what a spectrum is and how it is formed.

3.1 Spectroscopy

Spectroscopy gave birth to astrophysics as an observational science in the 1860s. This technique measures the flux emitted by an object in a certain wavelength (λ) range, providing consequently a unique flux-wavelength dependence for each celestial object. Spectroscopy implies the use of a spectrograph, which consists normally of a slit, a collimator, and a dispersive element, such as a grating. The slit is situated on the focal plane of the telescope, and isolates the light that comes from the target from other objects in the field. The light that passes through the slit is then directed to the grating by the collimator, where it is dispersed. The dispersed light is directed to a detector (usually a Charged Coupled Device, or CCD, see Chapter 4), where the spectrum is finally recorded.

A typical spectrum is normally composed of spectral lines embebbed in a contin-

uum. These spectral features can appear in absorption or emission depending on the temperature gradient in the atmosphere[1]. Let's consider as an example the stellar atmosphere of a single star. The crucial parameter in the formation of the spectral lines is in this case the optical depth

$$\tau_\nu = \int \chi_\nu dz \tag{3.1}$$

where ν is the frequency (or wavelength, since $\nu = c/\lambda$) considered, χ_ν is the absorption coefficient of the atmosphere at a given frequency, and z the geometric depth. A stellar atmosphere is optically thick when $\tau_\nu > 1$, and optically thin when $\tau_\nu < 1$. An optically thick atmosphere emits practically like a blackbody[2]

$$I_\nu \sim B_\nu \tag{3.2}$$

where I_ν is the intensity emitted by the atmosphere and B_ν is the intensity emitted by a blackbody. The energy emitted in an optically thin atmosphere is given approximately by

$$I_\nu \sim I_\nu(\tau_\nu) + B_\nu \tau_\nu \tag{3.3}$$

where $I_\nu(\tau_\nu)$ is the intensity emitted in the optically thick atmosphere layer immediately interior to the optically thin atmosphere. Spectral lines in a spectrum are formed when the optically thin atmosphere of the star becomes optically thick due to increases of the absorption coefficient. In this context, and depending on the temperature gradient between the thin and the thick atmospheres, the line will be in emission or in absorption. If $I_\nu(\tau_\nu)$ = 0, then B_ν will always be larger than $B_\nu\tau_\nu$ and hence an emission line will always form. Assuming that $I_\nu(\tau_\nu)$ is positive, then an emission line will form if $B_\nu > I_\nu(\tau_\nu) + B_\nu\tau_\nu$. In this case the inner layers of the atmosphere must be cooler than the outer layers, and the temperature gradient then points to the surface of the star. When the inner layers are hotter, the temperature gradient points the core of the star and $B_\nu < I_\nu(\tau_\nu) + B_\nu\tau_\nu$. In this case an absorption line is formed.

The crucial question is then why the absorption coefficient increases at a given frequency. The physics of stellar atmospheres tells us that χ_ν is strongly dependent on the population of electrons on a certain level l in a considered atom, and on the probability of

[1] The following text in this section is based on the book by Mihalas [1970].

[2] A theoretical object that is both a perfect absorber and a perfect radiator.

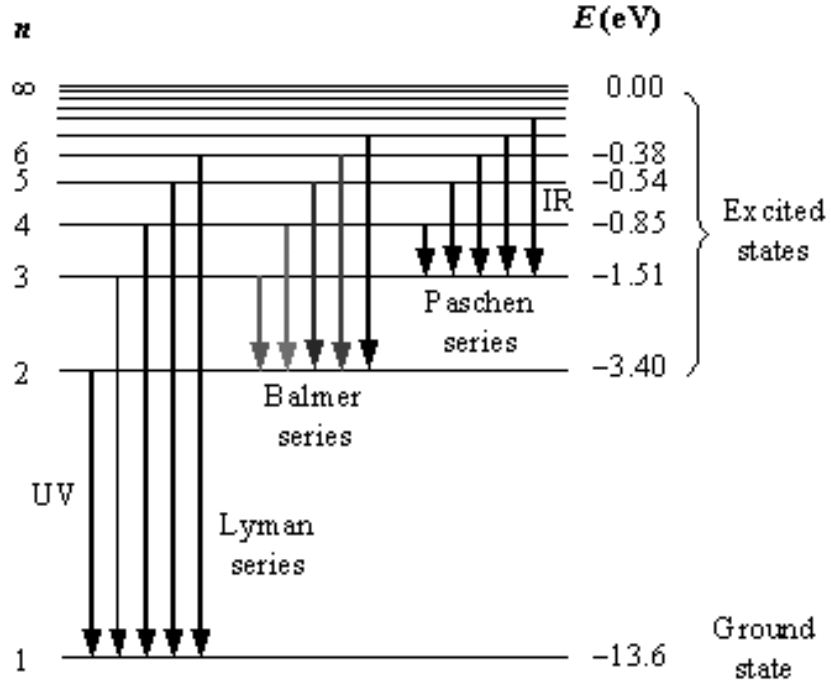

Figure 3.1: Three transition series of the atom of H. Transitions between the ground level and higher elements form the Lyman lines (e.g. Lyα, transition between levels 1 and 2), transitions between level 2 and higher levels form the Balmer lines (e.g. Hα, transition between levels 2 and 3), transitions between the third level and higher levels form the Paschen lines.

exciting an electron from the level l to another level u, f_{lu}. In a stellar atmosphere photons and atoms are continuously interacting, and consequently the probability of exciting an electron due to the absorption of a photon by an atom increases dramatically. After a certain time the electron is de-excited and liberates a photon which can be absorbed by another atom. These processes are called bound-bound interactions. Thus, if the atomic level is sufficiently populated, and the probability of exciting an electron is high, the absorption coefficient can be dramatically increased. Since the transition of the electrons are given at specific frequencies, the spectral lines are then always associated to specific transitions between the levels of an atom. All transitions starting from one level to other levels are called a series. In Fig. 3.1 I show as an example the Lyman (ultraviolet), Balmer (optical), and Paschen (infrared) series of the atom of H.

3.2 Optical spectral features of white dwarfs, low-mass main sequence stars and WDMS binaries

White dwarfs are hot stars, henceforth have blue spectra. Normally the outer layers of the white dwarf atmospheres contain H (see Chapter 2), and consequently the Balmer lines are the typical spectral features for DA white dwarfs. He dominated DB atmospheres are the second most commonly found in white dwarfs, after the H dominated DA-type stars. These objects show He I lines, with the complete absence of H or other elements. For the hot DO white dwarfs, the He can be completely ionised and observed in the atmospheres as He II. On occasion it is also possible to detect some H (DAO) or He I lines in this kind of star. As outlined in Chapter 2, a small number of white dwarfs contain C and metals on their atmospheres. Consequently only metal lines and C features (either atomic or molecular) are detected in any part of the spectra of DZ and DQ white dwarfs, respectively. Finally DC white dwarfs show no identifiable features in their spectra, as the effective temperature is too low to excite transitions in the optical wavelength range. In Fig. 3.2 I provide example spectra for all white dwarf types outlined above.

Low-mass MS stars are cool, and consequently their predominant features dominate the red part of the optical spectrum. The high surface gravity typical of these stars ($\log g \sim 5.5$ at the H burning limit, for a solar metallicity) makes the density in the photospheres to be $\rho \sim 10^{-6} - 10^{-4}$ g/cm^3. Consequently collision effects become important and induce molecular dipoles on H_2 or He-H_2, yielding the so called collision-induced absorption (CIA) between roto-vibrational states of molecules. The energy distribution is governed by the line absorption of TiO and VO (see Fig. 3.3), with some lines resulting from Na I, K I, Fe I, Mg I, Ca II, Li I, and Ba II transitions (see Kirkpatrick et al. [1991] for a complete list of features identifiable in the red/near-infrared spectra, and also Cushing et al. [2005] for an analysis in the infrared). Through the detection of specific atomic features and/or molecular bands it is possible to differentiate not only red giants from red dwarfs, but also early to late M-type stars [Kirkpatrick et al., 1991; Bessell, 1991; Martín et al., 1999; Cruz & Reid, 2002]. In fact, the strength of molecular bands has been used to define the spectral subtypes of low-mass stars (see Fig. 3.4). Near the H burning limit TiO and VO

disappear, and alkali metals are detected in atomic form. This leads to the domain of the sub-stellar L-type (brown) dwarfs. For even lower temperatures there is a strong signature of methane absorption, characteristic of the T-type (brown) dwarfs.

By knowing the spectral characteristics of white dwarfs and low-mass stars it is then straightforward to understand the spectral properties of WDMS binaries. In general, the white dwarf is clearly visible in the blue while the low mass companion dominates the red part of the spectrum. The overall shape of the WDMS spectra though depends on the effective temperatures of the stars. Thus for example, a hot white dwarf will dominate the spectrum if the low-mass companion is cool. In the same way, an early M-type MS star will dominate the spectrum if the effective temperature of the white dwarf is rather low (see Fig. 3.5). Hence the detection of WDMS binaries is obviously subject to observational biases (see Chapter 9). An additional feature in the spectra of WDMS binaries might be the presence of Balmer emission, Hα being the strongest among them. This occurs when the white dwarf is hot enough to irradiate the surface of the companion, i.e. heating effect (see Chapter 8). Balmer emission lines might also be detected due to magnetic activity on the secondary star.

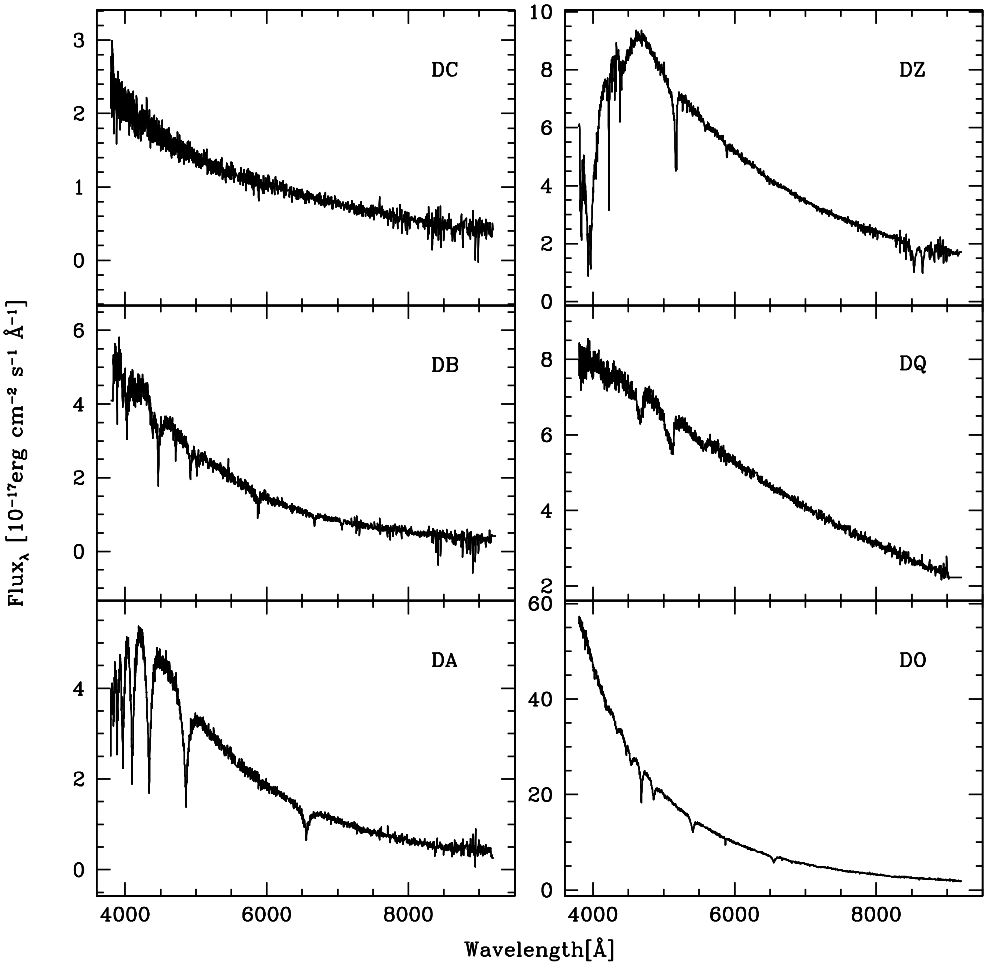

Figure 3.2: Optical example spectra for the different white dwarf-type stars described in Sect. 3.2. The Balmer and the He I lines are the typical features for the DA and DB white dwarfs respectively. No features are identified in the atmosphere of the DC white dwarf to a depth of 5%. Metal lines and C features are detected on the spectra of the DZ and DQ stars, respectively. The DO star shows ionised He (He II) lines typical for these hot stars. The sample is taken from Harris et al. [2003].

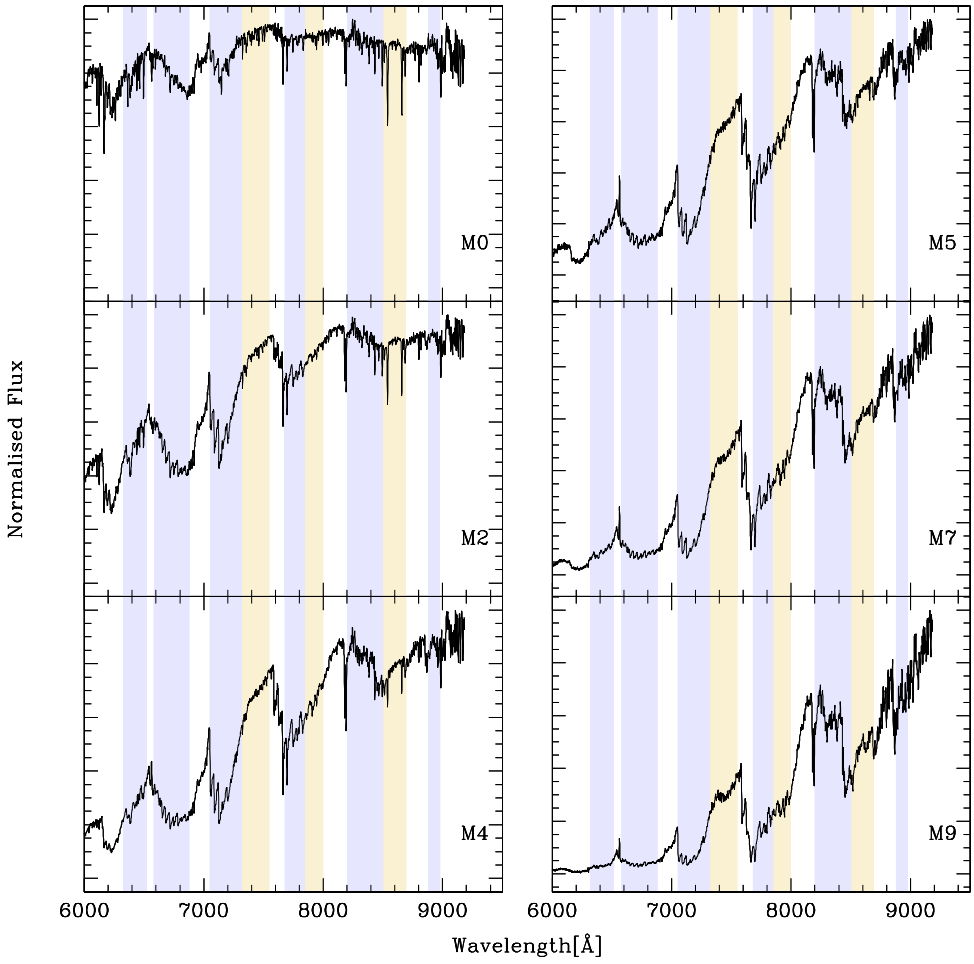

Figure 3.3: M-type star templates used in this thesis (see Chapter 7 for a complete description) for the spectral subclasses M0-2-4-5-7-9. The TiO and VO bands are highlighted in blue and yellow, respectively. The strengths of these bands vary significantly from one subclass to another, and are used to estimate the spectral subclass of low mass-stars (see Fig. 3.4).

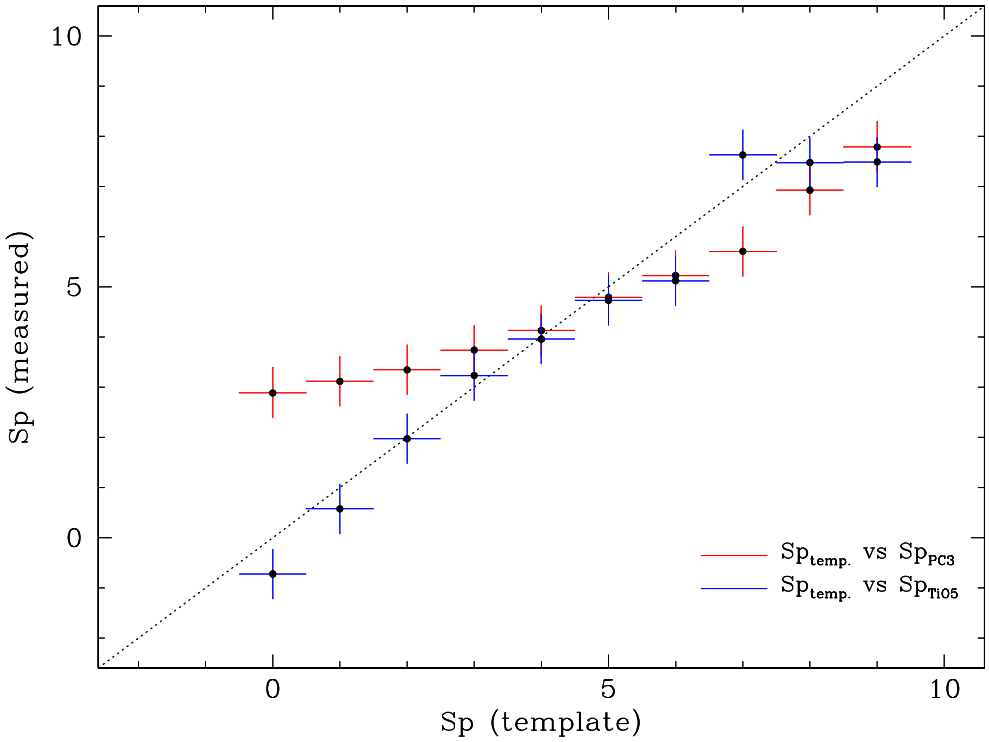

Figure 3.4: Comparison of the spectral subtypes measured for the M-type MS templates used in this thesis (see Chapter 7) applying the methods presented in Martín et al. [1999] (Sp_{PC3}, red, where PC 3 = F(8230-8270 Å)/F(7540-7580 Å) and Cruz & Reid [2002] (Sp_{TiO5}, blue, where TiO 5 = F(7126-7135 Å)/F(7042-7046 Å). I assume a 0.5 subclass error for our templates, and the values measured from the molecular bands. The figure suggests a good agreement between our templates and the values obtained from Cruz & Reid [2002], except for our M9 template. Discrepancies arise at earlier spectral subtypes when comparing our templates with the values obtained from Martín et al. [1999]. This is not surprising, since Sp_{PC3} is only valid for spectral types later than M2.5. The agreement between both methods and our templates is excellent for mid spectral subtypes ($3<Sp<5$).

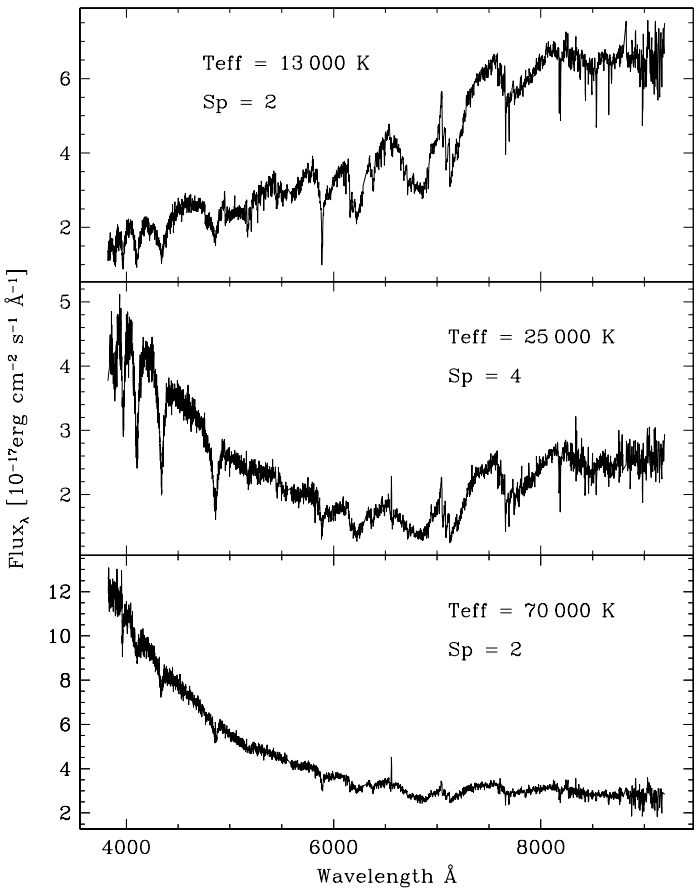

Figure 3.5: Three examples of WDMS binaries. Top: an MS dominant WDMS. Middle: a typical WDMS binary. Bottom: a white dwarf dominant WDMS. The white dwarf effective temperatures, and secondary spectral types are given for each WDMS binary in the top of each panel. The sample is taken from Chapter 9.

Chapter 4

Data Reduction and Observations

The major task of our project is to identify those WDMS binaries from SDSS that have undergone a CE phase, and to measure their binary parameters. This new sample of PCEBs will provide the much-needed constraints for further development of binary evolution theory. This implies a large amount of observations are necessary, and indeed our project has been awarded observational time on a large variety of telescopes around the world. Part of this thesis presents and discusses observational results (see Chapters 8 and 10). It is hence appropriate to dedicate some space to explain how to reduce raw data and to provide details of the instrumentation used for the observations.

4.1 Data Reduction

The use of charged coupled devices, CCDs, has certainly implied a dramatic advance in observational astrophysics. CCDs are silicon-based semiconductors composed of a two-dimensional array with a certain number of pixels in each direction. When the photons received from the observed object impact a pixel of the CCD a certain number of electrons are emitted due to the photoelectric effect[1]. These electrons are trapped by a potential well, and when the exposure ends, a control circuit causes each pixel to transfer its contents to its neighbour. The last pixel of the array converts this information into counts (digitisation) which are saved as a 2-dimensional data frame. Data reduction involves four steps: bias-

[1]The exact number of emitted electrons depends on the quantum efficiency of the CCD.

subtraction, flat-fielding, sky subtraction, and calibration.[2]

4.1.1 Bias-subtraction

A bias frame refers to the number of counts recorded for each CCD pixel with zero exposure time. In order to avoid negative numbers, an offset (bias level) is added to the zero level of the CCD. The bias level needs consequently to be removed from all data frames. A series of bias frames are combined and averaged together to build a master bias which is then subtracted from the science frames and the flat-fields (see next paragraph). A large number of bias frames is necessary to guarantee that we are not adding noise to the science frames. Another way to determine the bias level is by making use of the overscan. The overscan is simply a set of rows/columns of the CCD (typically selected at the right edge of the frame) that is read out once before the science data are taken. This region is used to compute the mean bias level by averaging the data over all the columns and fitting a certain function to these average values. The result is then subtracted from each column of the frame. The overscan hence can be very useful if the bias level varies in time[3].

4.1.2 Flat-fielding

Each pixel in a CCD camera has a different response to the same amount of light received. This response needs to be normalised by the use of flat-fields. Flat-field spectra are normally obtained using tungsten lamps, which are generally located inside the spectrograph, and before the entrance slit. A master flat is obtained by combining a certain number of flat-fields. To consider the response of the detector along the dispersion direction, it becomes necessary to average the master flat over the spatial direction. This one-dimensional master flat is then fitted with a polynomial of a certain order, which is used to normalise the master flat. The pixel-to-pixel variations in the normalised flat reflect the different pixel response. The flat-fielding process is completed by dividing the science frames by the normalised flat.

[2]Note that the following description, even though it is restricted to spectroscopic analysis, can be also applied to photometry.

[3]The bias level in a CCD camera is usually very stable but can vary on time-scales of months.

4.1.3 Sky subtraction

The sky background that surrounds the observed target also passes through the slit of the spectrograph and is dispersed. Sky lines are hence present in the CCD spectra, and consequently have to be subtracted. For this it is necessary to define the extraction aperture of the object spectrum and the width of the regions where sky will be computed. Given that the dispersion direction and the axis of the CCD are not parallel, it is also necessary to trace the spectra by fitting a polynomial of a certain order in the dispersion direction. The sky contribution is computed by interpolating sky data on each side of the object spectrum, and cosmic rays are eliminated by detecting the distortion they produce in the spatial profile. The one-dimensional object spectra are finally extracted by using the above defined aperture. All spectroscopic follow-up data presented in this thesis (Chapters 8 and 10) have been processed using the STARLINK packages FIGARO and KAPPA, and the spectra were optimally extracted [Horne, 1986] using the PAMELA package [Marsh, 1989].

4.1.4 Calibration

A spectrum gives a wavelength-dependent flux that is characteristic for every stellar object. After the sky subtraction though, the one-dimensional spectra are provided in counts per pixel, and consequently need to be calibrated both in wavelength and flux. These processes are called wavelength calibration and flux calibration.

All spectroscopic data presented in this thesis (Chapters 8 and 10) have been calibrated using the MOLLY package [Marsh, 1989].

Wavelength calibration

Obtaining a pixel-to-wavelength relation is carried out by the use of arc lamps (normally Ne, Ar, Cu, He, or a combination of some of them), which emit light in many specific and very narrow wavelength ranges. The wavelengths of the lines that form the arc spectrum are hence well known and can be used to obtain a pixel-to-wavelength relation, which can be applied to the rest of spectra. Ideally arc spectra have to be taken during the whole observing run to account for the flexure of the spectrograph. In practice, we intentionally obtained

one arc spectrum per night, and adjust the the wavelength-pixel dependence according to the position of sky emission lines[4]. In this way we were able to optimise the observing time on each night. Another way to count for the flexure of the spectrograph is to obtain a pixel-to-wavelength relation exclusively from the emission lines. We have found that reliable wavelength calibrations can be obtained from sky lines [Southworth et al., 2006], but that the scatter of the fit around the wavelength solution is quite a bit larger than for arc-lamp emission lines. In this case the statistical uncertainty [Marsh et al., 1994] is equivalent to 0.09 Å so the increased scatter is relatively unimportant.

Flux calibration

Flux standard stars are stars with a well-established and tabulated flux distribution. Generally, the statistical uncertainty of these tabulations is below $\pm 0^{\rm m}.05$ in the range 4000-8000Å. The calibration is less secure outside this wavelength range ($\pm 0^{\rm m}.06 - 0^{\rm m}.07$), and in a few cases the errors at the extreme ultraviolet (3300Å) can be extremely large ($\sim \pm 0^{\rm m}.1$). Flux standard stars are divided into Oke [Oke, 1990] and Filippenko-Greenstein [Filippenko & Greenstein, 1984] categories. The first category consists of measurements of many small parts of the spectrum containing no spectral lines, so are characterised by a central wavelength, a measurement, and a bandwidth (i.e. three columns in a datafile). The second category uses the whole spectrum so are better suited to faint standards, but can be affected by spectral lines which may give systematic errors. Observations of flux standard stars provide hence a flux-count dependence for a wavelength range, which can be applied to the science spectra. For red-wavelength spectra it is very important that telluric lines are removed. Telluric lines are due to absorption by gases such as oxygen, water vapour, or carbon dioxide in the Earth's atmosphere. In this thesis I have measured the radial velocities from both the Na I $\lambda\lambda$ 8183.27,8194.81 absorption doublet and the Hα emission (see Chapters 7, 8 and 9). The Na I doublet falls in the wavelength region where telluric absorptions are strong, and consequently telluric removal was applied in order to obtain a line profile free of telluric features.

[4]Note that we measure the radial velocities from the Na I $\lambda\lambda$ 8183.27,8194.81 absorption doublet (see Chapters 7, 8 and 9), and that at these wavelengths the emission lines are strong.

4.2 Observations

Our project has been awarded observational time on a large variety of telescopes around the world. In Table 4.1 I provide a list of the observing runs carried out so far (November 2008), the number of nights for each run, and the people involved in the observations and data reduction. The majority of the data taken from these observations are not analysed in this thesis (see Chapter 10 though), including also a substantial part of the data taken by myself. In addition, a certain amount of the data presented in this thesis has not been taken nor reduced by myself.

In Chapter 8 of this thesis I present time-resolved spectroscopy and photometry for 11 SDSS (see Chapter 6) WDMS binaries (Table 4.2, Fig. 4.1), henceforth designated SDSS J0052-0052, SDSS J0246+0041, SDSS J0309-0101, SDSS J0820+4314, SDSS J0314-0111, SDSS J1138-0011, SDSS J1151-0007, SDSS J1529+0020, SDSS J1724+5620, SDSS J2241+0027 and SDSS J2339-0020. In the following sections I briefly describe the instrumentation used for the observations.

4.2.1 Spectroscopy

(i) *VLT*. Intermediate resolution spectroscopy of SDSS J1138-0011 was obtained between August 16, 2007 and March 26, 2007 with FORS2 on the ESO VLT/UT1 (Antu). The exposure time was 900 sec, and the observations were carried out using the 1028z grism and a 1 arcsec slit, resulting in a spectral coverage of 7830–9570 Å. From measurements of the FWHMs of sky lines we find our observations have a resolution of approximately 2.5 pixels (2.2 Å) at 8200 Å. Wavelength calibration of the extracted spectra was done using only sky emission lines. The wavelengths of good sky lines were obtained from the atlas of Osterbrock et al. [1996, 1997]. 37 sky lines were included, and fitted with a fifth-order polynomial. The rms scatter around the fit was 0.11 Å, so the statistical uncertainty in the wavelength scale is 0.04 Å. Finally, the spectra were flux-calibrated and compensated for telluric absorption using a spectrum of the standard star Feige 110. The data were taken in service mode, and reduced by J.Southworth (see Table 4.1).

(ii) *Magellan-Clay*. Follow-up spectroscopy of SDSS J1138-0011, SDSS J1151-

Table 4.1: Telescopes, number of nights, and people involved in the overall observations of our dedicated project to identify PCEBs and measure their orbital periods. The lines in black represent observation runs in which I have been involved.

Telescope	Date	Nights	Observers	Data reduction
CA3.5	2008 Oct	5	R.Schwarz/M.Schreiber	A.Nebot
WHT	**2008 Jul**	**4**	*sm*	**A.Rebassa**
CA3.5	2008 Jul	5	A.Nebot/S.Pyrzas	A.Nebot
WHT	**2008 Jul**	**6**	**A.Rebassa/S.Pyrzas**	**A.Rebassa**
			L.Schmidtobreik	
CA3.5	2008 Jun	5	A.Nebot/R.Schwarz/M.Müller	A.Nebot
CA3.5	**2008 Jun**	**5**	**A.Nebot**	**A.Nebot**
			A.Rebassa	**A.Rebassa**
M-Baade	2008 Jun	4	J.Southworth/C.Tappert	J.Southworth
IAC80	2008 May	8	A.Nebot	A.Nebot
NTT	**2007 Oct**	**8**	**A.Rebassa/A.Nebot**	**A.Rebassa**
M-Baade	2007 Sep-Oct	4	J.Southworth/A.Nebot	J.Southworth
WHT	**2007 Sep**	**3**	**B.Gänsicke**	**A.Rebassa**
NTT	**2007 Aug**	**4**	**A.Rebassa**	**A.Rebassa**
CA3.5	2007 Jul	6	A.Nebot	A.Nebot
WHT	**2007 Jun**	**6**	**A.Rebassa**	**A.Rebassa**
			P.Rodríguez-Gil	
M-Clay	2007 May	5	J.Southworth/A.Schwope	J.Southworth
			M.Müller	
AIP 70 cm	2006 Mar	4	AIP group	A.Nebot
	2007 Sep			
Kry 1.2 m	2006 Nov	4	V.Karamanavis	V.Karamanavis
			E.Tremou	E.Tremou
CA 2.2 m	2006 Set	2	A.Aungwerojwit	A.Aungwerojwit
IAC80	**2006 Aug**	**6**	**A.Rebassa**	**A.Rebassa**
WHT	**2006 Jun-Jul**	**6**	**B.Gänsicke/A.Rebassa**	**J.Southworth**
			J.Southworth	

Telescope	Period	Hours	Observers	Data reduction
Gemini	2008B/25h	25	*sm*	J.Southworth
Gemini	2008A/25h	25	*sm*	J.Southworth
Gemini	2007B/25h	25	*sm*	J.Southworth
VLT	P82/30h	30	*sm*	J.Southworth
VLT	P80/30h	30	*sm*	J.Southworth
VLT	P79/30h	30	*sm*	J.Southworth
VLT	P78/30h	30	*sm*	J.Southworth

Notes: M-Baade and M-Clay refer to the two Magellan telescopes at Las Campanas observatory. We use *sm* to indicate that the data were taken in service mode. CA 2.2 and CA 3.5 are the 2.2 and 3.5 meter telescopes at Calar Alto observatory. Kry 1.2 is the Kryoneri 1.2 meter telescope at the National Observatory of Athens.

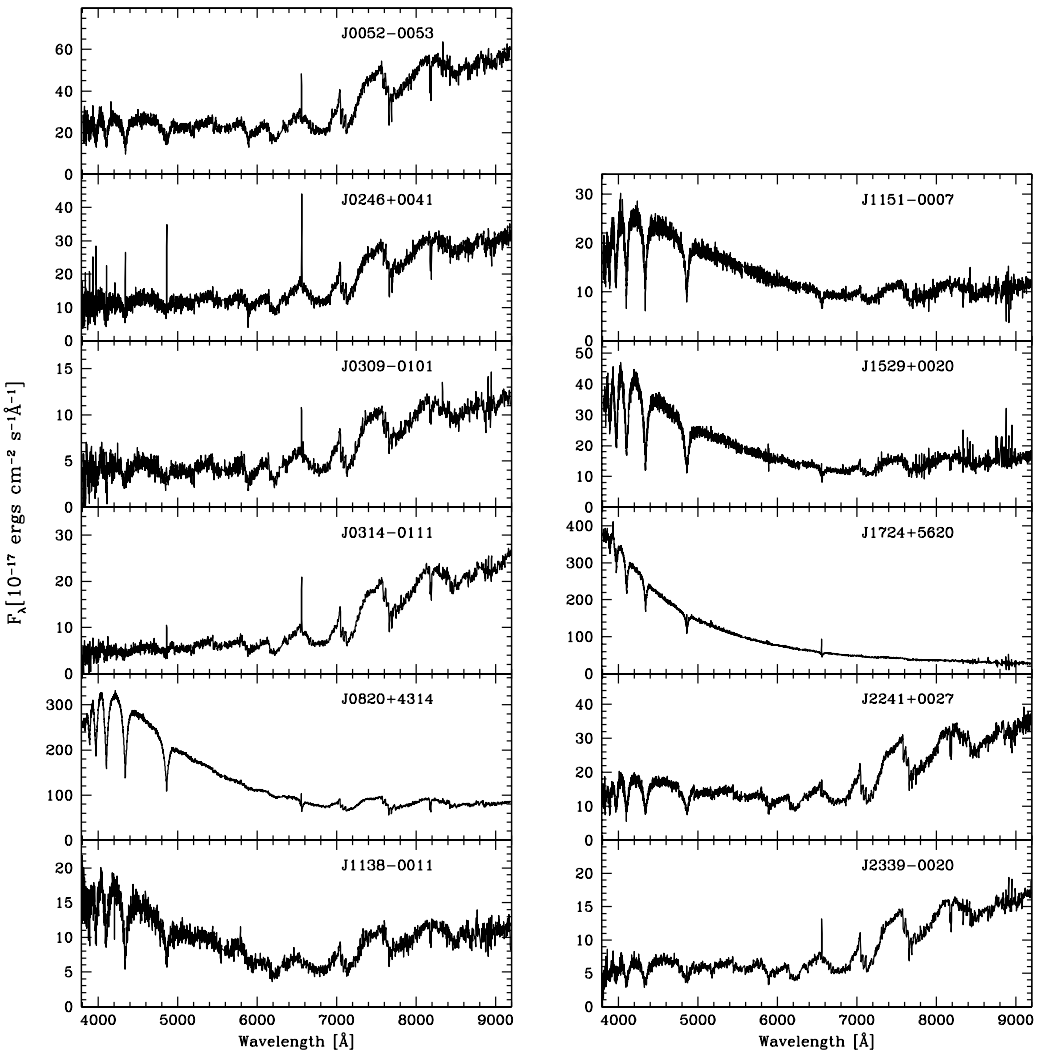

Figure 4.1: SDSS (Chapter 6) spectra of the 11 SDSS WDMS binaries studied in Chapter 8.

0007 and SDSS J1529+0020, were obtained over the period 2007 May 17–20 using the Magellan Clay telescope equipped with the LDSS3 imaging spectrograph. We used the VPH_Red grism and OG 590 order-sorting filter. The detector was an unbinned STA 4k×4k pixel CCD read out by two amplifiers. A 0.75 arcsec offset slit gave a wavelength coverage of 5800–9980 Å at a reciprocal dispersion of 1.2 Å px^{-1}. Measurements of the FWHMs of the sky lines indicate that our observational setup gave a resolution of approximately 4 pixels (4.8 Å) at 8200 Å. Wavelength calibration was done using only sky lines. A total of 36 sky lines were fitted by a fifth-order polynomial. The rms scatter around the fit was 0.25 Å, so the statistical uncertainty is 0.09 Å. Flux calibration and telluric line removal was performed using spectra of the standard star LTT 3218 obtained during the same observing run. The data were taken by J.Southworth, A.Schwope and M.Schreiber, and reduced by J.Southworth (see Table 4.1).

(iii) *Magellan-Baade*. Intermediate-resolution long-slit spectroscopy of SDSS J0314–0111 and SDSS J2241+0027 was obtained on the nights of 2007 October 2 and 3 using the IMACS imaging spectrograph attached to the Magellan Baade telescope at Las Campanas Observatory. The 600 ℓ mm^{-1} red-sensitive grating was used along with the slit-view camera and a slit width of 0.75 arcsec, giving a reciprocal dispersion of 0.39 Å px^{-1}. The IMACS detector is a mosaic of eight 2k×4k SITe CCDs, and long-slit spectra with this instrument are spread over the short axis of four of these CCDs. Using a grating tilt of 14.7° allowed us to position the Na I λλ 8183.27,8194.81 doublet towards the centre of CCD2 and the Hα line near the centre of CCD4. By fitting Gaussian functions to arc and sky emission lines we find that the spectra have a resolution of approximately 1.6 Å. He arc lamp exposures were taken at the start of each night in order to derive a wavelength solution with a statistical uncertainty of only 0.002 Å. This was applied to each spectrum taken on the same night. Detector flexure was measured and removed from the wavelength solution for each spectrum using the positions of sky emission lines. Flux calibration and telluric line removal was performed using spectra of the standard star BD +28°4211. The observations were carried out by J.Southworth and A.Nebot Gómez-Morán, and the data were reduced by J.Southworth (see Table 4.1).

(iv) *New Technology Telescope (NTT)*. Two observing runs were carried out at the

NTT in August (three nights) and October 2007 (eight nights), providing intermediate time-resolved spectroscopy of SDSS J0052–0053, SDSS J0246+0041, SDSS J0309-0101, SDSS J2241+0027 and SDSS J2339–0020. We used the EMMI spectrograph equipped with the Grat#7 grating, the MIT/LL red mosaic detector, and a 1 arcsec wide long-slit, resulting in a wavelength coverage of 7770-8830 Å. He-Ar arc lamp spectra were taken at the beginning of each night and were then used to establish a generic pixel-wavelength relation. Specifically, we fitted a fourth order polynomial which gave a rms smaller than 0.02Å for all spectra. We then used the night sky emission lines to adjust the zero-point of the wavelength calibration. The spectral resolution of our instrumental setup determined from the sky lines is 2.8Å. Finally, the spectra were calibrated and corrected for telluric absorption using observations of the standard star Feige 110. Observations and reduction were carried out by myself. During three of the eight observing nights in October 2007 A.Nebot Gómez-Morán helped me with the observations (see Table 4.1).

(v) *William Herschel Telescope (WHT).* One spectrum of SDSS J1138-0011 was taken with the 4.2 m William Herschel Telescope in June 2007 at the Roque de los Muchachos observatory on La Palma. The double-beam ISIS spectrograph was equipped with the R158R and the R300B gratings, and a 1 arcsec long-slit, providing a wavelength coverage of 7600-9000 Å. The spectral resolution measured from the sky lines is 1.6 Å. Calibrations were carried in the same way as described for the NTT above. Observations were carried out by P.Rodríguez-Gil and myself, and the data were reduced by myself (see Table 4.1).

(vi) *SDSS.* For one system, SDSS J1724+5620, we were able to determine an accurate orbital period from our photometry alone, but were lacking follow-up spectroscopy. SDSS Data Release 6 (DR6, Chapter 6) contains three 1-d calibrated spectra for SDSS J1724+5620 (MJD PLT FIB 51813 357 579, 51818 358 318, and 51997 367 564. See Chapter 6). Each of these spectra is combined from at least 3 individual exposures of 900 s, which are also individually released as part of DR6[5]. For SDSS J1724+5620, a total of 23 sub-spectra are available, of which 22 allowed reliable radial velocity measurements.

[5]http://www.sdss.org/dr6/dm/flatFiles/spCFrame.html

Table 4.2: Log of the observations. Included are the target names, the SDSS *ugriz* psf-magnitudes (see Chapter 6), the period of the observations, the telescope/instrument setup, the exposure time, and the number of exposures.

Spectroscopy											
SDSS J	*u*	*g*	*r*	*i*	*z*	Dates	Telesc.	Spectr.	Grating/Grism	Exp.[s]	# spec.
005245.11–005337.2	20.47	19.86	19.15	17.97	17.22	16/08/07-20/08/07	NTT	EMMI	Grat#7	1200	21
024642.55+004137.2	19.99	19.23	18.42	17.29	16.60	05/10/07-09/10/07	NTT	EMMI	Grat#7	650-800	19
030904.82–010100.8	20.77	20.24	19.50	18.43	17.77	07/10/07-12/10/07	NTT	EMMI	Grat#7	1500	4
031404.98–011136.6	20.78	19.88	19.03	17.76	16.98	02/10/07-03/10/07	M-Baade	IMACS	600 line/mm	600-900	12
113800.35–001144.4	19.14	18.86	18.87	18.15	17.53	16/08/06-23/03/07	VLT (*sm*)	FORS2	1028z	900	2
						18/06/07-23/06/07	WHT	ISIS	158R	1500	1
						17/05/07-20/05/07	M-Clay	LDSS-3	VPH-red	500-600	5
115156.94–000725.4	18.64	18.12	18.14	17.82	17.31	17/05/07-20/05/07	M-Clay	LDSS-3	VPH-red	450-600	17
152933.25+002031.2	18.69	18.20	18.33	17.98	17.48	18/05/07-20/05/07	M-Clay	LDSS-3	VPH-red	500-1000	18
172406.14+562003.0	15.83	16.03	16.42	16.42	16.52	25/09/00-29/03/01	SDSS			900	23
224139.02+002710.9	19.62	18.82	18.40	17.33	16.58	02/10/07-03/10/07	M-Baade	IMACS	600 line/mm	600	2
						07/10/07-12/10/07	NTT	EMMI	Grat#7	750-800	3
233928.35–002040.0	20.40	19.68	19.15	18.07	17.36	07/10/07-12/10/07	NTT	EMMI	Grat#7	1400-1700	15
Photometry											
SDSS J	*u*	*g*	*r*	*i*	*z*	Dates	Telesc.		Filter band	Exp.[s]	# hrs
031404.98–011136.6	20.78	19.88	19.03	17.76	16.98	19/09/06-20/09/06	CA 2.2 m		clear	35-60	10.3
082022.02+431411.0	15.92	15.85	16.11	15.83	15.38	21/11/06-24/11/06	Kryoneri 1.2 m		*R*	60	8.2
172406.14+562003.0	15.83	16.03	16.42	16.42	16.52	04/08/06-10/08/06	IAC80		*I*	80-180	12.2
						25/03/06-13/09/06	AIP 70 cm		*R*	60-90	55.6

Notes: M-Baade and M-Clay refer to the two Magellan telescopes at Las Campanas observatory. We use *sm* to indicate that the data were taken in service mode. CA 2.2 is the 2.2 meter telescope at Calar Alto observatory.

4.2.2 Photometry

(i) *IAC80 and AIP 70 cm telescopes.* We obtained differential photometry of SDSS J1724 +5620 with the IAC80 telescope at the Observatorio del Teide (Spain) and the 70 cm telescope of the Astrophysical Institute of Potsdam at Babelsberg (Germany) for a total of 13 nights during May, August and September 2006 and March 2007. The IAC80 cm telescope was equipped with a 2k×2k CCD. A binning factor of 2 was applied in both spatial directions and only a region of 270×270 (binned) pixels of size 0.66 arcsec was read. We used IRAF to reduce the images and to obtain the differential magnitudes. Observations and data reduction were carried out by myself (see Table 4.1). The detector used at the Babelsberg 70 cm telescope was a cryogenic 1k×1k Tek CCD. The whole frame was read with a binning factor of 3, resulting in a scale of 1.41 arcsec/pixel. A semiautomated pipeline involving DoPHOT [Schechter et al., 1993] was used to reduce the images and extract the photometric information. Observations and reduction were carried out by the Potsdam group (A.Nebot Gómez-Morán, M.Krumpe, R. Schwarz, A. Staude, and J. Vogel, see Table 4.1).

(ii) *Calar Alto 2.2 m telescope.* We used CAFOS with the SITe 2k×2k pixel CCD camera on the 2.2 meter telescope at the Calar Alto observatory to obtain filter-less differential photometry of SDSS J0314–0111. Only a small part of the CCD was read out in order to improve the time resolution. The data were reduced using the pipeline described in Gänsicke et al. [2004], which pre-processes the raw images in MIDAS and extracts aperture photometry using the SEXTRACTOR [Bertin & Arnouts, 1996]. Observations and data reduction were carried out by A.Aungwerojwit (see Table 4.1).

(iii) *Kryoneri 1.2 m telescope.* Filter-less photometry of SDSS J0820+4311 was obtained in November 2006 at the 1.2 m Kryoneri telescope using a Photometrics SI-502 516×516 pixel camera. The data reduction was carried out in the same way as described above for the Calar Alto observations. Observations and data reduction were carried out by V.Karamanavis and E.Tremou (see Table 4.1).

Chapter 5

Time-Series Analysis

5.1 Time-Series description

Time-series analysis is a mathematical tool that transforms time-dependent data from the time-domain to the frequency-domain. The most fundamental is the Fourier transform, and can both be applied from the time- to the frequency-domain and vice versa. Mathematically speaking, a Fourier transform decomposes a periodic function into a sum of sines and cosines and their harmonics. Each sine wave, when multiplied by an appropriate factor, will give the power carried by the wave, per unit frequency. Different sine power form the power spectrum of the variable. In a binary star, the analysis of time-dependent observables related to the orbital period, such as the radial velocities (RVs) and the differential magnitudes, then provide a power spectrum that can be used to determine the orbital periods (see Chapter 8). Ideally, the power spectrum would contain a single peak, or δ-function, corresponding to a pure sine variation of infinite duration, i.e. an exact orbital period in our context. Nevertheless, there are three important limitations.

The first limitation is related to the length of the observing night. The longer the time spent observing a particular system (on the same night), the more orbital phases are covered. According to this, in cases where the data do not cover enough phases, the power spectrum is then not a single δ-function but a much broader peak (Fig. 5.1 bottom). In order to cover additional orbital phases it is then necessary to observe on consecutive nights. This is related to the second limitation. Applying time-series analysis to data observed on

consecutive nights introduces an alias pattern, composed of several narrow power peaks around the true frequency in the power spectrum. The separation between the true peak and the aliases will be determined by the frequency of the observations. Since the shortest separation between observations is one night, the aliases will then be split by a minimum of 1 d^{-1} from the true signal in the power spectrum. This leads to the third limitation: more data are generally necessary to distinguish the true peak from the possible aliases. The longer the orbital period the more difficult it is to sample the complete orbital cycle, and consequently more data and/or nights are needed. Nevertheless, if these data are taken with similar sampling the statistical significance of the aliases and the true peak will be very similar. This is what is referred in the literature as *cycle count ambiguity*. To avoid this ambiguity it becomes necessary to observe the system with uneven sampling. In this way, time-series analysis of data combined from different nights will eventually provide a clear signal in the power spectrum and provide an accurate measurement of the orbital period. To illustrate these limitations I show in Fig. 5.1 the power spectra along four different nights of SDSS J0052-0053, a PCEB studied in Chapter 8. A broad peak in the power spectrum on the bottom panel of the figure (first observing night, labelled as t = 0) shows the typical feature obtained from running time-series analysis on a single night of data. The alias pattern obtained on the consecutive night (t = 1) gives a peak and two possible aliases, all three of them moderately broad. More data included on the following nights (t = 2 and t = 4) narrow the peaks considerably and finally provide a clear signal at 8.7 d^{-1}, i.e. an orbital period of 164.2 minutes for this system. In practice, to investigate the periodic nature of the velocity variations we run sine-fits to the velocity data sets adopting the frequencies corresponding to the strongest peaks in the power spectrum as initial conditions (see Chapter 8). Reduced χ^2 values obtained from the sine-fits allow generally a unique solution, in which case the reduced χ^2 is close to 1.

5.2 Time-Series methods

In this thesis I have used a MIDAS/TSA package written by A.Schwarzenberg-Czerny, which includes four different methods to apply time-series analysis. These are the methods:

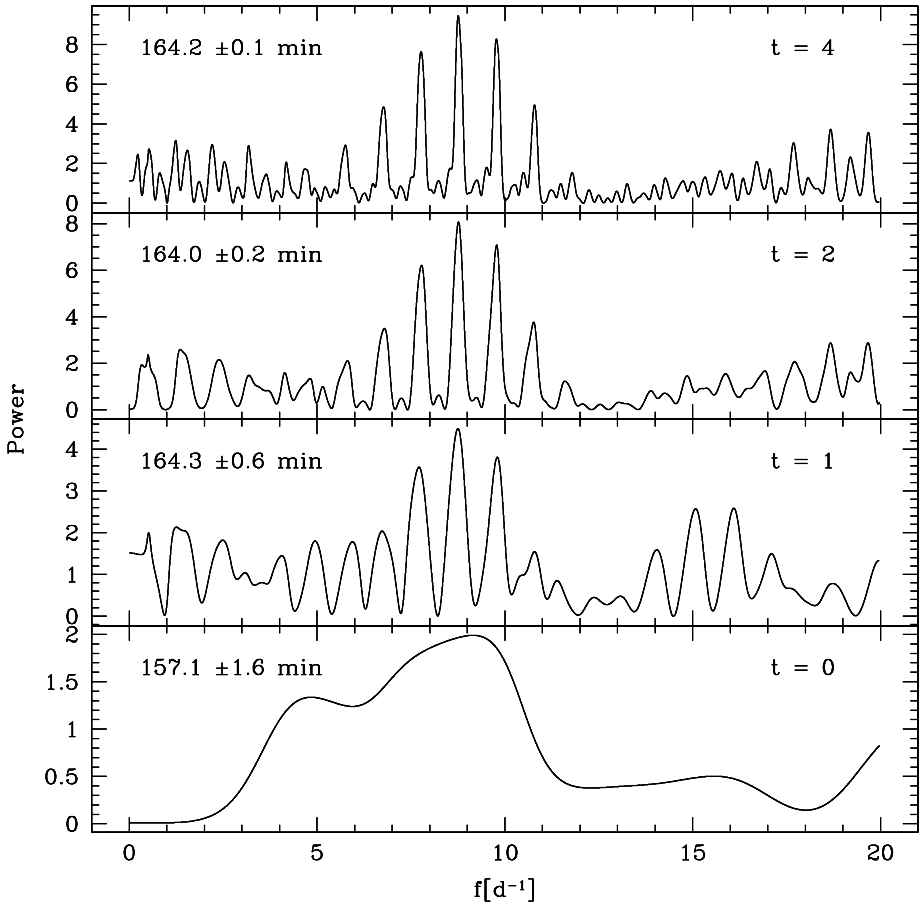

Figure 5.1: Power spectra of SDSSJ 0052-0053, a PCEB studied in Chapter 8. The power spectra are obtained running Scargle periodograms (see Sect. 5.2) to the Na I λλ 8183.27,8194.81 absorption doublet RVs. The numbers in the top right corner of each panel indicate the observing night, assuming t = 0 as the first night (note that no data were taken in the third night, t = 3). The corresponding measured orbital period is labelled on the top left of each panel. The power spectrum on the bottom panel illustrates the typical broad peak feature characteristic of a single observing night data. The alias pattern appears on the rest of the nights, decreasing the strength of the aliases as more data are included, and finally providing an accurate value of the orbital period.

POWER/TSA. Computes the Fourier transform to the data. This is the simplest method for time-series analysis.

SCARGLE/TSA. This method fits a pure sine fit model to the data by computing a Scargle [1982] periodogram.

AOV/TSA. Applies the code described by Schwarzenberg-Czerny [1989], which folds the data over different possible orbital periods, bins them in orbital phase, and analyses the variance of the resulting phase curves.

ORT/TSA. Based on Schwarzenberg-Czerny [1996] this method also folds the data over different possible orbital periods, this time fitting a set of orthogonal multi-harmonic sine waves to the phase-folded data.

The first two methods, POWER and SCARGLE, belong to the Fourier-type methods, and are effective for detecting faint signals, as well as quasi-sinusoidal variations. AOV and ORT belong to phase-folding methods, and are generally best-suited for abrupt changes in the time-dependent variation. These methods are hence effective in detecting non-sinusoidal variations, with ORT resulting in a smoother power spectrum than produced by AOV. It is important to note though, that there is no universal best method for time-series.

In Chapter 8 I use the RVs obtained from the Na I $\lambda\lambda$ 8183.27,8194.81 absorption doublet to measure the orbital periods of 6 PCEBs, and differential magnitudes to obtain an additional $P_{\rm orb}$. PCEBs are not affected by the presence of an accretion disc, and their RV variations are hence expected to be sinusoidal. Consequently POWER and SCARGLE periodograms obtained from these RVs generally provide clear signals in their power spectra (see Fig 5.1). In CVs non-sinusoidal RV variations might be expected due to multiple line components originating in different parts of the binary. Thus, phase-folding methods such as AOV and ORT might provide better results. This is also the case when applying time-series analysis to light curves of eclipsing binaries, which show abrupt changes.

Chapter 6

Sloan Digital Sky Survey

The Sloan Digital Sky Survey, SDSS, was an imaging and spectroscopic survey that covered approximately one-quarter of the celestial sphere. SDSS operated a 2.5 m wide-field altitude-azimuth telescope at Apache Point Observatory, New Mexico. The telescope had a 3° diameter field of view, and it was equipped with a large-format mosaic of 30 2048 × 2048 Tektronix CCD cameras that took *ugriz* imaging (Fig. 6.1). The detection limit for point sources in 1 arcsec seeing was 22.3, 23.3, 23.1, 22.3, and 20.8 magnitudes on the AB system respectively, at an air mass of 1.4. The five filters had effective wavelengths of 3560, 4680, 6180, 7500, and 8870 Å. The imaging survey was divided into two different areas (Fig 6.2). The first area (northern Galactic Cap) was situated above Galactic latitude 30°, and it was selected to achieve the minimum Galactic extinction. It was centred at $\alpha = 12^h20^m$, δ = +32.5°, and covered $\sim$ 10000 contiguous deg^2. The second area (southern Galactic Cap) comprised three stripes, one along the celestial equator ($\alpha = 20^h7^m, \delta$ = 0°) and the other two north and south of the equator.

Based on colours and morphology, objects were flagged for spectroscopic follow-up. The wavelength coverage of the spectrographs was continuous from about 3800–9200 Å, and the wavelength resolution, $\lambda/\delta\lambda$, varied from 1850 to 2200. Each "spectral plate" refered physically to a metal plate with holes drilled at the positions of 640 spectroscopic plus calibration targets, covering $\sim$ 7deg^2. Each SDSS spectrum was then unambiguously identified by the modified Julian date (MJD) of the observation, the spectroscopic plate (PLT) and the fibre (FIB). Up to nine spectral plates per night were observed, with the

necessary plates being plugged with fibres during the day. The spectra were observed with a total integration time of 45-60 minutes, split into individual ~ 15 min exposures, depending on observing conditions. The flux- and wavelength-calibrated spectra were provided on a vacuum wavelength scale and corrected to the heliocentric restframe.

Special care needs to be taken in establishing the date and time when the SDSS spectra were obtained: a significant fraction of SDSS spectra were *combined* from observations taken on different nights (which I will call "sub-spectra" in what follows) in which case the header keyword `MJDLIST` will be populated with more than one date. Hence, a meaningful time at mid-exposure can only be given for those SDSS spectra that were obtained in a single contiguous observation. The headers of the SDSS data provide the exposure start and end times in International Atomic Time (TAI), and refer to the start of the first spectrum, and the end of the last spectrum.

The photometric data were reduced by applying "photometric pipelines" which corrected the data for CCD defects, calculated overscan, biases, sky, flat-field values, and PSF (point-spread functions) magnitudes for all point sources. The mean errors were about 0.03 mag at 20 mag, increasing to about 0.05 mag at 21 mag and to 0.12 mag at 22 mag for the *g*, *r*, and *i* bands. The errors increased to 0.05 at 20 mag and 0.12 at 21 mag for the less sensitive *u* and *z* bands. Spectroscopic targets were selected by a "target selection pipeline", and reduced by the application of a "spectroscopic pipeline", which corrected, extracted and calibrated the spectra, and measured the redshifts. The reduced spectra were then stored in a science data base. SDSS completed its first phase of operations (SDSS-I) in June 2005, with more than 8000 deg^2 imaged, and nearly 200 million celestial objects detected, and it contained spectra of more than 675000 galaxies, 90000 quasars, and 185000 stars. A second phase, SDSS-II, continued with observations through June 2008 and ended in October 2008, finishing the original galaxy and quasar survey. SDSS-II carried out three distinct surveys: the Sloan Legacy Survey, SEGUE (Sloan Extension for Galactic Understanding and Exploration), and the Sloan Supernova Survey. Building on the legacy of SDSS and SDSS-II, SDSS-III, a program of four new surveys (BOSS, SEGUE-2, APOGEE, MARVELS) using SDSS facilities, began in July 2008 and will continue through 2014. This collaboration carries out a program focus on dark energy and cosmological parameters, on

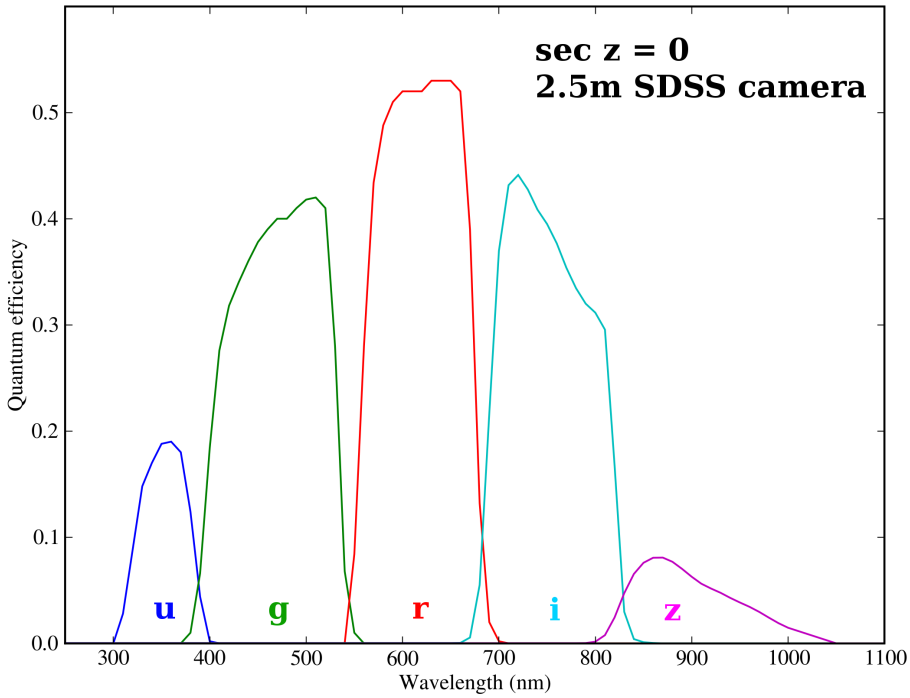

Figure 6.1: SDSS 2.5 m u, g, r, i and z filter responses. The curves include the quantum efficiency of the CCD at zero air mass. Provided by R.Hickman.

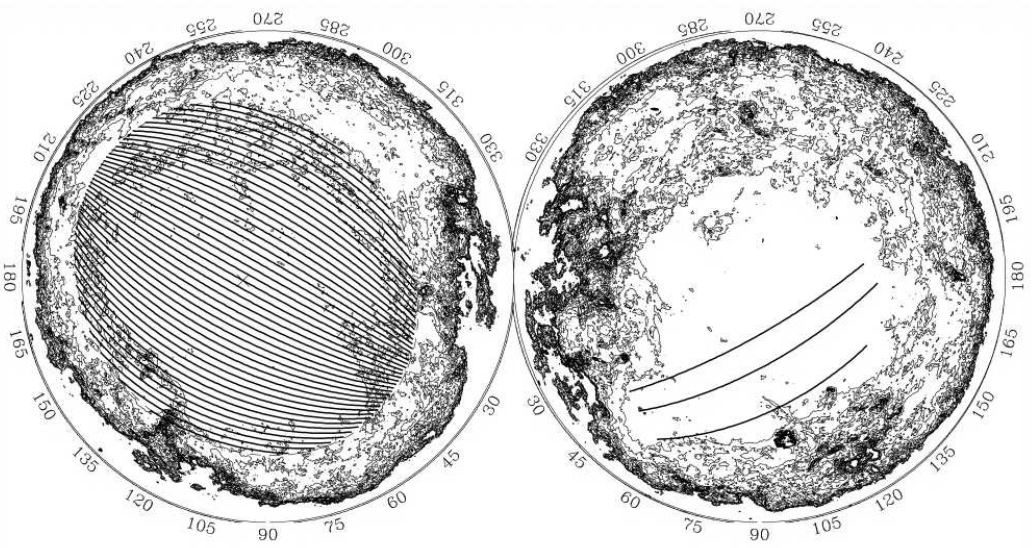

Figure 6.2: Northern and southern SDSS survey in galactic coordinates. The lines represent the area of the sky available for SDSS imaging. Taken from York et al. [2000].

the structure, dynamics and evolution of the Milky Way, and on studies of planetary systems.

SDSS data were initially available to public in 2001 [Stoughton et al., 2002] and its technical details were summarised in York et al. [2000]. After this different data releases (DR) have been increasing the amount of available data, with DR 7 the latest among them[1] [Abazajian et al., 2003, 2004, 2005; Adelman-McCarthy et al., 2006, 2007, 2008]. With DR 6 the imaging of the northern Galactic cap was completed. At this point the survey contained images and parameters of roughly 287 million objects over 9583 deg^2, plus 1.27 million spectra of stars, galaxies and quasars selected over 7425 deg^2. DR 6 included also the first year of data from the SDSS-II.

There exist three separate user interfaces which permit one to download SDSS data: a Catalog Archive Server (CAS), which contains the measured parameters from all objects in the imaging survey and the spectroscopic survey. The SDSS Query Tool is a stand-alone

[1]Note that DR 7 is just released and complete details are still not available via a refereed paper. In addition, this thesis focusses on the analysis of SDSS DR 5 (Chapters 7 and 8) and DR 6 (Chapters 9 and 10) data. For these reasons, I will focus on DR 6 in what follows.

application to manage and perform Catalog Archive Server queries available for downloading; a Data Archive Server (DAS) which makes the raw and reduced data (corrected frames, binned images, colour images, spectra) available; and a SkyServer, which offers web-based access to a relational data base server (SQL).

Even though the main aim of SDSS is the identification of galaxies [e.g. Strauss et al., 2002] and quasars [e.g. Adelman-McCarthy et al., 2006], its relevance on the observational studies of WDMS binaries and PCEBs has been clearly demonstrated in the last few years [see also the following Chapters of this thesis; Raymond et al., 2003; van den Besselaar et al., 2005; Schreiber et al., 2008; Silvestri et al., 2006, 2007; Augusteijn et al., 2008; Pyrzas et al., 2008; Nebot Gómez-Morán et al., 2009]. A crucial point is then to understand why SDSS observed WDMS binaries. These objects are a big source of contamination in the quasar search in a particular colour region (see Chapter 9). Thus, $\sim$ 40% of the SDSS spectroscopic WDMS binaries were initially targeted as UV-excess or high-redshift quasar candidates. Richards et al. [2002, see also Chapter 9] defined WDMS binary exclusion boxes with the aim to maximise the return of the quasar survey within SDSS. Nevertheless $\sim$33% of the observed SDSS spectroscopic WDMS binaries are within the WDMS binary exclusion boxes, half of them observed as CV candidates, and the rest probably observed as quasar candidates before the exclusion boxes were defined. A final $\sim$25% of the SDSS spectroscopic WDMS binaries were observed as quasar candidates fainter than the main SDSS quasar sample, or targets carried out especially in the equatorial region.

SEGUE has been specifically designed to fill in WDMS missing from SDSS-I (i.e. in the WDMS binary exclusion boxes and close to the main sequence), and contains $\sim$25% of the overall SDSS WDMS binaries, the remaining $\sim$75% were observed as discussed in the previous paragraph.

Chapter 7

130 White Dwarf-Main Sequence Binaries with multiple SDSS Spectroscopy

7.1 Introduction

A feature of SDSS hitherto unexplored in the study of WDMS binaries is the fact that $\sim$ 10 per cent of the spectroscopic SDSS objects are observed more than once (Chapter 6). SDSS occasionally re-observes entire spectral plates, where all targets on that plate get an additional spectrum, or has plates which overlap to some extent, so that a small subset of targets on each plate is observed again. The detection of RV variations between different SDSS spectra of a given WDMS binary will unambiguously identify such a system as a PCEB, or a strong PCEB candidate. In this Chapter I make use of a sample of 130 WDMS binaries with SDSS spectroscopic repeat observations to identify 18 PCEBs and PCEB candidates from RV variations. Using a spectral decomposition/fitting technique I determined the white dwarf effective temperatures and surface gravities, masses, and secondary star spectral types for all WDMS binaries in the sample. Two independent distance estimates are also obtained from the flux scaling factors between the WDMS binary spectra, and the white dwarf models and MS star templates, respectively.

The structure of the Chapter is as follows: I describe the WDMS binary sample and the methods used to determine RVs in Sect. 7.2. In Sect. 7.3 I determine the stellar parameters of the WDMS binaries in the sample. In Sect. 7.4, I discuss the fraction of PCEBs found, the distribution of stellar parameters, compare the results to those of Raymond et al. [2003] and Silvestri et al. [2006], discuss the incidence of stellar activity on the secondary stars in WDMS binaries, and outline the selection effects of SDSS regarding WDMS binaries with different types of stellar components. I finally conclude this Chapter in Sect. 7.5.

7.2 Identifying PCEBs in SDSS

We have searched the DR5 spectroscopic data base for multiple exposures of all the WDMS binaries listed by Silvestri et al. [2006] and Eisenstein et al. [2006], as well as a set of WDMS binaries independently found in the SDSS data by our team. This search resulted in a sample of 130 WDMS binaries with two to seven SDSS spectra. Among those WDMS, 101 systems have a clearly pronounced Na I $\lambda\lambda$ 8183.27,8194.81 absorption doublet and/or Hα emission in their SDSS spectra, and were subjected to RV measurements using one or both spectral features. The Na I doublet was fitted with a second order polynomial and double-Gaussian line profile of fixed separation. Free parameters were the amplitude and the width of each Gaussian and the velocity of the doublet. Hα was fitted using a second order polynomial plus a single Gaussian of free velocity, amplitude and width. We computed the total error on the RVs by quadratically adding the uncertainty in the zeropoint of the SDSS wavelength calibration (10 km s^{-1}, Stoughton et al. 2002) and the error in the position of the Na I/Hα lines determined from the Gaussian fits. Figure 7.1 shows the fits to the four SDSS spectra of SDSS J024642.55+004137.2, a WDMS binary displaying an extremely large RV variation identifying it as a definite PCEB. This figure also illustrates an issue encountered for a handful of systems, i.e. that the Hα and Na I RVs do not agree in the final spectrum (Table 7.1). This is probably related to the inhomogeneous distribution of the Hα emission over the surface of the companion star, and will be discussed in more detail in Sect. 7.4.1. In total, 18 WDMS show RV variations among their SDSS spectra at a 3σ level and qualify as PCEBs or strong PCEB candidates. Their RVs are listed in Table 7.1 and

illustrated in Fig. 7.2 and Fig. 7.3. Three systems (SDSS0251–0000, SDSS1737+5403, and SDSS2345–0014) are subject to systematic uncertainties in their RVs due to the rather poor spectroscopic data. The RVs for the remaining 83 WDMS binaries that did not show any significant variation are available in Rebassa-Mansergas et al. [2007, see also Chapter 9].

The $\geq 3\sigma$ criterion for the detection of RV variations in our sample of WDMS is only valid when considering two RV measurements. The inclusion of more RV data increases the false alarm rate of the detection, and consequently the probability of detecting a 3σ variation between two RV measurements increases with the number of measurements made. Thus for example, in the case of SDSSJ 0309-0101, which contains 7 RV values (the maximum in our sample), the false alarm rate is $\sim 4.2\%$, which is more than ten times the value expected when considering only two RVs (0.3%). Nevertheless, it will be shown in Chapter 8 that WDMS are considered as definite PCEBs only when large RV variations are detected, making it unlikely that these variations are given as a consequence of false alarm rate detections. We point the reader to Maxted et al. [2001] (their Sect. 3.3) for a description of a better variability criterion.

As outlined in Chapter 6 a significant fraction of SDSS spectra are combined from observations taken on different nights. A crucial question is obviously how the fact that some of the spectra in our sample are actually combinations of data from several nights impacts our aim to identify PCEBs via RV variations. To answer this question, we first consider wide WDMS binaries that did not undergo a CE phase, i.e. binaries with orbital periods of $\gtrsim$ years. For these systems, sub-spectra obtained over the course of several days will show no significant RV variation, and combining them into a single spectrum will make no difference except to increase the total signal-to-noise ratio (S/N). In contrast to this, for close binaries with periods of a few hours to a few days, sub-spectra taken on different nights will sample different orbital phases, and the combined SDSS spectrum will be a mean of those phases, weighted by the S/N of the individual sub-spectra. In extreme cases, e.g. sampling of the opposite quadrature phases, this may lead to smearing of the Na I doublet beyond recognition, or end up with a very broad Hα line. This may in fact explain the absence / weakness of the Na I doublet in a number of WDMS binaries where a strong Na I doublet would be expected on the basis of the spectral type of the companion. In most

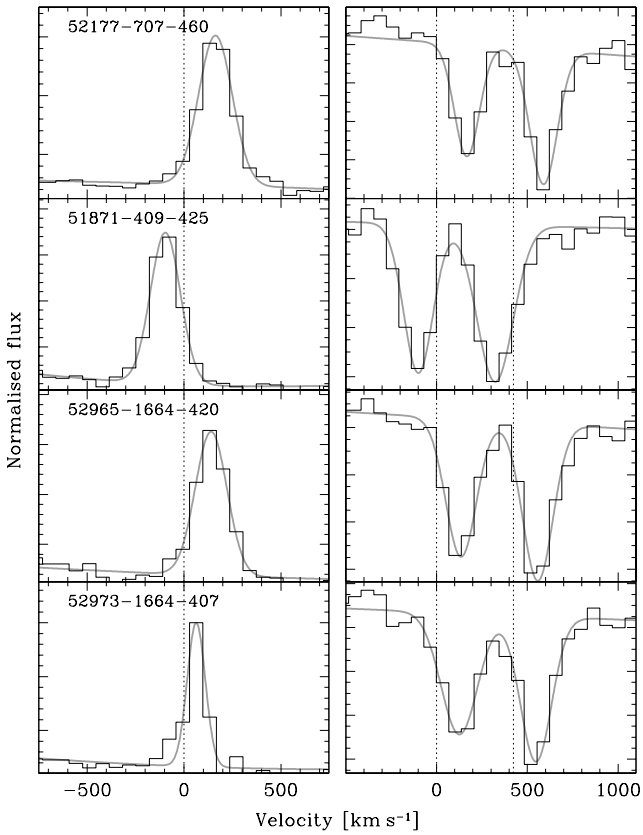

Figure 7.1: Fits to the Na I λλ 8183.27,8194.81 absorption doublet (right panels) and the Hα emission line (left panels) in the four SDSS spectra of the WDMS binary SDSS J024642.55+004137.2. The SDSS spectroscopic identifiers (MJD, Plate-ID and Fibre-ID) are given in the top left corner of the Hα panels. Na I has been fitted with a double-Gaussian of fixed separation plus a parabola, Hα with a Gaussian plus a parabola. In this system, RV variations are already obvious to the eye. The top three spectra are taken in a single night, the bottom one is combined from data taken on three nights, MJD = 52970, 52972, and 52973. The widths of the Gaussians fitting the Na I doublet are (top to bottom) 4.6 Å, 5.8 Å, 5.3 Å, and 6.0 Å.

cases, however, the combined SDSS spectrum will represent an "effective" orbital phase, and comparing it to another SDSS spectrum, itself being combined or not, still provides a measure of orbital motion. We conclude that the main effect of the combined SDSS spectra is a decreased sensitivity to RV variations due to averaging out some orbital phase information. Fig. 7.1 shows an example of a combined spectrum (bottom panel), which contains indeed the broadest Na I lines among the four spectra of this WDMS binaries.

In order to check the stability of the SDSS wavelength calibration between repeat observations, we selected a total of 85 F-type stars from the same spectral plates as our WDMS binary sample, and measured their RVs from the Ca II $\lambda\lambda$ 3933.67,3968.47 *H* and *K* doublet in an analogous fashion to the Na I measurement carried out for the WDMS binaries. None of those stars exhibited a significant RV variation, the maximum variation among all checked F-stars had a statistical significance of 1.5σ. The mean of the RV variations of these check stars was found to be $14.5\,\mathrm{km\,s^{-1}}$, consistent with the claimed $10\,\mathrm{km\,s^{-1}}$ accuracy of the zero-point of the wavelength calibration for the spectra from an individual spectroscopic plate [Stoughton et al., 2002]. In short, this test confirms that the SDSS wavelength calibration is stable in time, and, as anticipated above that averaging sub-spectra does not introduce any spurious RV shifts for sources that have no intrinsic RV variation (as the check stars are equally subject to the issue of combining exposures from different nights into a single SDSS spectrum). We are hence confident that any significant RV variation observed among the WDMS binaries is intrinsic to the system.

7.3 Stellar parameters

The spectroscopic data provided by the SDSS project are of sufficient quality to estimate the stellar parameters of the WDMS binaries presented in this Chapter. For this purpose, we have developed a procedure which decomposes the WDMS binary spectrum into its white dwarf and MS star components, determines the spectral type of the companion by means of template fitting, and derives the white dwarf effective temperature and surface gravity from spectral model fitting. Assuming an empirical spectral type-radius relation for the secondary star and a $M-R$ relation for the white dwarf, two independent distance

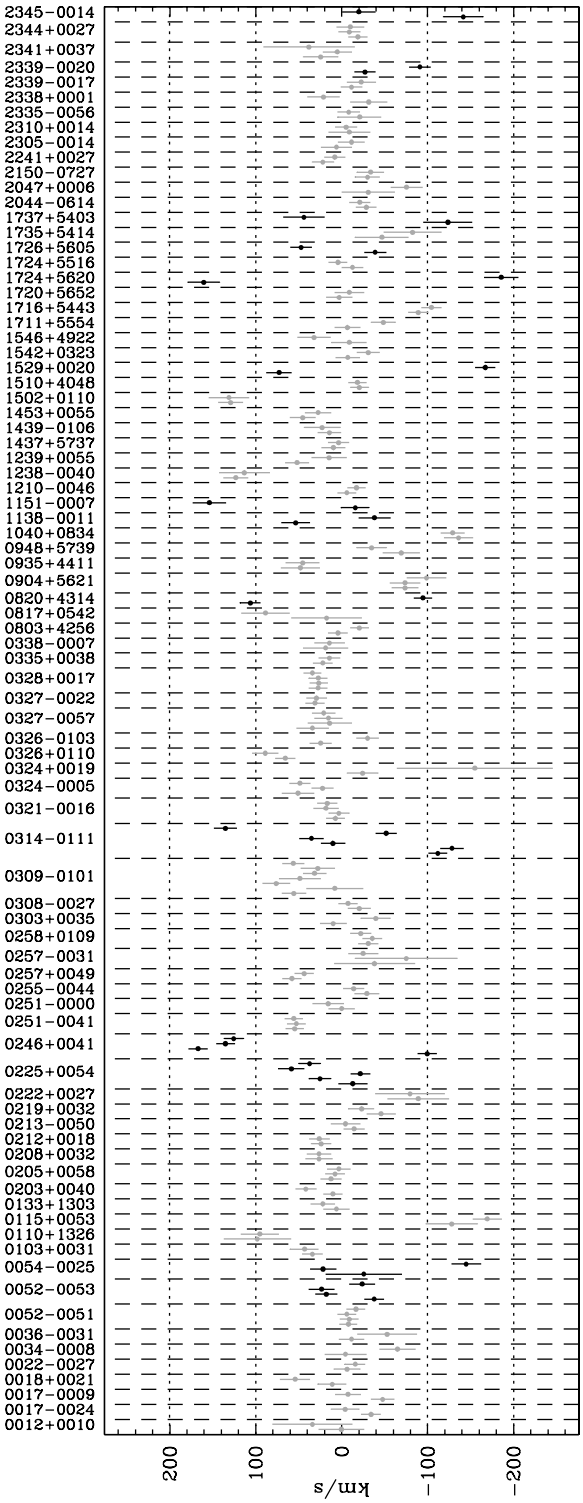

Figure 7.2: RVs obtained from the Na I absorption doublet. WDMS $\geq 3\sigma$ RVs variation, i.e. PCEBs, are shown in black.

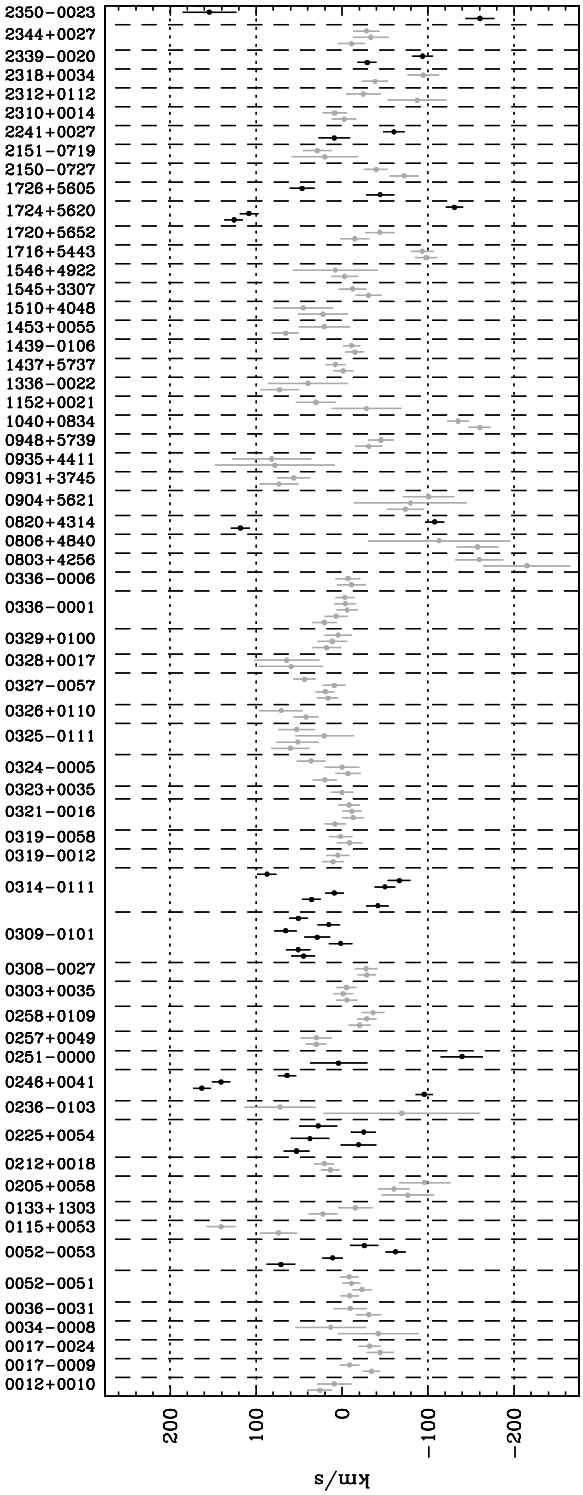

Figure 7.3: Same as Fig. 7.2 but for the Hα RVs.

Table 7.1: RVs of our 18 PCEBs and PCEB candidates, measured from the Hα emission line and/or the Na I λλ 8183.27,8194.81 absorption doublet. The HJDs for SDSS spectra that have been combined from exposures taken in several different nights (see Sect. 7.2) are set in italics. PCEB candidates with uncertain RV measurements are indicated by colons preceding and trailing the object name. Upper limits of the orbital periods are also provided (Sect. 7.4.2). The two spectral components identified in the spectra are coded as follows. DA = white dwarf with clearly visible Balmer lines; DC = clearly visible blue continuum without noticeable structure; blx = weak blue excess; dM = M-dwarf.

SDSS J	HJD	RV(Hα) km s^{-1}	RV(Na) km s^{-1}	$P_{\rm orb}$[d] <
0052–0053	2451812.3463	71.3 ± 16.6	23.4 ± 14.9	280
DA/dM	*2451872.6216*	11.0 ± 12.0	18.0 ± 12.7	
	2451907.0834	-62.1 ± 11.7	-37.7 ± 11.6	
	2452201.3308	-26.0 ± 16.0	-23.8 ± 14.9	
0054–0025	2451812.3463		21.6 ± 15.3	4
DA/dM	*2451872.6216*		-25.6 ± 44.2	
	2451907.0835		-144.7 ± 17.2	
0225+0054	2451817.3966	53.0 ± 14.9	58.6 ± 15.4	45
blx/dM	2451869.2588	-19.2 ± 20.7	-21.6 ± 11.6	
	2451876.2404	37.5 ± 22.4	25.3 ± 12.4	
	2451900.1605	-25.1 ± 14.0	-12.8 ± 17.0	
	2452238.2698	27.9 ± 22.3	37.4 ± 12.8	
0246+0041	2451871.2731	-95.5 ± 10.2	-99.3 ± 11.1	2.5
DA/dM	2452177.4531	163.1 ± 10.3	167.2 ± 11.3	
	2452965.2607	140.7 ± 10.8	135.3 ± 11.0	
	2452971.7468	64.0 ± 10.5	125.7 ± 11.3	
:0251–0000:	*2452174.4732*	4.1 ± 33.5	0.0 ± 15.4	0.58
DA/dM	2452177.4530	-139.3 ± 24.6	15.8 ± 18.3	
0309–0101	2451931.1241	44.8 ± 13.2	31.5 ± 13.7	153
DA/dM	2452203.4500	51.2 ± 14.1	48.7 ± 24.4	
	2452235.2865	27.4 ± 14.1	76.3 ± 16.2	
	2452250.2457	28.8 ± 15.0	8.1 ± 33.0	
	2452254.2052	53.9 ± 11.8	55.7 ± 14.3	
	2452258.2194	15.5 ± 13.0	27.9 ± 19.9	
	2453383.6493	50.7 ± 11.0	56.5 ± 12.8	
0314–0111	2451931.1242	-41.6 ± 12.4	-51.7 ± 12.4	1.1
DC/dM	2452202.3882	35.6 ± 10.9	35.2 ± 14.4	
	2452235.2865	9.1 ± 11.0	10.3 ± 14.2	
	2452250.2457	-49.8 ± 12.2	-128.2 ± 13.9	
	2452254.2053	-66.7 ± 12.8	-111.7 ± 10.9	
	2452258.2195	87.3 ± 10.8	135.2 ± 13.5	
0820+4314	2451959.3074	118.3 ± 11.4	106.3 ± 11.5	2.4
DA/dM	*2452206.9572*	-107.8 ± 11.2	-94.6 ± 10.8	
1138–0011	*2451629.8523*		53.5 ± 16.9	35
DA/dM	2451658.2128		-38.1 ± 18.6	
1151–0007	2451662.1689		-15.8 ± 15.1	4.4
DA/dM	2451943.4208		154.0 ± 19.5	
1529+0020	2451641.4617		73.0 ± 14.8	0.96
DA/dM	2451989.4595		-167.2 ± 11.8	
1724+5620	*2451812.6712*	125.6 ± 10.2	160.6 ± 18.4	0.43
DA/dM	2451818.1149	108.3 ± 11.1	- ± -	
	2451997.9806	-130.6 ± 10.3	-185.5 ± 20.1	
1726+5605	*2451812.6712*	-44.3 ± 16.7	-38.9 ± 12.9	29
DA/dM	*2451993.9805*	46.6 ± 14.6	47.3 ± 12.5	
:1737+5403:	2451816.1187		-123.5 ± 28.6	6.6
DA/dM	2451999.4602		44.0 ± 24.0	
2241+0027	2453261.2749	9.1 ± 17.9	22.0 ± 12.4	7880
DA/dM	2452201.1311	-60.3 ± 12.7	8.1 ± 12.2	
2339–0020	*2453355.5822*	-29.2 ± 10.4	-27.1 ± 12.3	120
DA/dM	2452525.3539	-93.6 ± 12.3	-90.1 ± 12.7	
:2345-0014:	2452524.3379		-141.5 ± 22.9	9.5
DA/dM	*2453357.5821*		-19.8 ± 19.3	
2350-0023	2451788.3516	-160.3 ± 16.6		0.74
blx/dM	2452523.3410	154.4 ± 31.3		

Notes on individual systems. 0246+0041, 0314–0111, 2241+0027, 2339–0020: variable Hα equivalent width; 0251–0000: faint, weak Hα emission with uncertain radial velocity measurements; 1737+5403, 2345–0014: very noisy spectrum; See additional notes in Table 7.3.

estimates are calculated from the flux scaling factors of the template/model spectra.

In the following sections, we describe in more detail the spectral templates and models used in the decomposition and fitting, the method adopted to fit the white dwarf spectrum, our empirical spectral type-radius relation for the secondary stars, and the distance estimates derived from the fits.

7.3.1 Spectral templates and models

In the course of decomposing/fitting the WDMS binary observations, we make use of a grid of observed M-dwarf templates, a grid of observed white dwarf templates, and a grid of white dwarf model spectra. High S/N ratio M-dwarf templates matching the spectral coverage and resolution of the WDMS binary data were produced from a few hundred late-type SDSS spectra from DR4 (see Fig. 3.3). These spectra were classified using the M-dwarf templates of Beuermann et al. [1998]. We averaged the $10-20$ best exposed spectra per spectral subtype. Finally, the spectra were scaled in flux to match the surface brightness at 7500 Å and in the TiO absorption band near 7165 Å, as defined by Beuermann [2006]. Recently, Bochanski et al. [2007] published a library of late type stellar templates. A comparison between the two sets of M-dwarf templates did not reveal any significant difference. We also compiled a library of 490 high S/N DA white dwarf spectra from DR4 covering the entire observed range of $T_{\rm eff}$ and $\log g$. As white dwarfs are blue objects, their spectra suffer more from residual sky lines in the *I*-band. We have smoothed the white dwarf templates at wavelengths > 7000 Å with a five-point box car to minimise the amount of noise added by the residual sky lines. Finally, we computed a grid of synthetic DA white dwarf spectra using the model atmosphere code described by Koester et al. [2005], covering $\log g = 5.0-9.5$ in steps of 0.25 and $T_{\rm eff} = 6000-100000$ K in 37 steps nearly equidistant in $\log(T_{\rm eff})$.

7.3.2 Spectral decomposition and typing of the secondary star

Our approach is a two-step procedure. In a first step, we fitted the WDMS binary spectra with a two-component model and determined the spectral type of the M-dwarf. Subsequently, we subtracted the best-fit M-dwarf, and fitted the residual white dwarf spectrum

(Sect. 7.3.3). We used an evolution strategy [Rechenberg, 1994] to decompose the WDMS binary spectra into their two individual stellar components. In brief, this method optimises a fitness function, in this case a weighted χ^2, and allows an easy implementation of additional constraints. Initially, we used the white dwarf model spectra and the M-dwarf templates as spectral grids. However, it turned out that the flux calibration of the SDSS spectra is least reliable near the blue end of the spectra, and correspondingly, in a number of cases the χ^2 of the two-component fit was dominated by the poor match of the white dwarf model to the observed data at short wavelengths. As we are in this first step not yet interested in the detailed parameters of the white dwarf, but want to achieve the best possible fit of the M-dwarf, we decided to replace the white dwarf models by observed white dwarf templates. The large set of observed white dwarf templates, which are subject to the same observational issues as the WDMS binary spectra, provided in practically all cases a better match in the blue part of the WDMS binary spectrum. From the converged white dwarf plus dM template fit to each WDMS binary spectrum (see Fig. 7.4), we recorded the spectral type of the secondary star, as well as the flux scaling factor between the M-star template and the observed spectrum. The typical uncertainty in the spectral type of the secondary star is ± 0.5 spectral class. The spectral types determined from the composite fits to each individual spectrum are listed in Table 7.3 for the PCEBs in the analysed sample, and in Rebassa-Mansergas et al. [2007] for the remaining WDMS binaries (see also Chapter 9). Inspection of those tables shows that for the vast majority of systems, the fits to the individual spectra give consistent parameters. We restricted the white dwarf fits to WDMS binaries containing a DA primary, consequently no white dwarf parameters are provided for those WDMS binaries containing DB or DC white dwarfs.

7.3.3 White dwarf parameters

Once the best-fit M-dwarf template has been determined and scaled appropriately in flux, it is subtracted from the WDMS binary spectrum. The residual white dwarf spectrum is then fitted with the grid of DA models described in Sect. 7.3.1. Because of the uncertainties in the flux calibration of the SDSS spectra and the flux residuals from the M-star subtraction, we decided to fit the normalised Hβ to Hε lines and omitted Hα where the residual con-

tamination from the secondary star was largest. While the sensitivity to the surface gravity increases for the higher Balmer lines [e.g. Kepler et al., 2006], we decided not to include them in the fit because of the deteriorating S/N and the unreliable flux calibration at the blue end. We determined the best-fit $T_{\rm eff}$ and $\log g$ from a bicubic spline interpolation to the χ^2 values on the $T_{\rm eff} - \log g$ grid defined by our set of model spectra. The associated 1σ errors were determined from projecting the contour at $\Delta\chi^2 = 1$ with respect to the χ^2 of the best fit onto the $T_{\rm eff}$ and $\log g$ axes and averaging the resulting parameter range into a symmetric error bar.

The equivalent widths of the Balmer lines go through a maximum near $T_{\rm eff} = 13\,000$ K, with the exact value being a function of $\log g$. Therefore, $T_{\rm eff}$ and $\log g$ determined from Balmer line profile fits are subject to an ambiguity, often referred to as "hot" and "cold" solutions, i.e. fits of similar quality can be achieved on either side of the temperature at which the maximum equivalent width occurs. We measured the Hβ equivalent width in all the model spectra within our grid, and fitted the dependence of the temperature at which the maximum equivalent width of Hβ occurs by a second-order polynomial,

$$T_{\rm eff}({\rm EW[H}\beta]_{\rm max}) = 20361 - 3997 \log g + 390 (\log g)^2 \qquad (7.1)$$

where the units of $T_{\rm eff}$ are [K] and the units of g are [cm/s^2]. Parallel to the fits to the normalised line profiles, we fit the grid of model spectra to the white dwarf spectrum over the wavelength range $3850 - 7150$ Å (see Fig. 7.5). The red end of the SDSS spectra, where the distortion from the M-dwarf subtraction is strongest is excluded from the fit. We then use the $T_{\rm eff}$ and $\log g$ from the fits to the whole spectrum, continuum plus lines, to select the "hot" or "cold" solution from the line profile fits. In the majority of cases, the solution preferred by the fit to the whole spectrum has a substantially lower χ^2 than the other solution, corroborating that it is likely to be the physically correct choice. In a few cases, the best-fit $T_{\rm eff}$ and $\log g$ from the whole spectrum are close to the maximum equivalent width given by Eq.7.1, so that the choice between the two line profile solutions is less well constrained. However, in most of those cases, the two solutions from the line profile fits overlap within their error bars, so that the final choice of $T_{\rm eff}$ and $\log g$ is not too badly affected.

Once that $T_{\rm eff}$ and $\log g$ are determined from the best line profile fit, we use an updated version of Bergeron et al. [1995b]'s tables to calculate the mass and the radius of the white dwarf (see Fig. 2.1). Systematic errors in the white dwarf parameters are expected due to uncertainties in the H-layer thickness, and due to the low $T_{\rm eff}$ $\log g$ problem for cool white dwarfs. The first kind of uncertainty affects mainly low-mass white dwarfs and is discussed in detail in Chapter 10. The low $T_{\rm eff}$ $\log g$ problem for cool white dwarfs is a consequence of increasing the surface gravity towards lower effective temperatures below $\lesssim$ 12000 K [Koester et al., 2008]. This leads to an increase in the white dwarf masses, and consequently to lower radii and distances (see Sect. 7.3.5). Only 14 systems among our sample of 95 WDMS binaries with $T_{\rm eff}$ estimates contain cool (less than 12000 K) white dwarfs, and systematic uncertainties might consequently be expected in $\sim$15% of our white dwarf masses, distances (see Sect. 7.4.7) and $\log g$ calculations. Table 7.3 reports $T_{\rm eff}$, $\log g$, and the white dwarf masses for the PCEBs in our sample, while the results for the remaining WDMS binaries can be found in Rebassa-Mansergas et al. [2007, see also Chapter 9]. We have carefully inspected each individual composite fit, and each subsequent fit to the residual white dwarf spectrum, and are confident that we have selected the correct solution in the majority of cases. Some doubt remains primarily for a few spectra of very low S/N. The fact that we have analysed at least two SDSS spectra for each system allows us to assess the robustness of our spectral decomposition/fitting method. Inspection of Table 7.3 shows that the system parameter of a given system, as determined from several different SDSS spectra, generally agree well within the quoted errors, confirming that our error estimate is realistic.

7.3.4 An empirical spectral type-radius relation for M stars

In order to use the flux scaling factor between the observed WDMS binary spectra and the best-fit M-dwarf templates for an estimate of the distance to the system (Sect. 7.3.5), it is necessary to assume a radius for the secondary star. Since we have determined the spectral types of the companion stars from the SDSS spectra (Sect. 7.3.2), we require a spectral type-radius relation ($Sp-R$) for M-dwarfs. The community working on CVs has previously had interest in such a relation [e.g. Mateo et al., 1985; Caillault & Patterson, 1990], but while

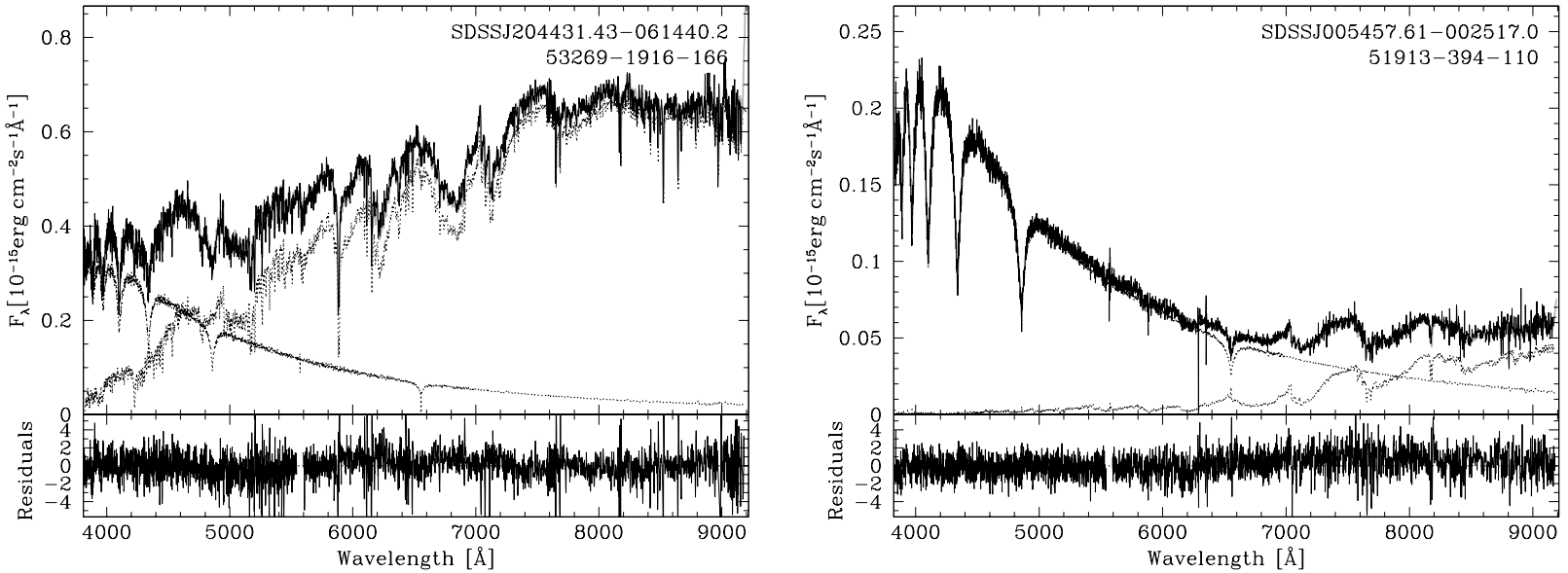

Figure 7.4: Two-component fits to the SDSS WDMS binary spectra. Shown are examples for objects with either the M-dwarf or the white dwarf dominating the SDSS spectrum. The top panels show the WDMS binary spectrum as black line, and the two templates, white dwarf and M-dwarf, as dotted lines. The bottom panels show the residuals from the fit. The SDSS spectrum identifiers MJD, PLT and FIB are given in the plots below the object names.

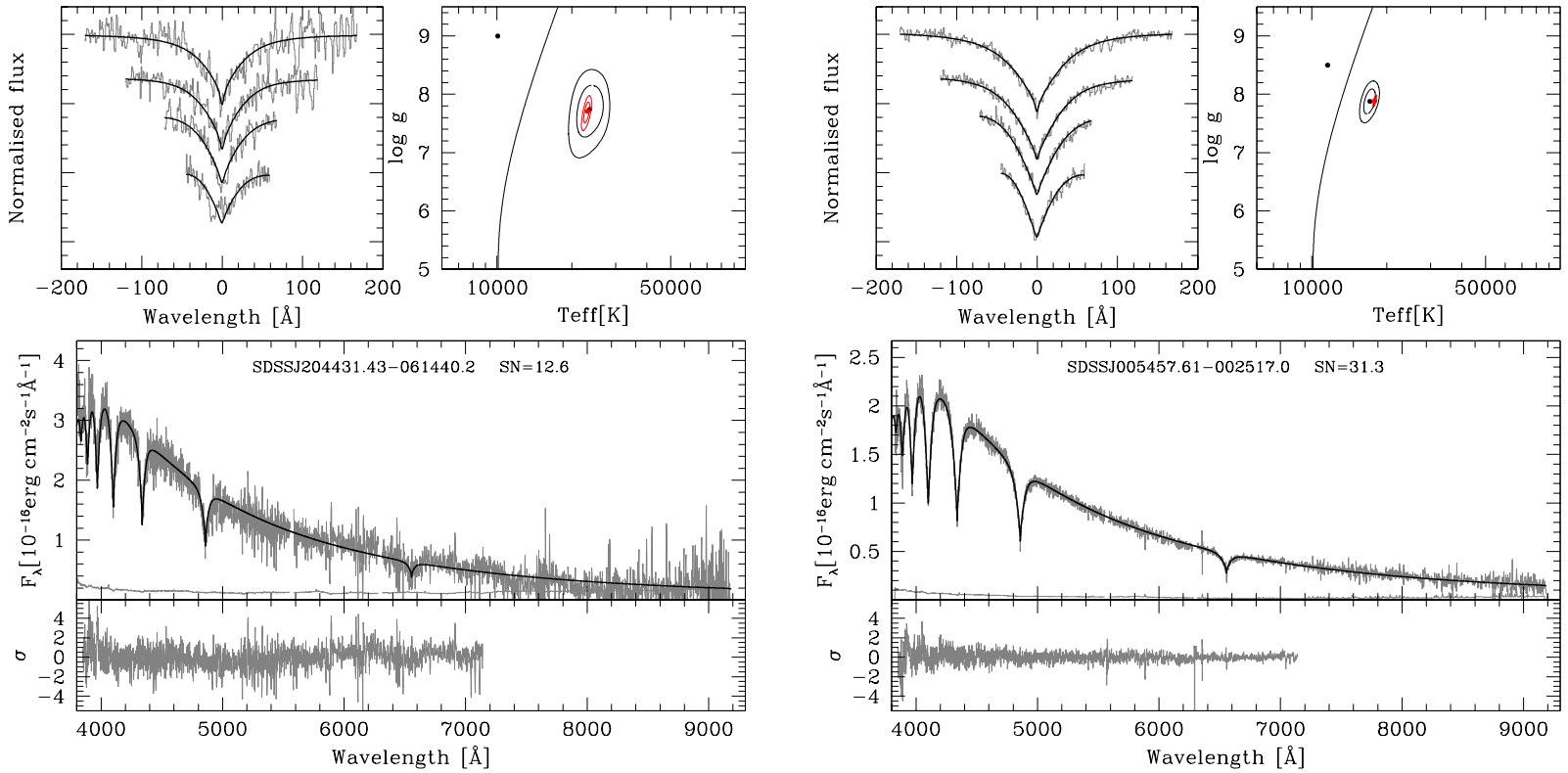

Figure 7.5: Spectral model fits to the white dwarf components of the two WDMS binaries shown in Fig.5, obtained after subtracting the best-fit M-dwarf template. Top left panels: best-fit (black lines) to the normalised Hβ to Hε (gray lines, top to bottom) line profiles. Top right panels: 3, 5, and 10σ χ^2 contour plots in the $T_{\rm eff} - \log g$ plane. The black contours refer to the best line profile fit, the red contours to the fit of the whole spectrum. The dashed line indicates the occurrence of maximum Hβ equivalent width. The best "hot" and "cold" line profile solutions are indicated by black dots, the best fit to the whole spectrum is indicated by a red dot. Bottom panels: the residual white dwarf spectra resulting from the spectral decomposition and their flux errors (gray lines) along with the best-fit white dwarf model (black line) to the 3850–7150 Å wavelength range (top) and the residuals of the fit (gray line, bottom). The $T_{\rm eff}$ and $\log g$ values listed in Table 7.3 are determined from the best line profile fit. The fit to the whole spectrum is only used to select between the "hot" and "cold" line fit.

Baraffe & Chabrier [1996] derived theoretical mass/radius/effective temperature-spectral type relationships for single M-dwarfs, relatively little observational work along these lines has been carried out for field low-mass stars. In contrast to this, the number of low-mass stars with accurate mass and radius measurements has significantly increased over the past few years [see e.g. the review by Ribas, 2006], and it appears that for masses below the fully convective boundary stars follow the theoretical models by Baraffe et al. [1998] relatively well. However, for masses $\gtrsim 0.3\,\mathrm{M}_{\odot}$, observed radii exceed the predicted ones. Stellar activity [e.g. López-Morales, 2007] or metallicity effects [e.g. Berger et al., 2006] were identified as possible causes (see Chapter 2).

Besides the lack of extensive observational work on the $Sp-R$ relation of single M-dwarfs, our need for an M-dwarf $Sp-R$ relation in the context of WDMS binaries faces a number of additional problems. A fraction of the WDMS binaries in our sample have undergone a CE phase, and are now short-period binaries, in which the secondary star is tidally locked and hence rapidly rotating. This rapid rotation might enhance the stellar activity in a similar fashion to the short-period eclipsing M-dwarf binaries used in the $M-R$ relation work mentioned above. In addition, it is difficult to assess the age[1] and metallicity of the secondary stars in our WDMS binary sample.

With the uncertainties on stellar parameters of single M-dwarfs and the potential additional complications in WDMS binaries in mind, we decided to derive an "average" $Sp-R$ relation for M-dwarfs irrespective of their ages, metallicities, and activity levels. The primary purpose of this is to provide distance estimates based on the flux scaling factors in Eq. 7.4, but also to assess potential systematic peculiarities of the secondary stars in the WDMS binaries.

We have compiled spectral types and radii of field M-dwarfs from Berriman & Reid [1987], Caillault & Patterson [1990], Leggett et al. [1996], Delfosse et al. [1999], Leto et al. [2000], Lane et al. [2001], Ségransan et al. [2003], Maceroni & Montalbán [2004], Creevey et al. [2005], Pont et al. [2005], Ribas [2006], Berger et al. [2006], Bayless & Orosz [2006]

[1] In principle, an age estimate can be derived by adding the white dwarf cooling age to the MS life time of the white dwarf progenitor. This involves the use of an initial mass-final mass relation for the white dwarf, e.g. Dobbie et al. [2006], which will not be strictly valid for those WDMS binaries that underwent a CE phase. Broadly judging from the distribution of white dwarf temperatures and masses in Fig. 7.9, most WDMS binaries in our sample should be older than 1 Gyr, but the data at hand does not warrant a more detailed analysis.

and Beatty et al. [2007]. These data were separated into two groups, namely stars with directly measured radii (in eclipsing binaries or via interferometry) and stars with indirect radii determinations (e.g. spectrophotometric). We complemented this sample with spectral types, masses, effective temperatures and luminosities from Delfosse et al. [1998], Leggett et al. [2001], Berger [2002], Golimowski et al. [2004], Cushing et al. [2005] and Montagnier et al. [2006], calculating radii from $L = 4\pi R^2 \sigma {T_{\rm eff}}^4$ and/or Caillault & Patterson's (1990) mass-luminosity and $M-R$ relations.

Figure 7.6 shows our compilation of indirectly determined radii as a function of spectral type (top panel) as well as those from direct measurements (bottom panel). A large scatter in radii is observed at all spectral types except for the very late M-dwarfs, where only few measurements are available. It is interesting that the amount of scatter is comparable for both groups of M-dwarfs, those with directly measured radii and those with indirectly determined radii. This underlines that systematic effects intrinsic to the stars cause a large spread in the $Sp-R$ relation even for the objects with accurate measurements. In what follows, we use the indirectly measured radii as our primary sample, as it contains a larger number of stars and extends to later spectral types. The set of directly measured radii are used as a comparison to illustrate the $Sp-R$ distribution of stars where the systematic errors in the determination of their radii is thought to be small. We determine an $Sp-R$ relation from fitting the indirectly determined radius data with a third order polynomial (RMS = 0.13),

$$R = 0.48926 + \ 0.00683\ \mathrm{Sp} - \ 0.01709\ \mathrm{Sp}^2 + \ 0.00130\ \mathrm{Sp}^3 \qquad (7.2)$$

The spectral type is not a physical quantity, and strictly speaking, this relation is only defined on the existing spectral classes. This fit agrees well with the average of the radii in each spectral class (Fig. 7.6, middle panel, where the errors are the standard deviation from the mean value). The radii from the polynomial fit are reported in Table 7.2, along with the average radii per spectral class. Both the radii from the polynomial fit and the average radii show a marginal upturn at the very latest spectral types, which should not be taken too seriously given the small number of data involved.

We compare in Fig. 7.6 (bottom panel) the directly measured radii with our $Sp-R$ relation. It is apparent that also stars with well-determined radii show a substantial amount

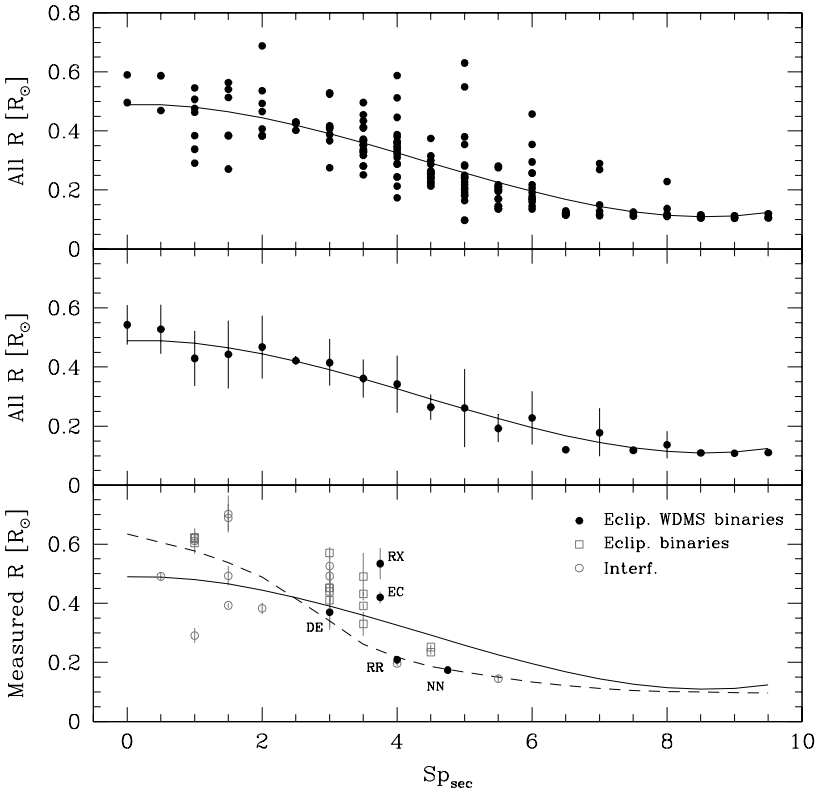

Figure 7.6: Top panel: indirectly measured radii of M-dwarfs vs spectral type. Our empirical $Sp-R$ relation is given by a third order polynomial fit (solid line) to these data. Middle panel: mean radii and corresponding standard deviations obtained by averaging the radii in the top panel for each spectral type. Our $Sp-R$ relation is again superimposed. Bottom panel: directly measured radii of M-dwarfs, again our empirical $Sp-R$ relation, the dashed line is the theoretical $Sp-R$ relation from Baraffe et al. [1998]. M-dwarf radii from the eclipsing WDMS binaries RR Cae, NN Ser, DE CVn, RX J2130.6+4710 and EC 13471–1258 are shown as solid dots.

Sp	R_{mean} ($R_\odot$)	R_σ ($R_\odot$)	R_{fit} ($R_\odot$)	M_{fit} ($M_\odot$)	T_{eff} (K)
M0.0	0.543	0.066	0.490	0.472	3843
M0.5	0.528	0.083	0.488	0.471	3761
M1.0	0.429	0.094	0.480	0.464	3678
M1.5	0.443	0.115	0.465	0.450	3596
M2.0	0.468	0.106	0.445	0.431	3514
M2.5	0.422	0.013	0.420	0.407	3432
M3.0	0.415	0.077	0.391	0.380	3349
M3.5	0.361	0.065	0.359	0.350	3267
M4.0	0.342	0.096	0.326	0.319	3185
M4.5	0.265	0.043	0.292	0.287	3103
M5.0	0.261	0.132	0.258	0.255	3020
M5.5	0.193	0.046	0.226	0.225	2938
M6.0	0.228	0.090	0.195	0.196	2856
M6.5	0.120	0.005	0.168	0.170	2773
M7.0	0.178	0.080	0.145	0.149	2691
M7.5	0.118	0.009	0.126	0.132	2609
M8.0	0.137	0.046	0.114	0.120	2527
M8.5	0.110	0.004	0.109	0.116	2444
M9.0	0.108	0.004	0.112	0.118	2362
M9.5	0.111	0.008	0.124	0.130	2281

Table 7.2: Empirical $Sp-R$, $Sp-M$ and $Sp-T_{eff}$ relations (R_{fit}, M_{fit}, T_{eff}) found in this work. R_{mean} and R_σ represent the mean radii and their standard deviation obtained from the sample of M-dwarfs described in Sect. 7.3.4.

of scatter, and are broadly consistent with the empirical $Sp-R$ relation determined from the indirectly measured radii. As a test, we included the directly measured radii in the fit described above, and did not find any significant change compared to the indirectly measured radii alone.

For a final assessment on our empirical $Sp-R$ relation, specifically in the context of WDMS binaries, we have compiled from the literature the radii of M-dwarfs in the eclipsing WDMS binaries RR Cae [Maxted et al., 2007], NN Ser [Haefner et al., 2004], DE CVn [van den Besselaar et al., 2007], RX J2130.6+4710 [Maxted et al., 2004], and EC 13471–1258 [O'Donoghue et al., 2003], (Fig. 7.6, bottom panel)[2]. Just as the accurate radii determined from interferometric observations of M-dwarfs or from light curve analyses of eclipsing M-dwarf binaries, the radii of the secondary stars in WDMS binaries display a substantial amount of scatter.

[2] An updated figure including the spectral types and radii of all current eclipsing WDMS binaries can be found in Chapter 10.

Comparison with the theoretical Sp-R relation from Baraffe et al. [1998]

We compare in the bottom panel of Fig. 7.6 our empirical $Sp-R$ relation with the theoretical prediction from the evolutionary sequences of Baraffe et al. [1998], where the spectral type is based on the $I-K$ colour of the PHOENIX stellar atmosphere models coupled to the stellar structure calculations. The theoretical $Sp-R$ relation displays substantially more curvature than our empirical relation, predicting larger radii for spectral types $\lesssim$M2, and significantly smaller radii in the range M3–M6. The two relations converge at late spectral types (again, the upturn in the empirical relation for $>$M8.5 should be ignored as an artifact from our polynomial fit). The "kink" in the theoretical relation seen around M2 is thought to be a consequence of H_2 molecular dissociation [Baraffe & Chabrier, 1996]. The large scatter of the directly determined radii of field M-dwarfs as well of M-dwarfs in eclipsing WDMS binaries could be related to two types of problem, that may have a common underlying cause. (1) In close binaries the stars are forced to extremely rapid rotation, which is thought to increase stellar activity that is likely to affect the stellar structure, generally thought to lead to an increase in radius [Spruit & Weiss, 1986; Mullan & MacDonald, 2001; Chabrier et al., 2007], and (2) the spectral types in our compilations of radii are determined from optical spectroscopy, and may differ to some extent from the spectral type definition based on $I-K$ colours as used in the Baraffe et al. [1998] models. Furthermore, stellar activity is thought to affect not only the radii of the stars, but also their luminosity, surface temperatures, and hence spectral types. The effect of stellar activity is discussed in more detail in Sect. 7.4.7.

$Sp-T_{\rm eff}$ and $Sp-M$ relations

For completeness, we fitted the spectral type-mass data and the spectral type-effective temperature data compiled from the literature listed above, and fitted the $Sp-M$ and $Sp-T_{\rm eff}$ relations with a third-order polynomial and a first-order polynomial, respectively. The results from the fits are reported in Table 7.2, and will be used in this Chapter only for estimating upper limits to the orbital periods of our PCEBs (Sect. 7.4.2) and when discussing the possibility of stellar activity on the WDMS binary secondary stars in Sect. 7.4.7.

7.3.5 Distances

The distances to the WDMS binaries can be estimated from the best-fit flux scaling factors of the two spectral components. For the white dwarf,

$$\frac{f_{\rm wd}}{F_{\rm wd}} = \pi \left(\frac{R_{\rm wd}}{d_{\rm wd}} \right)^2 \tag{7.3}$$

where $f_{\rm wd}$ is the observed flux of the white dwarf, $F_{\rm wd}$ the astrophysical flux at the stellar surface as given by the model spectra, $R_{\rm wd}$ is the white dwarf radius and $d_{\rm wd}$ is the distance to the white dwarf. For the secondary star,

$$\frac{f_{\rm sec}}{F_{\rm sec}} = \left(\frac{R_{\rm sec}}{d_{\rm sec}} \right)^2 \tag{7.4}$$

where $f_{\rm sec}$ is the observed M-dwarf flux, $F_{\rm sec}$ the flux at the stellar surface, and $R_{\rm sec}$ and $\rm d_{sec}$ are the radius and the distance to the secondary respectively.

The white dwarf radii are calculated from the best-fit $T_{\rm eff}$ and $\log g$ as detailed in Sect. 7.3.3. The secondary star radii are taken from Table 7.2 for the best-fit spectral type. The uncertainties of the distances are based on the errors in $R_{\rm wd}$, which depend primarily on the error in $\log g$, and in $R_{\rm sec}$, where we assumed the standard deviation from Table 7.2 for the given spectral type. Table 7.3 lists the values $d_{\rm wd}$ and $d_{\rm sec}$ obtained for our PCEBs. The remaining 112 WDMS binary's distances can be found in Rebassa-Mansergas et al. [2007, see also Chapter 9].

7.4 Discussion

7.4.1 Hα vs Na I radial velocities

As mentioned in Sect. 7.2, a few systems in Table 7.1 show considerable differences between their Hα and Na I RVs. More specifically, while both lines clearly identify these systems as being RV variable, and hence PCEBs or strong PCEB candidates, the actual RVs of Hα and Na I differ for a given SDSS spectrum by more than their errors.

In close PCEBs with short orbital periods the Hα emission is typically observed to arise from the hemisphere of the companion star facing the white dwarf. Irradiation from

a hot white dwarf is the most plausible mechanism to explain the anisotropic Hα emission, though also a number of PCEBs containing rather cool white dwarfs are known to exhibit concentrated Hα emission on the inner hemisphere of the companion stars [e.g. Marsh & Duck, 1996; Maxted et al., 2006]. The anisotropy of the Hα emission results in its RV differing from other photospheric features that are (more) isotropically distributed over the companion stars, such as the Na I absorption. In general, the Hα emission line RV curve will then have a lower amplitude than that of the Na I absorption lines, as Hα originates closer to the centre of mass of the binary system. In addition, the strength of Hα can vary greatly due to different geometric projections in high inclination systems. More complications are added in the context of SDSS spectroscopy, where the individual spectra have typical exposure times of 45–60min (Chapter 6), which will result in the smearing of the spectral features in the short-period PCEBs due to the sampling of different orbital phases. This problem is exacerbated in the case that the SDSS spectrum is combined from exposures taken on different nights (see Sect. 7.2). Finally, the Hα emission from the companion may substantially increase during a flare, which will further enhance the anisotropic nature of the emission.

Systems in which the Hα and Na I RVs differ by more than 2 σ are: SDSS J005245.11-005337.2, SDSS J024642.55+004137.2, SDSS J030904.82-010100.8, SDSS J031404.98-011136.6, and SDSS J172406.14+562003.0. Of these, SDSS J0246+0041, SDSS J0314-0111, and SDSS J1724+5620 show large-amplitude RV variations and substantial changes in the equivalent width of the Hα emission line, suggesting that they are rather short orbital period PCEBs with moderately high inclinations, which most likely explains the observed differences between the observed Hα and Na I RVs. This is later confirmed in Chapter 8. Irradiation is also certainly important in SDSS J1724+5620, which contains a hot ($\simeq$ 36000 K) white dwarf (see Fig. 8.4 in the following Chapter). SDSS J0052-0053 displays only a moderate RV amplitude, and while the Hα and Na I RVs display a homogeneous pattern of variation (Fig. 7.2 and 7.3), Hα appears to have a larger amplitude which is not readily explained. Similar discrepancies have been observed e.g. in the close magnetic WDMS binary WX LMi, and were thought to be related to a time-variable change in the location of the Hα emission [Vogel et al., 2007]. Finally, SDSS J0309-0101 is rather faint

($g = 20.4$), but has a strong Hα emission that allows reliable RV measurements that identify the system as a PCEB candidate. The RVs from the Na I doublet are more affected by noise, which probably explains the observed RV discrepancy in one out of its seven SDSS spectra. A more complete study of this system in Chapter 8 though suggests that this system is a wide WDMS binary rather than a PCEB.

7.4.2 Upper limits to the orbital periods

The RVs of the secondary stars follow from Kepler's 3rd law and depend on the stellar masses, the orbital period, and are subject to geometric foreshortening by a factor $\sin i$, with i the binary inclination with regards to the line of sight:

$$\frac{(M_{\rm wd}\sin i)^3}{(M_{\rm wd}+M_{\rm sec})^2} = \frac{P_{\rm orb}K_{\rm sec}^3}{2\pi G} \tag{7.5}$$

with $K_{\rm sec}$ the RV amplitude of the secondary star, and G the gravitational constant. This can be rearranged to solve for the orbital period,

$$P_{\rm orb} = \frac{2\pi G(M_{\rm wd}\sin i)^3}{(M_{\rm wd}+M_{\rm sec})^2 K_{\rm sec}^3} \tag{7.6}$$

From this equation, it is clear that assuming $i = 90^\circ$ gives an upper limit to the orbital period.

The RV measurements of our PCEBs and PCEB candidates (Table 7.1) sample the motion of their companion stars at random orbital phases. However, if we *assume* that the maximum and minimum values of the observed RVs sample the quadrature phases, e.g. the instants of maximum RV, we obtain *lower limits* to the true RV amplitudes of the companion stars in our systems. From Eq. 7.6, a lower limit to $K_{\rm sec}$ turns into an upper limit to $P_{\rm orb}$.

Hence, combining the RV information from Table 7.1 with the stellar parameters from Table 7.3, we determined upper limits to the orbital periods of all PCEBs and PCEB candidates, which range between 0.46–7880 d. The actual periods are likely to be substantially shorter, especially for those systems where only two SDSS spectra are available and the phase sampling is correspondingly poor. The orbital periods measured in Chapter 8 for seven of these systems confirms this hypothesis. More stringent constraints could be

obtained from a more complex exercise where the mid-exposure times are taken into account – however, given the fact that many of the SDSS spectra are combined from data taken on different nights, we refrained from this approach.

7.4.3 The fraction of PCEBs among the SDSS WDMS binaries

We have measured the RVs of 101 WDMS binaries which have multiple SDSS spectra, and find that 15 of them clearly show RV variations, three additional WDMS binaries are good candidates for RV variations (see Table 7.1). Taking the upper limits to the orbital periods at face value, and assuming that systems with a period $\lesssim 300$ d have undergone a CE (Willems & Kolb 2004) 17 of the systems in Table 7.1 qualify as PCEBs, implying a PCEB fraction of $\sim$15 % in our WDMS binary sample, which is in rough agreement with the predictions by the population model of Willems & Kolb [2004]. However, our value is likely to be a lower limit on the true fraction of PCEBs among the SDSS WDMS binaries for the following reasons. (1) In most cases only two spectra are available, with a non-negligible chance of sampling similar orbital phases in both observations. (2) The relatively low spectral resolution of the SDSS spectroscopy ($\lambda/\delta\lambda \simeq 1800$) plus the uncertainty in the flux calibration limit the detection of significant RV changes to $\sim 15\,\mathrm{km\,s^{-1}}$ for the best spectra. (3) In binaries with extremely short orbital periods the long exposures will smear the Na I doublet beyond recognition. (4) A substantial number of the SDSS spectra are combined, averaging different orbital phases and reducing the sensitivity to RV changes. Follow-up observations of a representative sample of SDSS WDMS binaries with higher spectral resolution and a better defined cadence will be necessary for an accurate determination of the fraction of PCEBs (see Chapter 10).

7.4.4 Comparison with Raymond et al. [2003]

In a previous study, Raymond et al. [2003] determined white dwarf temperatures, distance estimates based on the white dwarf fits, and spectral types of the companion star for 109 SDSS WDMS binaries. They restricted their white dwarf fits to a single gravity, $\log g = 8.0$, and a white dwarf radius of 8×10^8 cm (corresponding to $M_{\rm wd} = 0.6\,\mathrm{M}_\odot$), which is a fair match for the majority of systems (see Sect. 7.4.6 below). Our sample of WDMS binaries

with two or more SDSS spectra has 28 objects in common with Raymond's list, sufficient to allow for a quantitative comparison between the two different methods used to fit the data. As we fitted two or more spectra for each WDMS binary, we averaged for this purpose the parameters obtained from the fits to individual spectra of a given object, and propagated their errors accordingly. We find that $\sim 2/3$ of the temperatures determined by Raymond et al. [2003] agree with ours at the ~ 20 per cent level, with the remaining being different by up to a factor two (Fig. 7.7, left panels). This fairly large disagreement is most likely caused by the simplified fitting Raymond et al. adopted, i.e. fitting the white dwarf models in the wavelength range 3800–5000 Å, neglecting the contribution of the companion star. The spectral types of the companion stars from our work and Raymond et al. [2003] agree mostly to within ± 1.5 spectral classes, which is satisfying given the composite nature of the WDMS binary spectra and the problems associated with their spectral decomposition (Fig. 7.7, right panels). The biggest discrepancy shows up in the distances, with the Raymond et al. distances being systematically lower than ours (Fig. 7.7, middle panels). The average of the factor by which Raymond et al. underpredict the distances is 6.5, which is close to 2π, suggesting that the authors may have misinterpreted the flux definition of the model atmosphere code they used (TLUSTY/SYNSPEC from Hubeny & Lanz 1995, which outputs Eddington fluxes), and hence may have used a wrong constant in the flux normalisation (Eq. 7.3).

7.4.5 Comparison with Silvestri et al. [2006]

Having developed an independent method of determining the stellar parameters for WDMS binaries from their SDSS spectra, we compared our results to those of Silvestri et al. [2006]. As in Sect. 7.4.4 above, we average the parameters obtained from the fits to the individual SDSS spectra of a given object. Figure 7.8 shows the comparison between the white dwarf effective temperatures, surface gravities, and spectral types of the secondary stars from the two studies. Both studies agree in broad terms for all three fit parameters (Fig. 7.8, bottom panels). Inspecting the discrepancies between the two independent sets of stellar parameters, it became evident that relatively large disagreements are most noticeably found for $T_{\rm eff} \lesssim 20\,000$ K, with differences in $T_{\rm eff}$ of up to a factor two, an order of magnitude in sur-

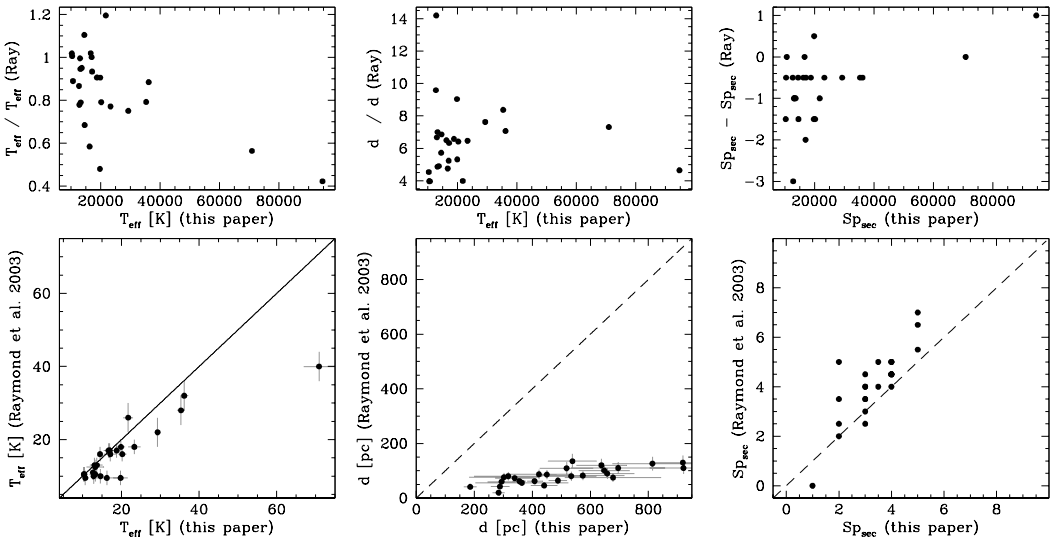

Figure 7.7: Comparison of the white dwarf effective temperatures, distances based on the white dwarf fit, and the spectral types of the secondary stars determined from our fits (Sect. 7.3.2, 7.3.3 and Table 7.3), and those of Raymond et al. [2003]. Top panels, from left to right: the ratio in $T_{\rm eff}$, the ratio in d, and the difference in the secondary's spectral types from the two studies as a function of the white dwarf temperature.

face gravity, and a typical difference in spectral type of the secondary of ± 2 spectral classes. For higher temperatures the differences become small, with nearly identical values for $T_{\rm eff}$, $\log g$ agreeing within ± 0.2 magnitude, and spectral types differing by ± 1 spectral classes at most (Fig. 7.8, top panels). We interpret this strong disagreement at low to intermediate white dwarf temperatures to the ambiguity between hot and cold solutions described in Sect. 7.3.3.

A quantitative judgement of the fits in Silvestri et al. [2006] is difficult, as the authors do not provide much detail on the method used to decompose the WDMS binary spectra, except for a single example in their Fig. 1. It is worth noting that the M-dwarf component in that figure displays constant flux at $\lambda < 6000$ Å, which seems rather unrealistic for the claimed spectral type of M5. Unfortunately, Silvestri et al. [2006] do not list distances implied by their fits to the white dwarf and MS components in their WDMS binary sample, which would provide a test of internal consistency (see Sect. 7.4.7).

We also investigated the systems Silvestri et al.'s (2006) method failed to fit, and found that we were able to determine reasonable parameters for the majority of them. It

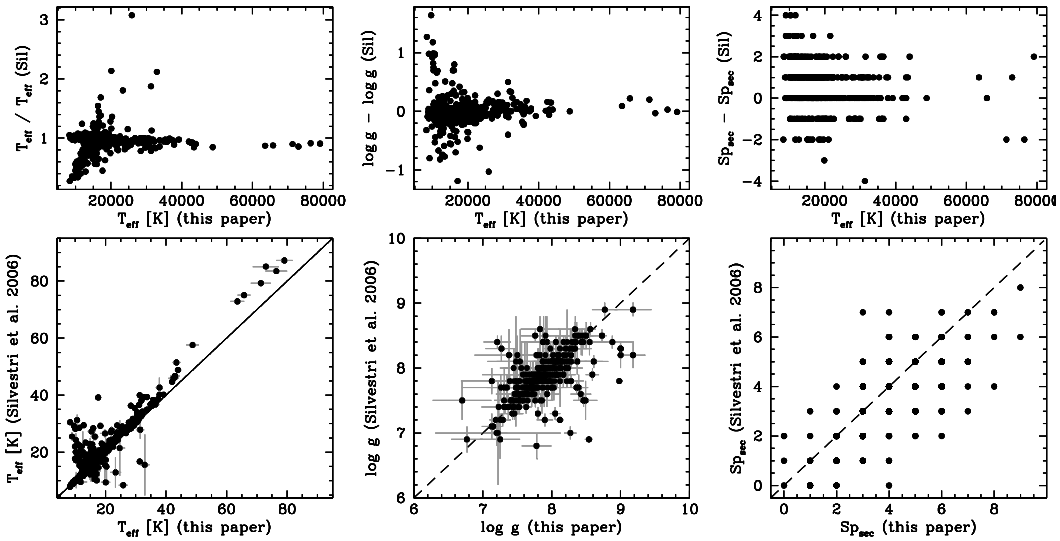

Figure 7.8: Comparison of the white dwarf effective temperatures and surface gravities and the spectral types of the secondary stars determined from our fits (Sect. 7.3.2, 7.3.3 and Table 7.3), and those of Silvestri et al. [2006]. Top panels, from left to right: the white dwarf effective temperature and surface gravity ratios, and the difference in the secondary's spectral types from the two studies as a function of the white dwarf temperature.

appears that our method is more robust in cases of low S/N, and in cases where one of the stellar components contributes relatively little to the total flux. Examples of the latter are SDSS J204431.45–061440.2, where an M0 secondary star dominates the SDSS spectrum at $\lambda \gtrsim 4600$ Å, or SDSS J172406.14+562003.1, which is a close PCEB containing a hot white dwarf and a low-mass companion. An independent analysis of the entire WDMS binary sample from SDSS appears therefore a worthwhile exercise, and will be provided in Chapter 9.

7.4.6 Distribution of the stellar parameters

Having determined stellar parameters for each individual system in Sect. 7.3, we look here at their global distribution within our sample of WDMS binaries. Figure. 7.9 shows histograms of the white dwarf effective temperatures, masses, $\log g$, and the spectral types of the MS companions.

As in Sect. 7.4.4 and 7.4.5 above, we use here the average of the fit parameters obtained from the different SDSS spectra of each object. Furthermore, we exclude all systems

with relative errors in their white dwarf parameters ($T_{\rm wd}, \log g, M_{\rm wd}$) exceeding 25 per cent to prevent smearing of the histograms due to poor quality data and/or fits, which results in 95, 81, 94, and 38 WDMS binaries in the histograms for the companion spectral type, $\log g$, $T_{\rm wd}$, and $M_{\rm wd}$, respectively. In broad terms, our results are consistent with those of Raymond et al. [2003] and Silvestri et al. [2006]: the most frequent white dwarf temperatures are between 10 000–20 000 K, white dwarf masses cluster around $M_{\rm wd} \simeq 0.6\,{\rm M}_{\odot}$, and the companion stars have most typically a spectral type M3–4, with spectral types later than M7 or earlier than M1 being very rare.

At closer inspection, the distribution of white dwarf masses in our sample has a more pronounced tail towards lower masses compared to the distribution in Silvestri et al. [2006]. A tail of lower-mass white dwarfs, peaking around $0.4\,{\rm M}_{\odot}$ is observed also in well-studied samples of single white dwarfs [e.g. Liebert et al., 2005], and is interpreted as He-core white dwarfs descending from evolution in a binary star [e.g. Marsh et al., 1995, see also Chapter 10]. In a sample of WDMS binaries, a significant fraction of systems will have undergone a CE phase, and hence the fraction of He-core white dwarfs among WDMS binaries is expected to be larger than in a sample of single white dwarfs.

Also worth noting is that our distribution of companion star spectral types is relatively flat between M2–M4, more similar to the distribution of single M-dwarfs in SDSS [West et al., 2004] than the companion stars in Silvestri et al. [2006]. More generally speaking, the cut-off at early spectral types is due to the fact that WDMS binaries with K-type companions can only be identified from their spectra/colours if the white dwarf is very hot – and hence, very young, and correspondingly only few of such systems are in the total SDSS WDMS binary sample. The cut-off seen for low-mass companions is not so trivial to interpret. Obviously, very late-type stars are dim and will be harder to be detected against a moderately hot white dwarf, such a bias was discussed by Schreiber & Gänsicke [2003] for a sample of ~ 30 well-studied WDMS binaries which predominantly originated from blue-colour (= hot white dwarf) surveys. However, old WDMS binaries with cool white dwarfs should be much more common [Schreiber & Gänsicke, 2003], and SDSS, sampling a much broader colour space than previous surveys, should be able to identify WDMS binaries containing cool white dwarfs plus very late-type companions. The relatively low frequency of

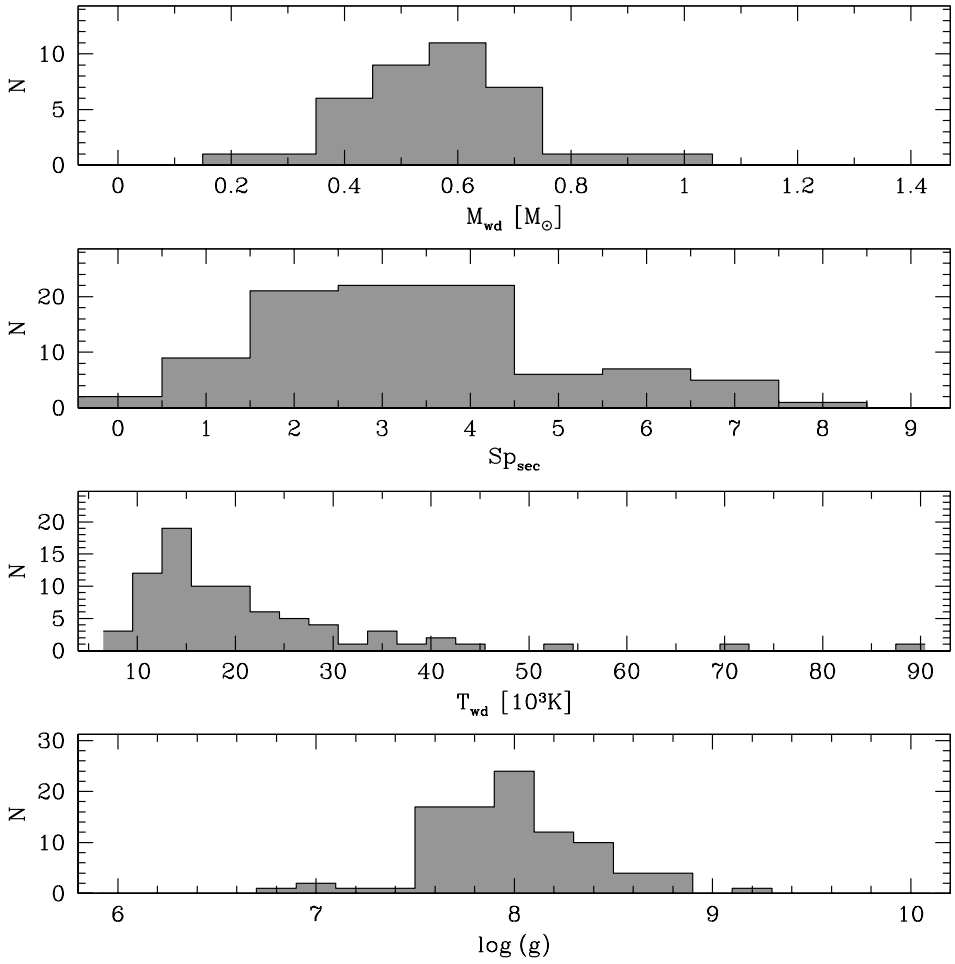

Figure 7.9: White dwarf mass, spectral types of the secondaries, effective temperature and $\log g$ histograms obtained from the SDSS WDMS binary sample. Excluded are those systems with individual white dwarf masses, $T_{\rm eff}$, and $\log g$ associated to relative errors larger than 25 per cent.

such systems in the SDSS spectroscopic data base suggests that either SDSS is not efficiently targeting those systems for spectroscopic follow-up, or that they are rare in the first place, or a combination of both. A detailed discussion is beyond the scope of this thesis, but we note that Farihi et al. [2005] have constructed the relative distribution of spectral types in the local M/L dwarf distribution, which peaks around M3–4, and steeply declines towards later spectral types, suggesting that late-type companions to white dwarfs are intrinsically rare. This is supported independently by Grether & Lineweaver [2006], who analysed the mass function of companions to solar-like stars, and found that it steeply decreases towards the late end of the MS (but rises again for planet-mass companions, resulting in the term "brown-dwarf desert"). In addition, spectral type distributions of field low-mass and ultracool stars have been found to be dominated by the M star population (peaking at Sp $\simeq$ M4-5), and to decline also towards later spectral types, with a broad minimum spanning $\sim$L5 to $\sim$T2 [Reid et al., 2007, 2008].

An assessment of the stellar parameters of all WDMS binaries in SDSS using our spectral decomposition and white dwarf fitting method will improve the statistics of the distributions presented here, and will be presented in Chapter 9.

7.4.7 Stellar activity on the secondary stars?

As outlined in Sect. 7.3.5, the scaling factors used in the modelling of the two spectral components of each WDMS binary provide two independent estimates of the distance to the system. In principle, both estimates should agree within their errors. Figure 7.10 compares the white dwarf and secondary star distance estimates obtained in Sect. 7.3.5, where the distances obtained from the individual SDSS spectra of a given object were averaged, and the errors accordingly propagated. In this plot, we exclude systems with relative errors in $d_{\rm wd}$ larger than 25 per cent to avoid cluttering by poor S/N data. The relative error in $d_{\rm sec}$ is dominated by the scatter in the $Sp-R$ relation, which represents an intrinsic uncertainty rather than a statistical error in the fit, and we therefore did not apply any cut in $d_{\rm sec}$. Taking the distribution of distances at face value, it appears that about $2/3$ of the systems have $d_{\rm sec} \simeq d_{\rm wd}$ within their 1σ errors, as expected from purely statistical errors. However, there is a clear trend for outliers where $d_{\rm sec} > d_{\rm wd}$. We will discuss the possible causes and

implications in the following sections.

Possible causes for $d_{\rm sec} \neq d_{\rm wd}$

We identify a number of possible causes for the discrepancy between the two independent distance estimates observed in $\sim 1/3$ of the WDMS binaries analysed here.

(1) *A tendency for systematic problems in the white dwarf fits?* $d_{\rm sec} > d_{\rm wd}$ could be a result of too small white dwarf radii for a number of systems, i.e. too high white dwarf masses. We therefore identify in the top panel of Fig. 7.10 those systems with massive ($> 0.75\,{\rm M}_{\odot}$) white dwarfs. It is apparent that the outliers from the $d_{\rm sec} = d_{\rm wd}$ relation do not contain a large number of very massive white dwarfs.

(2) *Problems in determining the correct spectral type of the secondary?* If the error on the spectral type of the companion star determined from the spectral decomposition is larger than ± 0.5, as assumed in Sect. 7.3.2, a substantial deviation from $d_{\rm sec} = d_{\rm wd}$ would result. However, as long as this error is symmetric around the true spectral type, it would cause scatter on both sides of the $d_{\rm sec} = d_{\rm wd}$ relation. Only if the determined spectral types were consistently too early for $\sim 1/3$ of the systems, the observed preference for outliers at $d_{\rm sec} > d_{\rm wd}$ could be explained (see Sect. 7.4.7 below for a hypothetical *systematic* reason for spectral types that are consistently too early).

(3) *Problems in the $Sp-R$ relation?* As discussed in Sect. 7.3.4, the $Sp-R$ relation of late-type stars is not particularly well defined. The large scatter of observed radii at a given spectral type is taken into account in the errors in $d_{\rm sec}$. If those errors were underestimated, they should cause an approximatively symmetric scatter of systems around $d_{\rm sec} = d_{\rm wd}$, which is not observed (the $Sp-R$ relation being non-linear lead to asymmetric error bars in the radius for a given symmetric error in the spectral type, however, over a reasonably small range in the spectral type this effect is negligible). A systematic problem over a small range of spectral types would result in a concentration of the affected spectral types among the outliers. For this purpose, we divide our sample into three groups of secondary star spectral classes, Sp > 5, $3 \leq$ Sp ≤ 5, and Sp < 3 (Fig. 7.10, bottom panel). The outliers show a slight concentration towards early types (Sp < 3) compared to the distribution of secondary star spectral types in the total sample (Fig. 7.9).

To explore the idea that our empirical $Sp-R$ relation is simply inadequate, we calculated a new set of secondary star distances, using the theoretical $Sp-R$ relation from Baraffe et al. [1998] (see Fig. 7.6, bottom panel), which are shown in the top panel of Fig. 7.11. The theoretical $Sp-R$ relation implies smaller radii in the range M3–M6, but the difference with our empirical relation is not sufficient enough to shift the outlying WDMS binaries onto the $d_{\rm sec} = d_{\rm wd}$ relation. For spectral types earlier than M2.5, our empirical $Sp-R$ relation actually gives *smaller* radii than the theoretical Baraffe et al. 1998 relation, so that using the theoretical $Sp-R$ actually exacerbates the $d_{\rm sec} > d_{\rm wd}$ problem.

(4) *A relationship with close binarity?* The fraction of PCEBs among the outliers is similar to the fraction among the total sample of WDMS binaries (Fig. 7.10), hence it does not appear that close binarity is a decisive issue.

(5) *An age effect?* Late-type stars take a long time to contract to their zero age main sequence (ZAMS) radii, and if some of the WDMS binaries in our sample were relatively young objects, their M-dwarfs would tend to have larger radii than ZAMS radii. As briefly discussed in Footnote 1, the majority of the WDMS binaries in our sample are likely to be older than ~ 1 Gyr, and the outliers in Fig. 7.10,7.11 do not show any preference for hot or massive white dwarfs, which would imply short cooling ages and MS life times.

(6) *Problems related to the surface gravity of the white dwarfs?* It is likely that the masses for $\sim$15% of the white dwarfs in our sample are overestimated due to the low $T_{\rm eff}$ $\log g$ problem discussed in Sect. 7.3.3. This effect translates into the distances to these white dwarfs being underestimated. We have inspected all $d_{\rm sec} > d_{\rm wd}$ outliers and found that only two objects contain cool (less than 12000 K) white dwarfs, and we conclude that the low $T_{\rm eff}$ $\log g$ problem can not reconcile the distance problem.

(7) *A systematic bias for overluminous M-dwarfs?* Given that for WDMS binaries to be selected for spectroscopy, both stellar components have to make a noticeable contribution in the SDSS *ugriz* photometry, one may speculate about a bias leading to the selection of overluminous main sequence companions. This may be a real effect for the very latest spectral types, where the low-luminosity M-dwarfs struggle to compete with the flux emitted even by cold white dwarfs. However, for spectral types earlier than $\sim$M6, the flux contribution of the M-dwarf is fully dominating the emission in the i- and z-bands, ruling

out a selection towards overluminous M-dwarfs.

Could stellar activity affect Sp_{sec}?

None of the points discussed in the previous section conclusively explains the preference for outliers having $d_{sec} > d_{wd}$. If we assume that the problem rests in the determined properties of the secondary star, rather than those of the white dwarf, the immediate implication of $d_{sec} > d_{wd}$ is that the assumed radii of the secondary stars are too large. As mentioned above and shown in Fig. 7.11, this statement does not strongly depend on which $Sp-R$ relation we use to determine the radii, either our empirical relation or the theoretical Baraffe et al. (1998) relation. Rather than blaming the radii, we explore here whether the secondary star spectral types determined from our decomposition of the SDSS spectra might be consistently too early in the outlying systems. If this was the case, we would pick a radius from our $Sp-R$ relation that is larger than the true radius of the secondary star, resulting in too large a distance. In other words, the question is: *is there a mechanism that could cause the spectral type of an M star, as derived from low-resolution optical spectroscopy, to appear too early?*

The reaction of stars to stellar activity on their surface, also referred to as spottedness (see Chapter 2) is a complex phenomenon that is not fully understood. Theoretical studies [e.g. Spruit & Weiss, 1986; Mullan & MacDonald, 2001; Chabrier et al., 2007] agree broadly on the following points: (1) the effect of stellar activity is relatively weak at the low-mass end of the MS ($M \lesssim 0.3\,M_{\odot}$), where stars are conventionally thought to become fully convective (though, see Mullan & MacDonald 2001; Chabrier et al. 2007 for discussions on how magnetic fields may change that mass boundary), (2) stellar activity will result in an increase in radius, and (3) the effective temperature of an active star is lower than that of an unspotted star.

Here, we briefly discuss the possible effects of stellar activity on the spectral type of a star. For this purpose, it is important not to confuse the *effective temperature*, which is purely a definition coupled to the luminosity and the stellar radius via $L = 4\pi R^2 \sigma T_{\rm eff}^4$ (and hence is a *global* property of the star), and the *local* temperature of a given part of the stellar surface, which will vary from spotted areas to inter-spot areas. In an unspotted star effective

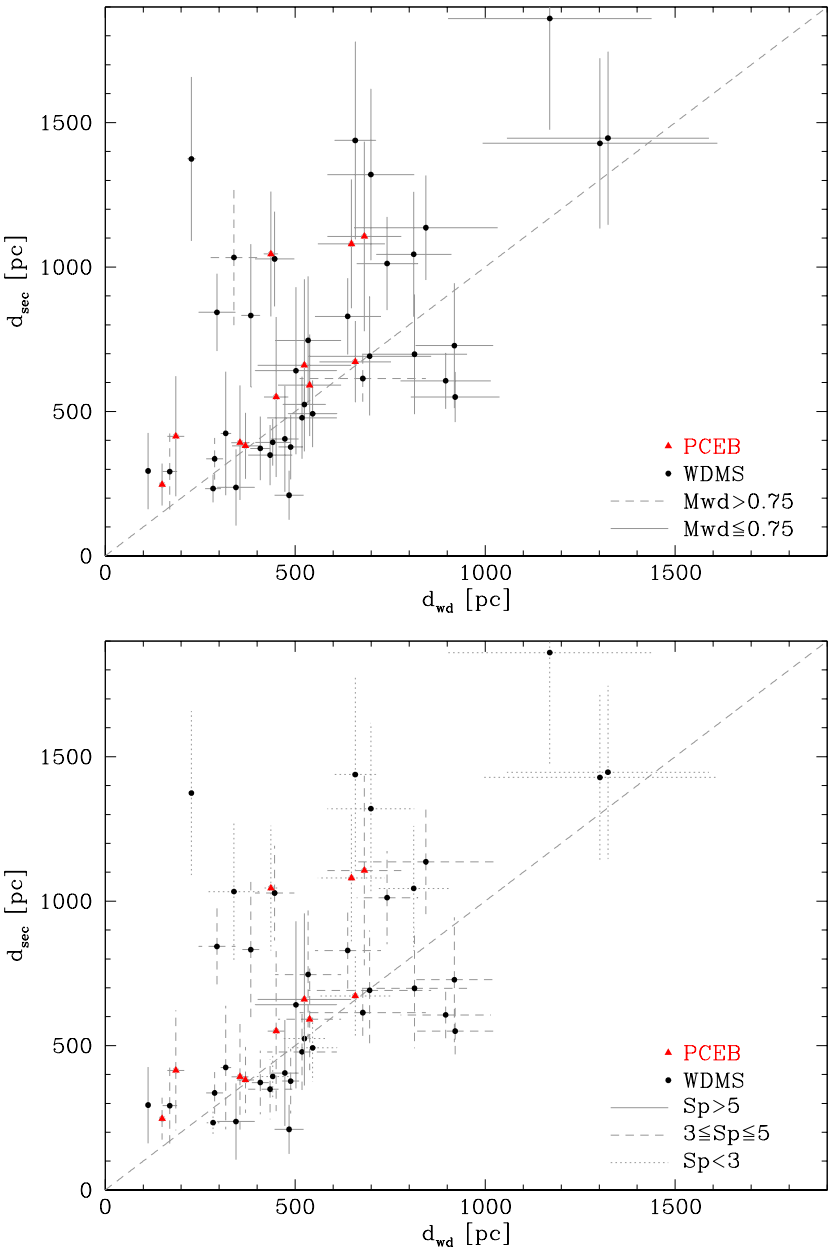

Figure 7.10: Comparison of $d_{\rm sec}$ and $d_{\rm wd}$ obtained from our spectral decomposition and white dwarf fits to the SDSS spectra. Approximately a third of the systems have $d_{\rm sec} \neq d_{\rm wd}$. The top panel splits the sample according to the mass of the white dwarfs, while the bottom panel divides the sample according to the spectral types of the secondaries. In both panels systems that we identify as PCEBs from RV variations in their SDSS spectra are shown in red.

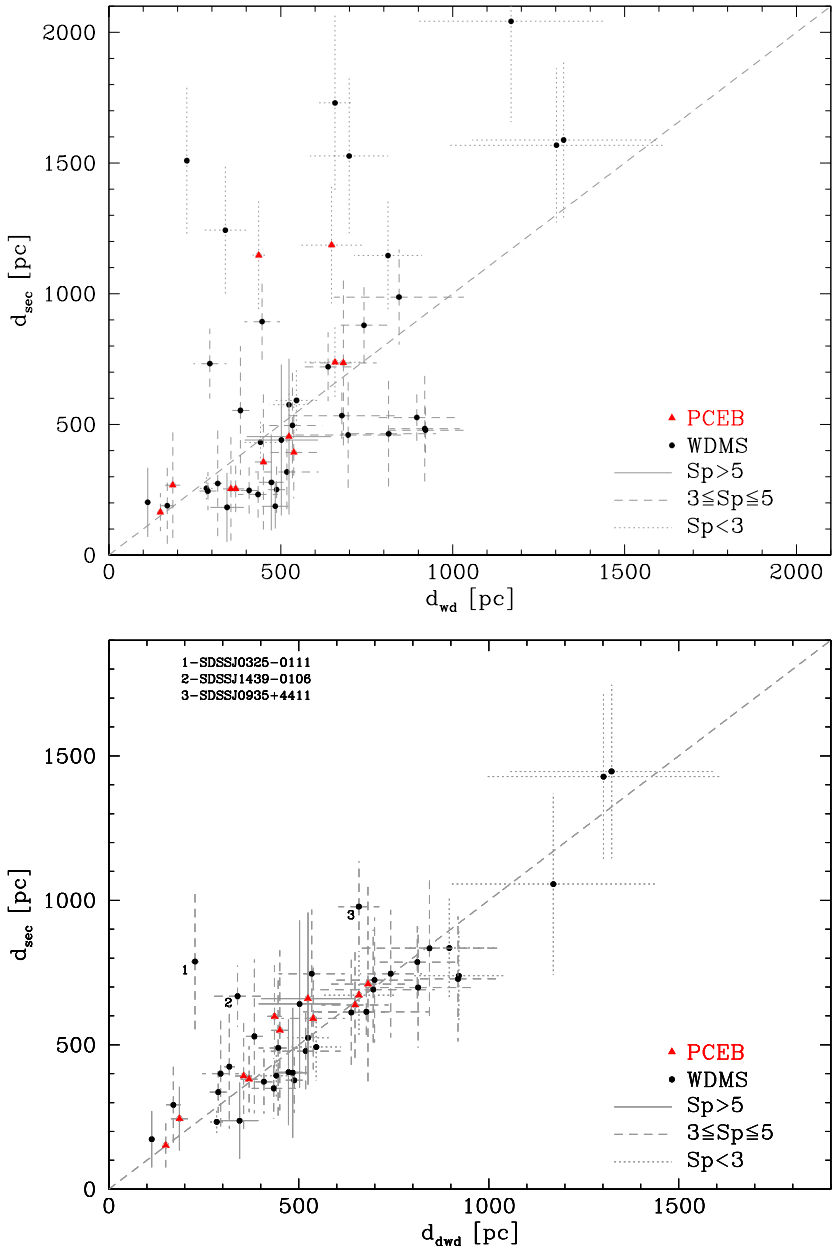

Figure 7.11: Top panel: the distances implied by the spectral decomposition were calculated by using the $Sp-R$ relation predicted by the models of Baraffe et al. [1998], instead of our empirical $Sp-R$ relation. Bottom panel: the spectral types of the secondary stars were adjusted by 1–2 spectral classes to achieve $d_{\rm wd} = d_{\rm sec}$. Only three systems can not be reconciled in this way, and are discussed individually in the text. We suggest that stellar activity in some WDMS binaries may change the spectral type of their secondary stars, being equivalent to a change in surface temperature by a few 100 K.

and local temperature are the same, and both colour and spectral type are well-defined. As a simple example to illustrate the difference between effective temperature and colour in an active star, we assume that a large fraction of the star is covered by zero-temperature, i.e. black spots, and that the inter-spot temperature is the same as that of the unspotted star. As shown by Chabrier et al. [2007], assuming constant luminosity requires the radius of the star to increase, and the effective temperature to drop. Thus, while intuition would suggest that a lower effective temperature would result in a redder colour, this ficticious star has *exactly* the same colour and spectral type as its unspotted equivalent – as the black spots contribute no flux at all, and the inter-spot regions with the same spectral shape as the unspotted star.

Obviously, the situation in a real star will be more complicated, as the spots will not be black, but have a finite temperature, and the star will hence have a complicated temperature distribution over its surface. Thus, the spectral energy distribution of such a spotted star will be the superposition of contributions of different temperatures, weighted by their respective covering fraction of the stellar surface. Strictly speaking, such a star has no longer a well-defined spectral type or colour, as these properties will depend on the wavelength range that is observed. Spruit & Weiss [1986] assessed the effect of long-term spottedness on the temperature distribution on active stars, and found that for stars with masses in the range $0.3 - 0.6\,\mathrm{M}_{\odot}$ the long-term effect of spots is to increase the temperature of the inter-spot regions by $\sim 100 - 200\,\mathrm{K}$ (compared to the effective temperature of the equivalent unspotted star), whereas the inter-spot temperature of spotted lower-mass stars remains unchanged. Spruit & Weiss [1986] also estimated the effects of stellar activity on the colours of stars, but given their use of simple blackbody spectra, these estimates are of limited value. As a general tendency, the hotter (unspotted) parts of the star will predominantly contribute in the blue end of the the spectral energy distribution, the cooler (spotted) ones in its red end. As we determine the spectral types of the secondary stars in the SDSS WDMS binaries from optical (= blue) spectra, and taking the results of Spruit & Weiss at face value, it appears hence possible that they are too early compared to unspotted stars of the same mass. A full theoretical treatment of this problem would involve calculating the detailed surface structure of active stars as well as appropriate spectral models for each surface element in order to compute the spatially integrated spectrum as it would be observed.

This is clearly a challenging task.

Given that theoretical models on the effect of stellar activity have not yet converged, and are far from making detailed predictions on the spectroscopic appearance of active stars, we pursue here an empirical approach. We assume that the discrepancy $d_{\rm sec} > d_{\rm wd}$ results from picking a spectral type too early, i.e. we assume that the secondary star appears hotter in the optical spectrum that it should for its given mass. Then, we check by how much we have to adjust the spectral type (and the corresponding radius) to achieve $d_{\rm sec} = d_{\rm wd}$ within the errors (Fig. 7.11 bottom panel). We find that the majority of systems need a change of 1–2 spectral classes, which corresponds to changes in the effective temperature of a few hundred degrees only, in line with the calculations of Spruit & Weiss [1986]. Bearing in mind that what we *see* in the optical is the surface temperature, and not the effective temperature, comparing this to the surface temperature changes calculated by Spruit & Weiss [1986], and taking into account that we ignored in this simple approach the change in radius caused by a large spottedness, it appears plausible that the large deviations from $d_{\rm sec} = d_{\rm wd}$ may be related to stellar activity on the secondary stars.

There are three WDMS binaries where a change of more than two spectral classes would be necessary: SDSS J032510.84-011114.1, SDSS J093506.92+441107.0, and SDSS J143947. 62-010606.9. SDSSJ 143947.62-010606.9 contains a very hot white dwarf, and the secondary star may be heated if this system is a PCEB. Its two SDSS spectra reveal no significant RV variation, but as discussed in Sect. 7.2 the SDSS spectra can not exclude a PCEB nature because of random phase sampling, low inclination and limited spectral resolution. SDSS J032510.84-011114.1 and SDSS J093506.92+441107.0 could be short-period PCEBs, as they both have poorly define Na I absorption doublets, possibly smeared by orbital motion over the SDSS exposure (see Sect. 7.2). In a close binary, their moderate white dwarf temperatures would be sufficient to cause noticeable heating of the secondary star.

We conclude that our study suggests some anomalies in the properties of $\sim 1/3$ of the M-dwarf companions within the WDMS binary sample analysed here. This is in line with previous detailed studies reporting the anomalous behaviour of the MS companions in PCEBs and CVs, e.g. O'Brien et al. [2001] or Naylor et al. [2005].

7.4.8 Selection effects among the SDSS WDMS binaries.

Selection effects among the WDMS binaries found by SDSS with respect to the spectral type of their MS component can be deduced from the bottom panel of Fig. 7.10[3]. No binaries with secondary spectral types later than M5 are found at distances larger than ~ 500 pc. Because of their intrinsic faintness, such late-type secondary stars can only be seen against relatively cool white dwarfs, and hence the large absolute magnitude of such WDMS binaries limits their detection within the SDSS magnitude limit to a relatively short distance. Hot white dwarfs in SDSS can be detected to larger distances, and may have undetected late-type companions. There are also very few WDMS binaries with secondary stars earlier than M3 within 500 pc. In those systems, the secondary star is so bright that it saturates the *z*, and possibly the *i* band, disqualifying the systems for spectroscopic follow up by SDSS. While these selection effects may seem dishearting at first, it will be possible to quantitatively correct them based on predicted colours of WDMS binaries and the information available within the SDSS project regarding photometric properties and spectroscopic selection algorithms.

7.5 Conclusions

We have identified 18 PCEBs and PCEB candidates among a sample of 101 WDMS binaries for which repeat SDSS spectroscopic observations are available in DR5. From the SDSS spectra, we determine the spectral types of the MS companions, the effective temperatures, surface gravities, and masses of the white dwarfs, as well as distance estimates to the systems based both on the properties of the white dwarfs and of the MS stars. In about 1/3 of the WDMS binaries studied here the SDSS spectra suggest that the secondary stars have either radii that are substantially larger than those of single M-dwarfs, or spectral types that are too early for their masses. Follow-up observations of the PCEBs and PCEB candidates is encouraged in order to determine their orbital periods as well as more detailed system parameters (see Chapter 8). Given the fact that we have analysed here only ~ 10 per cent of the WDMS binaries in DR5, it is clear SDSS holds the potential to dramatically

[3] A more complete description of selection effects among the SDSS WDMS binaries is provided in Chapter 9.

improve our understanding of CE evolution (see Chapters 9 and 10).

Table 7.3: White dwarf masses, effective temperatures, surface gravities, spectral types and distances of the SDSS PCEBs identified in Sect. 7.3, as determined from spectral modelling. The stellar parameters for the remaining 112 WDMS binaries can be found in Rebassa-Mansergas et al. [2007, see also Chapter 9]. We quote by *s* and *e* those systems which have been studied previously by Silvestri et al. [2006] and Eisenstein et al. [2006], repectively.

SDSS J	MJD	plate	fiber	$T_{\rm eff}$(K)	err	$\log g$	err	$M(M_{\odot})$	err	$d_{\rm wd}$(pc)	err	Sp	$d_{\rm sec}$(pc)	err	flag	notes
005245.11-005337.2	51812	394	96	15071	4224	8.69	0.73	1.04	0.38	505	297	4	502	149	s,e	
	51876	394	100	17505	7726	9.48	0.95	1.45	0.49	202	15	4	511	152		
	51913	394	100	16910	2562	9.30	0.42	1.35	0.22	261	173	4	496	147		
	52201	692	211	17106	3034	9.36	0.43	1.38	0.22	238	178	4	526	156		
005457.61-002517.0	51812	394	118	16717	574	7.81	0.13	0.51	0.07	455	38	5	539	271	s,e	
	51876	394	109	17106	588	7.80	0.14	0.51	0.07	474	40	5	562	283		
	51913	394	110	17106	290	7.88	0.07	0.55	0.04	420	19	5	550	277		
022503.02+005456.2	51817	406	533	-	-	-	-	-	-	-	-	5	341	172	s,e	1
	51869	406	531	-	-	-	-	-	-	-	-	5	351	177		
	51876	406	532	-	-	-	-	-	-	-	-	5	349	176		
	51900	406	532	-	-	-	-	-	-	-	-	5	342	172		
	52238	406	533	-	-	-	-	-	-	-	-	5	356	179		
024642.55+004137.2	51871	409	425	15782	5260	9.18	0.76	1.29	0.39	213	212	4	365	108	s,e	
	52177	707	460	-	-	-	-	-	-	-	-	3	483	77		
	52965	1664	420	16717	1434	8.45	0.28	0.90	0.16	515	108	3	492	78		
	52973	1664	407	14065	1416	8.24	0.22	0.76	0.14	510	77	3	499	80		
025147.85-000003.2	52175	708	228	17106	4720	7.75	0.92	0.49	0.54	1660	812	4	881	262	e	2
	52177	707	637	-	-	-	-	-	-	-	-	4	794	236		
030904.82-010100.8	51931	412	210	19416	3324	8.18	0.68	0.73	0.40	1107	471	3	888	141	s,e	
	52203	710	214	18756	5558	9.07	0.61	1.24	0.31	462	325	3	830	132		
	52235	412	215	14899	9359	8.94	1.45	1.17	0.75	374	208	4	586	174		
	52250	412	215	11173	9148	8.55	1.60	0.95	0.84	398	341	4	569	169		

Continued on Next Page...

Table 7.3 – Continued

SDSS J	MJD	plate	fiber	$T_{\rm eff}$(K)	err	$\log g$	err	$M(M_\odot)$	err	$d_{\rm wd}$(pc)	err	Sp	$d_{\rm sec}$(pc)	err	flag	notes
	52254	412	201	20566	7862	8.82	0.72	1.11	0.37	627	407	3	836	133		
	52258	412	215	19640	2587	8.70	0.53	1.04	0.27	650	281	3	854	136		
	53386	2068	126	15246	4434	8.75	0.79	1.07	0.41	522	348	4	628	187		
031404.98-011136.6	51931	412	45	-	-	-	-	-	-	-	-	4	445	132	s,e	1
	52202	711	285	-	-	-	-	-	-	-	-	4	475	141		
	52235	412	8	-	-	-	-	-	-	-	-	4	452	134		
	52250	412	2	-	-	-	-	-	-	-	-	4	426	126		
	52254	412	8	-	-	-	-	-	-	-	-	4	444	132		
	52258	412	54	-	-	-	-	-	-	-	-	4	445	132		
082022.02+431411.0	51959	547	76	21045	225	7.94	0.04	0.59	0.02	153	4	4	250	74	s,e	
	52207	547	59	21045	147	7.95	0.03	0.60	0.01	147	2	4	244	72		
113800.35-001144.4	51630	282	113	18756	1364	7.99	0.28	0.62	0.17	588	106	4	601	178	s,e	
	51658	282	111	24726	1180	8.34	0.16	0.84	0.10	487	60	4	581	173		
115156.94-000725.4	51662	284	435	10427	193	7.90	0.23	0.54	0.14	180	25	5	397	200	s,e	
	51943	284	440	10189	115	7.99	0.16	0.59	0.10	191	19	5	431	217		
152933.25+002031.2	51641	314	354	14228	575	7.67	0.12	0.44	0.05	338	25	5	394	199	s,e	
	51989	363	350	14728	374	7.59	0.09	0.41	0.04	372	21	5	391	197		
172406.14+562003.0	51813	357	579	35740	187	7.41	0.04	0.42	0.01	417	15	2	1075	222	s,e	
	51818	358	318	36154	352	7.33	0.06	0.40	0.02	453	24	2	1029	213		
	51997	367	564	37857	324	7.40	0.04	0.43	0.01	439	16	2	1031	213		
172601.54+560527.0	51813	357	547	20331	1245	8.24	0.23	0.77	0.14	582	94	2	1090	225	s,e	
	51997	367	548	20098	930	7.94	0.18	0.59	0.11	714	83	2	1069	221		
173727.27+540352.2	51816	360	165	13127	1999	7.91	0.42	0.56	0.26	559	140	6	680	307	s,e	
	51999	362	162	13904	1401	8.24	0.31	0.76	0.20	488	106	6	639	288		
224139.02+002710.9	53261	1901	471	12681	495	8.05	0.15	0.64	0.09	369	35	4	381	113	e	
	52201	674	625	13745	1644	7.66	0.36	0.43	0.19	524	108	4	378	112		
233928.35-002040.0	53357	1903	264	15071	1858	8.69	0.33	1.04	0.18	416	112	4	530	157	e	
	52525	682	159	12536	2530	7.92	0.79	0.56	0.48	655	291	4	528	157		
234534.49-001453.7	52524	683	166	19193	1484	7.79	0.31	0.51	0.17	713	132	4	1058	314	s,e	5
	53357	1903	103	18974	730	7.98	0.15	0.61	0.09	652	62	4	1155	343		

Continued on Next Page…

Table 7.3 – Continued

SDSS J	MJD	plate	fiber	$T_{\rm eff}$(K)	err	log$g$	err	$M(M_{\odot})$	err	$d_{\rm wd}$(pc)	err	Sp	$d_{\rm sec}$(pc)	err	flag	notes
235020.76-002339.9	51788	386	228	-	-	-	-	-	-	-	-	5	504	254		6
	52523	684	226	-	-	-	-	-	-	-	-	5	438	22		

(1) $T_{\rm eff}$ less than 6000; (2) Noisy spectra; (3) Cold white dwarf; (4) Diffuse background galaxy in the SDSS image; (5) Reflection effect; (6) Some blue excess, white dwarf?

Chapter 8

Seven new PCEB Orbital Periods from SDSS

8.1 Introduction

In this Chapter I present follow-up observations of 11 PCEB candidates identified from multiple SDSS spectroscopy in Chapter 7, and provide accurate values of the orbital periods (Sec. 8.2), as well stellar parameters and orbital inclination estimates for seven of these systems (Sect. 8.3). For one PCEB candidate no significant photometric modulation was detected, and its orbital period will need to be measured from RV studies. The three remaining objects showed no significant RV variation, and we suggest they may be wide WDMS binaries. These three systems are discussed in more detail in Sect. 8.4. PCEB evolution for the seven short binaries with accurate orbital period measurements is provided in Sect. 8.5. So far all our PCEB orbital periods are of less than 1 day, and I discuss this finding in Sect. 8.6. I finally give the conclusions of this Chapter in Sect. 8.7.

The instrumentation used for the observations and the reduction of the data are described in Chapter 4.

8.2 Orbital Periods

8.2.1 Radial Velocities

In Chapter 7 we measured the RVs fitting a second order polynomial plus a double-Gaussian line profile of fixed separation to the Na I $\lambda\lambda$ 8183.27,8194.81 absorption doublet. Free parameters were the amplitude and the width of each Gaussian and the RV of the combined doublet. Here we adopt a slightly modified approach, using just a single width parameter for both line components. This reduction in the number of free parameters increases the robustness of the fits. RVs measured in this way for nine WDMS binaries are given in Table 8.1. In addition, we measured the companion star RVs for SDSS J1724+5620 by means of a Gaussian fit to the Hα emission line clearly visible in 22 of the SDSS sub-exposures, which are also reported in Table 8.1.

Scargle [1982, see Chapter 5] periodograms calculated from the RVs of each system to investigate the periodic nature of the velocity variations contain a number of aliases due to the sampling pattern of the observations (Fig. 8.1). We carried out sine-fits of the form

$$V_{\rm r} = K_{\rm sec} \sin\left[\frac{2\pi(t-T_0)}{P_{\rm orb}}\right] + \gamma \qquad (8.1)$$

to the velocity data sets of each system, where γ is the systemic velocity, $K_{\rm sec}$ is the RV semi-amplitude of the companion star, T_0 is the time of inferior conjunction of the secondary star, and $P_{\rm orb}$ is the orbital period. Several fits were done, adopting the frequencies corresponding to the strongest peaks in the power spectra as initial conditions. The parameters resulting from these fits are reported in Table 8.2. For SDSS J0052–0053, SDSS J0246+0041, SDSS J0314–0111, SDSS 1151–0007, SDSS J1529+0020 and SDSS J2339–0020 the sine-fits allow a unique choice of the orbital period. For SDSS J1724+5620, the sampling of the SDSS spectra is very sparse, resulting in finely structured aliases superimposed on a sequence of large aliases spaced by $1\,{\rm d}^{-1}$. A sine fit to the RVs started off at the $3\,{\rm d}^{-1}$ alias provides a spectroscopic orbital period of 7.99243(16) h, which is consistent with the more accurate value determined from the photometry (Sect. 8.2.2). The RV data for all seven systems folded over their orbital periods are shown in Fig. 8.2.

The periodograms calculated from the RV measurements of the PCEB candidates

SDSS J0309–0101, SDSS J1138–0011, and SDSS J2241+0027 do not reveal any significant peak. The low amplitude of the RV variations observed in these three objects suggests that they may be wide WDMS binaries rather than PCEBs. This issue will be discussed further in Sect. 8.4.3.

8.2.2 Light curves

The light curves of SDSS J0314–0111 and SDSS J1724+5620 display variability with an amplitude of ~ 0.05 mag and ~ 0.1 mag, respectively. We calculated periodograms for both systems using the ORT/TSA command in MIDAS [Schwarzenberg-Czerny, 1996, see Chapter 5].

A strong peak is found in the periodogram of SDSS J0314–0111 at $3.8\,\mathrm{d}^{-1}$, i.e. 6.3 h (Fig. 8.3, top left panel). Folding the photometric data over that period results in a double-humped modulation which we identify as ellipsoidal modulation (Fig.8.3, middle left panel). The detection of ellipsoidal modulation indicates that the companion star must be filling a significant amount of its Roche-lobe radius and have a moderately high inclination, both of which hypotheses are confirmed below in Sect. 8.3. The two minima differ in depth, as expected for ellipsoidal modulation because of the stronger gravity darkening on the hemisphere facing the white dwarf. The two maxima are also unequal, which is observed relatively often in PCEBs, and thought to be related to the presence of star spots [e.g. Kawka & Vennes, 2003; Tappert et al., 2007]. We conclude that the strongest periodicity detected in the photometry of SDSS J0314–0111 is consistent with the spectroscopic orbital period (Table 8.2). As the RVs span a longer temporal baseline than the photometry, they provide the more accurate period measurement, and we adopt $P_{\mathrm{orb}} = 6.319 \pm 0.015$ h for SDSS J0314–0111.

For the analysis of SDSS J1724+5620 we separately merged the data for the *R* and *I* band (see Table 4.2), normalised both data sets to their respective mean values, and finally combined all data into a single data set. The ORT periodogram calculated from the full light curve displays a strong signal at $3\,\mathrm{d}^{-1}$, with weak aliases related to the sampling pattern inherent to the data (Fig. 8.3, top right panel). Given the large quasi-sinusoidal shape of the modulation, and the high effective temperature of the white dwarf (Table 8.3), we identify

Table 8.1: RVs measured from the Na I λλ 8183.27,8194.81 doublet, except for SDSS J1724+5620, where RVs measured from the Hα emission line in the 15 min SDSS sub-spectra are given. Note that the provided HJD is the resulted from HJD-2400000.

HJD	RV [km s^{-1}]	HJD	RV [km s^{-1}]	HJD	RV [km s^{-1}]	HJD	RV [km s^{-1}]	HJD	RV [km s^{-1}]
SDSS J0052–0053		54379.8169	106.6 ± 7.4	**SDSS J1138–0011**		54238.7778	59.7 ± 11.3	51993.9263	-81.3 ± 10.7
54328.7467	42.5 ± 18.7	54379.8622	42.5 ± 14.5	54205.5902	-12.8 ± 5.7	54238.8109	-156.4 ± 11.2	51993.9387	-101.9 ± 10.4
54328.7933	-15.0 ± 13.6	54380.8165	-97.1 ± 9.9	54207.7340	-7.7 ± 12.6	54238.8270	-160.8 ± 32.7	51993.9511	-111.0 ± 11.4
54328.8077	-40.7 ± 13.7	54380.8372	-92.3 ± 8.2	54237.5647	-13.9 ± 11.6	54238.8372	-188.3 ± 14.9	51994.9683	-127.4 ± 10.6
54328.8825	31.5 ± 27.5	54380.8762	-85.7 ± 7.8	54237.5721	5.1 ± 10.3	54239.5635	157.9 ± 9.9	51994.9805	-130.2 ± 10.5
54328.8969	-4.0 ± 9.9	54380.8842	-72.9 ± 8.0	54238.4936	9.9 ± 9.6	54239.6756	-121.3 ± 8.0	51994.9928	-131.6 ± 12.5
54329.6885	31.5 ± 9.3	54381.6121	-63.7 ± 12.7	54238.5352	-5.1 ± 8.5	54240.5548	202.6 ± 21.2	51997.9480	-106.9 ± 10.6
54329.7028	-12.1 ± 11.8	54381.7427	77.3 ± 7.6	54238.6889	23.1 ± 10.6	54240.6338	-182.8 ± 7.8	51997.9602	-132.0 ± 10.8
54329.7172	-50.9 ± 16.4	54381.8122	126.4 ± 8.0	54271.3996	9.2 ± 6.7	54240.6844	28.9 ± 10.1	51997.9724	-136.1 ± 11.4
54329.8269	-56.1 ± 14.1	54381.8958	157.2 ± 8.4	**SDSS J1151–0007**		54240.7296	204.4 ± 8.7	**SDSS J2241+0027**	
54329.8412	-60.8 ± 13.4	54382.8362	-31.9 ± 8.9	54237.5904	48.4 ± 14.9	54240.7357	194.9 ± 7.9	54376.5842	2.6 ± 14.0
54329.8556	-55.3 ± 14.8	54385.7884	-71.1 ± 11.5	54237.5976	129.3 ± 11.4	54240.7417	175.1 ± 9.5	54377.5637	6.6 ± 6.6
54330.7154	29.7 ± 10.8	**SDSS J0309–0101**		54238.5245	-147.6 ± 13.0	54240.8311	-114.7 ± 8.1	54378.5290	13.2 ± 9.9
54330.7298	-30.8 ± 12.3	54381.6726	60.4 ± 12.4	54238.5709	-81.0 ± 11.6	54240.8372	-87.6 ± 9.9	54379.5523	39.9 ± 13.3
54330.7441	-59.7 ± 16.0	54381.7714	31.5 ± 12.0	54238.7012	-160.1 ± 6.9	54240.8432	-54.6 ± 12.7	54382.5261	-20.1 ± 17.7
54330.8136	56.8 ± 17.7	54381.8386	41.0 ± 10.7	54239.5084	-129.0 ± 7.7	54240.8498	8.4 ± 31.7	**SDSS J2339–0020**	
54330.8279	28.2 ± 9.3	54382.8626	51.7 ± 15.9	54239.6047	233.4 ± 8.0			54380.5088	-25.3 ± 13.4
54330.8423	-29.3 ± 12.2			54239.6602	-175.8 ± 9.8	**SDSS J1724+5620**		54380.5511	3.7 ± 8.2
54330.9158	32.6 ± 14.1	**SDSS J0314–0111**		54240.4793	148.4 ± 11.7	51812.6531	133.8 ± 13.2	54381.5526	-116.1 ± 9.2
54332.7313	22.7 ± 11.1	54376.7386	-54.6 ± 8.2	54240.5236	-227.1 ± 12.5	51812.6656	114.2 ± 12.2	54382.5097	11.7 ± 10.2
54332.7457	59.3 ± 23.5	54376.7862	-151.3 ± 8.5	54240.5291	-207.4 ± 11.5	51813.5993	60.8 ± 25.2	54382.5869	94.2 ± 9.2
54332.8433	23.1 ± 9.6	54376.8051	-116.1 ± 11.4	54240.5346	-198.2 ± 8.5	51813.6161	77.2 ± 17.1	54382.6866	86.1 ± 10.0
		54376.8581	64.5 ± 10.8	54240.5400	-163.8 ± 9.5	51813.6284	132.0 ± 11.4	54382.7587	24.2 ± 9.1
SDSS J0246+0041		54376.8996	174.7 ± 30.0	54240.6033	219.8 ± 11.4	51813.6425	118.3 ± 12.3	54383.5274	-134.4 ± 11.2
54378.6386	-127.5 ± 11.4	54377.6572	119.8 ± 8.0	54240.6088	220.5 ± 9.3	51813.6631	121.1 ± 11.1	54385.5605	-181.3 ± 17.0
54378.6496	-122.7 ± 13.0	54377.6830	186.1 ± 9.3	54240.6142	161.2 ± 10.1	51813.6768	103.2 ± 10.6	54385.6462	-177.3 ± 9.0
54378.7955	18.3 ± 8.8	54377.7380	164.5 ± 8.0	54240.6197	111.7 ± 9.3	51813.6889	94.1 ± 10.7	54385.6663	-164.9 ± 23.9
54379.6704	176.9 ± 11.3	54377.7782	-2.6 ± 7.5			51818.5877	71.7 ± 22.8	54385.6864	-133.4 ± 12.8
54379.6789	159.0 ± 15.6	54377.8165	-116.1 ± 9.5	**SDSS J1529+0020**		51818.6178	109.6 ± 13.0	54385.7065	-104.0 ± 21.6
54379.6875	177.3 ± 9.7	54377.8672	-98.9 ± 8.1	54238.6219	-3.3 ± 23.9	51818.6297	122.4 ± 13.9	54385.7495	-49.8 ± 27.1
54379.7813	132.6 ± 7.9	54377.8866	-44.3 ± 12.1	54238.6795	-145.1 ± 11.7	51818.6418	127.4 ± 13.2	54385.7696	-16.9 ± 9.8

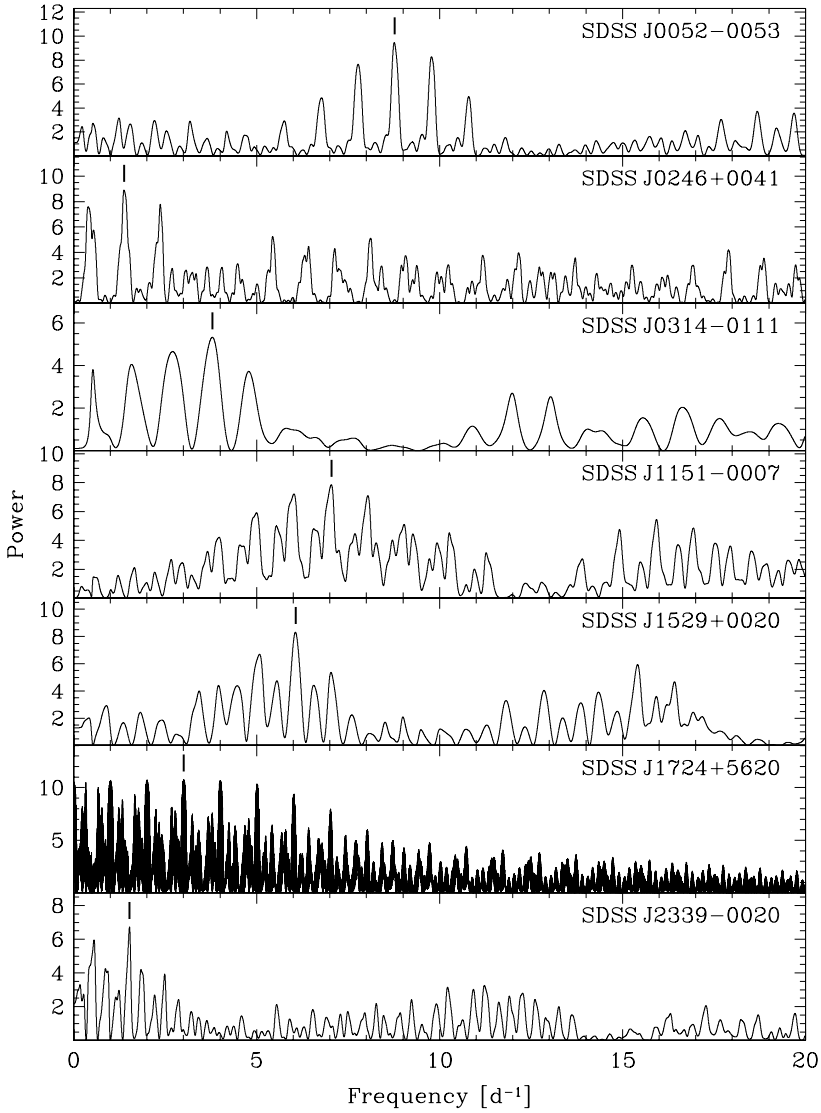

Figure 8.1: Scargle periodograms calculated from the RV variations measured from the Na I absorption doublet in SDSS J0052–0053, SDSS J0246+0041, SDSS J0314–0111, SDSS J1151–0007, SDSS J1529+0020, and SDSS J2339–0020, and from the Hα emission line in SDSS J1724+5620. The aliases with the highest power are indicated by tick marks.

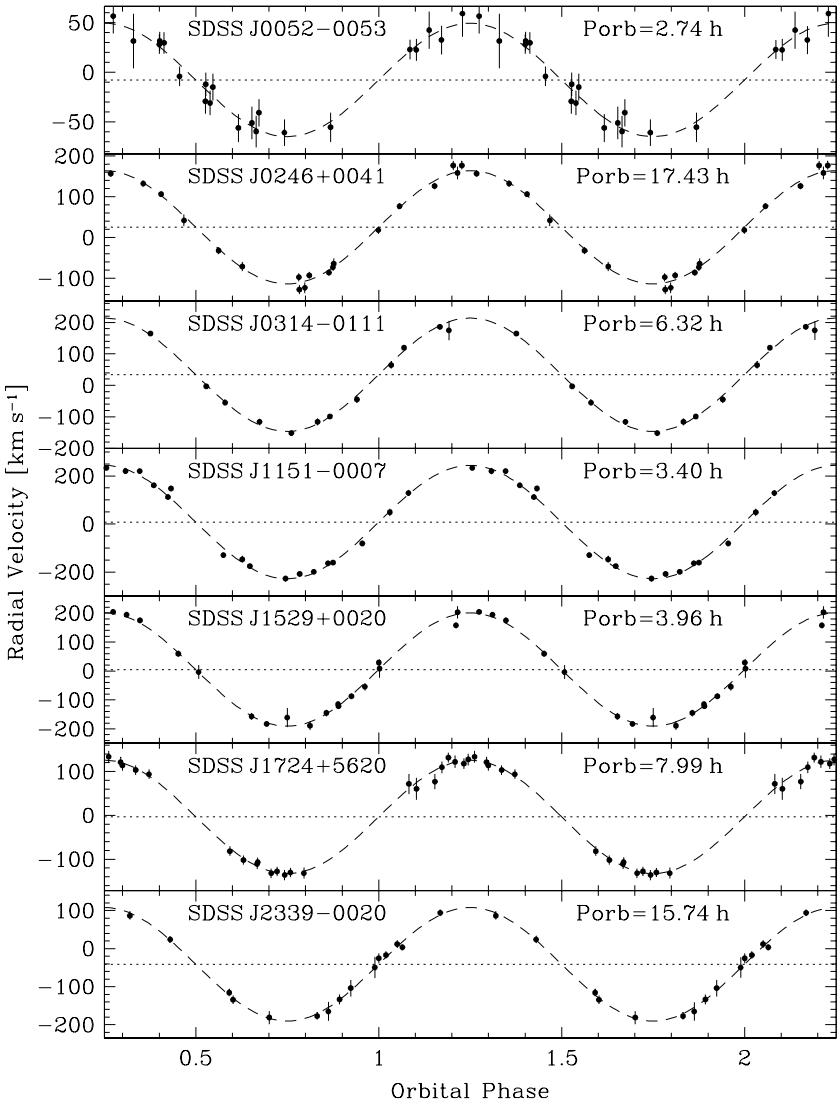

Figure 8.2: The RV measurements folded over the orbital periods of the systems, as determined from the best sine fits (Table 8.2).

the observed photometric variability as being due to heating effect (or reflection effect as it is often referred to in the literature). A sine fit to the combined data (dashed line) provided the following photometric ephemeris

$$\mathrm{HJD} = 2453865.29(1) + \phi \times 0.3330193(13), \tag{8.2}$$

where $\phi = 0$ refers to the occurrence of minimum light. The photometric period of 8 h is consistent with the alias pattern in the periodogram calculated from the Hα RV variations (Fig. 8.1). The phase-folded light curve using the photometric period is shown on the middle right hand panel of Fig. 8.3. Based on the above ephemeris, the accumulated phase error for the first SDSS sub-spectrum (Table 8.1) is 0.024 cycles, which is sufficiently good to phase the RVs obtained from the SDSS spectra with Eq. 8.2. The phase-folded light curve and RV curve are shown in Fig. 8.4. The phase offset between the two curves is 0.226 ± 0.005, which is close to ≈ 0.25. A 0.25 phase offset is what is expected from the assumption that the photometric modulation is related to a heating effect, i.e. maximum light and red-to-blue crossing of the RV corresponds to the superior conjunction of the secondary star, whereas minimum light and blue-to-red crossing of the RV corresponds to its inferior conjunction.

Finally, we show in the bottom panel of Fig. 8.3 a 3.5 hours light curve of SDSS J0820+4314. We monitored the system through a total of 8.2 hours on three different nights (see Table 4.2), and found no significant photometric modulation. This implies that the companion star is significantly under-filling its Roche lobe and/or that the binary inclination is very low. The orbital period of the system will hence need to be measured from a RV study.

8.3 Binary parameters

In Chapter 7 we developed a spectral decomposing/fitting technique for the analysis of WDMS binaries with SDSS spectroscopy. In brief, this analysis determines the white dwarf effective temperature, surface gravity, mass and radius, the spectral type and radius of the MS companion, as well as two independent distance estimates based on the properties of the

Table 8.2: Orbital periods, semi-amplitudes $K_{\rm sec}$, systemic velocities $\gamma_{\rm sec}$, and reduced χ^2 from sine fits to the Na I doublet RV data for the strongest two to three aliases in the periodograms shown in Fig. 8.1. The best-fit values are set in bold. The SDSS Hα RVs of SDSS J1724+5620 are folded on the photometric orbital period obtained in Sect. 8.2.2 (which is more accurate than the spectroscopically determined value of the orbital period). Note also that the semi-amplitude measurement of this system is underestimated, as it comes from RV measurements of Hα emission from the irradiated face of the companion (see Sect. 8.4.2).

System	$P_{\rm orb}$ [h]	$K_{\rm sec}$ [km s^{-1}]	$\gamma_{\rm sec}$ [km s^{-1}]	χ^2
SDSS J0052–0053	3.0850±0.0090	47.2±6.6	-2.9±5.8	3.74
	2.7350±0.0023	**57.0±3.1**	**-7.2±2.6**	**0.50**
	2.4513±0.0035	54.8±5.8	-9.1±4.6	1.96
SDSS J0246+0041	61.1±2.7	124±17	16±12	20.3
	17.432±0.036	**140.7±3.5**	**24.9±2.7**	**1.25**
	10.130±0.031	163±16	34±10	21.6
SDSS J0314–0111	8.66±0.17	154±19	44±16	27.1
	6.319±0.015	**174.9±4.8**	**31.0±3.4**	**1.15**
SDSS J1151–0007	3.979±0.013	202±20	-2±16	34.4
	3.3987±0.0027	**233.8±8.1**	**9.0±5.9**	**3.55**
	2.9849±0.0092	213±22	-22±23	64.7
SDSS J1529+0020	4.759±0.028	171±18	11±14	26.9
	3.9624±0.0033	**193.1±5.2**	**6.0±4.1**	**1.91**
	1.5558±0.0024	182±21	6±15	36.7
SDSS J1724+5620	**7.992463(31)**	**129.3±1.9**	**-3.5±1.8**	**0.41**
SDSS J2339–0020	43.18±0.78	121±18	-50±15	13.5
	15.744±0.016	**149.8±4.0**	**-40.9±2.6**	**0.69**

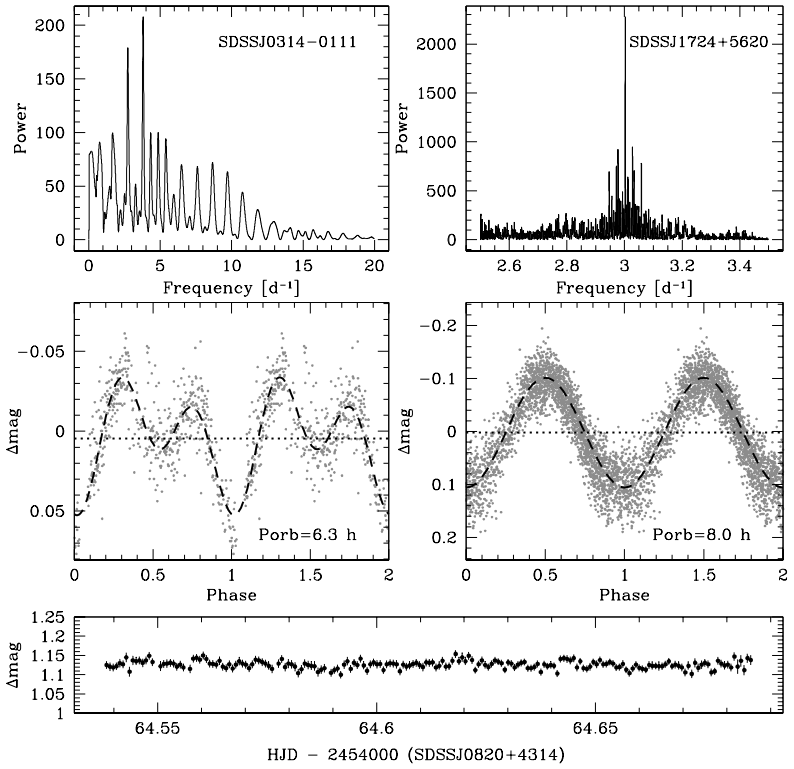

Figure 8.3: Top and middle panels: ORT periodograms and light curves folded on strongest photometric periodicities, $P_{\rm orb} = 6.32 \pm 0.02$ h for SDSS J0314–0111 and $P_{\rm orb} = 7.99246 \pm 0.00003$ h for SDSS J1724+5620. Bottom panel: the light curve of SDSS J0820+4314 is essentially flat, and a periodogram calculated from this data does not contain any significant periodicity.

two stellar components. Given that the SDSS spectra reduction pipeline has been improved with DR6 [Adelman-McCarthy et al., 2008], we have re-analysed here the seven PCEBs for which we were able to determine orbital periods. Comparison with the results from DR5 reported in Chapter 7 shows that the fit parameters differ slightly, but agree in the vast majority of cases within the errors. We report the average stellar parameters determined from fits to the multiple SDSS spectra in Table 8.3. Rewriting Kepler's third law (assuming common notation),

$$\frac{(M_{\rm wd}\sin i)^3}{(M_{\rm wd}+M_{\rm sec})^2} = \frac{P_{\rm orb}K_{\rm sec}^3}{2\pi G} \tag{8.3}$$

as

$$\sin i = \frac{K_{\rm sec}}{M_{\rm wd}}\left(\frac{P_{\rm orb}}{2\pi G}\right)^{1/3}(M_{\rm wd}+M_{\rm sec})^{2/3}, \tag{8.4}$$

and adopting the orbital period determined from the analysis of the RVs and the photometry, as well as the masses from the analysis of the SDSS spectra, we are now able to estimate the orbital inclinations for the seven systems in Table 8.3. Two systems require some additional notes: SDSS J0314–0111 contains a DC white dwarf, and hence no white dwarf parameters could be determined from the spectral analysis, and we assume $M_{\rm wd} = 0.65 M_{\odot}$ for the estimate of the inclination. In SDSS J1724+5620 the hot white dwarf is irradiating the companion star, and the implications are discussed in more detail in Sect. 8.4.2.

Inspecting Eq.(8.4), it is clear that the dominant uncertainties in the inclination estimates are only $M_{\rm wd}$ and $M_{\rm sec}$, as the orbital periods and $K_{\rm sec}$ velocities are accurately determined. The primary uncertainty in the inclination estimates is $M_{\rm sec}$, as it is based on the spectral type of the companion star, adopting the $Sp-M-R$ relation given in Chapter 7. $M_{\rm wd}$ is determined from fitting the Balmer line profiles, and relatively well constrained. Given that $\sin i \propto M_{\rm sec}^{2/3}$, but $\sin i \propto M_{\rm wd}$, the relative weight of the uncertainty in $M_{\rm sec}$ is alleviated. We estimate the uncertainties on the binary inclinations in Table 8.3 by assuming in Eq.8.4 the range in $M_{\rm sec}$ implied by a spectral type uncertainty of ± 0.5 spectral classes plus the associated errors in the $Sp-M$ relation, as well as the range in $M_{\rm wd}$ resulting from the Balmer line profile fits. Given the high estimate for the binary inclination, SDSS J1529+0020 is a good candidate for photometric follow-up observations probing for eclipses in its light curve.

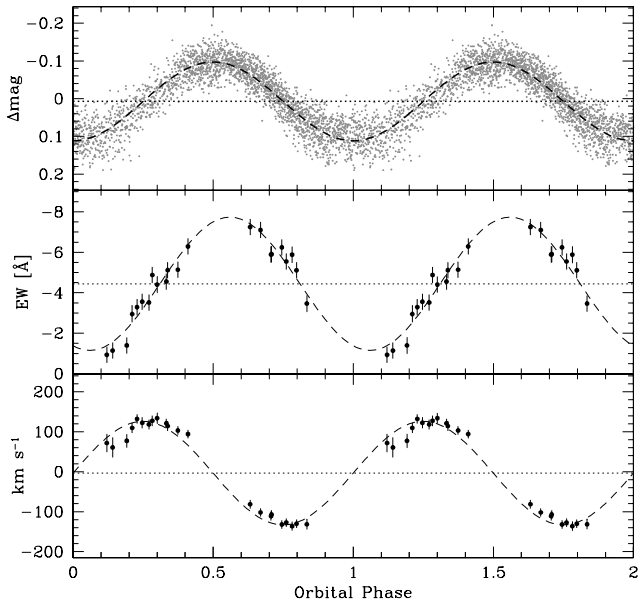

Figure 8.4: Top panel: The IAC 80 and AIP 70 cm photometry of SDSS J1724+5620 folded over the photometric period of 7.9924632 ± 0.0000312 h. Middle panel: the equivalent width variation of the Hα emission line measured from the SDSS spectra of SDSS J1724+5620 (Table 8.1) folded over the photometric period. Maximum equivalent width occur roughly in phase with the maximum in the light curve (see Sect. 8.4.2 for details). Bottom panel: the RV variation of the Hα emission line folded over the photometric orbital period. The relative phasing with respect to the photometry is consistent with the photometric modulation being caused by irradiation of the secondary star by the hot white dwarf.

Table 8.3: Average binary parameters obtained for the seven PCEBs which have orbital period and $K_{\rm sec}$ measurements. $M_{\rm wd}$, $M_{\rm sec}$, $R_{\rm sec}$, spectral type, $T_{\rm eff}$ and $\log g$ are obtained following Chapter 7, except for SDSS J0314–0111, where we assume a white dwarf mass of $0.65 \pm 0.1\ M_{\odot}$ (see text for details). $P_{\rm orb}$ and $K_{\rm sec}$ are measured in Sect. 8.2 of this Chapter. Estimates of orbital separations a, q, $K_{\rm wd}$, secondary Roche lobe radius $R_{\rm L_{sec}}$ and inclinations are obtained from the equations given in Sect. 8.3. SDSS J1724+5620 is a particular case, as the inner hemisphere of the companion is heated. Constraints on its orbital parameters are obtained assuming a spectral type between M3-5, and considering different $\rm K_{sec,corr}$ values for each mass and radius (see Sect. 8.4.2). An additional constraint for its inclination comes from the fact that SDSS J1724+5620 is not eclipsing.

	SDSS J0052–0053	SDSS J0246+0041	SDSS J0314–0111	SDSS J1151–0007	SDSS J1529+0020	SDSS J1724+5620	SDSS J2339–0020
$M_{\rm wd}[M_{\odot}]$	1.2 ± 0.4	0.9 ± 0.2	0.65 ± 0.1	0.6 ± 0.1	0.40 ± 0.04	0.42 ± 0.01	0.8 ± 0.4
$M_{\rm sec}[M_{\odot}]$	0.32 ± 0.09	0.38 ± 0.07	0.32 ± 0.09	0.19 ± 0.08	0.25 ± 0.12	$\sim$0.25 - 0.38	0.32 ± 0.09
q	0.3 ± 0.1	0.4 ± 0.1	0.5 ± 0.2	0.3 ± 0.2	0.6 ± 0.3	$\sim$0.6 - 0.9	0.4 ± 0.2
$a[R_{\odot}]$	1.1 ± 0.1	3.7 ± 0.2	1.7 ± 0.1	1.0 ± 0.1	1.1 ± 0.1	$\sim$1.8 - 1.9	3.3 ± 0.4
$P_{\rm orb}$ [h]	2.735 ± 0.002	17.43 ± 0.04	6.32 ± 0.02	3.399 ± 0.003	3.962 ± 0.003	7.992463(3)	15.74 ± 0.02
$K_{\rm sec}[\rm km\,s^{-1}]$	57 ± 3	141 ± 4	175 ± 5	234 ± 8	193 ± 5	$\sim$129 - 214	150 ± 4
$K_{\rm wd}[\rm km\,s^{-1}]$	15 ± 6	59 ± 15	86 ± 28	79 ± 38	123 ± 61	$\sim$78 - 194	57 ± 29
$\rm Sp_{sec}$	4 ± 0.5	3 ± 0.5	4 ± 0.5	6 ± 0.5	5 ± 0.5	3 - 5	4 ± 0.5
$R_{\rm sec}[R_{\odot}]$	0.33 ± 0.10	0.39 ± 0.08	0.33 ± 0.10	0.19 ± 0.10	0.26 ± 0.13	$\sim$0.26 - 0.39	0.33 ± 0.10
$R_{\rm sec}/R_{\rm Lsec}$	1.0 ± 0.6	0.3 ± 0.1	0.6 ± 0.2	$0\,6 \pm 0.5$	0.7 ± 0.5	$\sim$0.4 - 0.6	0.3 ± 0.1
$i[^{\circ}]$	8 ± 1	51 ± 7	53 ± 8	56 ± 11	70 ± 22	$>\sim 50^{\circ}$, $<\sim 75^{\circ}$	53 ± 18
$T_{\rm eff}$[k]	16100 ± 4400	16600 ± 1600	— ± —	10400 ± 200	14100 ± 500	35800 ± 300	13300 ± 2800
$\log g$	9.0 ± 0.7	8.5 ± 0.3	— ± —	8.0 ± 0.2	7.6 ± 0.1	7.40 ± 0.05	8.4 ± 0.7

In addition, knowing that $M_{\rm sec}/M_{\rm wd} = K_{\rm wd}/K_{\rm sec} = q$, we can also estimate the expected orbital velocity of the white dwarf $K_{\rm wd}$ (Table 8.3). The predicted $K_{\rm wd}$ amplitudes could easily be measured, e.g. using *HST/COS* observations, and such measurements would be very valuable to improve the overall constraints on the system parameters of these PCEBs. Finally, we can estimate the orbital separations and Roche-lobe radii of the secondary stars from Kepler's third law and Eggleton's (1983) expression

$$R_{\rm Lsec} = \frac{a\,0.49\,q^{2/3}}{0.6\,q^{2/3} + \ln(1+q^{1/3})} \tag{8.5}$$

8.4 Notes on individual systems

8.4.1 SDSS J0052–0053, a detached CV in the period gap?

SDSS J0052–0053 has the shortest orbital period, the smallest RV amplitude, and the lowest inclination in our sample (Fig. 8.2, Table 8.3). Another intriguing feature of SDSS J0052–0053 is that the Roche-lobe secondary radius and the secondary star radius overlap within the errors (see Table 8.3). The SDSS (see Fig. 4.1 in Chapter 4) and Magellan spectra certainly rule out ongoing mass transfer, i.e. that SDSS J0052–0053 is a disguised CV. Two possible scenarios could apply to the system. SDSS J0052–0053 could be either be a pre-CV that is close to develop in a semi-detached configuration, or it could be a detached CV in the 2–3 h period gap. Standard evolution models based on the disrupted MB scenario [e.g. Rappaport et al., 1983; Kolb, 1993; Howell et al., 2001] predict that CVs stop mass transfer and the secondary star shrinks below its Roche-lobe radius once they evolve down to $P_{\rm orb} \simeq 3$ h (see Chapter 1). Subsequently, these detached CVs evolve through the period gap, until the companion star fills its Roche-lobe again at $P_{\rm orb} \simeq 2$ h. Population models based on the disrupted MB hypothesis predict that the ratio of detached CVs to pre-CVs (with appropriate companion star masses to (re-)initiate mass transfer at $P_{\rm orb} \simeq 2$ h) should be $\gtrsim 4$ [Davis et al., 2008], hence a substantial number of such systems is expected to exist. So far, only one other system with similar properties is known, HS 2237+8154 [Gänsicke et al., 2004].

The white dwarf $T_{\rm eff}$ in a typical CV about to enter the period gap is approximately 40000 K [Townsley & Gaensicke, 2008], and a rapid cool down is expected once the CV

becomes detached. SDSS J0052–0053 is located close to the upper edge of the period gap (2.75 hours), and contains a $\sim$16000 K white dwarf, which supports the idea of this object being a detached CV, in which the white dwarf $T_{\rm eff}$ has started (and might have finished) to cool down. Inspecting the secondary mass and the mass ratio of this system we found that both are also in agreement with the above hypothesis [Howell et al., 2001, see their Figures 5 and 6]. White dwarfs in CVs are expected to be rapid-rotating, and the measurement of the white dwarf rotational velocity in SDSS J0052–0053 (e.g. through HST spectra) hence would help in confirming whether this system is indeed a detached CV.

8.4.2 SDSS J1724+5620, a PCEB with a strong heating effect

SDSS J1724+5620 contains the hottest white dwarf among our sample of PCEBs, which affects the determination of its system parameters in several ways. Firstly, irradiation heating the inner hemisphere of the companion will cause it to appear of earlier spectral type than an unheated star of same mass. This effect is observed in the analysis of the three SDSS spectra available in DR6. The spectral decomposition types the companion star as M3-4, and combining the flux scaling factor of the M star template and the $Sp-R$ relation (see Chapter 7 for details) indicates an average distance of $d_{\rm sec} = 633 \pm 144$ pc. This is roughly twice the distance implied from the model fit to the residual white dwarf spectrum, $d_{\rm wd} = 354 \pm 15$ pc, indicating that the spectral type of the companion star determined from the SDSS spectrum is too early for its actual mass and radius, as expected for being heated by the white dwarf. Fixing the spectral type of the companion to M5, the spectral decomposition results in $d_{\rm sec} = 330 \pm 150$ pc, consistent with the distance based on the white dwarf fit.

An additional complication is that the RV of the companion star was measured from the Hα emission line, as the Na I absorption doublet was too weak in the individual 900 s SDSS spectra. The equivalent width of the Hα emission shows a noticeable variation as a function of binary phase, with maximum equivalent with near the maximum in the light curve, indicating that the Hα emission is concentrated on the inner hemisphere of the companion star (Fig. 8.4). A phase offset of 0.046 ± 0.008 is observed between the photometry and the Hα equivalent width, which we attribute to systematic problems in

measuring the equivalent width of the Hα embedded in the photospheric absorption line from the white dwarf, given the poor quality of the individual SDSS sub-spectra. As a consequence of Hα predominantly originating on the inner hemisphere of the companion star, the observed $K_{\rm sec}$ is an underestimate of the true RV amplitude [e.g. Wade & Horne, 1988; Orosz et al., 1999; Vennes et al., 1999; Aungwerojwit et al., 2007]. The RV amplitude of the secondary star's centre of mass can be written as [Wade & Horne, 1988]:

$$K_{\rm sec,corr} = \frac{K_{\rm sec}}{1-(1+q)(\Delta R/a)}, \tag{8.6}$$

where ΔR is the displacement of the centre of light from the centre of mass. $\Delta R = 0$ implies that the centre of light and the centre of mass coincide, whilst $\Delta R = R_{\rm sec}$ gives the maximum possible displacement. If one assumes that the irradiated emission on the secondary is distributed uniformly over the inner hemisphere, and that the contribution of the irradiation is zero on its un-irradiated face, then $\Delta R = (4/3\pi)R_{\rm sec}$ [Wade & Horne, 1988; Orosz et al., 1999; Vennes et al., 1999]. Assuming that the spectral type is in the range M3–5, different combinations of secondary mass and radius, and RV amplitude, $K_{\rm sec,corr}$, can then constrain the orbital parameters of SDSS J1724+5620 (Table 8.3).

8.4.3 SDSS J0309-0101, SDSS J1138-0011 and SDSS J2241+0027: wide WDMS binaries?

SDSS J0309-0101, SDSS J1138-0011 and SDSS J2241+0027 were flagged as PCEB candidates in Chapter 7 on the basis of a 3σ RV variation in between their different SDSS spectra, as measured from either the Hα emission line or the Na I absorption doublet from the companion star. However, the additional intermediate-resolution spectra taken for these three objects (Table 4.2) do not show a significant RV variation (Table 8.1, Fig. 8.5). It is therefore important to review the criterion that we used in Chapter 7 to identify PCEBs from repeated SDSS spectroscopy in the light of two subtle changes.

On the one hand, we have slightly modified the procedure to fit the Na I absorption doublet, as outlined in Sect. 8.2.1. By comparing the Na I DR5 RVs in Chapter 7 with those obtained with the new procedure for the same spectra, we find an average difference of $5\,{\rm km\,s^{-1}}$ with a maximum difference of $10.5\,{\rm km\,s^{-1}}$. In all cases the measurements agree

within the errors.

On the other hand, we were using DR5 spectra in Chapter 7, but the analysis carried out here was done using DR6 spectra, which were processed with a different reduction pipeline [Adelman-McCarthy et al., 2008]. A comparison between the DR5 and DR6 RV values obtained in Chapter 7 and in this Chapter respectively (both measured following our new procedure) provides in this case an average difference of $6.5\,\mathrm{km\,s^{-1}}$, with a maximum of $22\,\mathrm{km\,s^{-1}}$. Again, the RV measurements agree, with the exception of a single spectrum, within the errors.

The conclusion from comparing our two methods, and the two SDSS data releases, is that the RV measurements obtained are in general consistent within their errors. However, the offsets can be sufficient to move a given system either way across our criterion to identify PCEB candidates, being defined a 3σ RV between their SDSS spectra. This is specifically the case for systems with either low-amplitude RV variations, or faint systems with noisy spectra. An additional note concerns the use of the Hα line as probe for RV variations. In Chapter 7 we identified SDSS J0309-0101 and SDSS J2241+0027 as PCEB candidates on the basis of a change in the Hα RVs between the available SDSS spectra. However, the velocities obtained from the Na I doublet did not differ significantly. Inspecting the spectra again confirms the results obtained in Chapter 7. This suggests that the absorption lines from the secondary star are a more robust probe of its RV.

A somewhat speculative explanation for the shifts found from Hα RV measurements is that the MS star is relatively rapidly rotating, and that the Hα emission is patchy over its surface. A nice example of this effect is the rapidly rotating ($P_{\mathrm{rot}} = 0.459$ d) active M-dwarf EY Dra, which displays Hα RV variations with a peak-to-peak amplitude of $\sim 100\,\mathrm{km\,s^{-1}}$ [Eibe, 1998]. In order to explain the Hα RV shifts of a few $10\,\mathrm{km\,s^{-1}}$ observed in e.g. SDSS J2241+0027, the companion star should be rotating with a period of ~ 1 d. According to Cardini & Cassatella [2007], low-mass stars such as the companions in our PCEBs that are a few Gyr old are expected to have rotational periods of the order of tens of days, which is far too long to cause a significant Hα RV variation at the spectral resolution of the SDSS spectra. However, sufficient angular momentum can be transferred to the secondary through the action of stellar wind from the primary once it evolved through the AGB, and produce

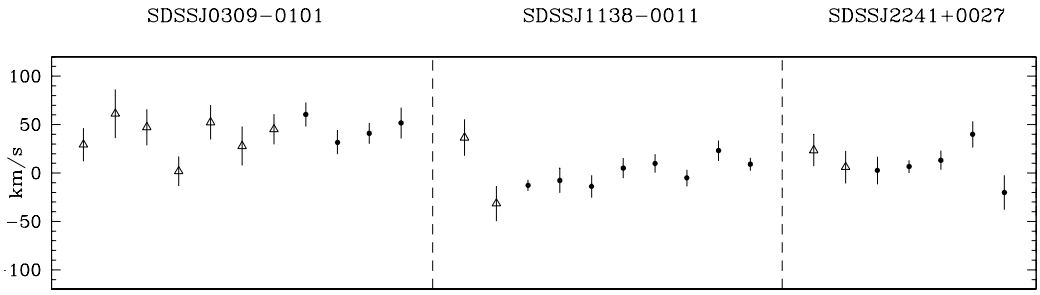

Figure 8.5: Na I SDSS RVs (triangles) along with the Na I RVs measured in this Chapter (solid dots) of SDSS J0309-0101, SDSS J1138-0011 and SDSS J2241+0027. The data at hand suggest that these three systems are wide WDMS binaries instead of PCEBs.

(wind-induced) rapid rotating secondaries [Jeffries & Stevens, 1996]. In addition Cardini & Cassatella's study was based on single stars, and the rotation rates of the companion stars in (wide) WDMS binaries is not well established.

8.5 PCEB evolution

Following Schreiber & Gänsicke [2003] we determine the cooling age and the future evolution of the new PCEBs. The numbers we obtained from the theoretical analysis are summarised in Table 8.4. We used the cooling tracks of Wood [1995] and find that most of the PCEBs left the CE about $1-5\times10^8$ years ago, the only exception being SDSS J1724+5620 which appears to be much younger. The estimated secondary masses are generally very close to the fully convective boundary (for which we assume $M_{\rm cc}=0.3M_{\odot}$), and the uncertainties involved in the secondary mass determination are quite large (see Table 8.3). The predicted evolution of all systems should therefore be considered highly uncertain as it is not clear whether MB applies or not. We therefore give in Table 8.4 the values obtained for two possible scenarios, disrupted MB [CMB, e.g. Verbunt & Zwaan, 1981], and AML given only by GR. The effect of not knowing whether MB or only GR will drive the evolution of the systems is illustrated in Fig. 8.6, which shows the expected post-CE evolution for SDSS J1152–0007 and SDSS J0246+0041 for both cases. The time still needed to enter the semi-detached CV configuration in the CMB scenario is shorter than the Hubble time for all the systems (see Table 8.4), qualifying them as strong representatives for the progenitors

Table 8.4: Parameters of the PCEBs derived from calculating their post-CE evolution according to Schreiber & Gänsicke [2003]. $t_{\rm cool}$ and $t_{\rm sd}$ are the cooling age and the predicted time until the system enters the semi-detached CV phase respectively. $P_{\rm sd}$ denotes the zero-age CV orbital period while $P_{\rm CE}$ is the orbital period the system had when it left the CE phase. As discussed in the text and displayed in Fig 8.6, the predicted evolution depends sensitively on the mass and the radius of the secondary star, in particular as the errors of all estimated secondary masses overlap with the value assumed for the fully convective mass limit. We therefore give values for the both scenarios.

			CMB			GR		
Name	$P_{\rm orb}$	$t_{\rm cool}$	$P_{\rm sd}$	$P_{\rm CE}$	$t_{\rm sd}$	$P_{\rm sd}$	$P_{\rm CE}$	$t_{\rm sd}$
SDSS J	[days]	[years]	[days]	[days]	[years]	[days]	[days]	[years]
0052–0053	0.114	4.2×10^{8}	0.125	0.46	0.0	0.114	0.145	0.0
0246+0041	0.726	3.1×10^{8}	0.146	0.78	1.1×10^{9}	0.113	0.73	8.1×10^{10}
0314–0111	0.263	—	0.12	—	3.7×10^{7}	0.11	—	6.2×10^{9}
1151–0007	0.142	5.0×10^{8}	0.12	0.55	2.7×10^{6}	0.07	0.15	1.8×10^{9}
1529+0020	0.165	1.3×10^{8}	0.11	0.41	4.7×10^{6}	0.10	0.17	2.5×10^{9}
1724+5620	0.333	3.2×10^{6}	0.12	0.34	6.1×10^{7}	0.11	0.33	1.7×10^{10}
2339–0020	0.656	5.1×10^{8}	0.12	0.74	1.0×10^{9}	0.11	0.66	6.5×10^{10}

of the current CV population.

Inspecting Table 8.4, the case of SDSS J0052–0053 is particularly interesting. The estimated secondary radius is consistent with its Roche-lobe radius and the system is supposed to be very close to the onset of mass transfer, which is reflected by $t_{\rm sd} = 0$ within the accuracy of our calculations. Clearly, SDSS J0052–0053 may be a detached CV in the period gap, or a pre-CV that has almost completed its PCEB lifetime. According to CV population studies [Kolb, 1993], the number of detached CVs in the gap is approximately five times higher than the number of CVs in the gap and the probability for SDSS J0052–0053 being a detached CV in the gap rather than a PCEB is $\sim$ 80%. This result is a simple consequence of the fact that all CVs with donor stars earlier than $\sim$M3 will become detached CVs in the gap while only a rather small fraction of PCEBs, i.e. those with secondary stars of spectral type $\sim$M3.5–M4.5, produces CVs starting mass transfer in the period gap. This is obviously only a rough estimate. A detailed population study by Davis et al. [2008, see also Chapter 1] confirms that the ratio of detached CVs to pre-CVs within the CV period gap is $\sim 4-13$, depending on different assumptions of the CE ejection efficiency, initial mass ratio distributions, and MB laws.

8.6 Discussion

As outlined in Chapter 1, despite some recent progress our understanding of the CE phase is still very limited. The classical α-formalism that is based on a simple energy equation seems to be unable to explain the observed existence of DDs with stellar components of comparable masses and rather long orbital periods. This disagreement motivated Nelemans et al. [2000] to develop an alternative prescription based on the conservation of angular momentum, the so-called γ-formalism. Binary population synthesis codes based on the α-formalism as well as those assuming the γ-formalism predict the existence of a significant number of PCEBs with orbital periods longer than a day. Using the α-formalism, Willems & Kolb [2004] calculated the expected period distribution of the present-day WDMS binaries in the Galaxy at the start of the WDMS binary phase. Their Fig. 10 clearly shows that the predicted PCEB distribution peaks around $P_{\rm orb} \sim 1$ day, but also has a long tail of systems with up to ~ 100 d. The γ-formalism, on the other hand, predicts an increase of the number of PCEBs with increasing orbital period up to $P_{\rm orb} \gtrsim 100$ days, i.e. the γ-formalism predicts the existence of even more long orbital period ($P_{\rm orb} > 1$ day) PCEBs (see Chapter 1).

We have measured a total number of nine orbital periods along this chapter and the paper by Schreiber et al. [2008]. All of them have short orbital periods of less than a day. RV variations are much easier to identify in short orbital period systems, so our sample is expected to be biased towards shorter orbital periods. The crucial question is whether our observational finding, the paucity of PCEBs with $P_{\rm orb} > 1$ d, is whether the result of that bias, or whether it reflects an intrinsic feature of the PCEB population. To answer this question we performed the following analysis. First, we carried out Monte-Carlo simulations similar to those presented in Schreiber et al. [2008] but assuming a resolution of 15km/s, corresponding to the typical error in the RV measurements from SDSS spectra. Clearly, as shown in Fig. 8.7, the bias towards short orbital period systems is larger due to the lower resolution of the SDSS spectra and, as a consequence, RV variations in multiple SDSS spectra of systems with $P_{\rm orb} > 10$ days are more difficult to detect. However, the probability to detect 3σ RV variations for systems in the orbital period range of $P_{\rm orb} \sim 1-10$ days still is $\sim 20-40$%. Second, we assumed a uniform orbital period distribution and integrated the 3σ-detection probability (lowest dotted line) for systems with $P_{\rm orb} \leq 1$ day and those with

10 days $> P_{\rm orb} >$ 1 day. In other words, we assume that there is no decrease for 10 days $> P_{\rm orb} >$ 1 day and calculate the total detection probability for 10 days $> P_{\rm orb} >$ 1 day and $P_{\rm orb} \leq$ 1 day. We find that if there was indeed no decrease, the fraction of PCEBs with $P_{\rm orb} >$ 1 day in our sample should be $\sim$ 84% and the number of PCEBs with $P_{\rm orb} >$ 1 day among our nine systems should be $\sim 7.6 \pm 2.8$. The result of our observations, i.e. no system with $P_{\rm orb} >$ 1 day among nine PCEBs disagrees with the hypothesis (i.e. there is no decrease) by 2.7σ. This indicates that the measured lack of PCEBs with $P_{\rm orb} >$ 1 day might indeed be a feature of the intrinsic population of PCEBs. An independent (photometric) study carried out by De Marco et al. [2008] showed that the orbital period distribution of 12 central stars of planetary nebulae is also concentrated to orbital periods shorter than 1 day, with no observable periods longer than 3 days.

How do our results for PCEBs from SDSS compare with the sample of all known PCEBs? Figure 8.8 shows in gray the orbital period distribution of all 41 known PCEBs consisting of a M or K-star plus a white dwarf from the latest version of the Ritter & Kolb [2003] catalogue (V7.9), including also the seven new periods from this paper, and the new recent discovery by Steinfadt et al. [2008, see also Pyrzas et al. [2008]]. As we are interested in analysing the bias of the sample towards shorter orbital periods in the context of detection probability, we superimpose in black a subsample of ten SDSS PCEBs, identified from RV snapshots of SDSS WDMS binaries, representing a homogenous selection mechanism (seven from the current Chapter, two from Schreiber et al. 2008, one [SDSS J112909.50+663704.4] from Raymond et al. 2003). So far, the period distributions of the two subsets seem very similar, with a steep decrease of the number of systems at $P_{\rm orb} \sim$ 1 day. The total sample of PCEBs contains only six systems with orbital periods larger than one day ($\sim$15% of the entire sample). This suggests that the number of PCEBs decreases for $P_{\rm orb} >$ 1 day, implying that the γ-formalism in its present form might not be an adequate description of the CE phase, and that the CE efficiency in the energy equation used in the α-formalism is perhaps smaller than assumed previously (lower efficiencies lead to stronger shrinkage of binary separations). However, a $P_{\rm orb} >$ 1 day PCEB can be a consequence not only of efficient AML during the CE phase, but also a consequence of a fairly large initial MS binary separation. Hence we can not exclude that the lack of $P_{\rm orb} >$ 1 day

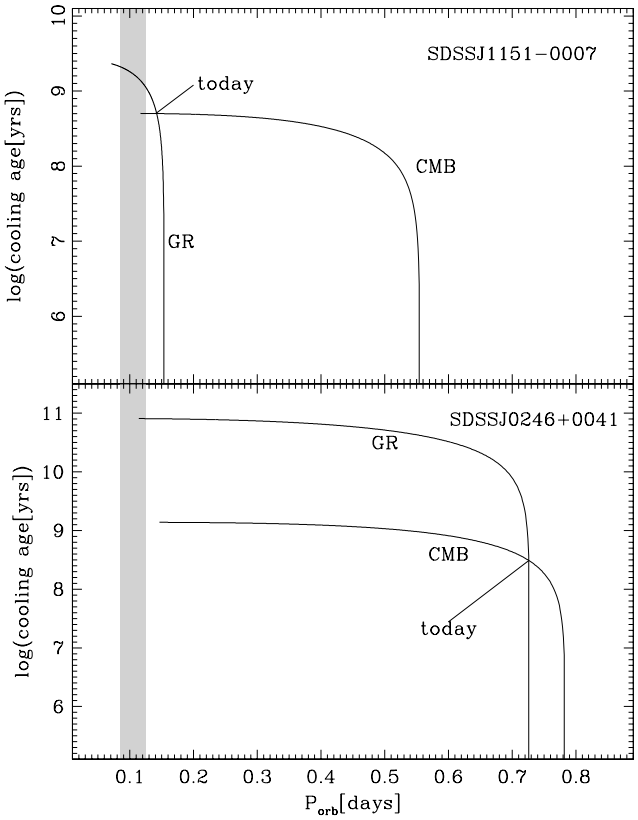

Figure 8.6: The predicted evolution of two PCEBs. The orbital period gap observed in the orbital period distribution of CVs is shaded. As the secondary masses of SDSS J1151–0007 and SDSS J0246+0041 are close to the fully convective boundary, we calculated the evolution assuming classical MB and assuming only GR. Obviously, the calculated orbital periods at the end of the CE phase ($P_{\rm CE}$), the evolutionary time scale, and the expected zero-age CV orbital period ($P_{\rm sd}$) differ significantly.

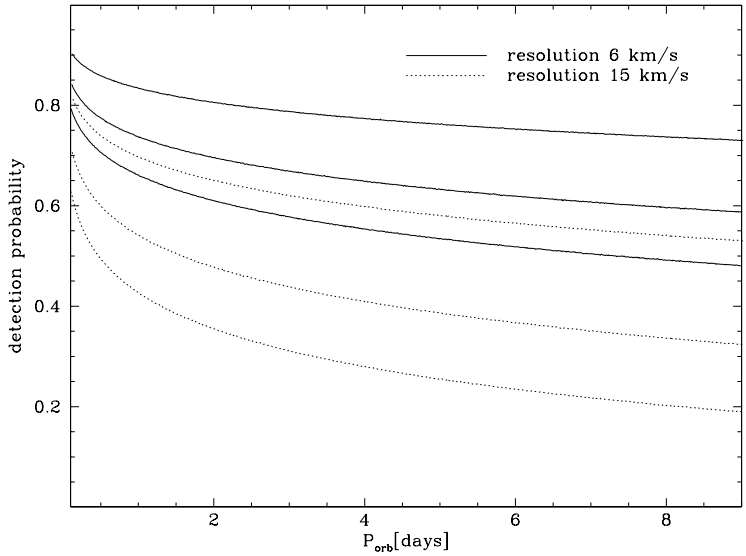

Figure 8.7: Monte-Carlo simulations of the detection probability of significant RV variations assuming measurement accuracy of $6\,\mathrm{km\,s^{-1}}$, corresponding to our previous VLT/FORS observations [Schreiber et al., 2008] and 15km/s, as appropriate for the SDSS spectra (Chapter 7). The three lines correspond to 1, 2, or 3σ significance of the RV variation. Clearly, even the PCEB identification based on multiple SDSS spectra should be sensitive to PCEBs with orbital periods of $\sim 1-10$ days.

systems is simply reflecting that there are few progenitors. In addition, one should bear in mind that the previously known PCEBs have been discovered by various methods, and therefore do not form a representative sample [see Schreiber & Gänsicke, 2003, for details]. The sample of PCEBs selected in a homogeneous way from the SDSS is still small, and the current sample of WDMS binaries from SDSS involves some selection effects, too [Schreiber et al., 2007], impeding a definite conclusion at this point (see Chapter 10 though). However, work is underway to enlarge the parameter space of the SDSS WDMS binaries in terms of ages and secondary star masses [Schreiber et al., 2007], to increase the number of PCEBs with orbital period measurements, and to model the remaining selection effects, paving the way for a more quantitative assessment of CE and post-CE evolution.

8.7 Conclusions

We have presented a study of 11 PCEB previously identified candidates, and measured the orbital periods of six and one of them from their Na I doublet RV variations and its differ-

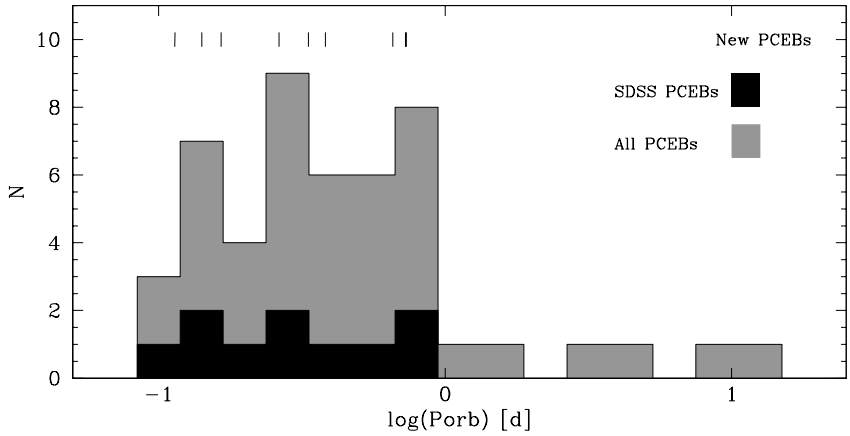

Figure 8.8: The period distribution of 41 PCEBs from the Ritter & Kolb [2003] (V7.9) catalogue containing a white dwarf plus M or K companion star (gray). The 7 systems studied in this work and the recent PCEB discovery SDSS J143547.87+373338.5 [Steinfadt et al., 2008] are also included. In black is shown a subsample of SDSS PCEBs obtained from RV variation studies. Both subsamples illustrate a clear lack of systems at orbital periods greater than 1 day. The 7 new systems from this work and the the two systems in Schreiber et al. [2008] are indicated as tick marks in the top of the figure.

ential photometry, respectively. Combining the $K_{\rm sec}$ velocity amplitudes with the results from spectroscopic decomposition/fitting of their SDSS spectra, we constrained the binary parameters of the seven systems for which we could determine orbital periods. No RV variations were detected for three PCEB candidates, suggesting that they may be wide WDMS binaries. We revisited the PCEB candidate selection of Chapter 7, and concluded that candidates with low amplitude velocity variations, noisy SDSS spectra, and RV shifts that only show up in the Hα emission line definitely need additional follow-up spectroscopy for the confirmation/rejection of their PCEB nature. Finally, we have had a first look at the period distribution of PCEBs from SDSS identified from RV snapshots of SDSS WDMS binaries, and noted that none of the ten systems published so far have an orbital period > 1 d. Using a Monte-Carlo simulation, we demonstrated that our method of finding PCEBs should be efficient also for systems with periods > 1 d, and that, subject to small number statistics, it appears that the PCEB period distribution peaks at $P_{\rm orb} < 1$ d. This is in agreement with the period distribution of the previously known PCEBs, which represents a heterogenous mix of systems identified by various different methods. In contrast, current binary population

models predict a large number of PCEBs with orbital periods > 1 day in clear disagreement with the currently observed sample. Additional effort is needed to improve the size of the sample of known PCEBs, as well as to fully model its selection effects, but with ~ 1600 SDSS WDMS binaries to draw from (see Chapter 9), the outlook for more quantitative tests of CE evolution seems promising.

Chapter 9

A catalogue of WDMS binaries from SDSS

9.1 Introduction

The theoretical understanding of both CE evolution and MB is currently very poorly constrained by observations (Chapter 1), and progress on this front is most likely to arise from the analysis of a large sample of PCEBs that are well-understood in terms of their stellar components. WDMS binaries appear most promising in that respect, as their stellar components are relatively simple, and the SDSS (Chapter 6) offers the possibility to dramatically increase the number of WDMS binaries available for detailed follow-up studies (Chapter 8).

Here I make use of the SDSS spectroscopic DR 6 data base to create a catalogue of 1591 WDMS binaries and candidates that were serendipitously observed. The structure of the Chapter is as follows. In Sect. 9.2 I present our method of identifying WDMS binaries. In Sect. 9.3 I estimate the completeness of the sample, and in Sec. 9.4 I provide our final catalogue. Using the spectral decomposition/model atmosphere developed in Chapter 7, I derive white dwarf effective temperatures, surface gravities, masses, and companion star spectral types and distances in Sect. 9.5. I also measure the Na I $\lambda\lambda$ 8183.27,8194.81 absorption doublet and/or the Hα emission RVs for 1062 objects. Finally in Sect. 9.6 I discuss our results, and conclude the Chapter in Sect. 9.7.

9.2 Identifying WDMS binaries in SDSS

9.2.1 Computational method

We have developed a procedure based on χ^2 template fitting in order to automatically identify WDMS binary candidates from the SDSS DR6 spectroscopic data base [Adelman-McCarthy et al., 2008]. Our initial template set consisted of several dozen SDSS spectra of confirmed WDMS binaries from Eisenstein et al. [2006] and Silvestri et al. [2007]. These spectra were chosen to sample a wide variety of white dwarfs and companion stars, and to be of high S/N. A set of representative templates is shown in Fig. 9.1. In addition, we compiled a set of 17 single DA white dwarf template spectra from Eisenstein et al.'s (2006) list, covering the entire observed range of $T_{\rm eff}$ and $\log g$, as well as the M0-M9 Bochanski et al. [2007] M-dwarf templates.

Each of these WDMS binary, white dwarf, and M-dwarf templates were then fitted to the full 1.27 million spectra in DR6. In this process, the template spectrum was normalised to the SDSS spectrum under scrutiny, and a reduced χ^2 was calculated using the errors of the two spectra added in quadrature. In practice, our fitting procedure produced for each of the WDMS binary, white dwarf, and M-dwarf templates a list of spectrum identifier (MJD-PLT-FIB), S/N of the spectrum, and χ^2 for all SDSS DR6 spectra. For each of the templates, we plotted χ^2 as a function of S/N (see Fig 9.2), and defined a minimum value of S/N, $\mathrm{S/N_{min}}$, and a linear relation $\chi^2_{\rm max} = a \times \mathrm{S/N}$. We considered any spectrum with

$$\chi^2_{\rm spec} < \chi^2_{\rm max} \;\text{ and }\; \mathrm{S/N_{spec}} > \mathrm{S/N_{min}} \tag{9.1}$$

as a WDMS binary, white dwarf, or M-dwarf (depending on the current template). $\mathrm{S/N_{min}}$ had to be set to avoid being swamped by spectra that are too noisy for any definite identification, and the S/N-dependent form of $\chi^2_{\rm max}$ accounts for the increase of χ^2 for higher values of S/N. Both constraints were defined individually for each of the templates, as the different spectral shapes resulted in a large spread of χ^2 distributions. The (χ^2, S/N) planes obtained from fitting the spectra of a single spectral plate (640 spectra) is shown for two different WDMS binary templates in Fig. 9.2.

After a first run through the DR6 spectra, we complemented the template set with the spectra of a number of newly identified WDMS binaries, and re-run the fitting for those

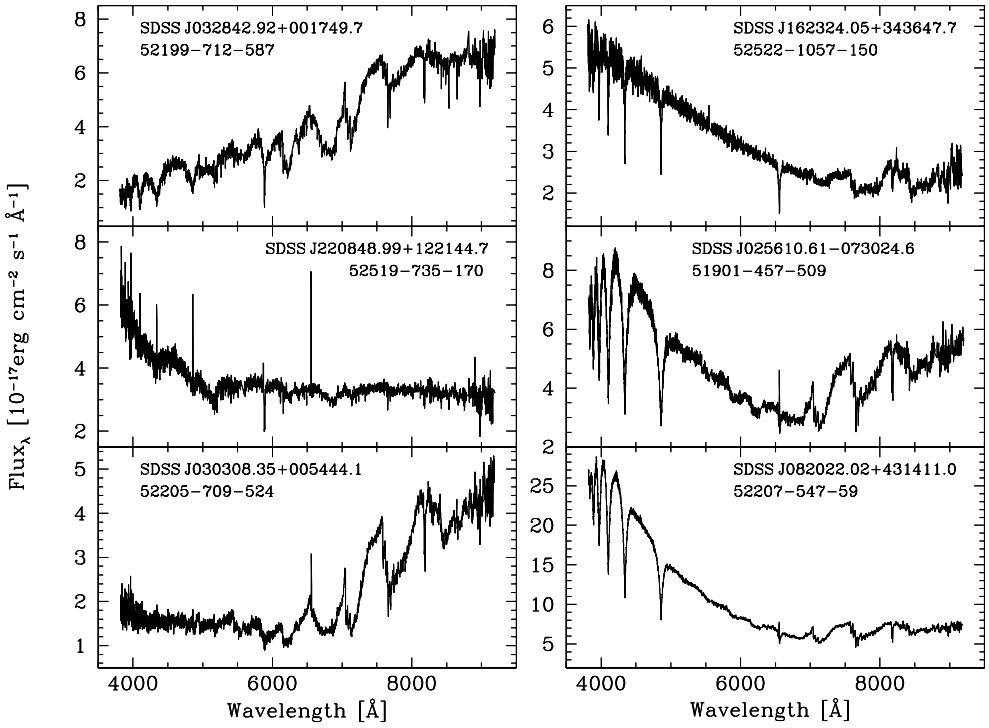

Figure 9.1: Six examples of previously known WDMS binaries used in this Chapter as WDMS binary templates. SDSS names and MJD-PLT-FIB identifiers are indicated for each of them.

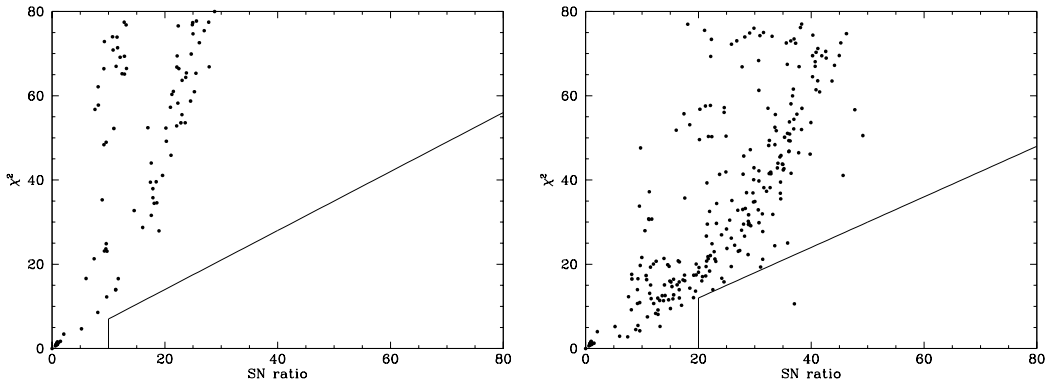

Figure 9.2: $\chi^2 - \mathrm{S/N}$ plane obtained fitting two of our WDMS binary templates (SDSS J103121.97+202315.1, left and SDSS J204431.44-061440.2, right) to the 640 objects contained in the SDSS spectral plate PLT = 2295. Objects falling in the area defined by $\chi^2_{\mathrm{spec}} < a \times \mathrm{S/N}$ and $\mathrm{S/N_{spec}} > \mathrm{S/N_{min}}$ were considered WDMS binary candidates. Left panel: $\mathrm{S/N_{min}} = 10$ and $\chi^2_{\mathrm{max}} = 0.7 \times \mathrm{S/N}$, no WDMS binary candidate is identified. Right panel: $\mathrm{S/N_{min}} = 20$ and $\chi^2_{\mathrm{max}} = 0.6 \times \mathrm{S/N}$, one WDMS binary candidate is found.

new templates again. That process was repeated until no new WDMS binary candidates were found – at which point we had used a total of 163 different WDMS binary template spectra.

Even though the above method efficiently identifies WDMS binary candidates among the spectra in DR6, the choice of χ^2_{max} and $\mathrm{S/N_{min}}$ alone does not avoid completely the filtering of other astronomical objects, such as quasars, MS stars, and galaxies. In addition, for templates that are dominated by the white dwarf (M-dwarf), the list of candidates will unavoidably contain a substantial number of single white dwarfs (M-dwarfs). Hence we first visually inspected all WDMS binary candidates, as well as the white dwarf and M-type star subsamples (a total of ~ 70000 spectra), and removed those objects that were not of our interest, i.e. neither WDMS binary, white dwarf, or M-dwarf candidates. The final result of the template fitting were a list of 1484 WDMS binary candidates, 8368 single white dwarf candidates, and 15379 single M-dwarf candidates.

9.2.2 Red and blue excess in SDSS spectra: help from GALEX and UKIDSS

While the template fitting proved to be a robust method to find WDMS binaries in which both stellar components contribute clearly visible amounts of flux, the procedure is prone

to mis-classify white-dwarf dominated WDMS binaries as single white dwarfs, and M-dwarf dominated WDMS binaries as single M-dwarfs. We therefore decided to probe more specifically for the presence of excess flux at the red (blue) end of the SDSS spectra in objects classified initially as single white dwarfs (M-dwarfs).

For the search of red flux excess in single white dwarf candidates, we fitted synthetic white dwarf spectra computed with the code described by Koester et al. [2005] to the SDSS spectra, and then calculated the reduced χ^2 over the wavelength ranges $4000-7000$ Å ($\chi^2_{\rm b}$) and $7000-9000$ Å ($\chi^2_{\rm r}$). Objects with $\chi^2_{\rm r}/\chi^2_{\rm b} > 1.5$ were "promoted" from single white dwarf candidates to WDMS binary candidates.

The search for blue flux excess proceeded in an analogous fashion for the single M-dwarf candidates, only that we used the set of high S/N M-dwarf templates from Chapter 7 instead of model spectra, and calculated the reduced χ^2 over the wavelength ranges $4000-5000$ Å and $7000-9000$ Å. Objects with $\chi^2_{\rm b}/\chi^2_{\rm r} > 1.5$ were "promoted" from single M-dwarf candidates to WDMS binary candidates.

On the left and right top panels of Fig. 9.3 we show the SDSS spectra (black line) and SDSS magnitudes (red dots) of SDSSJ 132925.21+ 123025.5 and SDSSJ 131928.80+ 580634.2, along with the best-fit white dwarf model and M-dwarf template (red lines, middle panels). The two objects were initially classified by our template fitting procedure as single white dwarf and single M star candidates, respectively, but "promoted" to WDMS binary candidates by the flux excess measurement as described above. The flux excess is more obvious when plotting F_ν (middle left panel) instead of F_λ (top left panel). However, in several cases, the detection of blue or red flux excess is rather marginal.

As a final step in our search for WDMS binaries, we have cross-correlated our entire list of above identified WDMS binary candidates with the GALEX [Galaxy Evolution Explorer, Martin et al., 2005; Morrissey et al., 2005] data release 4, providing near- and far-ultraviolet magnitudes, and with the data release 4 of UKIDSS [UKIRT Infrared Sky Survey, Dye et al., 2006; Hewett et al., 2006; Lawrence et al., 2007], providing infrared y,J,H,K magnitudes. We then inspected the observed ultraviolet-optical spectral energy distribution of all secondary star dominated WDMS binary candidates with available GALEX magnitudes, and the optical-infrared spectral energy distribution of all white

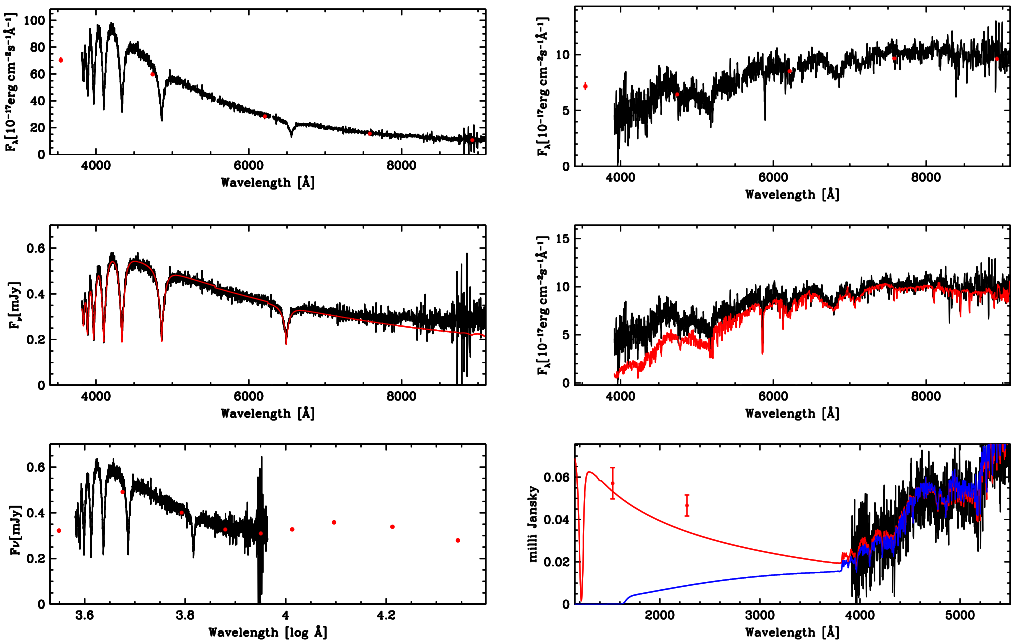

Figure 9.3: Top left: SDSS spectrum of SDSSJ 132925.21+123025.5, a WDMS candidate initially catalogued as single DA white dwarf. The red dots represent the SDSS magnitudes. Middle left panel: the best white dwarf model fit is superimposed in red, unambiguously identifying the red excess of the binary. Bottom left panel: SDSS and UKIDSS magnitudes superimposed to the SDSS spectrum. Again, the UKIDSS magnitudes clearly show the presence of a low mass companion. Top right panel: the same for SDSSJ 131928.80+580634.2, an initially catalogued early M-type star. Middle and bottom panels: the best M-type fit and the near- and far-ultraviolet GALEX magnitudes clearly confirm the presence of a white dwarf primary, respectively. The red and blue straight lines represent the white dwarf solutions (red for the hot, blue for the cold) obtained from decomposing/fitting the spectrum (see Sect 9.5).

dwarf dominated WDMS binary candidates with available UKIDSS magnitudes. Objects where a clear ultraviolet or infrared excess was detected were then included in our WDMS binary sample.

For SDSSJ 132925.21+123025.5, the UKIDSS magnitudes unambiguously confirm the existence of a low-mass companion (bottom left panel of Fig. 9.3). Similarly, the GALEX near- and far-ultraviolet magnitudes clearly confirm the presence of a white dwarf companion in SDSSJ 131928.80+580634.2 (bottom right panel of Fig. 9.3).

9.2.3 SDSS images

As a final check on the nature of the WDMS binary candidates, we inspected their SDSS DR6 images for morphological problems, and found primarily two types of issues.

Occasionally, single white dwarfs (M-dwarfs) may be located close to very bright M-dwarfs (white dwarfs or A-stars), which will cause scattered light to enter the spectroscopic fibre, and result in an (apparent) two-component spectrum. A spectacular example is SDSSJ 073531.86+315015.2 (left panels of Fig. 9.4), where the SDSS spectrum clearly exhibits an M-dwarf at red wavelengths, and a blue component with strong Balmer lines in the blue – the SDSS image reveals that this is a single M-dwarf at a distance of 12 arcmin of Castor A/B – two $V = 2-3$ A-stars. The SDSS magnitudes (red dots) are superimposed to the SDSS spectrum (black) and are consistent with those of a single red star. In addition, single M-dwarfs are also likely to be found superimposed with single early-type stars in the same image. An example is SDSSJ 162517.58+140134.6 (see middle top panel of Fig. 9.4). At first glance one could be tempted to consider a resolved WDMS binary pair. Nevertheless, the SDSS spectrum (middle bottom panel of the same figure) shows the typical Balmer lines of an A star in the blue, while at redder wavelengths the typical spectral features of a low-mass star can be detected. This implies that these two systems are superimposed stars in the same image rather than being a resolved WDMS binary pair (see below).

SDSS images can also help identifying WDMS binaries among our sample that are spatially-resolved in the SDSS images, but close enough that flux from both stars will enter into the spectroscopic fibre. In such cases, the SDSS magnitudes are often discrepant with the flux-calibrated SDSS spectrum, and/or have large errors as consequence from the

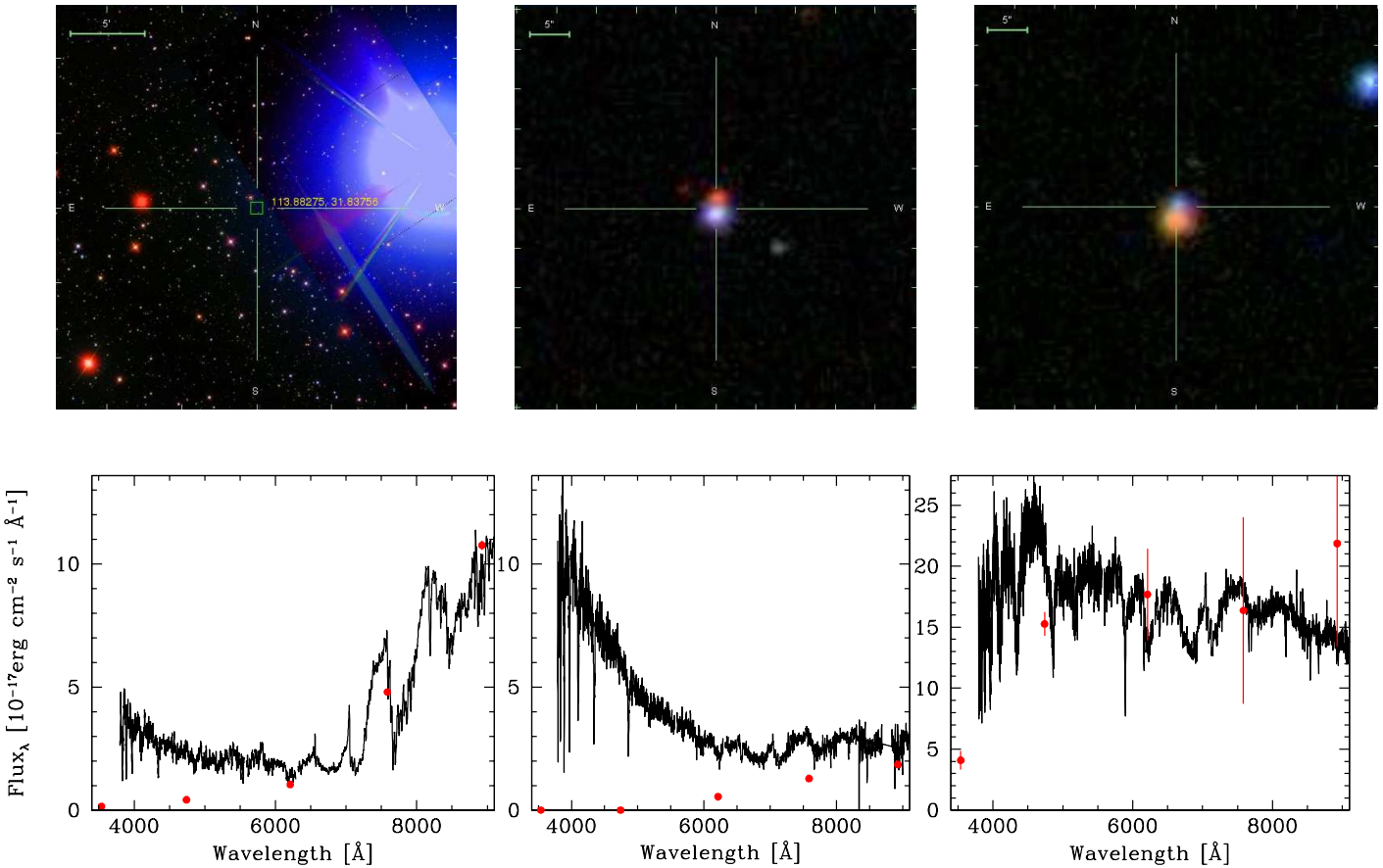

Figure 9.4: Top left panel: SDSS image of SDSSJ 073531.86+315015.2 (5 arcmin scale), a single red star initially considered as a WDMS binary candidate. Bottom left panel: SDSS magnitudes (red dots) and spectrum (black line) of the same system. The light from the saturated bright star (Castor A/B) is also dispersed in the spectrum. The magnitudes are consistent with a single red star. Top middle panel: SDSS image of SDSSJ 162517.58+140134.6 (5 arcsec scale). The image suggests a resolved WDMS binary pair. Middle bottom panel: the detection of the Balmer lines typical of an A star in the blue, together with the typical spectral features of a low-mass MS star in the red (black solid line), indicate that these are two single stars superimposed in the same image rather than a resolved WDMS binary pair. SDSS magnitudes are indicated with red dots, and are consistent with those of a low-mass star. Top right panel: SDSS image of SDSSJ 025306.37+001329.2 (5 arcsec scale), a resolved WDMS binary in our sample. Bottom right panel: SDSS magnitudes (red dots) and spectrum (black line) of the same system. Whilst the SDSS spectrum clearly shows both components, the SDSS magnitude errors are untypically large (see text for details).

deblending applied by the photometric pipeline. Figure. 9.4 (top right panel) shows the SDSS image of SDSSJ 025306.37+001329.2, which clearly reveals a spatially-resolved pair of red and blue stars. The SDSS spectrum of SDSSJ 025306.37+001329.2 contains the typical signatures of a WDMS binary, i.e. broad Balmer lines from the white dwarf and TiO absorption bands from the M-dwarf, however, the errors on the SDSS magnitudes are untypically large, and do not match well the flux calibrated SDSS spectrum.

9.2.4 Cross-checks with previous WDMS binary catalogues

A total number of 1484 WDMS binary candidates were identified in Sect. 9.2.1. From the analysis carried out in Sec. 9.2.2 and Sec. 9.2.3 we have increased the number of systems to 1552 WDMS candidates among the spectroscopic SDSS DR6 data base[1]. In order to evaluate the effectiveness of our procedure we compared our results to those presented in four previously published lists of WDMS binaries from SDSS, namely van den Besselaar et al. [2005], Eisenstein et al. [2006], Silvestri et al. [2007] (which includes Raymond et al. [2003] as a subset), and Augusteijn et al. [2008].

A comparison to the 13 WDMS binaries containing DB white dwarfs and the 2 WDMS binaries containing DC white dwarfs presented in van den Besselaar et al. [2005] revealed that our routine has successfully identified all these systems.

The WDMS binary sample presented in Eisenstein et al. [2006] overlaps almost completely with the WDMS binary catalogue provided in Silvestri et al. [2007] (see below), except for only ten objects. A comparison between the WDMS binary sample presented in this Chapter and these ten systems showed that we have successfully identified these objects.

We inspected the catalogue of Silvestri et al. [2007], and found that 995 systems are in common between the two works. We carefully inspected the remaining 230 systems from Silvestri et al. [2007][2] and concluded that 208 of them, i.e. $\sim$17% of the total systems, were inconsistent with the acclaimed WDMS binary nature, either because of their

[1] 94 and 89 WDMS binary candidates were identified to show blue and red excess respectively in their spectra. 115 WDMS binary candidates were removed after inspecting their SDSS images.

[2] Silvestri et al. [2007] claim that their catalogue contains 1253 objects. Note though that only 1228 spectra (i.e. 1225 objects) are listed in their electronic edition of the paper.

spectra, or because of their morphology in the SDSS images. Two examples are SDSSJ 032428.78-004613.8 (QSO) and SDSSJ J114334.70+455134.2 (galaxy). 22 objects were WDMS binaries in which one of the two components dominates the spectrum, and that were missed by our search algorithm. Those 22 WDMS binaries were consequently added to our sample.

Recently Augusteijn et al. [2008] provided a sample of 651 WDMS binary candidates obtained from combined colour and proper motion selection criteria in SDSS, of which they inspected 95 spectra from DR5. We cross-correlated their full list of 651 objects against the DR6 spectroscopic data base, and found spectra for 130 of them (176 SDSS spectra). We compared this sample with our systems and found that all but 20 objects in Augusteijn et al. [2008] were in our list. Four of them were WDMS binaries containing cold white dwarfs, and were consequently missed by our procedure. These four systems were added to our sample. The remaining 16 systems were nine QSOs, three CVs, one F star, one M-dwarf, one DA white dwarf, and one DC white dwarf [Augusteijn et al., 2008].

In summary, the comparison with previous works shows that our WDMS binary selection method is robust and efficient in recovering WDMS binaries identified both from their spectra [Silvestri et al., 2007], as well as from their photometric/astrometric properties [Augusteijn et al., 2008].

9.3 Completeness of the sample

In this section, we will briefly investigate both the intrinsic completeness of our catalogue (i.e. what fraction of the WDMS binaries that are contained in the DR6 spectroscopic data base were found by our algorithm), as well as the extrinsic completeness (i.e. what fraction of WDMS binaries were spectroscopically observed by SDSS).

Figure. 9.5 shows the distribution of our WDMS binaries (excluding the systems classified only as WDMS binary candidates) as black dots in the $(u-g, g-r)$, $(g-r, r-i)$, and $(r-i, i-z)$ colour-colour planes. Stellar sources are shown as gray dots, and QSOs in light gray. Highlighted in light blue are the white dwarf, A-star and WDMS binary exclusion regions that were defined by Richards et al. [2002] for the QSO fibre allocation

algorithm with the aim to maximise the return of the QSO survey within SDSS. For the analysis below, we adopted the WDMS binary exclusion region of Richards et al. [2002] in the $(g-r, r-i)$ and $(r-i, i-z)$ planes. In addition, we defined two small rectangular boxes in the $(g-r, r-i)$ plane, one in the A-star exclusion region (Box 1, $-0.5 < g-r < -0.2$, $0 < r-i < 0.2$), and one located in between the A-star exclusion region and the WDMS binary exclusion region (Box 2, $-0.3 < g-r < 0.1$, $0.3 < r-i < 0.5$). We then visually classified all SDSS point-source spectra of objects with $g \leq 20$ with colours in the WDMS binary exclusion region, Box 1, and Box 2. We also used the casjobs interface to the SDSS data base to determine the number of photometric SDSS point sources with $g \leq 20$ located within each of these boxes, as well as the fraction of those point sources that have SDSS spectra.

The Richards et al. [2002] WDMS binary exclusion box. We found 7099 SDSS point sources objects inside this area, of which 572 with available SDSS spectra. Of those 572, we identified 386 as WDMS binaries. The large number of WDMS binaries is not surprising since this area was defined by Richards et al. [2002] as a colour cut for this kind of system. The population of the remaining objects was dominated by single M stars. We also detected four CVs and eight QSOs. Cross-checking the 386 WDMS binaries found here against the list of systems identified in Sect. 9.2 showed that only nine WDMS binaries were missed by our template matching algorithm. Among these nine objects, one contains a DA white dwarf, one a DC white dwarf, the rest contain cool (probably DC) white dwarfs, and in all cases the spectra are dominated by the emission of their companion stars. Being close to the MS locus in colour space, these systems are a challenge for every WDMS binary selection, including our method.

Analysis in box 1. 708 SDSS point sources were found inside this area, 247 of them with available spectra. Among these 247 objects, 67 were WDMS binaries, the rest of them mainly QSOs, with a few single white dwarfs, early-type MS stars, and two CVs. All 67 WDMS binaries found in this box were already identified by our search algorithm (Sect. 9.2).

Analysis in box 2. This area contained 6689 SDSS point sources. SDSS spectroscopy is available for 2280 of them, of which 135 are WDMS binaries. As expected from the stud-

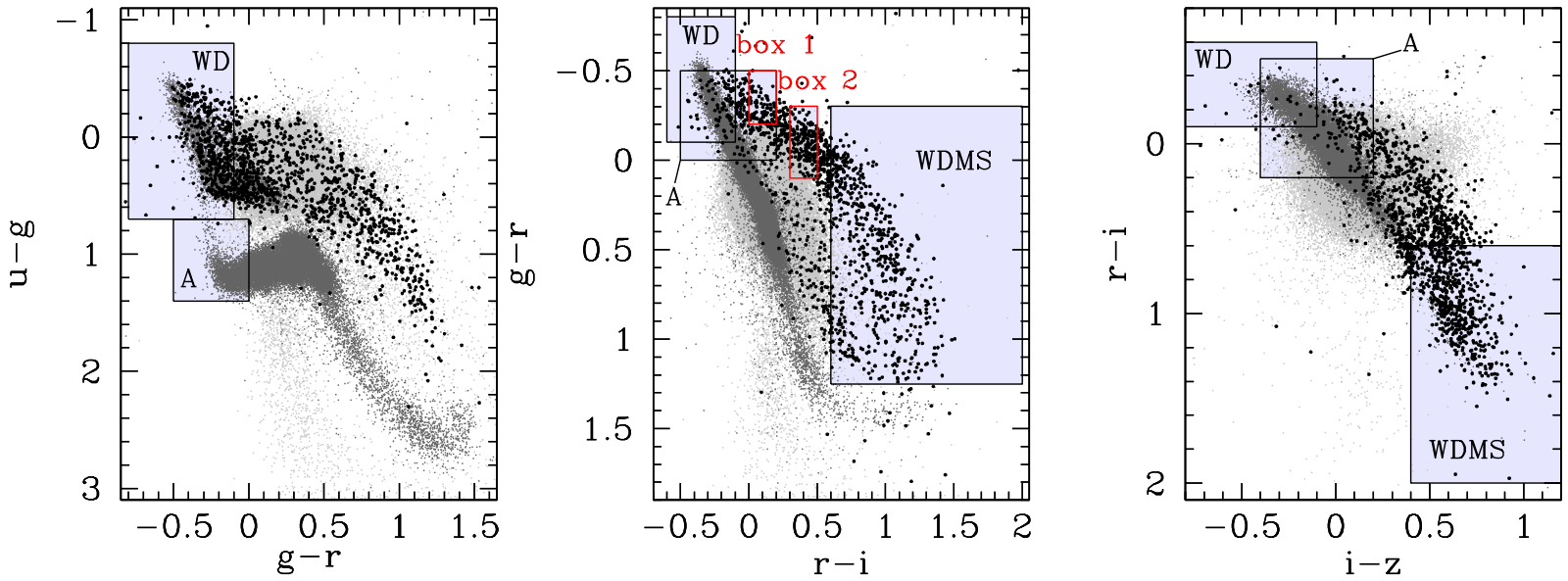

Figure 9.5: From left to right the $(u-g,g-r)$, $(g-r,r-i)$ and $(r-i,i-z)$ colour diagrams for the WDMS binaries in our sample (black; excluded are the WDMS binary candidates), stellar sources (dark ray), and QSOs (light gray). Blue boxes represent the loci of single white dwarfs, single A main sequence stars and WDMS binaries according to Richards et al. [2002]. The regions within the two red boxes in the $(g-r,r-i)$ plane, and the WDMS binary exclusion region of Richards et al. [2002] in the $(g-r,r-i)$ and $(r-i,i-z)$ planes are used to estimate the completeness of our WDMS binary sample (see Sect. 9.3).

ied colour space area, the vast majority of the remaining objects were again QSOs, with the exception of a few single MS stars, and one CV. Only four of the WDMS binaries identified here were not included in our catalogue: SDSS J110539.77+250628.6, which is in fact the semi-detached magnetic cataclysmic variable ST LMi observed during a deep low state; SDSS J124959.76+035726.6, a typical WDMS binary previously listed as a cataclysmic variable candidate by Szkody et al. [2004]; SDSS J150954.40+243449.3, which has a broken SDSS spectrum; and SDSS J204218.52-065638.4, a spatially-resolved MS dominated WDMS binary.

The WDMS binaries found in the above exercise were added to our sample.

From the above study two main conclusions arise. Firstly, as expected, the spectroscopic completeness in SDSS is dramatically larger in QSO dominated colour space areas, 27%, 34% in Box 1 and Box 2, respectively, compared to only 8% in the WDMS binary exclusion box of Richards et al. [2002]. The low completeness in the WDMS binary exclusion box, coupled with the high fraction of WDMS binaries among all objects in this region in colour space (67.5%), implies that the number of SDSS WDMS binaries could be *dramatically* increased to ~ 4800 binaries by additional identification spectroscopy within this region in colour-colour space. Secondly, only 13 new WDMS binaries have been identified, four in Box 2 and nine in the WDMS binary exclusion box, which implies a completeness of our search algorithm of 100% in Box 1, 97% in Box 2, and 97.5% in the WDMS binary exclusion region, and we conclude that we have identified $\gtrsim 98\%$ of the WDMS binaries contained in the SDSS DR6 spectroscopic data base.

9.4 The final catalogue

From the analysis provided in Sec. 9.2 and Sec. 9.3 a total number of 1591 WDMS binaries have been identified. We refer to this list as our catalogue of WDMS binaries and candidates. The 1591 WDMS binaries are listed in Table 9.1, together with their coordinates and GALEX DR4, SDSS DR6 and UKIDSS DR4 magnitudes[3]. GALEX and UKIDSS magnitudes are available for a total number of 1320 and 465 WDMS binaries respectively.

[3]On occasions multiple SDSS and GALEX magnitudes are available for the same system. In these cases we have averaged the magnitudes and obtained a single value for each magnitude.

Table 9.1: The complete catalogue. Coordinates, near- and far-ultraviolet, *ugriz* and *yJHK* GALEX, SDSS and UKIDSS magnitudes for the 1591 WDMS binaries and candidates are also included. Due to the large number of systems and due to space limitation of this thesis, the entire table (including also the photometric errors) is not presented here, and will be provided in the forthcoming submission of the paper. We use "-" to indicate that no magnitude is available.

SDSS J	ra[°]	dec[°]	*nuv*	*fuv*	*u*	*g*	*r*	*i*	*z*	*y*	*J*	*H*	*K*
000152.09+000644.7	0.467040	0.112420	18.45	17.90	19.03	18.61	17.94	17.50	17.25	16.51	16.05	15.40	15.28
000442.00–002011.6	1.175000	-0.336560	-	-	23.72	20.38	19.13	18.65	18.28	-	-	-	-
000611.94+003446.5	1.549750	0.579580	21.78	-	21.38	20.92	20.12	19.00	18.38	17.53	17.05	16.58	16.20
001029.87+003126.2	2.624460	0.523940	20.17	19.96	21.92	20.85	19.97	19.00	18.42	17.65	17.14	16.52	16.36
001247.18+001048.7	3.196580	0.180190	20.50	20.71	20.73	20.21	19.66	18.63	17.96	17.09	16.60	16.13	-
001339.20+001924.3	3.413330	0.323420	16.41	19.73	15.94	15.56	15.55	15.63	15.89	-	-	-	-
001359.39–110838.6	3.497493	-11.144057	17.77	17.42	18.30	18.43	18.31	20.75	22.82	-	-	-	-
001549.02+010937.3	3.954250	1.160360	20.97	20.68	21.23	20.86	20.60	19.85	19.27	18.46	17.86	17.45	17.12
001726.63–002451.1	4.360960	-0.414190	19.71	20.30	19.67	19.28	19.02	18.18	17.54	16.60	16.07	15.56	-
001733.59+004030.4	4.389960	0.675110	20.83	22.43	22.09	20.79	19.58	18.17	17.38	16.37	15.84	15.27	14.97
001749.24–000955.3	4.455170	-0.165360	15.87	15.40	16.56	16.86	17.03	16.78	16.47	15.75	15.33	14.76	14.56
001853.79+005021.5	4.724120	0.839310	20.46	20.27	21.00	20.38	19.64	18.80	18.35	17.52	17.09	16.51	16.27
001855.19+002134.5	4.729960	0.359580	22.42	22.12	21.60	20.60	19.87	18.97	18.38	17.54	17.09	-	-
002143.78–001507.9	5.432420	-0.252190	22.20	-	22.58	19.63	18.39	17.02	16.30	15.40	14.87	14.31	14.05
...	...	...	...	...	...	...	...	...	...	...	...	...	...

Table 9.2: The catalogue divided into the different WDMS-type classes defined in Sec. 9.4.

type	number	type	number
DA/M	1172	DA/M:	43
DB/M	45	DB/M:	1
DC/M	34	DA:/K	5
DA/K	48	DA/K:	8
DB/K	3	Mag/M	1
WD/M	133	(WD/M)	32
WD/K	26	(WD/K)	2
WD/M:	1	(DA/M)	4
DA:/M	27	(DC/M)	1
DB:/M	1	(DA/K)	1
DC:/M	3		

In Table 9.2 we divide the classification of our systems according to their binary components. For the white dwarfs we use the flags DA, DB, DC, WD when the white dwarf type is unknown, and Mag when the white dwarf is magnetic. For the secondary stars we use the flags M or K to refer to M-dwarf and K-dwarf companions respectively. In cases where the S/N of the spectra are relatively low it might become difficult to distinguish between the different types of white dwarfs and/or low-mass star companions outlined above. In these cases we quote the flag followed by a colon. Finally, we represent in brackets our WDMS binary candidates. On the one hand we consider WDMS candidates those systems which are faint and are associated to very low S/N in their SDSS spectra. On the other hand, in some cases the detection of blue or red excess in Sect. 9.2.2 is rather marginal, and no GALEX (UKIDSS) magnitudes are available to confirm the existence of a white dwarf (low-mass star). As we are not entirely sure of the existence of the two binary components in these cases, however the χ^2 analysis (Sec. 9.2.2) is in favour of this hypothesis and the SDSS images (Sec. 9.2.3) do not show any particular morphological problems, we consider these systems as WDMS binary candidates.

9.5 Stellar parameters, Distances and Radial Velocities

In Chapter 7 we developed a spectral decomposing/fitting technique for the analysis of WDMS binaries with SDSS spectroscopy. This procedure is also used in this Chapter to

determine the stellar parameters of the systems in our catalogue. However two new modifications are included.

On the one hand we have additionally used as DB templates a compiled library of 222 high S/N DB white dwarfs from SDSS DR 4 covering the entire observed range of $T_{\rm eff}$, and have consequently estimated effective temperatures for the DB white dwarfs in our catalogue. In this case, the fitting procedure follows just one step, in which the WDMS binary spectrum is decomposed and fitted in a same fashion as in Chapter 7, but using the above DB templates instead of DA templates. The estimated effective temperature and the associated error of the white dwarf component correspond then to those of the best fit DB template. The temperatures of the DB templates are taken from Eisenstein et al. [2006]'s table.

On the other hand we have used the near- and far-ultraviolet GALEX magnitudes, when available, to constrain the effective temperatures of our DA white dwarfs. A clear example of this is SDSSJ 082609.72+194126.3. In Fig. 9.6 we show the spectral decomposition of this system into its white dwarf and MS components, in Fig. 9.7 the white dwarf model fit to its white dwarf residual spectrum. This is a clear example where the fit to the whole spectrum falls exactly on the line of maximum equivalent width (Eq. 7.1), and consequently the solution given by the line profile fit is not well constrained. In the top panel of Fig. 9.8 we superimpose the cold (blue) and hot (red) white dwarf solutions from the fitting routine, as well as the best white dwarf models and M star template fits (black) to the spectrum of SDSSJ 082609.72+194126.3 (gray). In the bottom panel of the same figure the GALEX magnitudes (red dots), clearly constrain the white dwarf solution (the cold in this case) and solve the ambiguity found in our fitting procedure for this system.

Distances to the WDMS binaries were also estimated here from the best-fit flux scaling factors of the two spectral components, the white dwarf and the MS, respectively providing two independent estimates of the distances for each system (see Chapter 7 for details). The stellar parameters and distances of the 1591 WDMS binaries in our catalogue are presented in Table 9.3.

We have also measured the RVs of 1062 systems with clearly pronounced Hα emission and/or Na I $\lambda\lambda$ 8183.27,8194.81 absorption doublet in their SDSS spectra. For this, we

Table 9.3: White dwarf masses, effective temperatures, surface gravities, spectral types and distances of the 1591 WDMS binaries in our catalogue, as determined from spectral modelling. Due to space limitations the stellar parameters for the remaining WDMS binaries, as well as notes for individual systems will be provided in the forthcoming submission of the paper. We use the flags *e*, *s* and *a*, and "re" for those systems which have been studied previously by Eisenstein et al. [2006], Silvestri et al. [2007] and Augusteijn et al. [2008], and which are resolved WDMS binary pairs, respectively. Again, we indicate that no stellar parameters are measured with "-".

SDSS J	type	MJD	PLT	FIB	$T_{\rm eff}$[k]	err	log g	err	$M_{\rm wd}[M_{\odot}]$	err	$d_{\rm wd}$[pc]	err	Sp	$d_{\rm sec}$[pc]	err	flag
...	...	...	...	...	...	...	...	...	...	...	...	...	...	...	...	...
001359.39–110838.6	DA/M	52138	652	203	17707	1294	7.83	0.29	0.53	0.16	349	61	-	354	48	re
001359.39–110838.6	DA/M	52138	652	203	11302	596	8.67	0.27	1.02	0.15	114	24	-	354	48	re
001549.02+010937.3	DA/M	52518	687	455	-	-	-	-	-	-	-	-	3	1590	313	s/e
001549.02+010937.3	DA/M	52518	687	455	-	-	-	-	-	-	-	-	3	1590	313	s/e
001726.63–002451.1	DA/M	52559	1118	280	12828	2911	7.95	0.53	0.58	0.33	371	116	4	477	141	s/e
001726.63–002451.1	DA/M	52559	1118	280	15246	1139	7.76	0.26	0.48	0.14	486	76	4	477	141	s/e
001726.63–002451.2	DA/M	52518	687	153	13588	2300	8.11	0.43	0.68	0.27	374	104	4	503	148	s/e
001726.63–002451.2	DA/M	52518	687	153	15246	1585	8.02	0.30	0.63	0.19	427	83	4	503	148	s/e
001733.59+004030.4	DA/M	51795	389	614	10793	2980	7.26	1.12	0.29	0.56	673	356	4	469	138	s/re
001733.59+004030.4	DA/M	51795	389	614	13432	3261	6.96	1.24	0.23	0.51	1013	580	4	469	138	s
001749.24–000955.3	DA/M	52518	687	109	60000	3121	7.42	0.17	0.50	0.05	748	105	2	624	149	a/s/e
001749.24–000955.3	DA/M	52518	687	109	6969	223	9.50	0.29	1.46	0.11	9	7	2	624	149	a/s/e
001749.24–000955.3	DA/M	51795	389	112	65789	4192	8.12	0.18	0.78	0.10	419	59	2	570	136	a/s/e
001749.24–000955.3	DA/M	51795	389	112	6000	56	9.50	0.06	1.46	-	6	1	2	570	136	a/s/e
...	...	...	...	...	...	...	...	...	...	...	...	...	...	...	...	...

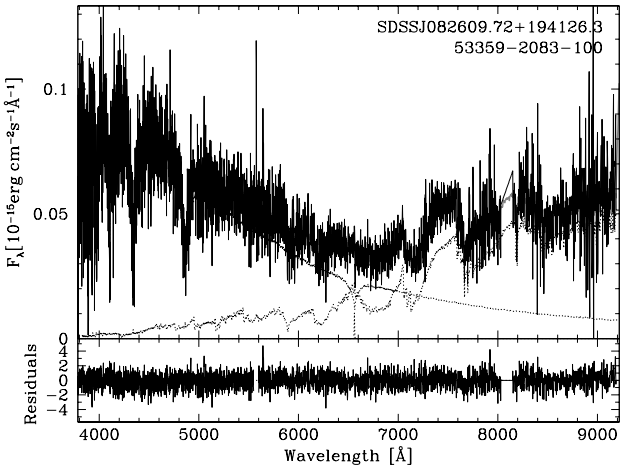

Figure 9.6: Two-component fits to SDSSJ 082609.72+194126.3, a WDMS binary in our sample. The top panel shows the WDMS binary spectrum as black line, and the two templates, white dwarf and M-dwarf, as dotted lines. The bottom panel shows the residuals from the fit. The SDSS spectrum identifiers MJD, PLT and FIB are given in the plots below the object names.

have followed the method described in Chapter 8 for the Na I doublet, and in Chapter 7 for Hα. The results are provided in Table 9.4.

9.6 Discussion

9.6.1 Identification of four new PCEB candidates

The detection of RV variations identifies the object as a close WDMS binary, or PCEB candidate (Chapter 7). In Figures 9.9 and 9.10 we show the Na I doublet and Hα emission RV variations measured in Sect. 9.5 for nine and 16 systems, respectively displaying more than 3σ RV variations. A comparison with Figures 7.2 and 7.3 in Chapter 7 drives the attention to two different issues.

On the one hand, four Na I doublet close binary candidates identified in Chapter 7 do not show more than 3σ RV variation in this Chapter: SDSS J113800.35-001144.5, SDSS J115156.94-000725.5, SDSS J173727.27+540352.2, and SDSS J234534.50- 001453.7. We used here the method described in Chapter 8 to measure the Na I doublet RVs, and conse-

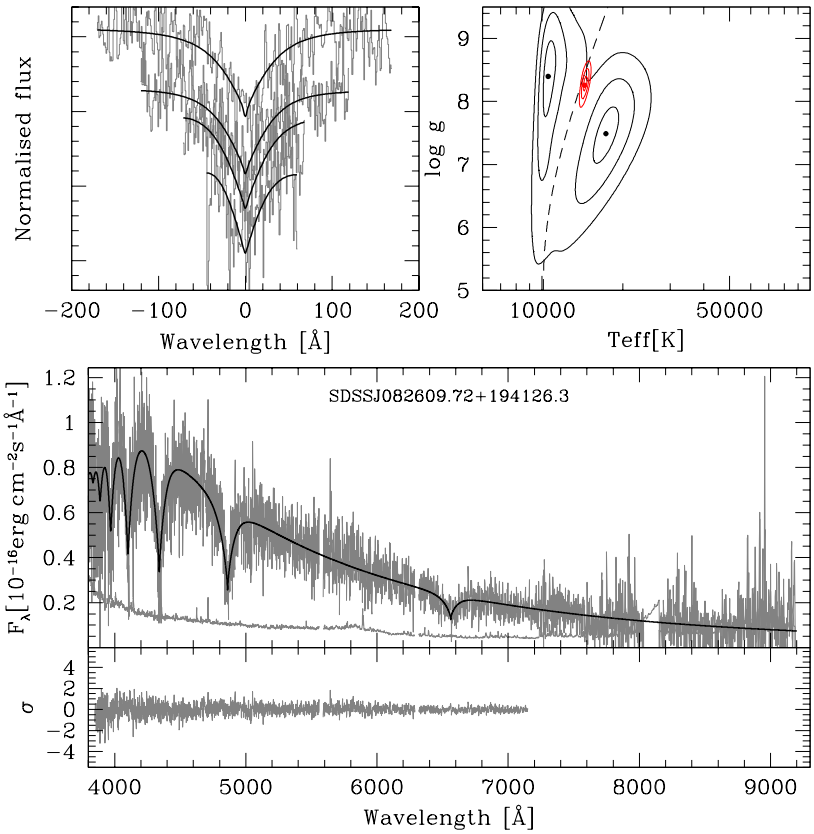

Figure 9.7: Spectral model fit to the white dwarf component of SDSSJ 082609.72+194126.3 obtained after subtracting the best-fit M-dwarf template. Top left panel: best-fit (black lines) to the normalised Hβ to Hε (gray lines, top to bottom) line profiles. Top right panels: 3, 5, and 10σ χ^2 contour plots in the $T_{\rm eff} - \log g$ plane. The black contours refer to the best line profile fit, the red contours to the fit of the whole spectrum. The dashed line indicates the occurrence of maximum Hβ equivalent width. The best "hot" and "cold" line profile solutions are indicated by black dots, the best fit to the whole spectrum is indicated by a red dot. Bottom panel: the residual white dwarf spectra resulting from the spectral decomposition and their flux errors (gray lines) along with the best-fit white dwarf model (black line) and the residuals of the fit (gray line, bottom).

Table 9.4: RVs measured from the Na I λλ 8183.27,8194.81 doublet and the Hα emission for the systems in our catalogue. Due to space limitations of this thesis the complete table will be included in the forthcoming submission of the paper. In the last column we quote with "y" and "n" those RV values obtained from spectra that have been, and have not been combined from different sub-spectra (see Chapter 6), respectively. We use "-" to indicate that no RV is available.

SDSS J	HJD 245	RV (Na) [km s^{-1}]	err	RV (Hα) [km s^{-1}]	err	sub.?
000152.09+000644.7	1791.8092	0.7	18.0	24.2	13.4	n
001247.18+001048.7	2519.8962	-	-	12.3	15.6	n
001247.18+001048.7	2518.9219	-14.3	28.4	30.6	10.3	n
001359.39–110838.6	2138.3933	28.9	16.9	-	-	y
001726.64–002451.2	2559.7852	-33.7	11.9	-30.1	5.5	n
001726.64–002451.2	2518.9219	-19.8	14.7	-26.5	6.2	n
001733.59+004030.4	1794.7737	-3.7	12.2	-	-	n
001749.25–000955.4	2518.9218	-18.3	14.2	-3.2	5.9	n
001749.25–000955.4	1794.7737	-36.6	11.8	-22.8	1.6	n
001855.20+002134.5	1816.8000	41.4	25.5	-	-	n
001855.20+002134.5	1893.0883	15.0	19.8	-	-	y
002143.78–001507.9	2581.7411	1.5	10.8	-	-	n
002143.78–001507.9	2581.7411	1.5	10.8	-	-	n
002157.91-110331.6	3318.6951	148.4	12.2	-9.1	8.8	y
...	...	...	...	...	...	...

Table 9.5: Upper limits to the orbital periods of the four PCEB candidates found in Sect. 9.6.1. White dwarf masses are taken from Table 9.3 except for SDSS J2346+4340, where we assume of mass of 0.5 $M_{\odot}$ (see Fig. 9.11). Secondary star masses are estimated from Table 7.2. K_{sec} values are obtained from Table 9.4, where we use the Na I RVs for SDSS J2346+4340.

SDSS J	074329.62 +283528.0	081942.67 +542608.1	231814.73 +003430.3	234638.76 +434041.7
P_{orb}[d]	121	19	5	2

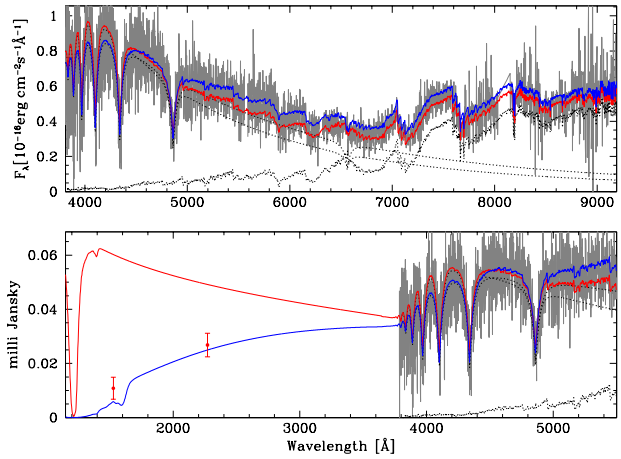

Figure 9.8: Top: in blue the cold white dwarf solution obtained in Fig. 9.7 plus the best-fit M-dwarf template obtained in Fig. 9.6; in red the same but for the hot solution; in gray the SDSS spectrum of SDSSJ 082609.72+194126.3; in black dotted line the best-fit M-dwarf template, and the white dwarf models that satisfy the cold and hot solutions in Fig. 9.7. Bottom: the same but including the near- and far-ultraviolet GALEX magnitudes of this object (red dots).

quently some RV offsets are expected when comparing the RV values to those measured in Chapter 7. As outlined in Chapter 8, the offsets can be sufficient to move a given system either way across our criterion to identify PCEB candidates. It is worth mentioning that SDSS J113800.35-001144.5 has been studied in detail in Chapter 8, and indeed no significant RV variation has been detected for this system. In addition SDSS J173727.27+540352.2 and SDSSJ 234534.50-001453.7 were flagged as PCEB candidates in Chapter 7 due to the very low S/N in their spectra.

On the other hand, we have identified four new systems which show more than 3σ RV variation: SDSS J0743+2835, SDSS J0819+5426, SDSS J2318+0034, and SDSS J2346+4340 (see complete coordinates in Table 9.5). SDSS J0743+2835 and SDSS J2318 +0034 display significant RV movement only in Hα. As discussed in Chapter 8 the Na I absorption lines from the secondary star are a more robust probe for RV variations, and we consequently consider that additional follow-up spectroscopy is necessary to confirm the post-CE nature of these two systems. 3σ Na I doublet RV variation is detected in both SDSS J0819+5426 and SDSS J2346+4340, which also displays RV movement in Hα, and

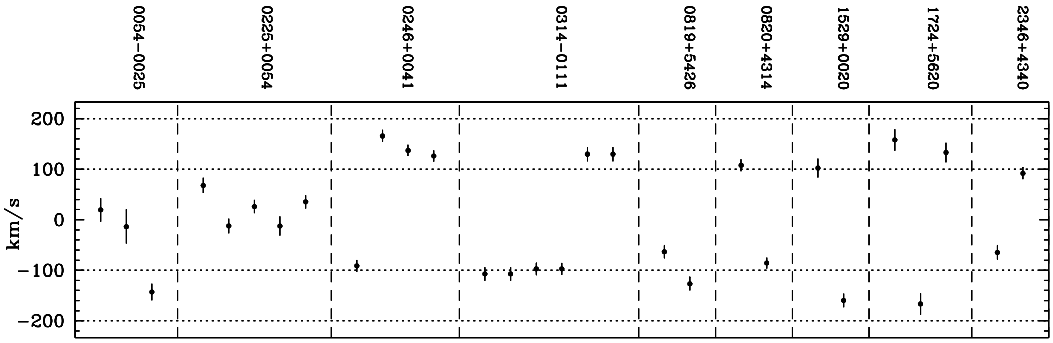

Figure 9.9: Na I doublet RVs for nine close binary candidates identified in Sect. 9.6.1.

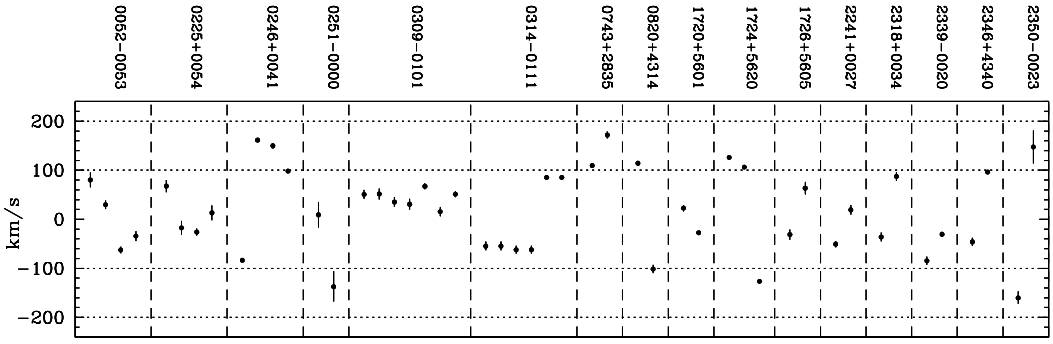

Figure 9.10: Same as Fig. 9.9 but for 16 systems that show more than 3σ Hα RV variation.

we consider these two systems to be strong PCEB candidates.

Upper limits to the orbital periods for the four new PCEB candidates have been estimated in the same way as described in Chapter 7. These values are given in Table 9.5.

9.6.2 Distribution of the stellar parameters

We present in this section distributions of surface gravity, mass and effective temperature of the white dwarfs, and spectral types of the companions for the WDMS binaries in our catalogue. We considered average values for those objects with multiple SDSS spectra, and only systems with relative errors in the white dwarf parameters smaller than 25%. This resulted in a number of 1339, 1196, 1126, and 558 WDMS binaries for the spectral type, $\log g$, $T_{\rm eff}$, and $M_{\rm wd}$ histograms, respectively (see Fig. 9.11). The most striking features of the distributions are similar to those provided in Chapter 7, which contain a considerably lower number of systems: the most frequent white dwarf temperatures range between 10000–20000 K, white dwarf masses cluster around $M_{\rm wd} \simeq 0.5\,{\rm M}_{\odot}$, the spectral type of the companion stars are typically M3–4, and $\log g \simeq 7.8$ for the vast majority of white dwarfs.

In Fig. 9.12 we show the $T_{\rm eff}$, $M_{\rm wd}$, $\log g$, and spectral type cumulative distributions obtained both from the WDMS binaries studied in this Chapter (blue lines), and the systems analysed in Chapter 7 (red lines). Kolmogorov-Smirnov (KS) tests were applied to compare both sets of stellar parameters, giving a 40%, 50%, 2% and 4% probability that both WDMS samples are drawn from the same parent population. From the above values, the $T_{\rm eff}$ and $M_{\rm wd}$ distributions seem to be consistent between both subsamples. The 2% obtained from the $\log g$ KS test is due to the scarcity of systems below $\log g = 7.5$ (i.e. less low-mass systems) in the WDMS binary $\log g$ distribution obtained from the systems studied in Chapter 7 (see Fig. 7.9). This could be an effect of our improved methods in determining the white dwarf solutions in this Chapter, as we have the advantage of GALEX UV fluxes for many systems. Inspecting the spectral type cumulative distributions in Fig. 9.12, the low probability obtained from the KS test is intriguing, as both distributions look like very similar. This is probably related to the fact that the spectral types are discrete values, and the KS test might not be a good prescription in this case. To complete the exercise we also compared the cumulative distributions obtained from the stellar parameters presented in this Chap-

ter to those obtained from a volume-limited sample of single white dwarfs [Holberg et al., 2008, green lines in Fig. 9.12]. As before, we run KS tests to compare both subsamples, and found probability zero in all cases ($T_{\rm eff}$, $M_{\rm wd}$, and $\log g$). Such result is not surprising given the fact that a large number of white dwarfs in the WDMS binary subsample have undergone a CE, and their properties have been modified (see next paragraph). In addition selection effects play an important role too (see Sect. 9.6.4).

The large number of white dwarfs at $M_{\rm wd} \simeq 0.4\,{\rm M}_{\odot}$ detected in the white dwarf mass distribution of Fig. 9.11 is thought to be the consequence that a significant amount of WDMS binaries have undergone a CE phase. This population of WDMS binaries will predominantly contain He-core, less massive white dwarfs. The mass distribution of WDMS binaries in which the initial MS binary separation was large enough to avoid the CE phase, will be similar to those mass distributions obtained from single white dwarfs, clustering at $M_{\rm wd} \simeq 0.6\,{\rm M}_{\odot}$ [Koester et al., 1979]. An independent analysis of the white dwarf mass distribution in PCEBs and wide WDMS binaries appears therefore a worthwhile exercise, and will be presented in Chapter 10.

The cut-off at early spectral types is a consequence of selection effects of WDMS binaries in SDSS, and is discussed in more detail in Sect. 9.6.4. The cut-off seen for low-mass companions might also be related to selection effects, as late-type stars are dim and will be harder to detect against a moderately hot white dwarf. Nevertheless, as already mention in Chapter 7, SDSS samples a much broader colour space than previous surveys and, in principle, should be able to identify more WDMS binaries containing cool white dwarfs plus very late-type companions. The relatively low frequency of such systems in the SDSS spectroscopic data base suggests that either SDSS is not efficiently targeting those systems for spectroscopic follow-up, or that they are rare in the first place, or a combination of both.

9.6.3 Distances and secondary star magnetic activity

In Sect. 9.5 we measured two independent distance estimates for the WDMS binaries in our catalogue. We compare these results in Fig. 9.13. We considered average white dwarf distances for objects with multiple sub-spectra, and only those systems with relative errors

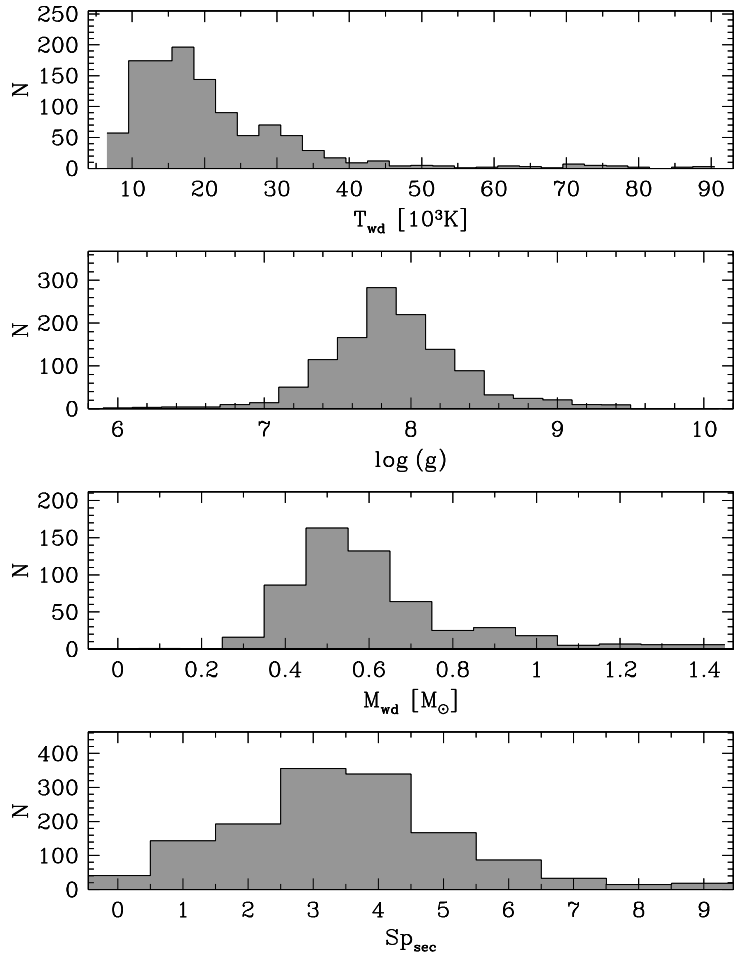

Figure 9.11: White dwarf mass, spectral type of the secondaries, effective temperature and $\log g$ histograms obtained from the SDSS WDMS binaries in our catalogue. Excluded are those systems with individual white dwarf masses, $T_{\rm eff}$, and $\log g$ associated to relative errors larger than 25 per cent.

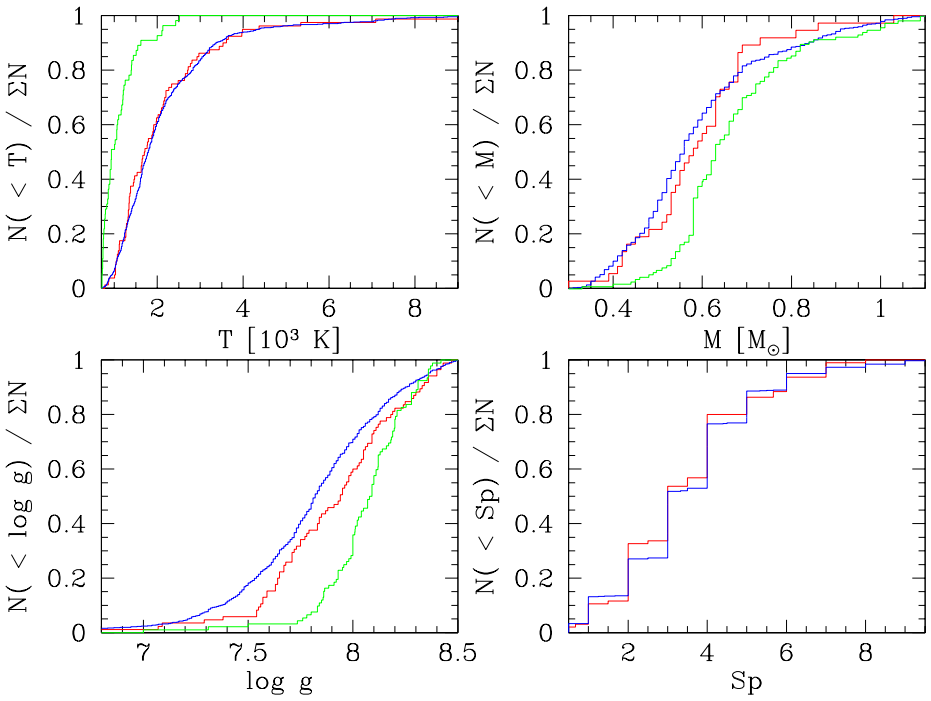

Figure 9.12: Effective temperature (top left), white dwarf mass (top right), surface gravity (bottom left) and spectral type (bottom right) cumulative distributions obtained from the stellar parameters of the WDMS binaries presented here (blue lines), analysed in Chapter 9 (red lines), and from a volume-limited sample of single white dwarfs (green lines).

in the white dwarf distance less than 25%[4]. This resulted in a sample of 703 WDMS binaries.

In the top panel of Fig. 9.13 we represent in black systems in which the distances overlap at 1.5σ level, in red objects where the distance disagreement is more than 1.5σ. In the majority of cases (∼80%) the distances agree with $d_{\rm sec} = d_{\rm wd}$. The same tendency for outliers found in Chapter 7 in which $d_{\rm sec} > d_{\rm wd}$ remains for ∼ 20% of the sample. The percentage of 1.5σ outliers above and below $d_{\rm sec} = d_{\rm wd}$ should be ∼ 7%, respectively expected for normally distributed errors. In contrast to this, the percentage of systems with $d_{\rm sec} > d_{\rm wd}$ is ∼ 15%, and only ∼ 5% for the systems with $d_{\rm sec} < d_{\rm wd}$. We adjusted the spectral type of the secondaries to achieve the same distances, and found that again a change of 1–2 spectral subclasses was enough for the majority of the cases. We consequently suggest that the possibility that magnetic activity raises the temperature of the inter-spot regions in active stars that are heavily covered by cool spots, leading to a bluer optical colour compared to inactive stars, remains the best explanation for this behaviour.

16 systems (2.3% of the sample) in the bottom panel of Fig. 9.13 need a change of more than two spectral subclasses to reach $d_{\rm sec} = d_{\rm wd}$. We have investigated these cases, and found that six of these objects contain hot white dwarfs, where some irradiation on the secondary is expected (SDSSJ 003221.86 +073934.4, SDSSJ 032510.84 -011114.1, SDSSJ 080229.99 +072858.1, SDSSJ 095719.25+ 234240.8, SDSSJ 101323.90+ 043946.1, SDSSJ 141536.40 +011718.2). These WDMS binaries are consequently candidates to probe for RV movement[5]. Seven systems (SDSSJ 025306.37 +001329.2, SDSSJ 103501.26 +104222.7, SDSSJ 131156.69 +544455.8, SDSS J153329.88 +033301.6, SDSSJ 160132.21 +063901.7, SDSSJ 204729.04 -064536.7, SDSSJ 210624.12 +004030.2) are resolved in their SDSS images, and consequently the amount of flux received from one of the stars is likely underestimated. This translates to an underestimated flux scaling factor and distance. In one object, SDSSJ 232624.72 -011327.2, the S/N of its SDSS spectrum is low (S/N = 4.2), and we blame this for the discrepancy found in the distances. Finally, SDSSJ 111424.65

[4]Note that the relative error in $d_{\rm sec}$ is dominated by the scatter in the $Sp-R$ relation provided in Chapter 7, which represents an intrinsic uncertainty rather than a statistical error in the fit, and we therefore did not apply any cut in $d_{\rm sec}$.

[5]Only SDSS 032510.84-011114.1 has two SDSS RV measurements in Table 9.4. No RV movement is detected. Note though the probability of sampling the same orbital phase is certainly present.

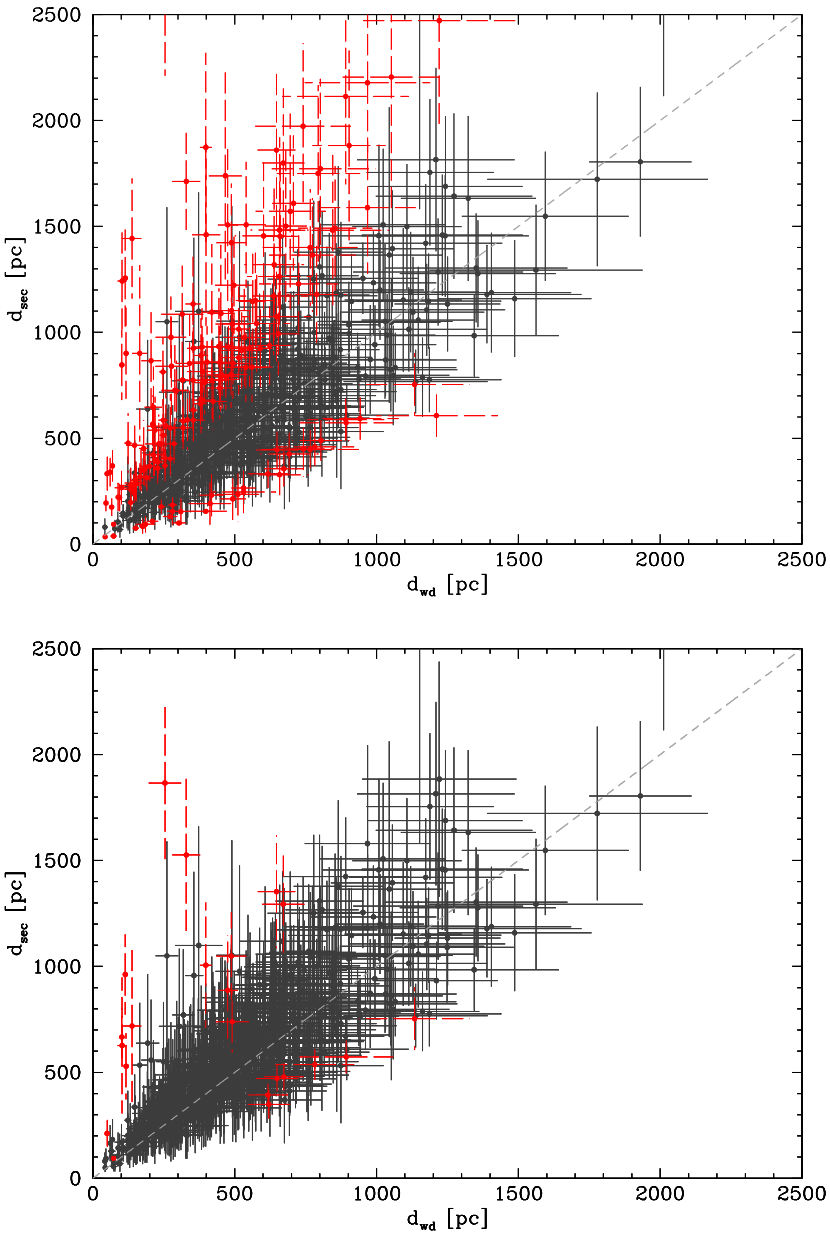

Figure 9.13: Top panel: Comparison of $d_{\rm sec}$ and $d_{\rm wd}$ obtained from our spectral decomposition and white dwarf fits to the SDSS spectra. Approximately 20% of the systems are $d_{\rm sec} > d_{\rm wd}$ outliers by more than 1.5σ (red dots). Bottom panel: the spectral types of the secondary stars were adjusted by 1–2 spectral classes to achieve $d_{\rm wd} = d_{\rm sec}$.

+334123.7 contains a cold white dwarf ($T_{\rm eff}$ = 8300 K), and a M9 companion. Due to the upturn for Sp >M8.5 in the empirical $Sp-R$ relation provided in Chapter 7 (see Fig. 7.6) the distance measured to the secondary star is overestimated ($d_{\rm sec}$ = 94 $\pm$ 3, $d_{\rm wd}$ = 73 $\pm$ 7), causing the discrepancy $d_{\rm sec} > d_{\rm wd}$.

9.6.4 Selection effects among WDMS binaries in SDSS

The large amount of data presented in this Chapter is of quality enough to study the selection effects of WDMS binaries in SDSS in a more complete way than discussed in Chapter 7. For this purpose we have collected the stellar parameters and distances provided in Table 9.3, and obtained in the top, middle and bottom panels of Fig. 9.14 the (log $T_{\rm eff}$,$d_{\rm wd}$), (Sp,$d_{\rm wd}$) and (log $T_{\rm eff}$,Sp) density maps, respectively for the systems in our catalogue. Only objects in which the relative errors in their (average) white dwarf parameters are less than 25% were selected for this purpose[6], resulting in a sample of 597, 692, and 1052 systems respectively in the top, middle and bottom panels of Fig. 9.14.

The top panel in Fig. 9.14 shows the (log $T_{\rm eff}$,$d_{\rm wd}$) density map. It becomes clear that whilst binaries in which the white dwarf primaries are cooler than 10000 K are detected at shorter distances, systems with hotter white dwarf components can be observed at a wider range of (longer) distances, the hottest among them the farthest. Cooler white dwarfs are then too faint to be detected at relatively long distances, and moderately hot white dwarfs saturate the lower magnitude limit of SDSS at shorter distances. The majority of objects are hence concentrated at $\sim$400-500 pc, with white dwarf effective temperatures between $\sim$15000-25000 K. This is in agreement with the effective temperature distribution provided in Fig. 9.11.

Having analysed how distance effects affect the detection of our white dwarf primaries in SDSS, we study in the middle panel of Fig. 9.14 the same effect for our secondary stars. Early-type M-dwarfs are hotter, and consequently saturate the SDSS lower magnitude limit at relatively short distances. On the contrary, later-type secondaries are cold enough

[6]We could, in principle, have also used the distances measured to the secondaries. Note though that magnetic activity is expected to affect the spectral type (and consequently the radii and the distances) of a large fraction of secondary stars (Sect. 9.6.3). We consequently considered here the distances measured to the white dwarfs, and quote them simply as distances in what follows.

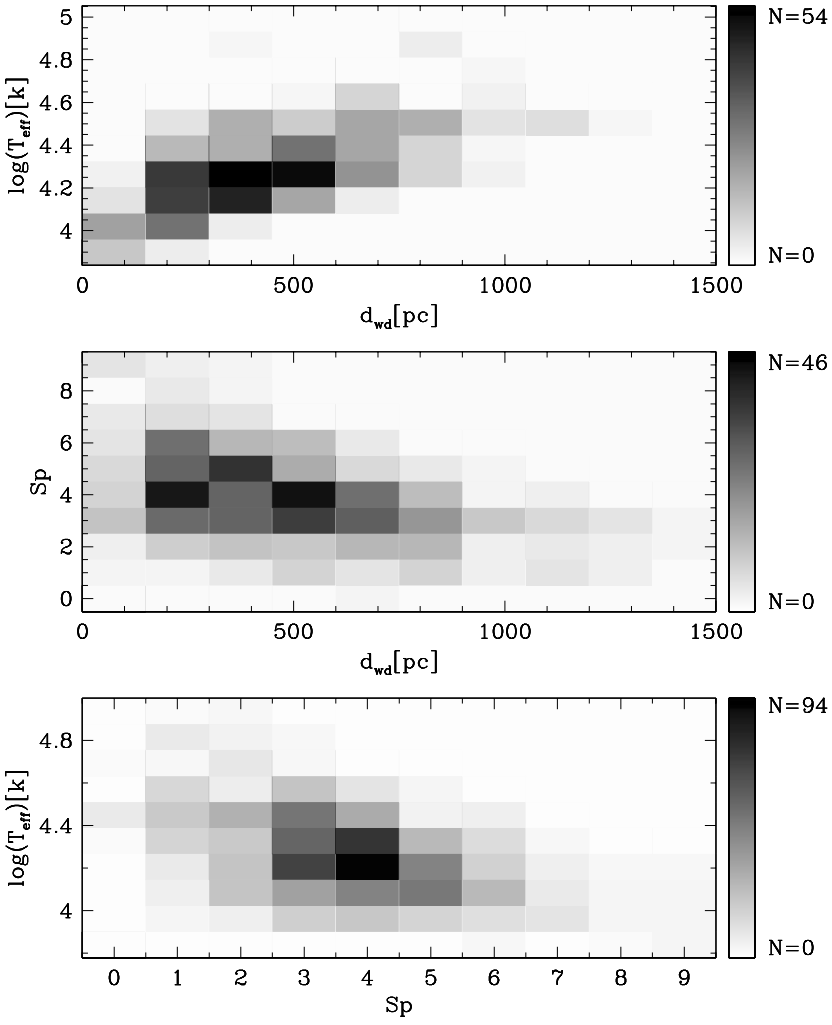

Figure 9.14: Selection effects in SDSS WDMS binaries can be understood by analysing the density maps obtained from their stellar parameters. From top to bottom the (log $T_{\rm eff}$,$d_{\rm wd}$), ($d_{\rm wd}$,Sp), and (log $T_{\rm eff}$,Sp) density maps. See Sect. 9.6.4 for details.

to be detected at shorter distances, but too dim to be observed at long distances. Thus hotter (earlier) companions are generally detected at d $\gtrsim$ 300pc, and cooler (later) secondaries are concentrated at $\sim 100-200$pc.

In the bottom panel of Fig. 9.14 we show the ($T_{\rm eff}$,Sp) density map. A clear trend of decreasing the $T_{\rm eff}$ of the white dwarfs for later-type companions can clearly be seen. In other words, high white dwarf temperatures are too hot for a late-type companion to be detected (in the optical). In the same way early spectral type secondaries are too hot for a cool white dwarf primary to be detected. With the above analysis the cut-off at early spectral types in Fig. 9.11 can be easily explained in a natural way. Selection effects then dominate the bottom left region of the ($T_{\rm eff}$,Sp) density map. The scarcity of systems with later-type (>M6) secondaries can also be seen here, and has been already discussed in Sect.9.6.2. This feature might be also related to the above selections effects. Nevertheless, as discussed in Chapter 7, spectral type distributions of field low-mass and ultracool stars [e.g. Reid et al., 2007, 2008] peak at Sp $\simeq$ M4-5, and decline towards later spectral types. Hence we suggest that the lack of WDMS binaries with late-type companions is probably both an intrinsic property of the WDMS binary population and a consequence of selection effects. Distance effects play also an important role. Thus for example, those WDMS binaries which contain both a hot primary and secondary components can not be observed at short distances, since they saturate the SDSS magnitude limit. On the contrary, WDMS binaries containing faint stars can only be observed at short distances.

From the analysis of Fig. 9.14 we conclude that a "typical" SDSS WDMS binary contains a M3–4 companion, a $\sim$10000-20000 K primary, and is observed at a distance $\sim$400-500 pc. Note though that the distributions presented in Fig. 9.14 are a combination of the real distribution of WDMS binary properties and the selection effects in the sample. Consequently a typical SDSS WDMS binary is unlikely to be representative of the "real" (corrected for selection effects) WDMS binary population.

The top and middle panels of Fig. 9.14 help in understanding brightness limited selection effects of WDMS binaries in SDSS. In order to avoid this it becomes necessary to use different magnitude limited surveys from SDSS, with lower and larger magnitude cuts respectively. The bottom panel of Fig. 9.14 helps to understand selection effects related to

the spectral appearance of WDMS binaries. Detection of systems with hotter white dwarfs and later-type companions is then most likely to arise from the use of infrared magnitude surveys such us UKIDSS or 2MASS. In the same way, to identify cool white dwarfs with early-type dominated M-dwarfs it is necessary to make use of blue surveys such as GALEX.

9.7 Conclusions

We have presented a catalogue of 1591 WDMS binaries from the spectroscopic SDSS DR6. We have used a decomposing/fitting technique to measure the effective temperatures, surface gravities, masses and distances to the white dwarfs, as well as the spectral types and distances to the companions in our catalogue. Distributions and density maps obtained from these stellar parameters have been used to study both the general properties and the selection effects of WDMS binaries in SDSS. A comparison between the distances measured to the white dwarfs and the MS companions shows $d_{\rm sec} > d_{\rm wd}$ for $\sim$20% of the systems, a tendency found in previous Chapters. We suggest that the possibility that magnetic activity raises the temperature of the inter-spot regions in active stars that are heavily covered by cool spots, leading to a bluer optical colour compared to inactive stars, remains the best explanation for this behaviour. We also provide RVs for 1062 WDMS binaries measured from the Na I $\lambda\lambda$ 8183.27,8194.81 absorption doublet and/or the Hα emission line. Among the systems with multiple SDSS spectroscopy, we find four new WDMS binaries exhibiting significant RV variations, identifying them as PCEB candidates.

Chapter 10

Discussion and Conclusions

I conclude my thesis with this Chapter, in which I discuss the results obtained by our ongoing project at the present date, e.g. November 2008. For this, I make use of the analysis provided in Chapters 7, 8 and 9[1], and also use data that have not been published yet, but will be in the near future. The inclusion of these data provides a more complete and robust analysis. I will also outline my future research plan.

10.1 The orbital period distribution of SDSS PCEBs

Currently, we have observed 244 WDMS binaries, of which 89 have been identified as PCEBs, and 42 had their orbital periods measured, including also the seven orbital periods measured in Chapter 8. I show in Fig. 10.1 the orbital period distribution of these 42 systems. This histogram represents an homogeneous selected sample of PCEBs, but is still subject to selection effects. Orbital periods of several SEGUE PCEBs have also been already measured (Nebot Gómez-Morán, private communication), and it is expected that the inclusion of these data will help in solving the observational bias in SDSS. Inspecting Fig. 10.1 it becomes clear that the number of long period PCEBs has increased in comparison with the orbital period distribution shown in Chapter 8. This confirms our Monte-Carlo simulations that showed that our survey has the potential of finding PCEBs with orbital

[1] In the following sections I do not include systems identified as PCEB candidates in Chapters 7 and 9 that have not yet been confirmed as definite close binaries by our own follow-up observations

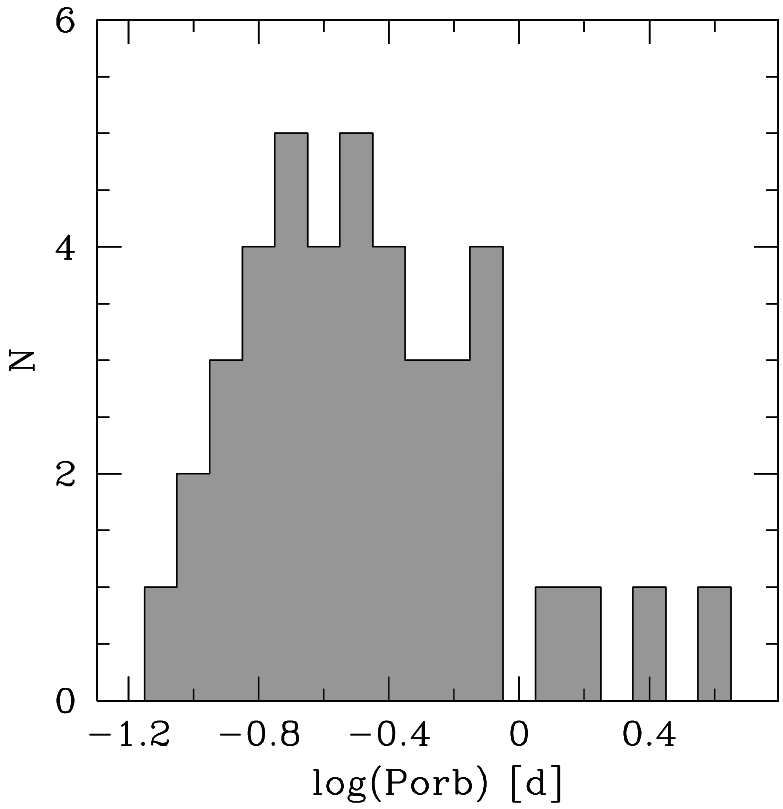

Figure 10.1: Orbital period distribution of current SDSS PCEBs. The accumulation of systems at periods shorter than a day suggests that the CE efficiency is less than frequently assumed.

periods in the range ∼1-10 days. Nevertheless the number of long period PCEBs is still rather low compared to the number of short period systems, supporting the hypothesis of the PCEB orbital period distribution peaking at $P_{\rm orb} < 1$ day. The orbital energy of the binary hence might be less efficiently used (lower CE efficiency) to expel the envelope than frequently assumed. In addition, the decrease of the number of PCEBs at $P_{\rm orb} > 1$ day seems to imply that the γ-formalism in its present form might not be an adequate description of the CE phase, as a more pronounced tail towards longer orbital periods is expected in this formalism.

10.2 The PCEB fraction

The analysis provided in Chapter 7 resulted in a $\sim$ 15% fraction of PCEBs among a sample of 101 SDSS WDMS binaries with multiple SDSS spectroscopy. I have shown that this number is likely to be a lower limit. Since 89 of the 244 systems for which we have follow-up observations show more than 3σ RV variations in the Na I $\lambda\lambda$ 8183.27,8194.81 absorption doublet, this implies a PCEB fraction of $\sim$ 1/3. This result is considerably higher than the value estimated by population synthesis studies [Willems & Kolb, 2004], and more than doubles the PCEB fraction measured in Chapter 7.

In the bottom panel of Fig. 10.2, I show the distribution of our observed systems (WDMS binaries in white, PCEBs in gray) according to the spectral type of their secondary components, and show the PCEB fraction for each spectral type in the middle panel of the same figure. Making use of the $Sp-M$ relation for M-dwarfs provided in Chapter 7, I give also values of secondary masses in the top of the bottom panel of Fig. 10.2. The PCEB fraction appears to increase for later-type secondaries. This is confirmed by a linear fit to the solid dots in the middle panel of Fig. 10.2 (red dashed line):

$$\frac{N_{\rm PCEB}}{N_{\rm All}} = (0.07 \pm 0.03) \times Sp + (0.17 \pm 0.14) \qquad (10.1)$$

The χ^2 of the fit is 19.7. In addition I also fitted a constant function (green dashed line), in which case the χ^2 is 61. It is expected that if these two models, linear and constant value fits, produce minimum χ^2 values χ^2_2 and χ^2_1, respectively then the quantity

$$F = \frac{(\chi^2_1 - \chi^2_2)/(m_2 - m_1)}{\chi^2_2/(n - m_2)},$$

where m_1 and m_2 are the number of free parameters ($m_1 = 1$, and $m_2 = 2$ in our case), and n is the number of points, follows an $F(m_2 - m_1; n - m_2)$ distribution. In our case $F = 12.6$, and the 95th and 99th percentiles of $F(1,6)$ give 6.6 and 13.7 respectively. This result implies that, even though the χ^2 of the linear fit is considerably lower, a constant value fit can not be completely ruled out.

In order to account for distance effects I represent in the top panel of Fig. 10.2 the average distances of the observed systems for each spectral type. In agreement with the density diagrams provided in Chapter 9, the average distance is $\sim$ 500 pc. This excludes

that we have a magnitude-distance bias against wide low luminosity WDMS binaries, and consequently the PCEB fractions for the different spectral subtypes are likely real.

An increase of the PCEB fraction in the range M3-M4 has been predicted in the context of the disrupted MB model [Politano & Weiler, 2006, see Chapter 1]. The reason is that the evolutionary time scales on which PCEBs evolve into CVs becomes dramatically longer if MB ceases for fully convective secondaries. Although suffering from low number of statistics, by analysing the distribution of PCEB secondary star masses in the bottom panel of Fig. 10.2, one may interpret this result as an indication for a discontinuity in the dependence of the relative number of PCEBs on the spectral type of the secondary, as predicted by Politano & Weiler [2006].

10.3 The white dwarf mass distribution in WDMS binaries

Our follow-up observations have led to the identification of 89 PCEBs, and 155 wide WDMS binary candidates[2]. Statistically speaking, these numbers are large enough to provide robust distributions of the stellar parameters in both subsamples, PCEBs and wide WDMS binaries, and also robust distributions of the parameters for the combined population, PCEBs *plus* wide WDMS binaries. In this section I study the distribution of white dwarf masses in the overall sample of our observed WDMS binaries, and also in both our PCEB and wide WDMS binary subsamples. With this I attempt to confirm that the low mass peak at $\sim 0.4 M_{\odot}$ identified in the mass distribution of single white dwarfs is associated with a binary origin [Willems & Kolb, 2004; Liebert et al., 2005].

In Fig. 10.3, I show in black the white dwarf mass distribution of all WDMS binaries, in dark gray the white dwarf distribution of our wide WDMS binaries, and in light gray the white dwarf mass distribution of our PCEBs[3]. The overall distribution of white dwarf masses peaks at 0.5 $M_{\odot}$ (see Chapter 9), and shows also a "high" mass peak at 0.9 $M_{\odot}$. This latter feature has been also identified in mass distributions of single white dwarfs [Liebert et al., 2005], and is supposed to be a consequence of mergers of low mass double

[2]Note that all PCEBs with periods longer than $\gtrsim$10 days will be considered as wide WDMS binaries, as the detection probability for PCEBs with $P_{orb} \gtrsim 10$ days is low (see Chapter 8).

[3]The white dwarf masses, as well as the remaining stellar parameters in the following sections, are taken from Chapter 9.

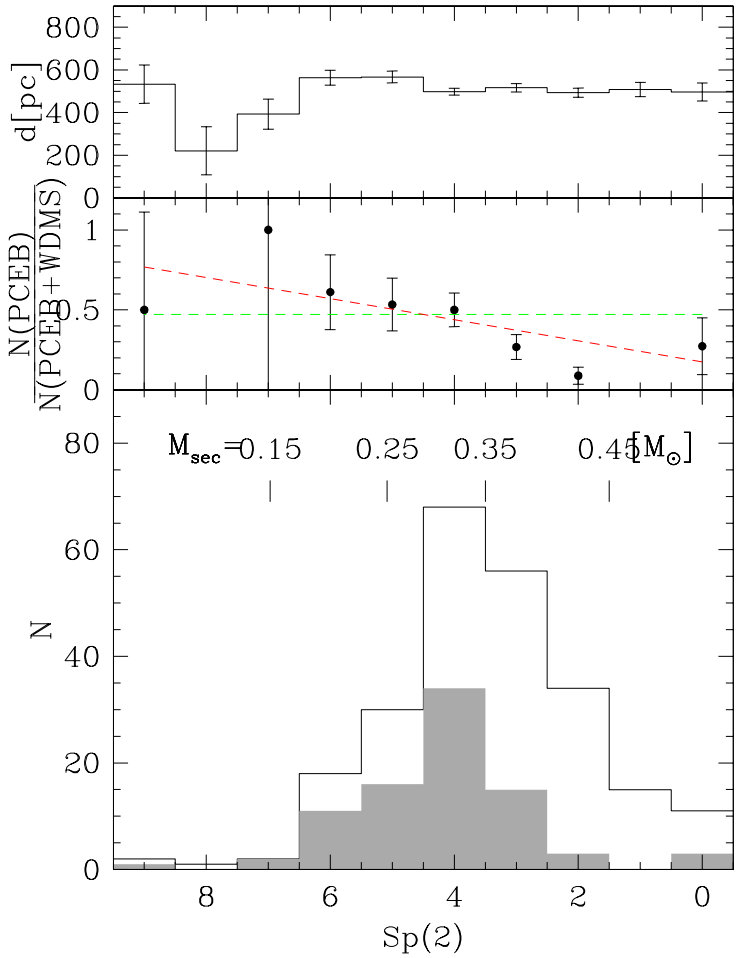

Figure 10.2: Bottom: Distribution of PCEBs (gray) and WDMS binaries (white) according to the spectral type of their companions. Secondary star masses are indicated in the top of the panel. Middle: PCEB fraction among our observed WDMS binaries. There is a clear tendency to an increased PCEB fraction for later-type PCEB secondaries. This is confirmed by a linear fit to the data (red dashed line). The green dashed line represents a constant value fit to the data. Top: average distances of the observed systems.

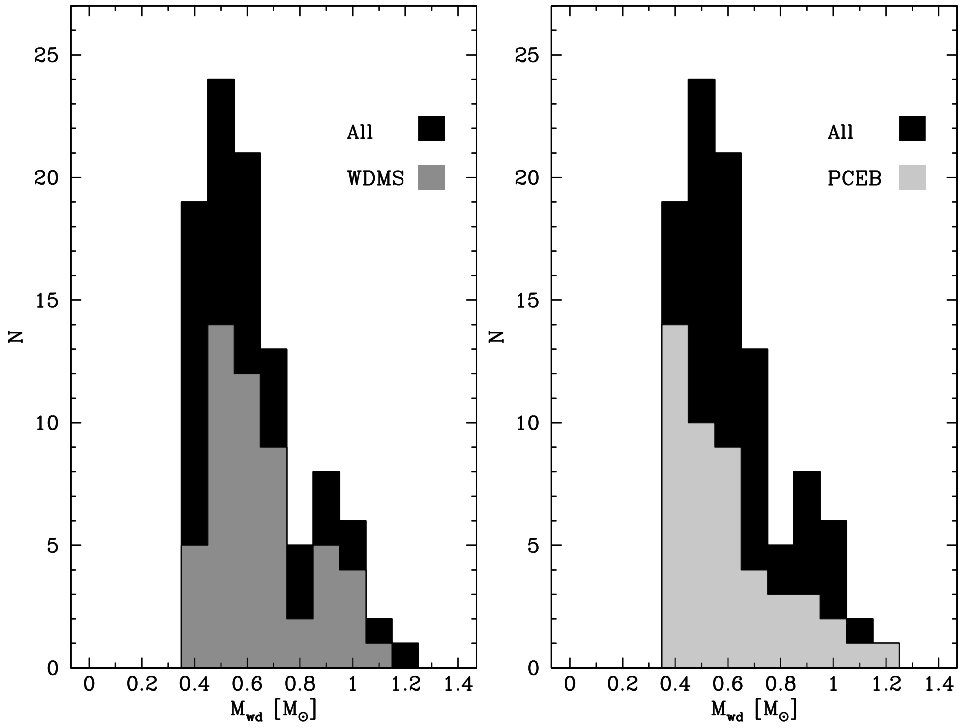

Figure 10.3: White dwarf mass distribution for all our observed WDMS binaries (black), PCEBs (right panel, light gray), and wide WDMS binaries (left panel, dark gray). The peak at 0.4 $M_\odot$ in the distribution of PCEB white dwarf masses confirms the hypothesis that these systems have undergone a CE phase.

degenerate stars. The 0.5 and 0.9 $M_\odot$ peaks are also detected in the distribution of wide WDMS binaries (see left panel of Fig. 10.3). The fact that we see a peak at 0.9 $M_\odot$ in the mass distribution of wide WDMS binaries suggests that a certain fraction of these objects might be descendents of triple systems.

A peak at 0.4 $M_\odot$ is not detected in the white dwarf mass distribution of wide WDMS binaries. Nevertheless, it is clearly evident in the white dwarf mass distribution of PCEBs (see right panel of Fig. 10.3). Since these systems have undergone a CE phase, I can confirm from the mass distribution of PCEBs provided in the right panel of Fig. 10.3, that the low mass peak at 0.4 $M_\odot$ in the global distribution of single white dwarfs is indeed related to binary evolution, as previously suggested.

As a final exercise we obtained the wide WDMS binary (red line) and PCEB (blue line) white dwarf mass cumulative distributions (see Fig. 10.4), and use a KS test to compare

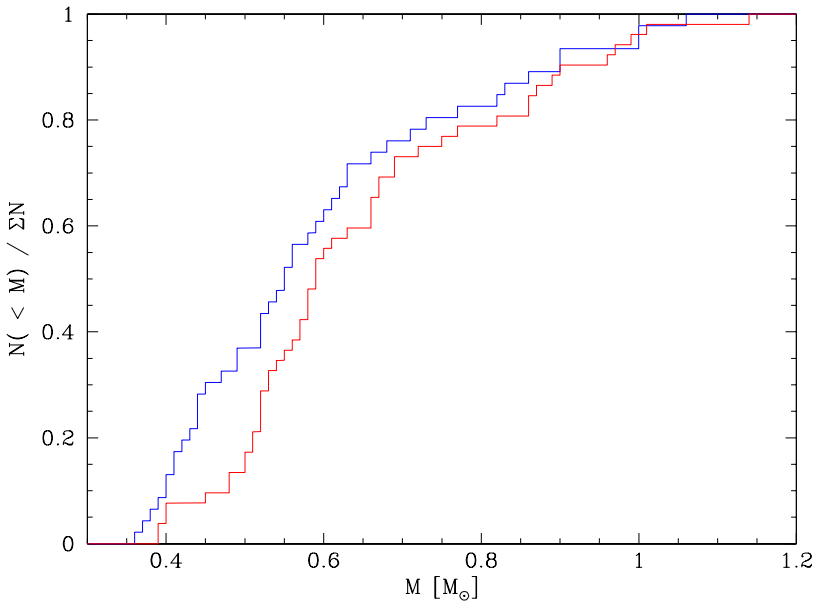

Figure 10.4: PCEB (blue line) and wide WDMS binary (red line) white dwarf mass cumulative distributions. The probability obtained from a KS test for the hypothesis of both subsamples being consistent is 10%.

both subsamples. We found a 10% probability for the distributions being drawn from the same parent population, which supports the idea of both wide WDMS binaries and PCEBs white dwarf mass subsamples being independent.

10.4 The white dwarf $M-R$ relation

The fitting procedure developed in Chapter 7 for determining the stellar parameters of the white dwarfs in our WDMS binaries assumes an $M-R$ relation for white dwarfs obtained from an updated version of the Bergeron et al. [1995b]'s tables. These relations are developed for C/O-core white dwarfs, but extend also below $0.5 M_{\odot}$, where white dwarfs are expected to predominantly contain He cores. A crucial question is obviously if these relations provide reliable values of mass and radius below this limit for our white dwarfs. To answer this I show in Fig. 10.5 the $M-R$ relations from Panei et al. [2000] for a $T_{\rm eff}$ = 15000 K white dwarf containing a He- (top left), a C- (top right), and an O-core (bottom left), with or without a H/He envelope/envelopes. Panei et al. [2000] assume a H mass en-

velope of $M_{\rm H}/M_{\rm WD} = 3 \times 10^{-4}$ in their He-core models, and a H and He mass envelope of $M_{\rm H}/M_{\rm WD} = 10^{-5}$ and $M_{\rm He}/M_{\rm WD} = 10^{-2}$ respectively for their C- and O-core models. In black dots are shown the $M-R$ relation used in this thesis for the same effective temperature. The C/O relations are in reasonably good agreement with ours even below $0.5 M_{\odot}$. The He-core relations are also in reasonably good agreement with ours when no H envelope is considered, but predict larger radii than ours for $M_{\rm WD} \lesssim 0.35 M_{\odot}$ when a H envelope is included in the models. Given that we do not know $M_{\rm H}/M_{\rm He}$ in our white dwarfs, using Bergeron et al. [1995b]'s $M-R$ relations is as good as any other guess. In addition, the number of white dwarfs with masses below $\sim 0.35 M_{\odot}$ is very low (see Fig. 7.9, Fig. 9.11, and Fig. 10.3), and I conclude that the effect of increasing the white dwarf radius in the low mass range does not dramatically affect the white dwarf mass and radius distribution of our WDMS binaries.

The fact that larger white dwarfs radii might be expected below $\sim 0.35 M_{\odot}$ could, in principle, explain the distance disagreement found in previous Chapters (in which $d_{\rm sec} > d_{\rm wd}$ for $\sim$ 20% of the WDMS binaries), since a larger radius implies a larger white dwarf distance. In the bottom right panel of Fig. 10.5, I show the white mass distribution of all outliers ($d_{\rm sec} > d_{\rm wd}$) in Fig. 9.13. As one can clearly see, very few white dwarfs have masses $\lesssim 0.35 M_{\odot}$, and consequently this feature can not reconcile the distance problem.

10.5 A test for magnetic activity

Recently West et al. [2008] studied the age-activity relations for cool (M-dwarf) stars, and concluded that young stars are, in general, more active than older stars. In other words, the fraction of active stars increases with decreasing the Galactic height at all spectral types. In Chapters 7 and 9, a relatively large percentage ($\sim$20%) of WDMS binaries show larger distances measured from the secondaries than those obtained from their white dwarfs. I have shown that these objects are likely to contain magnetically active companions.

As a test for this hypothesis I provide in the bottom panel of Fig. 10.6 the distribution in Galactic height of all WDMS binaries in our catalogue (black, see Chapter 9), together with the distribution of all WDMS binaries containing candidate active compan-

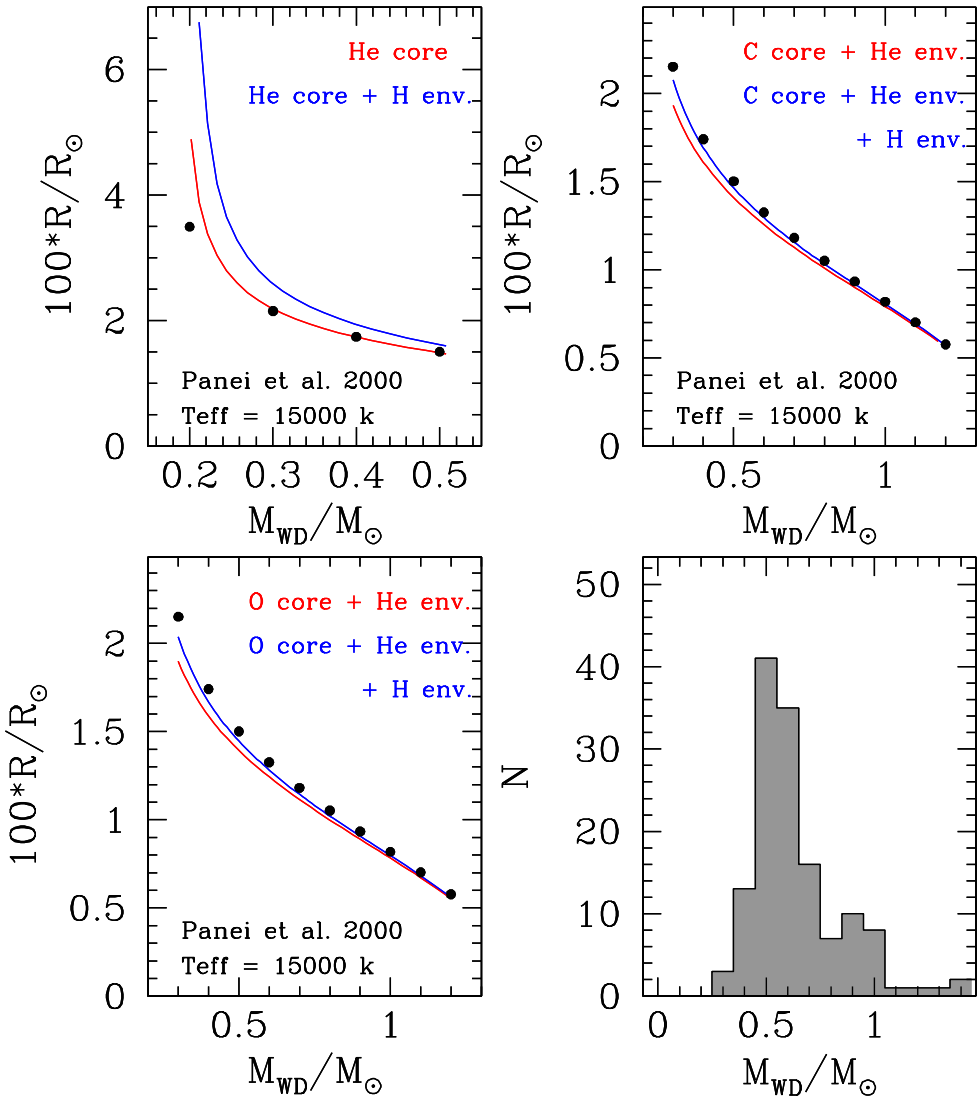

Figure 10.5: Top and bottom left panels: comparison of the $M-R$ relation used in this thesis (black solid dots) and those provided in Panei et al. [2000] (blue and red straight lines) for a $T_{\rm eff}$ = 15000 K white dwarf. Bottom right: white dwarf mass distribution for the WDMS binaries studied in Chapter 9 in which $d_{\rm sec} > d_{\rm wd}$ (relative error in the mass is 20% or less). The low number of systems below $\sim 0.35 M_{\odot}$ indicates that an increase in $R_{\rm WD}$ can not explain the distance disagreement found in previous Chapters (see text for details).

ions (i.e. systems in which the distance to the secondary is 1.5σ larger than the distance to the white dwarf, gray)[4]. In the top panel of the same figure I give the fraction of active systems to the total number of systems.

A clear tendency of increasing fraction of active systems at lower Galactic heights (younger secondaries) can be seen. A linear fit to the data (red dashed line) confirms this tendency and supports our suggestion of magnetic activity causing the discrepancy between the distances found in previous Chapters.

10.6 Active secondaries as a product of close binarity?

M stars in close binaries rotate faster than single M stars or M stars in wider binaries, in general [Cardini & Cassatella, 2007]. Since fast rotators are expected to be more active [Delfosse et al., 1998], then close binarity and activity in our PCEBs may be related. In order to check this I show in Fig. 10.7 the distances measured both to the secondaries and to the white dwarfs for our observed WDMS binaries. As in the previous Chapters, I considered only those systems with relative error of less than 25% in the white dwarf distance. This resulted in a sample of 166 WDMS binaries. PCEBs are represented in cyan dots. In dark gray I show systems in which the distances overlap at 1.5σ level, in red WDMS binaries where the distance disagreement is more than 1.5σ. The same tendency for outliers found in previous Chapters can be seen in $\sim$ 17% of the sample. If secondaries in which $d_{\rm sec} > d_{\rm wd}$ are active, then the same amount of close and wide WDMS can be found among the systems containing active secondaries. Consequently magnetic activity and close binarity, i.e. fast rotation, in our M-dwarf sample seem to be not related.

Recently West & Basri [2008] showed that rotation and magnetic activity in single late-type M-dwarfs might not always be linked, in agreement with the above results. Nevertheless, it has to be stressed that once the primary evolved through the AGB, sufficient angular momentum might have been transferred to the secondary, producing wind-induced rapid rotating stars [Jeffries & Stevens, 1996]. We would expect then a fraction of (wide) WDMS binaries containing rapid-rotating secondaries. As a consequence these secondaries

[4]The Galactic heights have been obtained using the distances measured for the white dwarfs. In addition only systems in which the relative error in their white dwarf distances is less than 25% were considered.

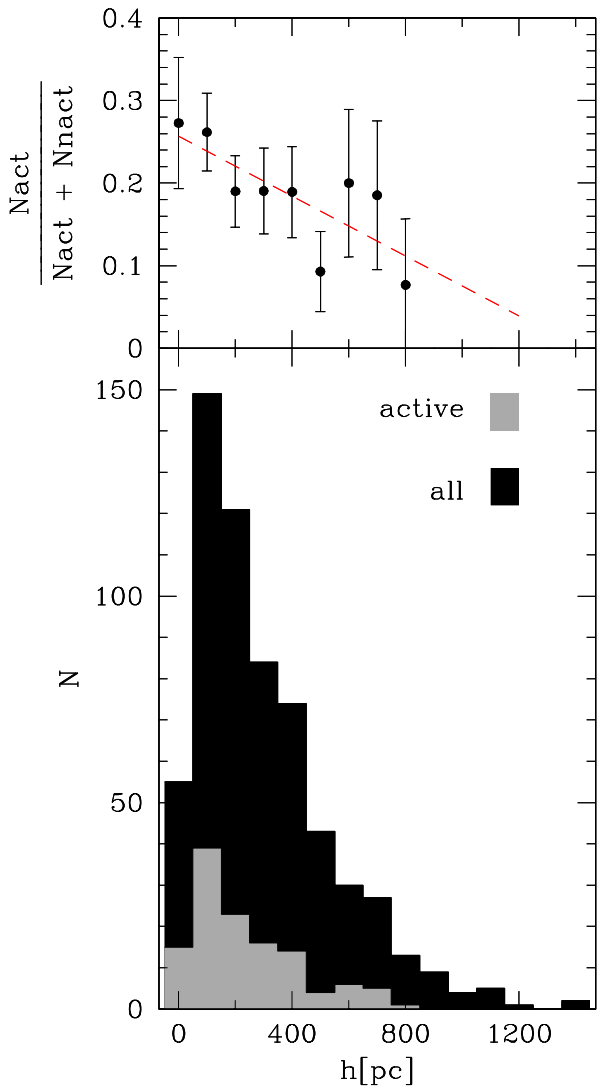

Figure 10.6: Bottom left: distribution of WDMS binaries with candidate active companions (gray), and total number of systems (black) as a function of the Galactic height (h) for our catalogue of WDMS binaries (Chapter 9). The fraction of systems that contain active secondary candidates increases at lower Galactic heights (younger systems), supporting the idea of these binaries containing magnetically active companions.

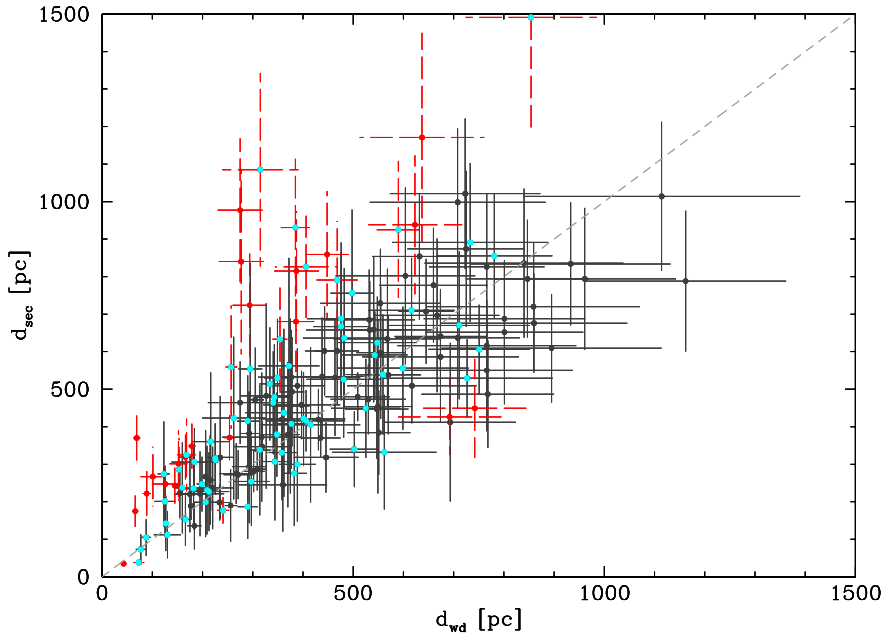

Figure 10.7: Comparison of $d_{\rm sec}$ and $d_{\rm wd}$ for our observed WDMS binaries. In dark gray are shown systems whose distances agree at a 1.5σ level, and in red those whose distances are 1.5σ outliers. The same tendency of outliers found in previous Chapters can be seen here. Cyan dots represent PCEBs. Roughly the same amount of close and wide WDMS binaries can be found among the WDMS binaries that contain active secondaries, indicating that magnetic activity might not be correlated with close binarity (fast rotation) in our PCEB M-dwarf sample.

would show high levels of magnetic activity, leaving our hypothesis of magnetic activity and close binarity not always being linked as inconclusive.

10.7 Colour-colour diagrams and colour-cuts of WDMS binaries

A feature unexplored in Chapter 9 is the use of GALEX-SDSS-UKIDSS magnitudes to study the distribution of WDMS binaries in colour-colour diagrams, and the search of colour-cuts for this kind of system. I briefly show in this section that WDMS binaries can be very efficiently separated from single MS stars when using a combined ultraviolet, optical, and infrared colour selection. For this purpose I provide in Fig. 10.8 the (nuv$-i$,nuv$-H$), ($i-J, J-H$), ($u-g, g-r$), and (fuv-nuv, $r-z$) colour-colour diagrams for the WDMS

binaries in our catalogue (Table 9.1, excluding all WDMS binary candidates) and all SDSS stellar sources. A general feature evident in all diagrams is that a certain number of systems appear to be outliers from the apparent locus of WDMS binaries. I have investigated these cases and found that in the majority of cases these objects are resolved pairs in SDSS. In these cases a large photometric error is expected from the deblending applied by the SDSS photometric pipeline (see Chapter 9).

WDMS binaries can be efficiently separated from the main locus of MS stars by applying the following colour-cuts to the four colour-colour diagrams provided in Fig. 10.8, respectively:

$$(\mathrm{nuv}-i) < -0.85 + 0.83 \times (\mathrm{nuv}-h) \tag{10.2}$$

$$0.3 < (j-H) < 0.7 \tag{10.3}$$

$$(i-J) > 1.2 \tag{10.4}$$

$$(i-J) > 0.4 + 1.85 \times (j-H) \tag{10.5}$$

$$(u-g) < 0.93 - 0.27(g-r) - 4.70(g-r)^2 + 12.38(g-r)^3 + \tag{10.6}$$
$$3.08(g-r)^4 - 22.19(g-r)^5 + 16.67(g-r)^6 - 3.89(g-r)^7$$

$$-0.5 < (g-r) < 1.5 \tag{10.7}$$

$$(r-z) > -0.3 \tag{10.8}$$

$$(\mathrm{fuv}-\mathrm{nuv}) < 0.85 + 3.9 \times (r-z) \tag{10.9}$$

A more complete colour-cut selection analysis for WDMS binaries using different combinations of GALEX-SDSS-UKIDSS magnitudes seems to be a worthwhile exercise (see next section).

10.8 Future work

10.8.1 PCEB studies

The major task of our project is to identify and follow-up those WDMS binaries that have undergone a CE phase. Future follow-up observations will increase both the number of

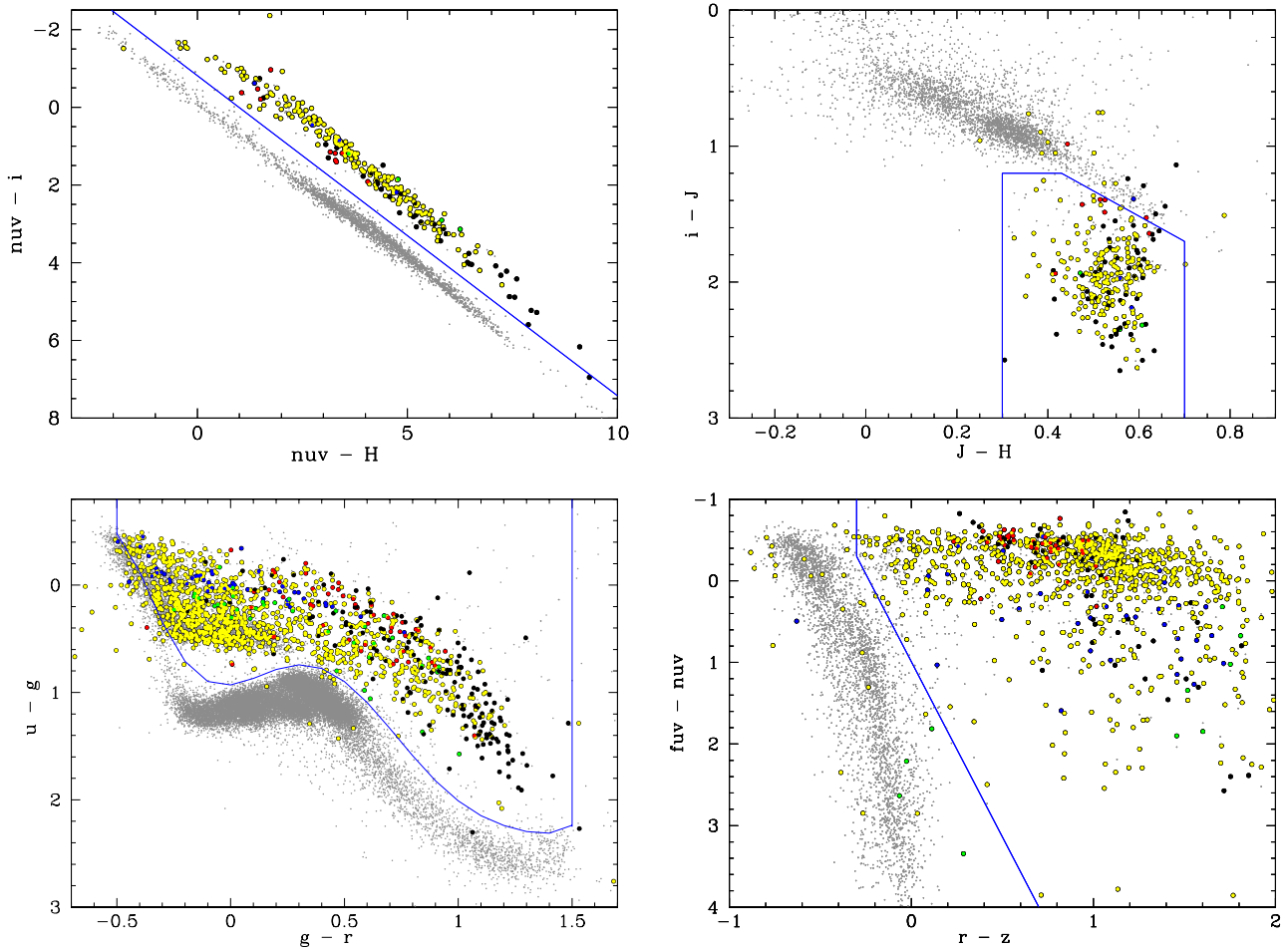

Figure 10.8: (nuv$-i$,nuv$-H$) (top left), $(i-J, J-H)$ (top right), $(u-g, g-r)$ (bottom left), and (fuv-nuv, $r-z$) (bottom right) colour-colour diagrams for WDMS binaries and stellar sources. WDMS binaries are represented according to their binary components as follows (see Table 9.2): DA/M binaries in yellow, DB/M in blue, DC/M in green, DA-DB-DC/K in red, and WD/M in black. Stellar sources are represented with gray dots. Straight blue lines represent colour-cuts of WDMS binaries for each colour-colour diagram.

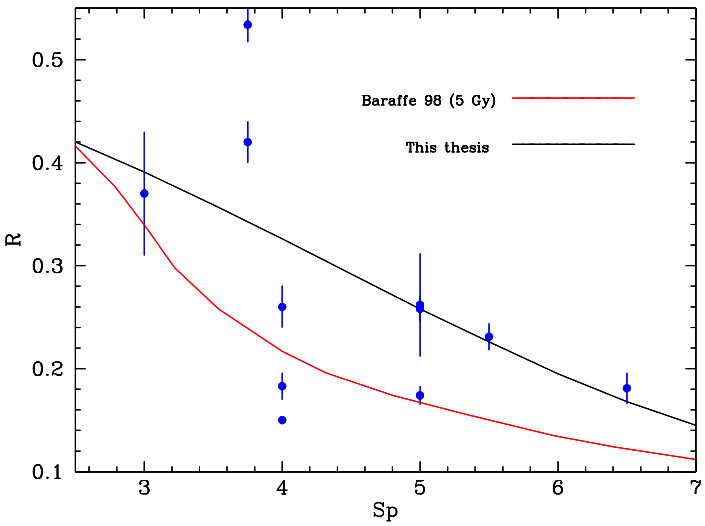

Figure 10.9: Sp type vs R for M stars in eclipsing WDMS binaries [blue dots, Pyrzas et al., 2008, and references therein]. The black solid line is the empirical $Sp-R$ relation for M stars obtained in Chapter 7, the solid red line is the theoretical $Sp-R$ relation from Baraffe et al. [1998].

identified SDSS PCEBs and wide WDMS binaries, and the number of measured PCEB orbital periods. Hence we will be able to improve the statistics of the distributions presented in the above sections, and constrain further the theory of evolution of compact binaries: to confirm or disprove that MB is indeed disrupted we need to identify at least 100 new PCEBs; to identify the long period end of the PCEB population we need at least $\sim$ 50 PCEBs with long orbital periods (5-50 days); in order to estimate the strength of AML we need orbital periods of $\sim$ 300 PCEBs at different times of PCEB evolution ($T_{\rm eff}$ $\sim$ 8000-40000 K, which translates to white dwarf cooling ages of $\sim 5\times10^6$ to $\sim 2\times10^9$). To sum up, solving the three most important problems in close binary evolution needs a sample of $\sim 300-500$ systems.

10.8.2 A catalogue of WDMS binaries from SDSS DR 7

SDSS DR 7 has just been released, and it is expected that a significant number of new WDMS binaries have been observed. An analysis such as the one described in Chapter 9 is desirable to identify these new systems. This will consequently update our catalogue of WDMS binaries, and also provide new and updated distributions of WDMS binary stel-

lar parameters. In addition, the number of WDMS binaries available for future follow-up studies will also increase.

10.8.3 Physical properties of white dwarfs and M-dwarfs

The number of eclipsing WDMS binaries has increased in the last few years, and more eclipsing systems remain to be discovered. Nevertheless both the $Sp-R$ relation provided in Chapter 7, and the theoretical Baraffe et al. [1998] $Sp-R$ relation still can not match the observational results (see Fig. 10.9). The same occurs in both the $M-R$ relation of white dwarfs and single M stars (see Chapter 2). The identification of new eclipsing WDMS binaries will provide new empirical values that will help in constraining the $Sp-R$ relation for M stars, and also the $M-R$ relations of both white dwarfs and M-dwarfs.

10.8.4 WDMS colour-cuts

A good colour-cut selection of WDMS binaries is necessary to identify those WDMS binaries that have not been spectroscopically followed-up in SDSS. In this thesis it has been demonstrated that the combination of GALEX-SDSS-UKIDSS magnitudes is a powerful tool to isolate WDMS binaries from other stellar sources. The use of red and blue surveys such as GALEX and UKIDSS will also increase the number of WDMS binaries containing cold white dwarfs and later-type companions, and consequently will help in solving the biassed selection of WDMS binaries in SDSS.

10.8.5 Future Surveys

In the following years different sky surveys from SDSS will provide data releases that might help in improving the study of WDMS binaries. Thus, surveys such as Pan-STARRS, and LSST will map very large sky areas in search of objects that move and/or vary, among them eclipsing WDMS binaries and CVs. Accurate distances will be determined for approximately 2.5 million stars by the GAIA mission. Identifying SDSS WDMS binaries among these objects will fix the distance of these systems, and consequently their white dwarf radius, which would help in constraining also the white dwarf $M-R$ relation (since we determined their masses in an independent way).

Bibliography

Abazajian, K., et al., 2003, AJ, 126, 2081

Abazajian, K., et al., 2004, AJ, 128, 502

Abazajian, K., et al., 2005, ApJ, 129, 1755

Adelman-McCarthy, J. K., et al., 2006, ApJS, 162, 38

Adelman-McCarthy, J. K., et al., 2007, ApJ, 172, 634

Adelman-McCarthy, J. K., et al., 2008, ApJ, 175, 297

Afşar, M., Ibanoğlu, C., 2008, MNRAS, 1232

Ak, T., Bilir, S., Ak, S., Eker, Z., 2008, New Astronomy, 13, 133

Andronov, N., Pinsonneault, M., Sills, A., 2003, ApJ, 582, 358

Augusteijn, T., Greimel, R., van den Besselaar, E. J. M., Groot, P. J., Morales-Rueda, L., 2008, A&A, 486, 843

Aungwerojwit, A., Gänsicke, B. T., Rodríguez-Gil, P., Hagen, H.-J., Giannakis, O., Papadimitriou, C., Allende Prieto, C., Engels, D., 2007, A&A, 469, 297

Baraffe, I., Chabrier, G., 1996, ApJ Lett., 461, L51

Baraffe, I., Chabrier, G., Allard, F., Hauschildt, P. H., 1998, A&A, 337, 403

Baraffe, I., Chabrier, G., Allard, F., Hauschildt, P. H., 2002, A&A, 382, 563

Baraffe, I., Chabrier, G., Barman, T. S., Allard, F., Hauschildt, P. H., 2003, A&A, 402, 701

Barker, J., Kolb, U., 2003, MNRAS, 340, 623

Bayless, A. J., Orosz, J. A., 2006, ApJ, 651, 1155

Beatty, T. G., et al., 2007, ApJ, 663, 573

Beer, M. E., Dray, L. M., King, A. R., Wynn, G. A., 2007, MNRAS, 375, 1000

Berger, D. H., et al., 2006, ApJ, 644, 475

Berger, E., 2002, ApJ, 572, 503

Bergeron, P., Saumon, D., Wesemael, F., 1995a, ApJ, 443, 764

Bergeron, P., Wesemael, F., Beauchamp, A., 1995b, PASP, 107, 1047

Bergeron, P., Leggett, S. K., Ruiz, M., 2001, ApJS, 133, 413

Berriman, G., Reid, N., 1987, MNRAS, 227, 315

Bertin, E., Arnouts, S., 1996, A&AS, 117, 393

Bessell, M. S., 1991, AJ, 101, 662

Beuermann, K., 2006, A&A, 460, 783

Beuermann, K., Baraffe, I., Kolb, U., Weichhold, M., 1998, A&A, 339, 518

Bochanski, J. J., West, A. A., Hawley, S. L., Covey, K. R., 2007, AJ, 133, 531

Bodenheimer, P., Taam, R. E., 1984, ApJ, 280, 771

Caillault, J., Patterson, J., 1990, AJ, 100, 825

Cardini, D., Cassatella, A., 2007, ApJ, 666, 393

Carrier, F., Barblan, F., Burki, G., Bartholdi, P., Nicolet, B., 2003, A&A, 398, 1073

Chabrier, G., 2003, PASP, 115, 763

Chabrier, G., Baraffe, I., 2000, Annual Reviews, 38, 337

Chabrier, G., Brassard, P., Fontaine, G., Saumon, D., 2000, ApJ, 543, 216

Chabrier, G., Baraffe, I., Allard, F., Hauschildt, P. H., 2005, ArXiv Astrophysics e-prints

Chabrier, G., Gallardo, J., Baraffe, I., 2007, A&A, 472, L17

Chandrasekhar, S., 1935, MNRAS, 95, 207

Creevey, O. L., et al., 2005, ApJ Lett., 625, L127

Cruz, K. L., Reid, I. N., 2002, ApJ, 123, 2828

Cushing, M. C., Rayner, J. T., Vacca, W. D., 2005, ApJ, 623, 1115

D'Antona, F., Mazzitelli, I., 1990, Annual Reviews, 28, 139

Davis, P. J., Kolb, U., Willems, B., Gänsicke, B. T., 2008, MNRAS, 1028

de Kool, M., 1990, ApJ, 358, 189

de Kool, M., 1992, A&A, 261, 188

de Kool, M., Ritter, H., 1993, A&A, 267, 397

De Marco, O., Hillwig, T. C., Smith, A. J., 2008, ApJ, 136, 323

Delfosse, X., Forveille, T., Perrier, C., Mayor, M., 1998, A&A, 331, 581

Delfosse, X., Forveille, T., Mayor, M., Burnet, M., Perrier, C., 1999, A&A, 341, L63

Dewi, J. D. M., Tauris, T. M., 2000, A&A, 360, 1043

Dhillon, V., et al., 2002, in Gänsicke, B. T., Beuermann, K., Reinsch, K., eds., The Physics of Cataclysmic Variables and Related Objects, ASP Conf. Ser. 261, p. 672

Dobbie, P. D., et al., 2006, MNRAS, 369, 383

Downes, R. A., Mateo, M., Szkody, P., Jenner, D. C., Margon, B., 1986, ApJ, 301, 240

Dye, S., et al., 2006, MNRAS, 372, 1227

Eggleton, P. P., 1983, ApJ, 268, 368

Eibe, M. T., 1998, A&A, 337, 757

Eisenstein, D. J., et al., 2006, ApJS, 167, 40

Farihi, J., Becklin, E. E., Zuckerman, B., 2005, ApJS, 161, 394

Filippenko, A., Greenstein, J. L., 1984, PASP, 96, 530

Finley, D. S., Koester, D., Basri, G., 1997, ApJ, 488, 375

Gänsicke, B. T., Araujo-Betancor, S., Hagen, H.-J., Harlaftis, E. T., Kitsionas, S., Dreizler, S., Engels, D., 2004, A&A, 418, 265

Golimowski, D. A., et al., 2004, AJ, 127, 3516

Grether, D., Lineweaver, C. H., 2006, ApJ, 640, 1051

Haefner, R., Fiedler, A., Butler, K., Barwig, H., 2004, A&A, 428, 181

Hamada, T., Salpeter, E. E., 1961, ApJ, 134, 683

Hameury, J. M., Lasota, J. P., King, A. R., Ritter, H., 1988, MNRAS, 231, 535

Han, Z., Podsiadlowski, P., Eggleton, P. P., 1994, MNRAS, 270, 121

Han, Z., Podsiadlowski, P., Maxted, P. F. L., Marsh, T. R., Ivanova, N., 2002, MNRAS, 336, 449

Hansen, B., 2004, Physics Reports, 399, 1

Hansen, B. M. S., 1999, ApJ, 520, 680

Harris, H. C., et al., 2003, ApJ, 126, 1023

Hewett, P. C., Warren, S. J., Leggett, S. K., Hodgkin, S. T., 2006, MNRAS, 367, 454

Hjellming, M. S., Taam, R. E., 1991, ApJ, 370, 709

Holberg, J. B., Sion, E. M., Oswalt, T., McCook, G. P., Foran, S., Subasavage, J. P., 2008, ApJ, 135, 1225

Horne, K., 1986, PASP, 98, 609

Howell, S. B., Rappaport, S., Politano, M., 1997, MNRAS, 287, 929

Howell, S. B., Nelson, L. A., Rappaport, S., 2001, ApJ, 550, 897

Hubeny, I., Lanz, T., 1995, ApJ, 439, 875

Iben, I. J., Livio, M., 1993, PASP, 105, 1373

Ivanova, N., Taam, R. E., 2003, ApJ, 599, 516

Jeffries, R. D., Stevens, I. R., 1996, MNRAS, 279, 180

Kawka, A., Vennes, S., 2003, AJ, 125, 1444

Kepler, S. O., Castanheira, B. G., Costa, A. F. M., Koester, D., 2006, MNRAS, 372, 1799

Kiraga, M., Stepien, K., 2007, Acta Astronomica, 57, 149

Kirkpatrick, J. D., Henry, T. J., McCarthy, D. W., J., 1991, ApJS, 77, 417

Koester, D., 2002, A&AR, 11, 33

Koester, D., Wilken, D., 2006, A&A, 453, 1051

Koester, D., Schulz, H., Weidemann, V., 1979, A&A, 76, 262

Koester, D., Napiwotzki, R., Voss, B., Homeier, D., Reimers, D., 2005, A&A, 439, 317

Koester, D., Kepler, S. O., Kleinman, S. J., Nitta, A., 2008, ArXiv e-prints

Kolb, U., 1993, A&A, 271, 149

Kolb, U., Baraffe, I., 1999, MNRAS, 309, 1034

Lada, C. J., 2006, ApJ, 640, L63

Lane, B. F., Boden, A. F., Kulkarni, S. R., 2001, ApJ Lett., 551, L81

Langer, N., Deutschmann, A., Wellstein, S., Höflich, P., 2000, A&A, 362, 1046

Lawrence, A., et al., 2007, MNRAS, 379, 1599

Leggett, S. K., Allard, F., Berriman, G., Dahn, C. C., Hauschildt, P. H., 1996, ApJS, 104, 117

Leggett, S. K., Allard, F., Geballe, T. R., Hauschildt, P. H., Schweitzer, A., 2001, ApJ, 548, 908

Leto, G., Pagano, I., Linsky, J. L., Rodonò, M., Umana, G., 2000, A&A, 359, 1035

Liebert, J., Bergeron, P., Holberg, J. B., 2005, ApJS, 156, 47

Livio, M., 1989, in Cassatella, A., Viotti, R., eds., Physics of Classical Novae, no. 369 in LNP, Springer, Heidelberg, p. 342

Livio, M., 1996, in Milone, E. F., Mermilliod, J.-C., eds., The Origins, Evolution, and Destinies of Binary Stars in Clusters, vol. 90 of *Astronomical Society of the Pacific Conference Series*, p. 291

Livio, M., Soker, N., 1984, MNRAS, 208, 783

Livio, M., Soker, N., 1988, ApJ, 329, 764

López-Morales, M., 2007, ApJ, 660, 732

Maceroni, C., Montalbán, J., 2004, A&A, 426, 577

Marks, P. B., Sarna, M. J., 1998, MNRAS, 301, 699

Marsh, T. R., 1989, PASP, 101, 1032

Marsh, T. R., Duck, S. R., 1996, MNRAS, 278, 565

Marsh, T. R., Robinson, E. L., Wood, J. H., 1994, MNRAS, 266, 137

Marsh, T. R., Dhillon, V. S., Duck, S. R., 1995, MNRAS, 275, 828

Martin, D. C., et al., 2005, ApJ Lett., 619, L1

Martín, E. L., Delfosse, X., Basri, G., Goldman, B., Forveille, T., Osorio, M. R. Z., 1999, AJ, 118, 2466

Mateo, M., Szkody, P., Bolte, M., 1985, PASP, 97, 45

Maxted, P. f. L., Heber, U., Marsh, T. R., North, R. C., 2001, MNRAS, 326, 1391

Maxted, P. F. L., Marsh, T. R., Morales-Rueda, L., Barstow, M. A., Dobbie, P. D., Schreiber, M. R., Dhillon, V. S., Brinkworth, C. S., 2004, MNRAS, 355, 1143

Maxted, P. F. L., Napiwotzki, R., Dobbie, P. D., Burleigh, M. R., 2006, Nat, 442, 543

Maxted, P. F. L., O'Donoghue, D., Morales-Rueda, L., Napiwotzki, R., 2007, MNRAS, 376, 919

Mestel, L., 1952, MNRAS, 112, 583

Mestel, L., Spruit, H. C., 1987, MNRAS, 226, 57

Meyer, F., Meyer-Hofmeister, E., 1979, A&A, 78, 167

Mihalas, D., 1970, Stellar atmospheres, W. H. Freeman & Co, San Francisco

Montagnier, G., et al., 2006, A&A, 460, L19

Morales, J. C., Ribas, I., Jordi, C., 2008, A&A, 478, 507

Morrissey, P., et al., 2005, ApJ, 619, L7

Mullan, D. J., MacDonald, J., 2001, ApJ, 559, 353

Naylor, T., Allan, A., Long, K. S., 2005, MNRAS, 361, 1091

Nebot Gómez-Morán, A., et al., 2009, ArXiv e-prints

Nelemans, G., Tout, C. A., 2005, MNRAS, 356, 753

Nelemans, G., Verbunt, F., Yungelson, L. R., Portegies Zwart, S. F., 2000, A&A, 360, 1011

O'Brien, M. S., Bond, H. E., Sion, E. M., 2001, ApJ, 563, 971

O'Donoghue, D., Koen, C., Kilkenny, D., Stobie, R. S., Koester, D., Bessell, M. S., Hambly, N., MacGillivray, H., 2003, MNRAS, 345, 506

Oke, J. B., 1990, AJ, 99, 1621

Orosz, J. A., Wade, R. A., Harlow, J. J. B., Thorstensen, J. R., Taylor, C. J., Eracleous, M., 1999, AJ, 117, 1598

Osterbrock, D. E., Fulbright, J. P., Martel, A. R., Keane, M. J., Trager, S. C., Basri, G., 1996, PASP, 108, 277

Osterbrock, D. E., Fulbright, J. P., Bida, T. A., 1997, PASP, 109, 614

Paczyński, B., 1971, ARA&A, 9, 183

Paczynski, B., 1976, in Eggleton, P., Mitton, S., Whelan, J., eds., IAU Symp. 73: Structure and Evolution of Close Binary Systems, D. Reidel, Dordrecht, p. 75

Paczynski, B., Sienkiewicz, R., 1981, ApJ, 248, L27

Panei, J. A., Althaus, L. G., Benvenuto, O. G., 2000, MNRAS, 312, 531

Panei, J. A., Althaus, L. G., Chen, X., Han, Z., 2007, MNRAS, 382, 779

Parthasarathy, M., Branch, D., Jeffery, D. J., Baron, E., 2007, New Astronomy Review, 51, 524

Patterson, J., 1998, PASP, 110, 1132

Politano, M., 1996, ApJ, 465, 338

Politano, M., 2004, ApJ, 604, 817

Politano, M., Weiler, K. P., 2006, ApJ Lett., 641, L137

Politano, M., Weiler, K. P., 2007, ApJ, 665, 663

Pont, F., Melo, C. H. F., Bouchy, F., Udry, S., Queloz, D., Mayor, M., Santos, N. C., 2005, A&A, 433, L21

Pretorius, M. L., Knigge, C., O'Donoghue, D., Henry, J. P., Gioia, I. M., Mullis, C. R., 2007, MNRAS, 382, 1279

Provencal, J. L., Shipman, H. L., Hog, E., Thejll, P., 1998, ApJ, 494, 759

Provencal, J. L., Shipman, H. L., Koester, D., Wesemael, F., Bergeron, P., 2002, ApJ, 568, 324

Pyrzas, S., et al., 2008, ArXiv e-prints

Rappaport, S., Joss, P. C., Webbink, R. F., 1982, ApJ, 254, 616

Rappaport, S., Joss, P. C., Verbunt, F., 1983, ApJ, 275, 713

Raymond, S. N., et al., 2003, AJ, 125, 2621

Rebassa-Mansergas, A., Gänsicke, B. T., Rodríguez-Gil, P., Schreiber, M. R., Koester, D., 2007, MNRAS, 382, 1377

Rebassa-Mansergas, A., et al., 2008, MNRAS, 1112

Rechenberg, I., 1994, Evolutionsstrategie '94, Froomann–Holzboog, Stuttgart

Reid, I. N., 1996, ApJ, 111, 2000

Reid, I. N., Cruz, K. L., Allen, P. R., 2007, ApJ, 133, 2825

Reid, I. N., Cruz, K. L., Kirkpatrick, J. D., Allen, P. R., Mungall, F., Liebert, J., Lowrance, P., Sweet, A., 2008, ApJ, 136, 1290

Ribas, I., 2006, ASS, 304, 89

Ribas, I., Morales, J. C., Jordi, C., Baraffe, I., Chabrier, G., Gallardo, J., 2008, Memorie della Societa Astronomica Italiana, 79, 562

Richards, G. T., et al., 2002, AJ, 123, 2945

Ricker, P. M., Taam, R. E., 2008, ApJ, 672, L41

Ringwald, F. A., 1996, in Evans, A., Wood, J. H., eds., Cataclysmic Variables and Related Objects, no. 158 in IAU Coll., Kluwer, Dordrecht, p. 89

Ritter, H., Kolb, U., 2003, A&A, 404, 301

Sarna, M. J., Marks, P. B., Smith, R. C., 1995, MNRAS, 276, 1336

Scargle, J. D., 1982, ApJ, 263, 835

Schechter, P. L., Mateo, M., Saha, A., 1993, PASP, 105, 1342

Schenker, K., King, A. R., Kolb, U., Wynn, G. A., Zhang, Z., 2002, MNRAS, 337, 1105

Schmidt, H., 1996, A&A, 311, 852

Schreiber, M. R., Gänsicke, B. T., 2003, A&A, 406, 305

Schreiber, M. R., Nebot Gomez-Moran, A., Schwope, A. D., 2007, in Napiwotzki, R., Burleigh, M. R., eds., 15th European Workshop on White Dwarfs, vol. 372 of *Astronomical Society of the Pacific Conference Series*, p. 459

Schreiber, M. R., Gänsicke, B. T., Southworth, J., Schwope, A. D., Koester, D., 2008, A&A, 484, 441

Schwarzenberg-Czerny, A., 1989, MNRAS, 241, 153

Schwarzenberg-Czerny, A., 1996, ApJ Lett., 460, L107

Ségransan, D., Kervella, P., Forveille, T., Queloz, D., 2003, A&A, 397, L5

Silvestri, N. M., et al., 2006, AJ, 131, 1674

Silvestri, N. M., et al., 2007, ApJ, 134, 741

Sion, E. M., Greenstein, J. L., Landstreet, J. D., Liebert, J., Shipman, H. L., Wegner, G. A., 1983, ApJ, 269, 253

Soker, N., Harpaz, A., 2003, MNRAS, 343, 456

Soker, N., Livio, M., Harpaz, A., 1984, MNRAS, 210, 189

Southworth, J., Gänsicke, B. T., Marsh, T. R., de Martino, D., Hakala, P., Littlefair, S., Rodríguez-Gil, P., Szkody, P., 2006, MNRAS, 373, 687

Spruit, H. C., Ritter, H., 1983, A&A, 124, 267

Spruit, H. C., Weiss, A., 1986, A&A, 166, 167

Steinfadt, J. D. R., Bildsten, L., Howell, S. B., 2008, ApJ Lett., 677, L113

Stoughton, C., et al., 2002, AJ, 123, 485

Strauss, M. A., et al., 2002, AJ, 124, 1810

Szkody, P., et al., 2004, AJ, 128, 1882

Taam, R. E., Bodenheimer, P., 1989, ApJ, 337, 849

Taam, R. E., Bodenheimer, P., 1991, ApJ, 373, 246

Taam, R. E., Ricker, P. M., 2006, ArXiv Astrophysics e-prints

Taam, R. E., Spruit, H. C., 2001, ApJ, 561, 329

Taam, R. E., Bodenheimer, P., Ostriker, J. P., 1978, ApJ, 222, 269

Tappert, C., Gänsicke, B. T., Schmidtobreick, L., Aungwerojwit, A., Mennickent, R. E., Koester, D., 2007, A&A, 474, 205

Terman, J. L., Taam, R. E., Hernquist, L., 1994, in Bulletin of the American Astronomical Society, vol. 26 of *Bulletin of the American Astronomical Society*, p. 1520

Townsley, D. M., Gaensicke, B. T., 2008, ArXiv e-prints

Tuffs, R. J., Popescu, C. C., Völk, H. J., Kylafis, N. D., Dopita, M. A., 2004, A&A, 419, 821

Tutukov, A. V., Yungelson, L. R., 1979, Acta Astronomica, 29, 665

van den Besselaar, E. J. M., Roelofs, G. H. A., Nelemans, G. A., Augusteijn, T., Groot, P. J., 2005, A&A, 434, L13

van den Besselaar, E. J. M., et al., 2007, A&A, 466, 1031

van der Sluys, M. V., Verbunt, F., Pols, O. R., 2006, A&A, 460, 209

Vennes, S., Thorstensen, J. R., Polomski, E. F., 1999, ApJ, 523, 386

Verbunt, F., Zwaan, C., 1981, A&A, 100, L7

Vogel, J., Schwope, A. D., Gänsicke, B. T., 2007, A&A, 464, 647

Wade, R. A., Horne, K., 1988, ApJ, 324, 411

Webbink, R. F., 2008, Short-Period Binary Stars: Observations, Analyses, and Results, 233

West, A. A., Basri, G., 2008, ArXiv e-prints

West, A. A., Hawley, S. L., Bochanski, J. J., Covey, K. R., Reid, I. N., Dhital, S., Hilton, E. J., Masuda, M., 2008, ApJ, 135, 785

West, A. A., et al., 2004, AJ, 128, 426

Willems, B., Kolb, U., 2004, A&A, 419, 1057

Wolff, B., Koester, D., Montgomery, M. H., Winget, D. E., 2002, A&A, 388, 320

Wood, M. A., 1995, in Koester, D., Werner, K., eds., White Dwarfs, no. 443 in LNP, Springer, Heidelberg, p. 41

York, D. G., et al., 2000, AJ, 120, 1579